ADAPTIVE DISPERSION COMPENSATION AND ULTRASONIC IMAGING FOR STRUCTURAL HEALTH MONITORING

A Dissertation
Presented to
The Academic Faculty

by

James Stroman Hall

In Partial Fulfillment
of the Requirements for the Degree
Doctor of Philosophy in the
School of Electrical and Computer Engineering

Georgia Institute of Technology
August 2011

ADAPTIVE DISPERSION COMPENSATION AND ULTRASONIC IMAGING FOR STRUCTURAL HEALTH MONITORING

Approved by:

Jennifer E. Michaels, Advisor
School of Electrical and Computer Engineering
Georgia Institute of Technology

James H. McClellan
School of Electrical and Computer Engineering
Georgia Institute of Technology

Laurence J. Jacobs
School of Civil and Environmental Engineering
Georgia Institute of Technology

Maysam Ghovanloo
School of Electrical and Computer Engineering
Georgia Institute of Technology

Michael J. Leamy
George W. Woodruff School of Mechanical Engineering
Georgia Institute of Technology

Thomas E. Michaels
School of Electrical and Computer Engineering
Georgia Institute of Technology

Date Approved: June 23, 2011

ACKNOWLEDGMENTS

First and foremost, I would like to thank my advisor, Prof. Jennifer E. Michaels. I am most appreciative of your guidance over the last four years, from the basics of elastic waves to both short- and long-term career advice. I have grown a tremendous amount, both professionally and personally, and am deeply grateful for your mentorship, patience, and support.

I would also like to thank my Ph.D. committee for their valuable insight and suggestions: Prof. James H. McClellan, Prof. Laurence J. Jacobs, Prof. Maysam Ghovanloo, Prof. Thomas E. Michaels, and Prof. Michael J. Leamy. Your time, efforts, and constructive criticisms are sincerely appreciated.

I am also grateful for the financial support provided by NASA's Graduate Student Research Program. As part of this program, I have had the great honor of working with Dr. Janine Captain, Dr. Mark Nurge, Dr. Robert Youngquist, and Stan Starr in the Applied Physics Lab at NASA's Kennedy Space Center. Thank you all for such a fantastic experience. From blast analysis and ultrasonic air flow estimation to *in situ* dielectric spectroscopy, I learned a tremendous amount and truly enjoyed working on such a wide range of applications.

I had the privilege of spending the Fall 2009 semester at the Georgia Tech - Lorraine campus in Metz, France. I would like to thank Prof. Yves H. Berthelot for helping to make that happen. I would also like to thank Prof. Nico F. Declercq and Dr. L. "Satya" Satyanarayan for their laboratory support and guidance. A special thanks to Peter McKeon and Sarah Herbison for their cultural and linguistic assistance throughout my time in France, you both really made my study abroad experience something that I will remember and cherish for many years to come.

After spending four years in the U.S. Navy and another four years in industry, the

decision to return to school was not an easy one. I would like to thank Dr. Pat Martin and Dr. Jerry Brand at Harris, Corp., for their mentorship. Your openness and encouragement to undertake this endeavor is very much appreciated. Dr. Brand, you made it clear to me that the single most important factor in choosing the right research program was not the research itself, *but my choice of advisor*. I took that advice to heart and could not have been more happy with the results. My most sincere thanks for your honest insight.

I would also like to acknowledge the Georgia Tech Sport Parachute Club for helping me to keep my sanity for the past four years. In particular, I would like to thank John Nahabedian, my 2-way partner on the Flying Bricks team, and Greg Lennartz, Nathan Briggs, and Christopher Wallace who made up the 4-way GT Wreckless team with me. Your teamwork and comraderie sincerely made the two silver medals that we won at the 2008 and 2010 USPA National Collegiate Parachuting Championships something to remember for the rest of my life. I have found formation skydiving to provide a level of excitement, satisfaction, and fulfillment that I never knew before my first jump and I am not likely to have taken that path without you.

Finally, I would like to thank my wife, Natalie. Your encouragement to quit my job and pursue a Ph.D. at Georgia Tech was a key factor in my decision to do so. I am so thankful for your unwavering support throughout this process, from the financial burdens that we have had to endure to the weekends, weeks, and even months apart. I could not have done this without you and am grateful everyday to have you in my life.

TABLE OF CONTENTS

LIST OF TABLES

LIST OF FIGURES

LIST OF SYMBOLS OR ABBREVIATIONS

b Unknown integer variable

c Context-dependent variable with the following notation:
- c Potential value of $\hat{c}_\kappa$
- $\hat{c}$ Imaging performance metric based on exponential fit to pixel values as a function of distance from known defect location
- c_g Frequency-independent group velocity
- $c_g(\omega)$ Frequency-dependent group velocity
- $c_{\min}$ Minimum group velocity for any frequency considered
- $c_p(\omega)$ Frequency-dependent phase velocity
- $\hat{c}_\kappa$ Null space coefficient corresponding to $\vec{\mathbf{a}}_\kappa^{\neq}$

d Propagation distance with the following subscript and superscript definitions:
- d_i Total propagation distance from transmitter to the i^{th} scatterer to receiver
- $d_\times$ Total propagation distance from transmitter to defect to receiver
- d_δ Path accuracy, indicating to what degree the propagation path is known
- d_t Uncertainty in propagation distance / transducer location
- d_{ixy} Distance from the i^{th} transducer to pixel location (x,y)
- d_{mxy} Total propagation distance from transmitter to pixel location (x,y) to receiver for the m^{th} trasmitter-receiver pair
- $d_{mxy}^{\times}$ Product of propagation distances from transmitter to pixel (x,y) and pixel (x,y) to receiver for the m^{th} transducer pair
- $d_{\max}$ Maximum propagation distance for any received signal
- $d_\varkappa$ Coefficient corresponding to the projection of $\vec{\mathbf{d}}_{\text{m}}$ onto $\vec{\mathbf{v}}_{\text{TR}}^{\varkappa}$

D_{xy} State variable indicating that damage is present at pixel location (x,y)

e Weighting coefficient with the following subscript definitions:
- e_{ijxy} Weighting coefficient for pixel location (x,y) associated with the i^{th} transmitter and j^{th} receiver
- e_{mxy} Weighting coefficient for pixel location (x,y) associated with the m^{th} transducer pair

e Euler's number, base of the natural logarithm

$\text{erf}(x)$ Error function

f Frequency (Hz)

$f\left(\vec{\mathbf{b}},\vec{\mathbf{h}}\right)$ Nonlinear function that performs a floor operation on each element of $\vec{\mathbf{b}}$ for which $\vec{\mathbf{h}}$ is a zero, and a ceiling operation on each element of $\vec{\mathbf{b}}$ for which $\vec{\mathbf{h}}$ is a one

$\gcd(\cdot)$ Greatest common denominator for all vector elements within the parentheses

F_s Sampling frequency

$G(\omega)$ Propagation-specific components of $M(\omega)$

$I_0(z)$ Modified Bessel function of the first kind

j Square root of -1

$k(\omega)$ Wavenumber (radians/mm)
- $k(\omega)$ Wavenumber as a function of frequency
- $k_\delta(k)$ Wavenumber *error* as a function of wavenumber

m Measured (noisy) data with the following associated notation:
- $m(t)$ Time-domain representation of measured data
- $\hat{m}(x)$ Distance-domain (a.k.a. spatial-domain) representation of measured data
- $\bar{m}(x)$ Distance-domain representation of measured data *after frequency-domain deconvolution*

M Measured (noisy) data with the following associated notation:
- $\hat{M}$ Actual, or true value of underlying measurement value (noise-free version)
- $M(\omega)$ Frequency-domain representation of measured data
- $\bar{M}(\omega)$ Frequency-domain representation of measured data *after deconvolution*
- $M(k)$ Wavenumber-domain representation of measured data
- $\bar{M}(k)$ Wavenumber-domain representation of measured data *after deconvolution*

n Quantity indicated by subscript and superscript:
- n_m Number of measured signals
- n_n Number of time-domain samples
- n_r Number of unique receivers
- n_s Number of unique sensors
- n_t Number of unique transmitters
- n_x Number of discrete pixel location in the x-direction
- n_y Number of discrete pixel location in the y-direction
- n_z Arbitrary quantity corresponding to one of the above definitions
- $n_{TR}^{\shortparallel}$ Dimensionality of column space of $\mathbf{Q}_{\mathrm{TR}}$
- $n_{TR}^{\neq}$ Dimensionality of null space of $\mathbf{Q}_{\mathrm{TR}}$
- $n_{\tau\rho}^{\shortparallel}$ Dimensionality of column space of $\mathbf{Q}_{\tau\rho}$
- $n_{\tau\rho}^{\neq}$ Dimensionality of null space of $\mathbf{Q}_{\tau\rho}$

N Additive noise term with the following subscript definitions:
- N Noise associated with measured data, M
- $N_{|\cdot|}$ Noise associated with magnitude of measured data, $|M|$
- $N_{\ln|\cdot|}$ Noise associated with log-magnitude of measured data, $\ln|M|$)
- $N_{\Re}$ *Real* component of N
- $N_{\Im}$ *Imaginary* component of N

$p(x)$ Probability density function (PDF) with the following variations:
- $p(x, y)$ Two-dimensional PDF in Cartesian coordinates
- $p_M(r, \theta)$ Two-dimensional PDF in polar coordinates of measured data, M
- $p_{|M|}(r)$ PDF of magnitude of measured data, $|M|$
- $p_{|\cdot|}(\nu)$ PDF of *noise* associated with magnitude of measured data, $N_{|\cdot|}$
- $p_{\ln|\cdot|}(\nu)$ PDF of *noise* associated with log-magnitude of measured data, $N_{\ln|\cdot|}$
- $p_{\angle}(\theta)$ PDF of phase noise of measured data, M

$p(\omega)$ Frequency-dependent propagation loss

P Pixel value with the following superscript and subscript notation:
- $\hat{P}_{xy}$ Ratio of pixel value when damage is present at (x,y) over the maximum pixel value at (x,y) when damage is present elsewhere in the structure
- $P(x)$ Pixel value as a function of distance from known damage location
- $P_{xy}(D_{ab})$ Pixel value at pixel location (x,y) when damage is present at pixel location (a,b)
- P_{xy}^{DS} Pixel computed per conventional (delay and sum) imaging for pixel location (x,y)
- P_{xy}^{MV} Pixel computed per minimum variance imaging for pixel location (x,y)

Q Signal-to-noise ratio with the following subscript definitions:
- $Q_{\min}$ Minimum SNR for any frequency considered
- $Q(\omega)$ SNR for a specific frequency measurement
- Q_{ij} SNR for the i^{th} column (FFT frequency bin) and j^{th} received signal

r Radius variable

$R(\omega)$ Receiver-specific components of $M(\omega)$

$s(t)$ Time-domain representation of differenced signals with the following superscript and subscript definitions:
- $s_{ij}(t)$ Differenced signals corresponding to transmission from the i^{th} transducer and reception at the j^{th} transducer
- $\hat{s}_{ij}(t)$ Hilbert transform of $s_{ij}(t)$
- $s_{ij}^{\text{ENV}}(t)$ Envelope of the analytic representation of $s_{ij}(t)$
- $s_m(t)$ Differenced signal corresponding to the m^{th} transmitter-receiver pair

$S(\omega)$ Frequency-domain representation of differenced signals
- $\hat{S}(\omega)$ Frequency-domain representation of a *backpropagated*, differenced signal

t Time variable

T_{xy} Threshold for pixel location (x,y)

$T(\omega)$ Transmitter-specific components of $M(\omega)$

$w(t)$ Time-domain window function

x Distance variable corresponding to the x-direction with the following subscript definitions:
- x_i i^{th} x-coordinate
- $x_{r(m)}$ x-coordinate of the receiver for the m^{th} transmitter-receiver pair
- $x_{t(m)}$ x-coordinate of the transmitter for the m^{th} transmitter-receiver pair

$x(t)$ Time-domain signal common to all recorded measurements

X Arbitrary propagating guided wave
- $X(\omega)$ Frequency-domain representation of $x(t)$
- $X(k)$ Wavenumber-domain representation of $x(t)$

y Distance variable corresponding to the y-direction with the following subscript definitions:
- y_i i^{th} y-coordinate
- $y_{r(m)}$ y-coordinate of the receiver for the m^{th} transmitter-receiver pair
- $y_{t(m)}$ y-coordinate of the transmitter for the m^{th} transmitter-receiver pair

α Arbitrary scaling coefficient with the following subscript definitions:
- α_{BSS} Frequency-scaling coefficient for baseline-signal stretch ($\alpha_{\text{BSS}} \approx 1$)

$\gamma(x)$ Deconvolved and filtered transducer transfer function in the distance-domain

Γ Deconvolved and filtered transducer transfer function
- $\Gamma(\omega)$ Frequency-domain deconvolved and filtered transducer transfer function
- $\Gamma(k)$ Wavenumber-domain deconvolved and filtered transducer transfer function
- $\Gamma_\delta(k)$ Deconvolution error

ϵ Modeling error present in the unit look direction

θ Phase or argument of a complex value
- $\Delta\theta(\omega)$ Maximum angular deviation in phase for a specific frequency

κ Wavenumber-associated coefficient
- κ Frequency-independent component of $\vec{\mathbf{k}}$
- $\hat{\kappa}$ True value of frequency-independent component of $\vec{\mathbf{k}}$
- κ_δ Error in estimate of frequency-independent component of $\vec{\mathbf{k}}$
- κ_{min} Smallest value of κ_δ that results in an all-integer $\vec{\mathbf{b}}_\delta$
- κ_i Coefficient associated with the i^{th} power of k in polynomial representation of $k_\delta(k)$

λ_i — i^{th} eigenvalue of the autocorrelation matrix, $\mathbf{Z}_{xy}$ (eigenvalues are assumed to be arranged in descending order with λ_1 corresponding to the *largest* eigenvalue)

μ — Mean value of random variables with the following subscript definitions:
- $\mu^2_{\Re}$ Variance of real part of complex Gaussian random variable, N
- $\mu^2_{\Im}$ Variance of imaginary part of of complex Gaussian random variable, N

σ^2 — Noise variance with the following subscript definitions:
- $\sigma^2_{n_m}$ Average noise power observed across all measured signals
- σ^2_N Variance of complex Gaussian random variable, N
- $\sigma^2_{\Re}$ Variance of real part of complex Gaussian random variable, N
- $\sigma^2_{\Im}$ Variance of imaginary part of complex Gaussian random variable, N
- σ^2_{bi} Variance of noise in $\vec{\mathbf{N}}_{\text{bi}}$

τ — Time reference corresponding to the maximum amplitude of the excitation signal

ϕ — Squared-norm of the projection of $\vec{\mathbf{e}}_{xy}$ onto the null-space of $\vec{\mathbf{v}}_1$

ψ^m_{xy} — Scattering coefficient of an incident wave at pixel location (x,y) for the m^{th} transmitter-receiver pair

$\Psi(\omega)$ — Frequency-dependent transfer coefficient representing scattering and propagation loss
- $\Psi_{\text{ai}}(\omega)$ Scattering and propagation loss transfer function for the i^{th} scatterer associated with the ath data set ("b" for baseline or "c" for current, or test data)
- $\Psi_{\times}(\omega)$ Scattering and propagation loss transfer function associated with a defect

ω — Angular frequency
- $\omega(k)$ Angular frequency as a function of wavenumber
- $\Delta\omega$ Angular frequency spacing between FFT frequency bins

$\mathbf{A}$ — Matrix associated with the assumed propagation model with the following superscript and subscript definitions:

$\mathbf{A}$ $[3n_m \times 3(n_t + n_r + 1) + n_m]$ Matrix relating desired parameters to measured data

$\mathbf{A}^{\neq}$ $[3(n_t+n_r+1)+n_m \times 2n_{TR}^{\neq}+n_t+n_r+1]$ Orthonormal vectors spanning null space of $\mathbf{A}$

$\mathbf{A}_{\Re}^{\neq}$ $[3(n_t+n_r+1)+n_m \times n_{TR}^{\neq}]$ Columns of $\mathbf{A}^{\neq}$ associated with ambiguities in $\mathbf{T}_{\Re}$ and $\mathbf{R}_{\Re}$ estimates

$\mathbf{A}_{\Im}^{\neq}$ $[3(n_t+n_r+1)+n_m \times n_{TR}^{\neq}]$ Columns of $\mathbf{A}^{\neq}$ associated with ambiguities in $\mathbf{T}_{\Delta}$ and $\mathbf{R}_{\Delta}$ estimates

$\mathbf{A}_{\tau}^{\neq}$ $[3(n_t + n_r + 1) + n_m \times n_t]$ Columns of $\mathbf{A}^{\neq}$ associated with ambiguities in $\vec{\boldsymbol{\tau}}$ estimates

$\mathbf{A}_{\rho}^{\neq}$ $[3(n_t + n_r + 1) + n_m \times n_r]$ Columns of $\mathbf{A}^{\neq}$ associated with ambiguities in $\vec{\boldsymbol{\rho}}$ estimates

$\vec{\mathbf{a}}_{\kappa}^{\neq}$ $[3(n_t + n_r + 1) + n_m \times 1]$ Column of $\mathbf{A}^{\neq}$ associated with ambiguities in κ estimate

$\vec{\mathbf{b}}$ $[n_m \times 1]$ Vector containing unknown integer values with the following superscript and subscript definitions:

$\hat{\mathbf{b}}_{\mathrm{A}}^{=}$ Actual, or true, component of $\vec{\mathbf{b}}$ that resides in column space of $\mathbf{BA}^{\dagger}$

$\vec{\mathbf{b}}_{\delta}$ *All-integer* error term associated with an estimate of $\vec{\mathbf{b}}$

$\vec{\mathbf{b}}(\vec{\mathbf{c}})$ Estimate of $\vec{\mathbf{b}}$ as a function of null-space coefficients, $\vec{\mathbf{c}}$

$\vec{\mathbf{b}}_{\tau\rho}(\vec{\mathbf{c}}_{\tau\rho})$ Component of $\vec{\mathbf{b}}(\vec{\mathbf{c}})$ that is strictly dependent on $\vec{\mathbf{c}}_{\tau\rho}$ estimate

$\vec{\mathbf{b}}_{\kappa}(c)$ Component of $\vec{\mathbf{b}}(\vec{\mathbf{c}})$ that is strictly dependent on estimates of $\hat{c}_{\kappa}$

$\mathbf{B}$ Matrix associated with the all-integer $\vec{\mathbf{b}}$ vector

$\mathbf{B}$ $[n_m \times 3(n_t + n_r + 1) + n_m]$ Matrix used to isolate $\vec{\mathbf{b}}$ elements of $\mathbf{Z}$ ($[\ \mathbf{0}\quad \mathbf{I}_m\ ]$)

$\mathbf{B}_{\mathrm{A}}^{=}$ $[n_m \times n_w]$ Collection of n_w separate estimates of $\vec{\mathbf{b}}$ that reside in column space of $\mathbf{BA}^{\dagger}$

$\vec{\mathbf{c}}$ Vector of frequency-independent null-space coefficients with the following subscript definitions:

$\hat{\mathbf{c}}_b$ $[(n_t+n_r+1)\times 1]$ Null-space coefficients satisfying all-integer model constraints associated with $\vec{\mathbf{b}}$

$\vec{\mathbf{c}}_{\tau\rho}$ $[(n_t + n_r) \times 1]$ Null-space coefficients associated with $\vec{\boldsymbol{\tau}}$ and $\vec{\boldsymbol{\rho}}$ estimates

$\vec{\mathbf{c}}_{\tau}$ $[n_t \times 1]$ Null-space coefficients associated with $\vec{\boldsymbol{\tau}}$ estimates

$\vec{\mathbf{c}}_{\rho}$ $[n_r \times 1]$ Null-space coefficients associated with $\vec{\boldsymbol{\rho}}$ estimates

$\hat{c}_{\kappa}$ $[1 \times 1]$ Null-space coefficients associated with "true" value of κ

$\mathbf{C}$ Matrix of unknown coefficients with the following superscript and subscript definitions:

$\mathbf{C}_{\mathrm{A}}^{\neq}$ Unknown null space coefficients associated with $\mathbf{A}^{\neq}$

$\vec{\mathbf{d}}$ $[n_m \times 1]$ Propagation distance vector composed of d specific to each transducer pair with the following subscript and superscript definitions:

$\vec{\mathbf{d}}_{\mathrm{m}}$ *Measured* propagation distance vector

$\vec{\mathbf{d}}^{\vee}$ Logarithm of scaled propagation distance vector

$\vec{\mathbf{d}}_{\shortparallel}$ Coefficients corresponding to the projection of $\vec{\mathbf{d}}_{\mathrm{m}}$ onto the basis vectors, $\mathbf{Q}_{\mathrm{TR}}^{\shortparallel}$

$\hat{\mathbf{D}}_m$ $[n_x \times n_y]$ Matrix with elements corresponding to the distance from the transmitter of the m^{th} transmitter-receiver pair to each pixel location

$\check{\mathbf{D}}_m$ $[n_x \times n_y]$ Matrix with elements corresponding to the distance from the receiver of the m^{th} transmitter-receiver pair to each pixel location

$\vec{\mathbf{e}}_{xy}$ $[n_m \times 1]$ Steering vector associated with pixel location (x,y) composed of e_{mxy} weighting coefficients

$\mathbf{E}_m$ $[n_x \times n_y]$ Matrix with elements corresponding to the m^{th} element of the steering vector, $\vec{\mathbf{e}}_{xy}$, for each pixel location

$\mathbf{F}_m$ $[n_x \times n_y]$ Matrix with elements corresponding to the m^{th} element of the steering vector, $\vec{\mathbf{e}}_{xy}$, for each pixel location *prior to* normalization

$\vec{\mathbf{h}}$ $[n_m \times 1]$ Binary vector of ones and zeros indicating whether a fix or floor operation should be used in f with the following additional notation:

$\hat{\mathbf{h}}(c)$ Set of fix and floor operations that minimize (5.65) for a given value of c

$\mathbf{I}_z$ $[n_z \times n_z]$ Identity matrix

$\vec{\mathbf{k}}$ $[n_w \times 1]$ Wavenumber vector with the following subscript definitions:

$\vec{\mathbf{k}}_{\Delta}$ Frequency-dependent components of $\vec{\mathbf{k}}$ (see κ for frequency-independent components)

$\mathbf{M}$ $[3n_m \times n_w]$ Measured, noisy frequency-domain data with the following subscript definitions:

$\hat{\mathbf{M}}$ True, or actual values without additive noise

$\mathbf{M}_{\Im}$ Phase response of receiver-specific signals in the frequency-domain

$\mathbf{M}_{\Re}$ Log-magnitude of receiver-specific signals in the frequency-domain

$\mathbf{M}_{TR}^{\varkappa}$ Projection of frequency-dependent components of $\mathbf{M}_{\Im}$ onto $\mathbf{Q}_{\mathrm{TR}}^{\varkappa}$

$\mathbf{N}$ $[n_m \times n_w]$ Matrix containing additive noise terms. Specific noise distributions are indicated by the following subscripts:

$\mathbf{N}_{\mathrm{b}}$ $[n_m \times n_w]$ Matrix containing additive noise terms associated with $\mathbf{B}_{\mathrm{A}}^{=}$

$\vec{\mathbf{N}}_i$ $[n_m \times 1]$ The i^{th} column of $\mathbf{N}$. Composed of the following sub-vectors::

$\vec{\mathbf{N}}_{\Re i}$ Log-magnitude noise associated with the i^{th} column of $\mathbf{M}$

$\vec{\mathbf{N}}_{\Im i}$ Phase noise associated with i^{th} column of $\mathbf{M}$

$\vec{\mathbf{N}}_{\mathrm{b}i}$ Noise associated with i^{th} column of $\mathbf{B}_{\mathrm{A}}^{=}$

$\vec{\mathbf{p}}$ $[n_w \times 1]$ Propagation loss vector

P Matrix with context-dependent definition as indicated by the following superscripts and subscripts:

- $\mathbf{P}^{DS}$ $[n_x \times n_y]$ Conventional imaging pixel values
- $\mathbf{P}^{MV}$ $[n_x \times n_y]$ Minimum variance imaging pixel values
- $\mathbf{P}_{\Delta}$ $[n_w \times n_w]$ Projection matrix onto null space of $\vec{\mathbf{1}}_w^{\mathrm{T}}$
- $\mathbf{P}_{TR}^{\nu}$ $[n_m \times n_m]$ Projection matrix onto $\mathbf{Q}_{TR}^{\nu}$
- $\mathbf{P}_{\tau\rho}^{\nu}$ $[n_m \times n_m]$ Projection matrix onto $\mathbf{Q}_{\tau\rho}^{\nu}$

$\vec{\mathbf{Q}}_i$ $[3n_m \times 1]$ Vector of squared complex SNR values for the i^{th} column of $\mathbf{Q}$

Q Mixing matrix with the following subscript and superscript definitions:

- $\mathbf{Q}$ $[3n_m \times 3n_m]$ Estimated SNR for each frequency-domain measurement in $\mathbf{M}$
- $\mathbf{Q}_{\mathrm{R}}$ $[n_m \times n_r]$ Relates frequency-dependent components of $\mathbf{M}$ to frequency-dependent components of $\mathbf{R}$
- $\mathbf{Q}_{\rho}$ $[n_m \times n_r]$ Relates frequency-independent components of $\mathbf{M}$ to frequency-independent components of $\mathbf{R}$
- $\mathbf{Q}_{\mathrm{T}}$ $[n_m \times n_t]$ Relates frequency-dependent components of $\mathbf{M}$ to frequency-dependent components of $\mathbf{T}$
- $\mathbf{Q}_{\tau}$ $[n_m \times n_t]$ Relates frequency-independent components of $\mathbf{M}$ to frequency-independent components of $\mathbf{T}$
- $\mathbf{Q}_{\mathrm{TR}}$ $[n_m \times (n_t + n_r)]$ Composite matrix($[\ \mathbf{Q}_{\mathrm{T}} \quad \mathbf{Q}_{\mathrm{R}}\ ]$)
- $\mathbf{Q}_{\tau\rho}$ $[n_m \times (n_t + n_r)]$ Composite matrix($[\ \mathbf{Q}_{\tau} \quad \mathbf{Q}_{\rho}\ ]$)
- $\mathbf{Q}_{TR}^{\shortparallel}$ $[n_m \times n_{TR}^{\shortparallel}]$ Orthonormal basis for column space of $\mathbf{Q}_{TR}$
- $\mathbf{Q}_{\tau\rho}^{\shortparallel}$ $[n_m \times n_{\tau\rho}^{\shortparallel}]$ Orthonormal basis for column space of $\mathbf{Q}_{\tau\rho}$
- $\mathbf{Q}_{TR}^{\nu}$ $[n_m \times (n_m - n_{TR}^{\shortparallel})]$ Orthonormal basis for left null space of $\mathbf{Q}_{TR}$
- $\mathbf{Q}_{\tau\rho}^{\nu}$ $[n_m \times (n_m - n_{\tau\rho}^{\shortparallel})]$ Orthonormal basis for left null space of $\mathbf{Q}_{\tau\rho}$
- $\mathbf{Q}_{TR}^{\neq}$ $[(n_t + n_r) \times n_{TR}^{\neq}]$ Orthonormal basis for null space of $\mathbf{Q}_{TR}$
- $\mathbf{Q}_{\tau\rho}^{\neq}$ $[(n_t + n_r) \times n_{\tau\rho}^{\neq}]$ Orthonormal basis for null space of $\mathbf{Q}_{\tau\rho}$
- $\mathbf{Q}_{(T)R}^{\neq}$ $[n_t \times n_{TR}^{\neq}]$ Sub-matrix of $\mathbf{Q}_{\mathrm{TR}}^{\neq}$ associated with the $\mathbf{Q}_{\mathrm{T}}$ portion of $\mathbf{Q}_{\mathrm{TR}}$
- $\mathbf{Q}_{T(R)}^{\neq}$ $[n_r \times n_{TR}^{\neq}]$ Sub-matrix of $\mathbf{Q}_{\mathrm{TR}}^{\neq}$ associated with the $\mathbf{Q}_{\mathrm{R}}$ portion of $\mathbf{Q}_{\mathrm{TR}}$

R $[n_r \times n_w]$ Receiver-specific frequency-domain signals with the following superscript and subscript definitions:

- $\mathbf{R}_{\Im}$ Phase response of receiver-specific signals in the frequency-domain
- $\mathbf{R}_{\Re}$ Log-magnitude of receiver-specific signals in the frequency-domain
- $\mathbf{R}_{\Delta}$ Frequency-dependent components of $\mathbf{R}_{\Im}$ (see $\vec{\boldsymbol{\rho}}$ for frequency-independent components)

$\vec{\mathbf{s}}$ Vector of back-propagated, differenced signals arranged in vector format with the following additional notation:

- $\vec{\mathbf{s}}_{xy}(t)$ $[n_m \times 1]$ Backpropagated, differenced signals associated with pixel location (x,y) at time t
- $\hat{\mathbf{s}}_{xy}$ $[n_m \times 1]$ Unit-norm vector representing the *relationship* between backpropagated, differenced signals at pixel location (x,y)

$\mathbf{S}$ Matrix associated with scattered differenced signals with the following subscript definitions:

- $\mathbf{S}_m$ $[n_x \times n_y]$ Matrix with elements corresponding to the m^{th} back-propagated, instantaneous-windowed signal for each pixel location
- $\mathbf{S}_{xy}$ $[n_m \times n_m]$ Autocorrelation matrix for pixel location (x,y)
- $\hat{\mathbf{S}}_{xy}$ $[n_m \times n_m]$ Diagonally loaded autocorrelation matrix for pixel location (x,y)

$\mathbf{T}$ $[n_t \times n_w]$ Transmitter-specific frequency-domain signals with the following superscript and subscript definitions:

- $\mathbf{T}_{\Im}$ Phase response of transmitter-specific signals in the frequency-domain
- $\mathbf{T}_{\Re}$ Log-magnitude of transmitter-specific signals in the frequency-domain
- $\mathbf{T}_{\Delta}$ Frequency-dependent components of $\mathbf{T}_{\Im}$ (see $\vec{\boldsymbol{\tau}}$ for frequency-independent components)

$\mathbf{U}$ $[n_w \times n_w]$ Matrix used in computation of $\vec{\boldsymbol{\Sigma}}^{\bullet}$

$\vec{\mathbf{v}}$ $[n_m \times 1]$ Unit-norm Eigenvector with the following subscript definitions:

- $\vec{\mathbf{v}}_i$ Eigenvector associated with the i^{th} eigenvalue, λ_i
- $\vec{\mathbf{v}}_{\text{TR}}^{\nu}$ Eigenvector corresponding to projection of $\vec{\mathbf{d}}$ onto space spanned by $\mathbf{Q}_{\text{TR}}^{\nu}$

$\mathbf{V}$ Context-dependent Eigenvector matrix associated with the following superscript and subscript definitions:

- $\mathbf{V}_m$ $[n_x \times n_y]$ Matrix with elements corresponding to the m^{th} element of the Eigenvector associated with the largest eigenvalue for each pixel location
- $\mathbf{V}_1^{\nu}$ $[n_m x(n_m - 1)]$ Orthonormal vectors spanning on the left null space of $\vec{\mathbf{v}}_1$

$\vec{\mathbf{w}}_{xy}$ $[n_m \times 1]$ Optimal weighting coefficients associated with pixel location (x,y)

$\mathbf{X}$ $[n_y \times n_x]$ Matrix of x-coordinates corresponding to each pixel location

$\mathbf{Y}$ $[n_y \times n_x]$ Matrix of y-coordinates corresponding to each pixel location

$\mathbf{Z}$ $[3(n_t + n_r + 1) + n_m \times n_w]$ Matrix of unknown parameters

$\vec{\boldsymbol{\gamma}}$ $[3n_m \times 1]$ Vector containing diagonal elements of $\boldsymbol{\Gamma}$

$\boldsymbol{\Gamma}$ $[3n_m \times 3n_m]$ Intermediate matrix used to relate noise in $\mathbf{M}$ to resulting noise in $\vec{\mathbf{b}}$ estimates

$\boldsymbol{\Theta}$ $[n_x \times n_y]$ Matrix of inner product values $\vec{\mathbf{v}}_1^H \vec{\mathbf{e}}_{xy}$ for each pixel location

$\boldsymbol{\Lambda}_1$ $[n_x \times n_y]$ Matrix with elements corresponding to the largest eigenvalue for each pixel location

$\vec{\boldsymbol{\rho}}$ $[n_r \times 1]$ Frequency-independent components of $\mathbf{R}_{\Im}$

$\vec{\boldsymbol{\sigma}}^2_{\mathrm{m}}$ $[n_m \times n_w]$ Measured noise variance

$\vec{\boldsymbol{\Sigma}}$ $[n_w \times 1]$ Vector for performing a weighted average over frequency with the following additional superscript and subscript notations:

- $\vec{\boldsymbol{\Sigma}}^{\bullet}$ Optimal weights for performing a weighted average over frequency under assumptions of circularly-symmetric Gaussian noise

$\vec{\boldsymbol{\tau}}$ $[n_t \times 1]$ Frequency-independent components of $\mathbf{T}_{\Im}$

$\boldsymbol{\Phi}$ $[n_x \times n_y]$ Matrix of $\vec{\mathbf{e}}^{H}_{xy}\mathbf{N}\mathbf{N}\vec{\mathbf{e}}_{xy}$ values for each pixel location

$\boldsymbol{\Psi}_m$ $[n_x \times n_y]$ Matrix with elements corresponding to the scattering coefficient for each pixel location and m^{th} transmitter-receiver pair

$\boldsymbol{\Omega}_{\mathrm{N}}$ $[n_w \times n_w]$ Diagonal matrix with diagonal elements comprised of $\sigma^2_{\mathrm{b}i}$ values

$\vec{0}_z$ $[n_z \times 1]$ All zeros vector

$\mathbf{0}$ Null matrix of arbitrary size

$\vec{1}_z$ $[n_z \times 1]$ All ones vector

SUMMARY

Structural health monitoring (SHM) is the periodic interrogation of man-made structures to detect damage and characterize structural integrity. The motivation for performing SHM is to identify defects or damage in a structure *before* they become problematic, either through a degradation in performance or catastrophic failure. SHM plays a key role in condition-based maintenance, wherein parts and equipment are repaired or replaced on an *as needed* basis. Condition-based maintenance offers significant cost savings over more traditional time-based maintenance and obsolescence, which replaces parts based on time in service, frequently resulting in the replacement of good parts.

Ultrasonic guided waves are able to propagate over long-distances with minimal loss and are capable of interacting with both surface and subsurface defects. As such, many SHM research efforts are exploring the use of ultrasonic guided waves for the interrogation of large, plate-like structures, such as aircraft skins, ship hulls, bridge gusset plates, and storage tanks. Of these, spatially distributed arrays of permanently attached, inexpensive transducers are of particular interest since they offer an economical solution that can be made completely automated and available to interrogate the structure at any time. The research presented here uses such a distributed array of permanently attached transducers to produce useful images of a large, plate-like structure with ultrasonic guided waves.

The work is largely split into five areas: minimum variance imaging, parameter estimation, parameter compensation, array configuration performance, and damage characterization. Minimum variance imaging, which involves the incorporation of minimum variance techniques into conventional delay-and-sum imaging, is shown to significantly improve

resolution and reduce artifacts with only minor increases in computational complexity. Parameter estimation is achieved through the model-based parameter estimation algorithm (MBPE). The MBPE algorithm was developed to adaptively estimate dispersion relations, transducer-specific transfer functions, transducer spacings, and propagation loss. Additional improvements in guided wave imaging are then demonstrated through deconvolution and dispersion compensation using MBPE parameter estimates rather than nominal parameters. A preliminary investigation into the factors that affect distributed array imaging performance is conducted. The imaging algorithm employed, excitation function, number of sensors, sensor arrangement, array aperture, and array location are all considered. Finally, damage characterization, which represents a new capability for distributed array imaging, is performed by leveraging the inherent sensitivity of minimum variance imaging to scattering behavior.

This dissertation consists of the following contributions:

- Adaptation of the MVDR algorithm for guided wave imaging.
- Development of a model-based algorithm for adaptively estimating wave propagation parameters with minimal *a priori* information.
- Incorporation of adaptively estimated parameters into guided wave imaging algorithms through the use of distance domain signals.
- A methodology for quantitatively characterizing the ability of an array to detect and locate damage throughout a structure.
- A methodology for characterizing defects or damage using guided waves generated from a spatially distributed array.

CHAPTER I

INTRODUCTION

Both commercial and government entities, whether due to budgetary constraints or a need for competitive advantage, have always been driven to minimize costs, while simultaneously maintaining or improving capability and safety. In some cases, this may entail extending the service-life of a structure beyond its original design-life, such as for many bridges and aircraft, or finding ways to reduce maintenance costs. The concept of condition-based maintenance often arises in these contexts, because it involves repairing or replacing parts and equipment *on an as-needed basis*, and offers significant cost savings over the more traditional time-based obsolescence and maintenance schedules. In order to perform repair or replacement at the correct time, however, the condition of the structure must be known. As such, there is significant interest, both from the government and commercial industry, in *inexpensive* methods to monitor the condition of a structure and identify potential defects or damage.

The excellent safety record of both commercial and military aircraft is largely due to the inspection and maintenance requirements of in-service airframes. Commercial aircraft are required by federal law to undergo thorough, periodic inspections in accordance with FAA regulations [1, 2], while military aircraft are subject to similar inspection requirements governed by their respective services, such as the U.S. Navy's OPNAVINST 4790 [3]. Unfortunately, however, due to the sheer size and complexity of these aircraft, the required inspections are extremely expensive and time-consuming and there is an inherent risk that damage may be introduced by the inspection itself. Adding to the cost, many parts are replaced based simply on how long they have been in use with no regard for their actual condition, which results in the unnecessary replacement of good parts. As such, both

government and commercial aviation industries are looking to incorporate new inspection technologies into current and future aircraft designs to reduce costs and maintain or improve safety.

The relatively new field of structural health monitoring (SHM) involves the periodic interrogation of man-made structures to detect damage and characterize the structural health of a system. SHM systems are commonly based upon nondestructive evaluation (NDE) techniques that quantitatively characterize materials and structures through noninvasive means. Although a wide range of methods can be used for NDE, such as radiographic, thermographic, electromagnetic, and optical methods, the work here is primarily focused on the use of ultrasound for SHM. SHM systems offer a tool to rapidly inspect large, inaccessible, or complex components, reducing the need for expensive, time consuming, and invasive inspections.

Most current ultrasonic inspection techniques use bulk waves to penetrate the material and detect subsurface damage in the immediate vicinity of a movable ultrasonic transducer. Because the sensor only interrogates a localized area, a complete raster scan of the structure is required to generate a comprehensive image of large plate-like components. These manual or automated scans can be very time consuming and often require custom hardware.

Many SHM research efforts [4, 5, 6] are exploring the use of ultrasonic guided waves for the interrogation of large, plate-like structures, such as aircraft skins, ship hulls, bridge support gussets, storage tanks, and architectural structures. Guided waves are able to propagate over long-distances with minimal loss and are capable of interacting with both surface and subsurface defects [7]. The goal is to obtain useful images of large plate-like structures with a small number of sampling locations, avoiding the need to scan the entire surface. Further, if a set of permanently attached transducers is employed for interrogation, rather than a single movable transducer, then an SHM system could be completely automated and made available to evaluate the structure at almost any time [8].

Although there are major economic advantages to using guided waves for *in situ* interrogation of large, plate-like structures over traditional NDE methods, a significant number of challenges are associated with obtaining sufficient information from a sparse, distributed array of transducers as compared to a complete bulk wave evaluation. Geometric dispersion, multimode propagation, and multiple reflections within the structure result in complex waveforms that are difficult to interpret. Additionally, geometric dispersion changes with environmental conditions, such as temperature, further complicating analysis. These complexities, if unaddressed, cause artifacts in guided wave images that are often indistinguishable from actual damage. As a result, many proposed guided wave imaging systems are forced to compensate by increasing the number of required transducers to increase system signal-to-noise ratio (SNR), which increases system cost and complexity.

The research presented here advances the state of the art in *in situ* guided wave imaging techniques in several respects. First, minimum variance imaging is presented in Chapter IV as a method that significantly improves resolution and reduces artifacts with only minor increases in computational complexity. To address the challenges posed by the effects of dispersion, Chapter V describes the model-based parameter estimation (MBPE) algorithm, which is capable of simultaneously estimating dispersion relations, transducer transfer functions, propagation loss, and transducer spacing using signals recorded from an *in situ* distributed array. Chapter VI then presents two methods for using these estimated parameters to *compensate* for their *in situ* variations, which further improves both conventional and minimum variance imaging. Finally, Chapter VII describes two areas of ongoing research that seek to (1) characterize the ability of a specific array configuration to detect and locate damage and (2) leverage the minimum variance imaging algorithm to perform damage *characterization* with a sparse, distributed array of transducers.

CHAPTER II

ORIGIN AND HISTORY OF THE PROBLEM

Although the fields of NDE and SHM are currently experiencing rapid growth, both fields have been in existance for quite some time. The requirement for periodic, nondestructive inspections for the purpose of structural health monitoring can be traced back at least as early 1854. At that time, when a boiler exploded in Hartford, CT, killing 21 people and injuring 50 more, the State of Connecticut passed a law requiring annual visual inspections of similar boilers [9]. Since then, a wide range of techniques and technologies has been adapted to perform nondestructive inspections, including but not limited to radiographic, thermographic, electromagnetic, optical, and ultrasonic methods. Each technique has inherent benefits and constraints, with no single technique having global applicability. A brief historical overview and thorough comparison of NDE techniques can be found in Hellier [10].

2.1 Elastic Waves

Of all the available NDE methods, the use of ultrasonics, and particularly ultrasonic guided waves, is of primary interest here. A history of the science of sound can be found in the book by Pierce [11]. The first mathematical description of sound propagation began with Sir Isaac Newton's *Principia Mathematica* in 1687 [12]. In this work, sound is described as pressure pulses flowing through fluid particles and experimental measurements are even provided for the speed of sound through air. In the 1700's, Euler, Lagrange, and d'Alembert all made significant additional contributions to our current mathematical models of sound propagation, including the introduction of today's wave equation. Then in 1877, Lord Rayleigh published his comprehensive *Theory of Sound* [13], which introduced a mathematical analysis of propagation modes.

The study of guided waves in elastic solids began with Lord Rayleigh in 1885. His original work on the subject focused on a single free surface of an infinite homogeneous isotropic elastic solid [14]. The waves that he predicted in 1885 are now known as Rayleigh waves. He later realized that this work was a special case of waves propagating in thin, plate-like structures and generalized his analysis in 1889 [15]. In 1917, the English mathematician Horace Lamb simplified Rayleigh's work on the waves propagating inside the plate, establishing what is today known as the Lamb (or Rayleigh-Lamb) Equations [16]. Two fundamental realizations about guided waves are derived directly from the work of Rayleigh and Lamb: (1) in contrast to an unbounded medium, in which only longitudinal and transverse waves propagate, plate-like structures support three infinite sets of propagating modes, and (2) the physical wave velocity of these propagating modes is frequency dependent. Unfortunately, the simplified characteristic equations that resulted from Lamb's work cannot be solved analytically; they require numerical solutions. As such, it was not until 1967 (after the advent of computers) that I. A. Viktorov published a comprehensive work on the behavior of both Lamb and Rayleigh waves that is still used today [17], including his description of how guided waves interact with surface and subsurface defects. At the time, guided waves were already being used for damage detection and localization in a pulse-echo configuration for a number of different applications, from automotive sheet metal inspection, to gas turbine blades, combustor casings, and other aircraft components.

2.2 Ultrasonic NDE

The use of elastic waves for NDE started in 1929, when Sergei Y. Sokolov proposed the use of a single transducer on a steel shaft to detect material flaws through the use of a reflectogram [18]. Note that in order for his system to work, he had to use frequencies greater than 20 kHz, which are inaudible to the human ear and are typically referred to as ultrasonic. He also proposed the first "ultrasonic camera" in 1935 [19], wherein the

use of a sufficiently high frequency (3 MHz) theoretically enabled images to be generated with a resolution “comparable to that of a microscope”. About the same time, in 1931, Muhlhauser submitted the first patent for a system that transmitted ultrasonic energy into a test sample and detected the ultrasonic energy emerging from the sample with a second transducer [20], known today as a pitch-catch configuration. Later, during World War II, Floyd Firestone and Donald Sproule independently developed the bulk-wave inspection technique known today as pulse-echo. The pulse-echo technique uses a single transducer [21], or pair of co-located transducers [22], to transmit a pulse of energy into a sample and receive the reflected energy from geometric structures like the front and back wall, cracks or other defects.

Traditional ultrasonic bulk wave inspection, such as described in the previous paragraph, is capable of reliably inspecting surface and subsurface features of a structure and is widely used today. Although bulk wave inspection inspects a localized area directly underneath the sensor at any given time, acoustic images can be generated by combining multiple measurements [23]. The one-dimensional recorded data are referred to as an A-scan, wherein the recorded ultrasonic echoes correspond to the front wall, back wall, and one or more subsurface scatterers. The time-of-arrival of each echo provides an indication of the depth of the reflector. When multiple A-scans are recorded along a spatial path, a two-dimensional B-scan can be generated that provides the equivalent of a cross-sectional view of the structure along that path. A B-scan can provide an indication of both the depth and size (along the path) of a subsurface feature. A C-scan comprises multiple B-scans, obtained by raster-scanning the structure, and is typically represented as a two-dimensional cross-section of the structure corresponding to a specific depth or range of depths. Because a complete raster scan of the structure is required for interrogation of large, plate-like components, bulk wave inspection can be very time consuming and often requires custom hardware.

2.3 Ultrasonic Phased Arrays

One major development in bulk wave inspection, relevant to the work presented here, is the use of ultrasonic phased arrays. The concept of a phased array was first introduced by Karl Ferdinand Braun in 1906 [24] in the context of a "directive antenna". Braun used three antenna wires with a common transmitter to achieve significant directivity of the radiated signal. The directivity was a result of the *constructive* interference of the propagating signals in a specific direction. In fact, this connection between the spatial relationship of array elements and the propagating wavefront lies at the heart of every phased array system in existence today. Although rooted in electromagnetic applications, phased arrays are now used in a broad range of applications, including ultrasonics.

Early work on ultrasonic phased arrays first appear in the literature, for both biomedical applications [25] as well as NDE [26], in the late 1960s and has experienced considerable growth over the past 50 years [27]. Ultrasonic phased arrays use multiple elements to electronically focus both transmitted and recorded energy on specific directions and depths, thereby allowing for volumetric scanning without moving the probe. This feature can be invaluable for reducing inspection times, as well as inspecting parts or equipment with limited access [28]. Also, the use of multiple elements increases the signal-to-noise ratio (SNR), resulting in an ability to discern greater detail from the interrogation structure [23]. The trade-off for these improvements is an increase in cost, for both the probe and signal processing equipment, and a need for increased operator training. Today, hand-held NDE sensors with 256 sensors are commercially available [28]. A comprehensive review on ultrasonic arrays in NDE is provided by Drinkwater and Wilcox [29].

2.4 Minimum Variance Distortionless Response (MVDR)

Although phased arrays represent an entire research field unto themselves that is not discussed here, the signal processing associated with phased arrays, referred to as beamforming, is of particular interest. From a beamforming perspective, early methods simply delayed or phase shifted (hence the term "phased array") each channel an appropriate amount to compensate for propagation delay and then summed each of the signals to obtain a composite signal. If the same signal is present in each channel and any additive noise is assumed to be Gaussian, this delay-and-sum technique can be shown to increase SNR by a factor of n_m, the number of independent measurements [30].

More advanced beamforming techniques, however, started appearing in the mid-1960s. Although a comprehensive review of these advanced methods is beyond the scope of this text, the work leading up to the development of minimum variance distortionless response (MVDR) is provided here due to its relevance. Readers are encouraged to consult a text or review article on phased arrays [31, 32] or beamforming [30, 33] for further details.

In 1964, Claerbout [34] found that the ambient noise from the seismic array at Uinta Basin Observatory could be predicted and canceled, significantly improving the system's ability to detect nuclear events. In the same year, Burg [35] expanded Wiener linear least-mean-square-error filtering [36] to three dimensions, introducing the concept of temporal-spatial filtering. Note that the traditional delay-and-sum techniques employed at the time correspond to a specific subset of temporal-spatial filtering, namely filters that are all-pass, linear-phase in time and rectangularly windowed in space. Backus *et al.* [37] then used this spatial filtering technique to improve the SNR for three different seismic arrays. In both Burg [35] and Backus *et al.* [37], the power spectral density of both the noise and signal must be known or assumed *a priori*. Also, the multidimensional Wiener filtering technique requires a matrix inversion operation, which can become computationally intensive as the dimensionality of the problem is increased. An alternative to computing the matrix inversion explicitly is to use recursive techniques. In 1965, Wiggins and Robinson [38] improved

upon the recursive techniques developed previously by Robinson [39] and Levinson [36] to reduce the computational costs of obtaining the Wiener filtering coefficients.

In 1967, Widrow *et al.* [40] proposed a recursive filtering technique that minimizes the mean-square-error between the filter output and an artificially injected pilot tone. The recursive technique, now known as Least Mean Squares (LMS), is based on the technique of steepest descent, using an instantaneous estimate of the gradient [41]. The pilot tone is injected in such a way as to mimic the characteristics of the expected signal and provides a reference signal to "train" the system with. The filtering technique, known today as a Multiple Sidelobe Canceller (MSC), assumes that the incident angle and power spectrum of the signal of interest are known, but makes no assumption about the noise characteristics. In 1969 however, Griffiths [42] modified the LMS algorithm to include assumed or expected information about second-order statistics of the target signal, which avoids the need for a pilot tone and removes estimator bias that is observed in some cases with the technique proposed by Widrow *et al.* [40].

Also in 1967, Capon *et al.* [43] developed two multidimensional maximum-likelihood (ML) filtering techniques that make no assumptions about the shape of the underlying signal. These filtering techniques were constrained to provide a distortionless signal estimate while simultaneously minimizing output noise power. Griffiths [44] demonstrated that although the ML technique does not distort the output signal, Wiener filtering provides an output signal with higher SNR. He further showed that both techniques converge to the same result as input SNR is increased. In 1969, Capon [45] applied the ML filtering technique to frequency-wavenumber spectrum analysis. The new technique provided visibly improved resolution in frequency-wavenumber analysis of seismic array data.

In 1968, Claerbout [46] addressed the challenge of applying specific constraints to least-squares, or minimum variance, filters. Using a more general framework for the constraints, Frost presented the Constrained LMS (CLMS) filter [47] in 1972, which is today known as the Minimum Variance Distortionless Response (MVDR) filter. He pointed out that if

the CLMS filter is constrained to be all-pass and linear phase in time (distortionless), then the CLMS filter output is identical to the ML filter output. For this reason, MVDR is sometimes referred to as Capon's method.

Since the introduction of MVDR in 1972, many enhancements to MVDR have been made [48, 49, 50, 51] and the algorithm has been successfully applied to biomedical ultrasound applications [52, 53, 54, 55]. Additionally, several alternative adaptive techniques have been developed [33], many of which can be applied to the work presented here.

2.5 Guided Wave NDE

Since guided waves are capable of propagating along the plane of plate-like structures with little propagation loss and are sensitive to both surface and subsurface features, they offer an efficient alternative to the traditional bulk wave inspection method described in Section 2.2. While Rayleigh and Lamb were able to predict and explain the existence, modality, and behavior of guided waves around the turn of the century, there is no evidence of a method to perform experimental verification of their findings prior to 1946, when Firestone and Ling submitted a patent for generating and recording guided waves and using guided waves for "the purpose of testing, measuring, or otherwise investigating the properties of solid sheets or plates of material" and "testing plates for defects" [56]. A decade later, Worlton used ultrasonic guided waves to reveal shallow laminar defects in solid objects and plates that traditional ultrasonic methods were unable to detect [57]. Grigsby and Tajchman [58] then experimentally verified group velocities and evaluated the effects of saw cuts of various depths. As mentioned earlier, by 1967 guided waves were already being used for damage detection and localization in a pulse-echo configuration for a number of different applications [17].

It should be noted that early guided wave NDE methods treated guided wave data similar to bulk wave data. A single guided wave measurement was analogous to an A-scan. By repeating the measurement along a path perpendicular to the guided wave propagation, a

graphical image of the plate can be generated by combining multiple guided wave measurements, similar to a bulk wave B-scan. While a dramatic improvement over conventional bulk-wave methods, this approach still requires a manual, linear scan of the structure (as opposed to a raster-scan).

Guided wave tomography, however, first suggested by Jansen and Hutchins [59] in 1990, departed from this mentality and is still widely used today. These systems typically use time-of-flight and amplitude information to generate an image localized *within* a polygon arrangement of ultrasonic transducers. Although the sensors *can* be permanently attached, they are generally air- or liquid-coupled, which provides the ability to collect a large number of datasets with a small number of sensors and transmit/receive equipment. These techniques rely on the assumption that damage causes a change in arrival time of a specific propagating mode, and they vary based on the sensor pattern [60, 61, 62], signal features used to quantify velocity changes [63], diffraction assumptions [64], and image generation method [65, 66].

The use of phased arrays with guided waves started appearing in the late 1990s. Deutsch *et al.* [67] first demonstrated an ability to dynamically focus an ultrasonic guided wave on a scatterer through the use of a time-reversal technique [68, 69]. For experimental verification, Deutsch *et al.* excited guided waves using a linear eight-sensor array coupled to the plate through an acrylic wedge. Due to the use of a wedge for guided wave excitation, however, the angular range of the array was only $\tilde{3}0^{\circ}$.

In contrast to the use of a wedge transducer for exciting guided waves, Monkhouse *et al.* [70] and Rose *et al.* [71] used interdigital and comb transducers, respectively, to excite and record guided waves. Although these transducers excited waves forward and backward along a single line and did not have the ability to perform beamforming, they were able to achieve some degree of mode-selectivity, addressing one of the major challenges inherent in working with guided waves. Improving on this work, Zhu *et al.* [72] used a more general time-delay periodic linear array to launch guided waves *either* forward or backward, and

Monkhouse *et al.* [73] created a 60° radial transducer to improve upon the directionality limitations of interdigital transducers.

In 2000, Wilcox *et al.* [74] first introduced the concept of using a compact-array of individually addressed, inexpensive piezoelectric elements for inspecting large, plate-like structures. The data acquisition process used a single transmitter and receiver to excite and record from each individual element of an array, storing the data for post processing. This method of storing all available information from the array was later termed full-matrix capture by Holmes *et al.* [75] in the context of ultrasonic bulk wave inspection. Since that time, both linear [74, 76] and circular array patterns [74, 77, 78, 79, 80] of 9-32 elements have been investigated with both piezoelectric and electromagnetic acoustic transducers (EMAT) to produce images using radar imaging algorithms, such as the synthetic aperture focusing technique (SAFT). Methods to further improve imaging quality have been proposed through deconvolution of the array's spatial response [77] and for maximizing axial resolution [80]. It should be noted that in all of the above cases, the array imaging algorithms all treated the incoming waves as originating in the "far field", meaning that the incident waves impinging on the array are treated as having a *planar* wavefront.

2.6 Dispersion

One significant challenge encountered when working with guided waves is geometric dispersion, meaning that the propagation speed of Lamb waves is frequency-dependent [16]. As such, signals spread in time as they propagate and thus decrease in amplitude. The spreading of the signals is also accompanied by a change in phase. These phase changes have significant negative impacts on the ability of guided wave systems to detect and locate damage [81].

One common solution to address the dispersive nature of guided wave signals is the use of the envelope of the signals [82], which is the absolute value of the analytic representation of the signal. Some of the costs and benefits of using the envelope *vs.* RF signals were

identified by Croxford *et al.* [83]. Alternatively, the dispersive nature of the waves can be addressed with dispersion compensation directly in the frequency domain as demonstrated by Sicard *et al.* [84], or by converting the time domain signals to the spatial domain, as performed by Wilcox [85]. Dispersion compensation has been incorporated into the generation of guided wave B-scan images by Sicard *et al.* [86] and compact guided wave array imaging by Wilcox [77].

Although dispersion estimates *can* be obtained by computing the nominal dispersion curves, errors in bulk-wave speeds and plate thickness, such as may result from manufacturing variability and temperature variations, are compounded with numerical errors when solving the Rayleigh-Lamb equations. As such, several methods have been developed to *characterize*, or estimate, the frequency-dependent propagation velocity of guided waves.

In 1977, Sachse and Pao [87] proposed a phase spectral analysis method using received signals from two different distances from the transmitter to extract phase velocity of longitudinal waves. The change in phase of the received signals was analyzed, assuming a known transmitted signal and propagation distance. Their work was extended by Peters and Petit [88] to avoid the use of a reference medium, and by Hutchins *et al.* [89] to apply the technique to Lamb waves with an excitation spectrum that does not extend to 0 Hz. Hutchins *et al.* [89] obtained the dispersion estimate by assuming that the effects of dispersion are the only factor affecting the phase response of the recorded signal, and performing a nonlinear least-squares fit between an assumed propagation model and measured data.

Time-frequency representations (TFRs) have also been applied to estimate frequency-dependent group velocities for Lamb waves [90, 91, 92]. One benefit unique to TFR analysis is the ability to extract both group velocity and attenuation information from a single multi-mode signal. However, without determination of an unknown integration constant, group velocity cannot be translated to phase velocity or a wavenumber *vs.* frequency dispersion curve.

As yet another example of dispersion estimation, Alleyne and Cawley [93] successfully

demonstrated a two-dimensional Fourier transform method that is capable of accurately estimating dispersion relations from a set of multi-mode signals. One of the few limitations associated with the two-dimensional Fourier transform method is the requirement for linear spatial sampling at sufficiently close intervals to avoid spatial aliasing. In addition, both the two-dimensional Fourier transform method and TFR methods result in a graphical representation of dispersion relations that requires additional post-processing, such as a ridge-following algorithm, to extract useful estimates.

In all of the above approaches, the propagation distances are assumed known. Holland *et al.* [94] demonstrated that the propagation distance can be estimated from a single received guided wave signal via analysis of its TFR. Their method requires a search for the distance that provides the best match between theoretical dispersion curves and features of the TFR. The matching procedure was based upon a visual comparison and was not automated.

With respect to the work presented in this text, it should be pointed out that with the exception of the TFR methods, which are only capable of estimating *group velocity*, none of the methods described here are capable of estimating dispersion relations *in situ* with a sparse, distributed array. The two-dimensional FFT requires sampling at small spatial intervals, which is impractical for a sparse array. Alternatively, the method proposed by Hutchins [89], based on the approach of Sachse and Pao [87], effectively ignores any transfer functions or time delays associated with electromechanical transduction and establishment of the guided waves. While most likely similar in nature, the variation in transfer functions *do* have a measurable impact on dispersion estimation, as will be demonstrated in Chapter 5.

2.7 Guided Wave SHM

While the methods presented in Section 2.5 for guided wave NDE *are* capable of detecting and localizing surface and subsurface features, such as geometric boundaries, they are

unable to discern damage from geometric boundaries and lack sufficient dynamic range to reliably detect relatively small defects or damage. Unlike traditional NDE methods, SHM techniques can detect *changes* in a structure over time. This is often accomplished through signal differencing, or baseline subtraction. Baseline subtraction isolates scattered energy from defects or damage by subtracting known good baseline signals recorded prior to the introduction of any damage from the experimental, or in-service, signals. This process of baseline subtraction inherently assumes that any changes in the signals are related to damage. Unfortunately, however, benign changes in the signal can result from a wide range of factors, including both environmental factors and measurement variation (e.g. sensor coupling, spatial registration, orientation, etc.).

One of the most dominant environmental effects on guided waves is that of temperature changes [95]. Michaels and Michaels [4] used the short-time cross-correlation to calculate features that discriminate between damage and benign environmental effects, such as temperature. Croxford *et al.* [83] quantified the impact of baseline mismatch due to temperature changes and related baseline mismatch to a system's sensitivity to damage. The impact of a homogeneous temperature change can be successfully modeled through appropriate models of the sensors, their bonding, and the dispersive material properties [96]. Weaver and Lobkis [97] observed in experimental measurements that the diffuse field exhibited an almost pure dilation in time with temperature. From this observation, a baseline signal stretch (BSS) algorithm was proposed by Lu and Michaels [98] for temperature compensation whereby a global time-dilation is applied that scales the time axis by a linear factor. The dilation factor can be determined from local time shifts as measured by the short-time cross-correlation [98], or by determining the dilation factor that minimizes the residual after baseline subtraction [99]. The efficacy of the BSS method depends upon many factors, including signal complexity and modal content, but in general suffers degraded performance as temperature differences increase. Since the BSS method causes some undesired changes in the propagating wavepacket, however, further improved results were shown to

be obtained by compensating for these changes through deconvolution if the propagating wavepacket is known. Alternatively, the optimal baseline subtraction (OBS) algorithm is a knowledge-based approach that stores a bank of baseline signals recorded over a range of environmental conditions [98, 100, 95]. Test signals are then compared to each of the baseline signals and the closest matching baseline signal is used for baseline subtraction. Although proven effective over a broad range of temperatures (20°-150°) [101], the temperature compensation performance of OBS is directly related to the number of baseline signals employed over a range of environmental conditions. As the number of baseline signals is increased, however, so is the system storage and computational cost of comparison. As such, the OBS algorithm has been combined with the BSS algorithm [98, 102, 103, 104] to take advantage of the inherent benefits of OBS, while minimizing the computational and storage requirements.

One method to minimize measurement variation is by *permanently attaching* sensors to the structure. Permanently attaching sensors to the structure minimizes measurement variation from coupling, spatial registration, and orientation. Depending on the application, however, structural integration may present alternative challenges, such as limitations on the number of sensors, associated wiring, etc. which are directly related to the system, installation, and maintenance costs, as well as potential operational limitations on the structure (e.g. aerospace applications can have very narrow weight margins). As such, many research efforts, including the work presented here, have been evaluating the use of permanently attached, distributed arrays of inexpensive piezoelectric sensors to perform SHM.

Although tomographic techniques can be used with a small number of sensors, imaging quality is highly dependent on the number of recorded signals and reported results are often shown with the input of thousands of signals, which is orders of magnitude more than would be available with an economically feasible system of permanently attached sensors. Techniques such as the reconstruction algorithm for probabilistic inspection of damage

(RAPID) method [105, 106] have been used successfully with far fewer sensors than traditional tomographic methods by employing signal differencing and spatially distributing the corresponding signal difference coefficients. These tomographic methods, however, are still limited to inspecting an area *within* a polygon and require a much larger number of sensors than other alternatives.

In contrast to the tomographic techniques, inspection with a compact phased array under far-field assumptions inspect areas *far outside* of the sensor polygon. As suggested by Giurgiutiu [76] for addressing complex geometries, compact guided wave phased arrays have also been used with differenced signals [107]. Since the focusing performance of an array is directly related to the effective aperture size, a natural extension to the compact phased array work is the use of larger apertures.

Distributed arrays were originally introduced by Heimiller in 1983 [108] for radar applications, but the concept is equally applicable to the problem of structural health monitoring in plate-like structures. The general idea is to use a small number of *randomly distributed* sensors to create a very large aperture array. Heimiller demonstrated that many of the spatial ambiguities that result from large sensor spacings can be addressed through irregular sensor spacings and highlighted the impact that positioning errors can have on array performance. In 2000, Flaig and Arce [109] introduced the concept of *spot-beamforming* within the near-field of distributed arrays, showing that a distributed array can be focused (or defocused) on an arbitrary point in space and proposed a technique for finding an optimal arrangement of sensors. Flaig and Arce also suggest the use of high-resolution beamforming algorithms to reduce the spatial aliasing inherent with distributed arrays.

In 2004, Wang *et al.* [110] demonstrated guided wave imaging in the near field of a distributed array. The technique used by Wang used uniform aperture weighting, which is typically referred to now as conventional delay-and-sum imaging or the ellipse method. In this approach, each pixel value is based on the summation of the received signals at different points in time. The specific times are a function of the total distance from transmitter,

to pixel location, to receiver, and represent a generalization of the phased array imaging algorithms to spherical or, in this case, cylindrical waves. The ellipse nomenclature is derived from the fact that the locus of a constant time curve is an ellipse. Michaels and Michaels [111] expanded the approach of Wang *et al.* to sum the signals over a time window of data, as opposed to a single point in time, establishing the pixel value as the energy contained within the resulting summed signal. Michaels *et al.* [112] later demonstrated improved imaging performance by applying an exponential window to each received signal beginning at the time of the direct arrival. Finally, Michaels and Michaels [113] showed that images generated from different frequency excitation signals could be fused to obtain higher-quality images.

A third technique for guided wave imaging is the hyperbola algorithm [112, 114], which applies the conventional delay-and-sum approach to cross-correlations between baseline subtracted signals. The hyperbola nomenclature is used because the locus of constant time differences between the same arrival at two receivers is a hyperbola. Because this method groups receivers in pairs with a third transmitting transducer to obtain cross-correlation information, there is a much larger number of contributing signals for imaging as compared to the ellipse algorithm.

Recently, the use of time-of-flight techniques with a sparse, distributed array of sensors has been proposed to generate damage maps based on the assumption that scattering and possibly mode conversion occur when a guided wave interacts with damage (e.g., an incident S_0 mode scatters a portion of the incident energy as an SH_0 mode [115]). The difference in the time-of-arrival between each of the direct arrivals and scattered signals, which can be measured by several different techniques [116, 117], is used to estimate the propagation distances of the scattered signals. The estimated propagation distances are then used in a localization algorithm to identify the scattering location [118, 119, 120, 121]. Although these techniques have been successfully employed under laboratory conditions, the

measurement of discrete arrival times is a non-trivial task. The measurement can be complicated, or even prohibited, by the overlap between the direct arrival and scattered signals, interference from geometric reflections, and dispersive effects.

CHAPTER III

STATE OF THE ART

This chapter introduces the reader to some of the challenges encountered in *in situ* guided wave imaging and describes the algorithms representing current state of the art. Specifically, the optimal baseline subtraction (OBS) and baseline signal stretch (BSS) methods will be described for reducing baseline subtraction residual, the conventional delay-and-sum imaging algorithm will be presented, and finally, dispersion compensation methods will be discussed for addressing the frequency-dependent propagation velocities.

3.1 Experimental and Simulation Setup

The algorithms presented in this chapter, as well as those described in later chapters, will be presented using both simulation and experimental data from a 914 mm × 914 mm × 3.18 mm aluminum 6061 plate with six permanently attached, identical PZT transducers,

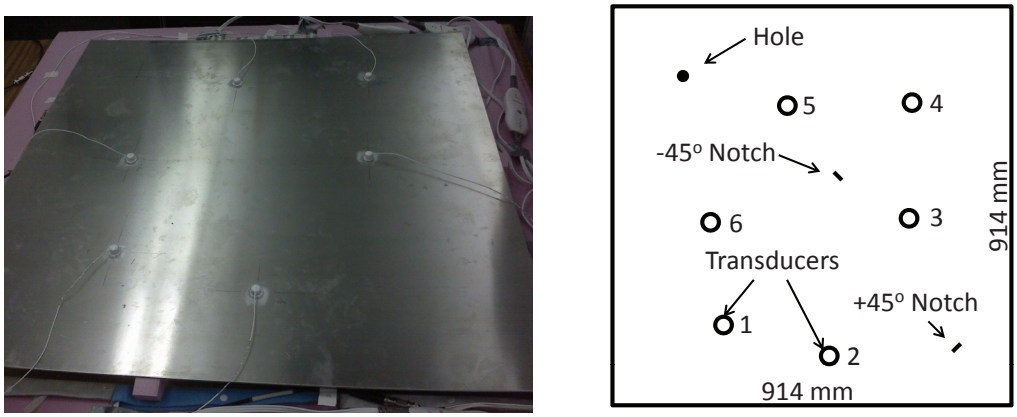

(a) (b)

Figure 3.1: Experimental setup. A sparse, distributed array of six transducers are attached to a 914 mm × 914 mm × 3.18 mm aluminum plate. A through-hole and two notches at ±45° are introduced at the indicated locations to simulate damage.

shown in Figure 3.1. The size of the plate was chosen to be sufficiently large to demonstrate the feasibility of the proposed algorithms, yet small enough to be practical within the QUEST laboratory. Although experimental data will be presented for validation purposes, simulation data is often employed to demonstrate algorithms without the additional complications of realistic systems.

All simulations are performed with MATLAB (The Mathworks, Natick, MA). For simplicity, transducers are modeled identically and are capable of coupling the excitation signal into an isotropic guided wave without attenuation, phase changes, or time delays. A ray-tracing model with the method of images is used to account for edge reflections, which are simulated as non-absorbing with the reflected wave 180° out-of-phase with the incident wave. Scattering characteristics are based on through-hole scattering fields generated using the low frequency approximation derived by Grahn [122] for 300 kHz S_0 incident and scattered waves. Scattered energy from damage is assumed to be sufficiently small so that multiple scattering effects can be ignored. All simulations assume a noise-free environment.

Although six transducers allow for 30 different combinations ($6\,(6-1) = 30$), ideal reciprocal pairs produce identical results. So, only one signal from each unique transmitter-receiver pair is used, resulting in 15 signals. Data collection was performed in the following round-robin fashion: $1 \rightarrow 2$, $1 \rightarrow 3$, $\cdots$, $5 \rightarrow 6$, where $1 \rightarrow 2$ indicates Transducer 1 was used to transmit and Transducer 2 to record the signal.

A block diagram of the experimental setup is shown in Figure 3.2. Signals are excited using an 33250A Arbitrary Waveform Generator (Agilent Technologies Inc., Santa Clara, CA), which controls the pulse repetition frequency and excitation waveform. Measurements are obtained with a TDS5034B Digital Phosphor Oscilloscope (Tektronix Inc., Beaverton, OR) after amplification with a 5072PR (Olympus NDT Inc., Waltham, MA). A custom multiplexor, designed and developed in the QUEST Laboratory at Georgia Tech,

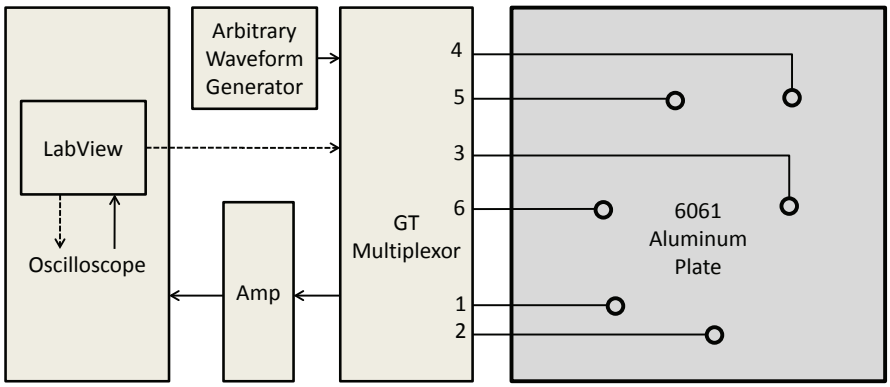

Figure 3.2: Block diagram of experimental setup. Solid lines indicate data flow, dotted lines represent control signals. GT Multiplexor is a bank of relays that is capable of connecting any of the six transducers to either of the two front-panel connectors, corresponding to the arbitrary waveform generator and amplifier, respectively.

was used to provide consistent, reliable switching between transducer pairs. The multiplexor was controlled via USB through a LabView (National Instruments Corp., Austin, TX) script running on the Windows XP operating system (Microsoft Corp., Redmond, WA) of the oscilloscope. The LabView script, which was developed by other past and current members of the QUEST Lab, also controlled the data acquisition functions of the oscilloscope.

The experiment was conducted as follows. First, 209 baseline datasets were recorded under known damage-free conditions over a range of temperatures that spanned 15° C. After collecting baseline data, a through-hole with a radius of 5 mm was drilled to simulate damage at the location indicated at Figure 3.1, and datasets were again recorded over a range of temperatures. Then, a 15 mm × 2 mm × 3.18 mm notch oriented +45° from horizontal was introduced in the lower-right corner of the plate. Several datasets were then collected at room-temperature. Finally, a second 15 mm × 2 mm × 3.18 mm notch was introduced near the center of the plate, this time oriented -45° from horizontal. A final set of data was then obtained at room temperature, completing the experimental data acquisition.

Each of the six piezoelectric transducers measured 12 mm in diameter and was excited

with a chirp excitation. The chirp pulse had a 10 V peak to peak amplitude and increased in frequency linearly from 40 kHz to 600 kHz over a 200 μs period. The pulse repetition frequency was 10 Hz, which allowed the propagating waves in the plate to essentially die out between excitations.

The use of a chirp excitation allows a significant amount of energy to be transferred into the material over a relatively long time-window without high voltages or excessive displacement. This is in contrast to the traditional use of an impulse function, which induces much larger displacements using hundreds or thousands of volts over a much shorter period of time. The ability to transfer roughly *the same amount of energy* into the plate with a 10 V peak-to-peak signal allows for a comparable signal-to-noise ratio (SNR) to be obtained without special equipment or high-voltage concerns.

Since the mechanical waves have relatively small displacements, particularly since a chirp excitation is used, the interrogation system can be treated as a linear, time-invariant (LTI) system. The waveform generator produces an excitation signal, which is translated to mechanical energy by the transducer. The plate itself introduces a transfer function that converts the mechanical vibrations from the transducer to a guided wave. Finally, the receiving transducer transfers the surface vibrations of the guided wave to an electrical signal, which is recorded by the oscilloscope.

The trade-off for using an excitation signal that is not time-compact is a reduction in spatial resolution. Since the system can be treated as LTI, however, the chirp excitation can be "shaped" to produce an arbitrary waveform that is more compact in time with a bandwidth that is contained within the bandwidth of the chirp signal [123]. Throughout this work, deconvolution of the chirp signal is performed in the frequency domain through frequency domain division. Additional band-pass filtering and/or pulse shaping with a finite impulse response (FIR) filter is typically performed in combination with the frequency domain division to address the numerical instability associated with division by small numbers.

3.2 Primary Guided Wave Challenges

Although sparse, distributed arrays of ultrasonic guided waves present an economical solution to interrogation of large, plate-like structures, there are significant challenges associated with this approach. This section illustrates some of these challenges using experimental data obtained from the setup described in the previous section.

3.2.1 Dispersion

The propagation velocities of guided waves are frequency-dependent. This phenomenon, referred to as dispersion, causes the waves to change shape as they propagate through the material.

Dispersion can be expressed in one of two forms, although a third is sometimes used as well to express a subset of the dispersive behavior. The relationship between propagation velocity and frequency can be expressed as a frequency-dependent phase velocity, $c_p(\omega)$, expressed in mm/μs, *or* as a frequency-dependent wavenumber, $k(\omega)$, expressed in rad/mm. The two are related to one another through the following relationship:

$$c_p(\omega) = \frac{\omega}{k(\omega)}, \tag{3.1}$$

where ω is the angular frequency, usually in rad/μs. Phase velocity refers to the propagation velocity of constant *phase*, which, for dispersive waves, is slightly different from the velocity of the wavepacket itself. The wavepacket propagates at the group velocity, $c_g(\omega)$, which is the third representation of dispersion and is analogous to the velocity of energy transport [124]. Group velocity is related to the wavenumber through this equation:

$$c_g(\omega) = \frac{d\omega}{dk(\omega)}. \tag{3.2}$$

If the media is *non*-dispersive, then $c_p(\omega) = c_g(\omega)$, which is only true if $k(\omega)$ is some linear multiple of ω. Note that since $c_g(\omega)$ is related to the inverse of the derivative of the wavenumber with respect to frequency, neither the wavenumber nor the phase velocity can be uniquely determined from the group velocity alone. Figure 3.3 and Figure 3.4 illustrates

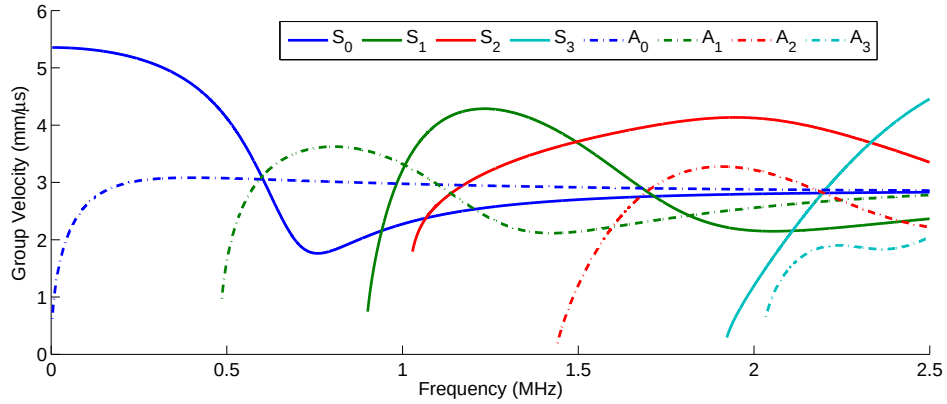

(a)

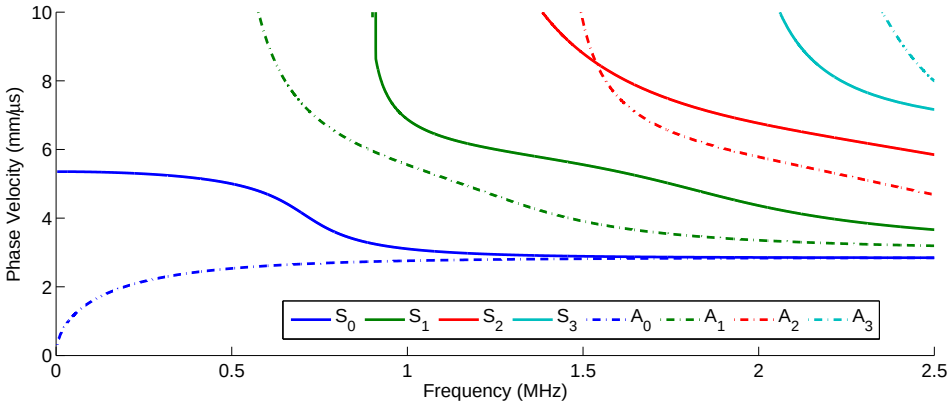

(b)

Figure 3.3: Nominal group (a) and phase (b) velocities in a 3.18 mm thick aluminum plate for several symmetric (solid lines) and asymmetric (dotted lines) propagating modes.

the group and phase velocity (Figure 3.3) and corresponding frequency-wavenumber relationships (Figure 3.4), or ω–k relationships, for several modes that are applicable to the experimental setup considered here.

In a LTI system model for guided waves, the measured data from an ultrasonic transducer, $M(\omega)$, can be represented in the frequency domain as:

$$M(\omega) = X(\omega)\left(\frac{1}{\sqrt{x}}\right)\mathrm{e}^{-jk(\omega)x}, \tag{3.3}$$

where $X(\omega)$ is the propagating wave packet, the $\frac{1}{\sqrt{x}}$ accounts for the geometric spreading loss, and the complex exponential accounts for dispersion with $j = \sqrt{-1}$ and $k(\omega)$ representing the frequency-dependent wavenumber. Note that if the wavenumber is a scalar

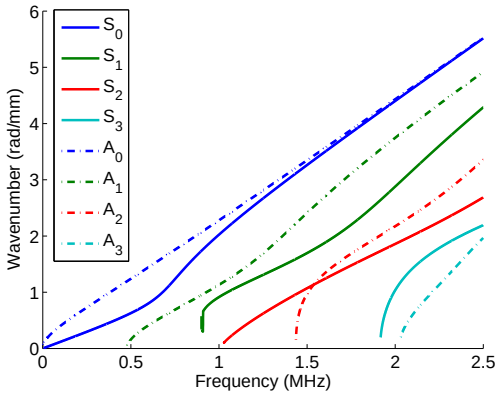

Figure 3.4: Nominal frequency-dependent wavenumbers in a 3.18 mm thick aluminum plate for several (solid lines) symmetric and (dotted lines) asymmetric propagating modes.

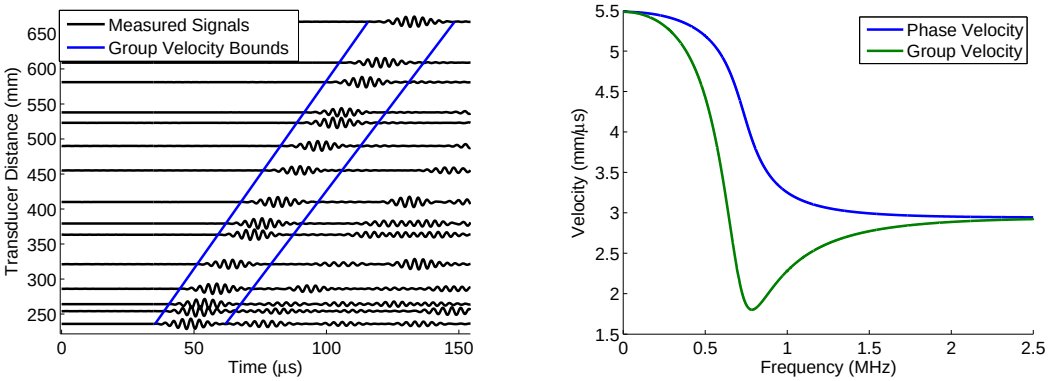

(a) (b)

Figure 3.5: Dispersion in the experimental data. (a) Waterfall plot of 7-cycle 300 kHz toneburst. (b) Group and phase velocity curves for the S_0 mode.

multiple of frequency, meaning $k(\omega) = \alpha\omega$, then the above equation decomposes to a *non*-dispersive case:

$$M(\omega) = X(\omega)\left(\frac{1}{\sqrt{x}}\right)\mathrm{e}^{-j\omega t}, \tag{3.4}$$

where $t = \alpha x$, which is equivalent to a frequency-independent group velocity, $c_g = \frac{1}{\alpha}$.

To illustrate the effects of dispersion, consider the waterfall plot shown in Figure 3.5a. The waterfall plot shows each of the signals recorded from the distributed array in Figure 3.1 arranged vertically by the distance between transducers. Each of the signals is scaled for visibility, so the relative amplitude of each displayed waveform is similar. In order to highlight the dispersive behavior of the propagating wave, the chirp excitation was

deconvolved from each recorded signal and a 7-cycle Hamming-windowed sinusoid with a 300 kHz center frequency was convolved with the result to produce a narrowband toneburst. From Figure 3.5a, the direct arrival is clearly changing as it propagates, increasing in duration, and although it cannot be inferred from the display, in addition to loss due to geometric spreading, the law of conservation of energy dictates that the amplitude must further decrease as the waveform spreads in time.

Figure 3.5b shows the nominal group and phase velocities for the S_0 mode. Since the group velocity is equivalent to the energy transfer velocity, bounds on the time-of-arrival can be established for a propagating wavepacket by evaluating the group velocity values [81]. A 7-cycle Hamming-windowed sinusoid at 300 kHz has a main lobe that spans 213 kHz to 387 kHz. Therefore, the energy transport of the wavepacket will range from 5.0 mm/μs (c_g (213 kHz)) to 5.4 mm/μs (c_g (387 kHz)). As a result, a 23 μs toneburst propagating along the plate will last 27 μs after propagating 236 mm and 33 μs after 667 mm. These bounds are illustrated in Figure 3.5a. Since the phase velocity is much higher than the group velocity (5.3-5.4 μs), the individual waves, or points of constant phase, *within the wavepacket* will appear to move faster than the wavepacket itself.

Dealing with the effects of dispersion is a challenging task that is discussed throughout this work. It is important to point out, however, that it is possible to minimize the degree of dispersion by selecting an operating spectrum that spans a relatively narrow range of propagation velocities [81], either by using a narrow bandwidth signal or carefully choosing the operating frequency. In many cases, however, dispersion is unavoidable and as such, must be addressed through the methods presented later in this text.

3.2.2 Multi-mode

Another challenge inherent in guided wave systems is the existence of multiple propagating modes. The presence of more than one propagating mode is problematic for guided wave imaging algorithms because each mode propagates at a different velocity. The difference

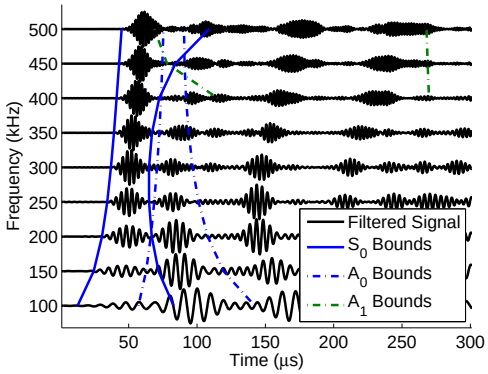

Figure 3.6: Mode excitability of experimental data as a function of frequency. Signals were excited from transducer 1 and recorded from transducer 2.

in group and phase velocity for several modes can be seen in Figure 3.3.

In addition to the propagation velocity, each mode also distributes the propagating energy differently through the thickness of the plate. This, in turn, makes each mode respond to a defect or damage differently. As such, there is no easy answer as to which propagating mode is "best" for detecting damage, and the most appropriate mode depends on the application. The reader is referred to chapter 8 of [124] for through-thickness profiles for several modes.

From Figure 3.5b, note that although multiple modes are indicated for *all* frequencies, only two modes exist below the cutoff frequency of the A_1 mode. As such, one of the most common methods to address the issue of multiple modes, and the one used throughout this text, is to operate at frequencies at or below the A_1 cutoff frequency, which is 486 kHz here.

One mechanism to further improve mode purity is to take advantage of the fact that for any particular system, the *excitability* of each mode varies with frequency. In other words, the energy coupling between transducer and each guided wave mode is not necessarily equal and the energy coupling ratio changes with frequency. Therefore, improved mode purity can be obtained by operating at frequencies that asymmetrically couple to the propagating mode of interest.

Figure 3.6 demonstrates the existence of multiple modes and the variation in excitability

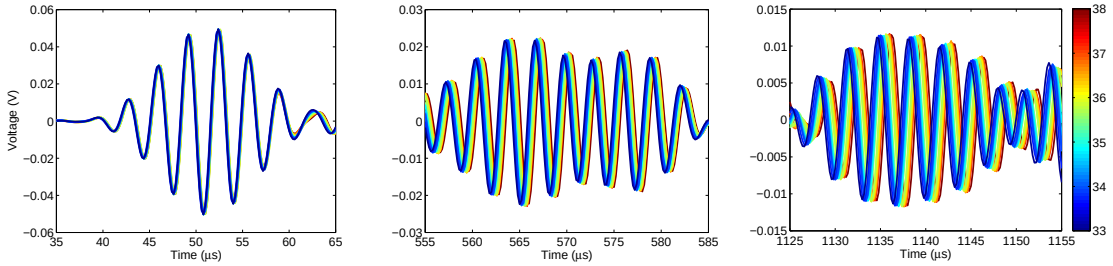

(a) (b) (c)

Figure 3.7: Experimental data color-coded for temperatures ranging from 33°-38° for several different time-windows. Signals were excited from transducer 1 and recorded from transducer 2.

of these mode. The signals in Figure 3.6 all correspond to experimental data excited with transducer 1, recorded with transducer 2, and filtered with 7-cycle tonebursts of various frequencies, which are indicated by the vertical offset of each result. From Figure 3.6, one can see that for this particular setup, the A_0 mode is dominant at 100 kHz, while the S_0 mode is dominant at 400 kHz.

3.2.3 Environmental Effects

As pointed out in the previous chapter, the effects of temperature on ultrasonic guided waves are well documented. Figure 3.7 illustrates the effects of benign environmental changes, such as temperature, for the experimental setup considered here for signals excited by transducer 1 and recorded with transducer 2.

Figure 3.7 shows that the signals appear to be “stretched”, with the signal differences increasing with time. The changes visible in Figure 3.7 *far* exceed those of a defect or damage, which are typically very small compared to the structural echoes (one to three orders of magnitude smaller, see Figure 3.8). Therefore, it is critical for any ultrasonic SHM system to address the issue of environmental changes.

3.3 Baseline Subtraction

SHM applications, by their very nature, are primarily interested in *changes* to the interrogation structure. As such, baseline subtraction, which is the act of differencing known good baseline data and test data obtained after some service period, is commonly used in these applications. Damage detection and localization is then performed under the inherent assumption that any baseline subtraction residual is due to the introduction of a defect or damage.

Unfortunately, not all changes in the recorded data are due to defects or damage. Benign environmental changes can cause significant variations in recorded data since temperature, pressure, humidity, and load differences can affect the transducer transfer functions, excitability of guided wave modes, frequency-dependent propagation velocity (dispersion), and scattering behavior of structural components. Of these environmental influences, temperature changes have been shown to have a significant impact on baseline subtraction [95]. Temperature changes are primarily manifested in guided wave measurements as variations in the transducer transfer functions, the dispersive properties of the material, and even propagation distances due to thermal expansion and contraction. Thus, temperature changes are used throughout this work as a representative case for significant environmental changes. To minimize these changes, two methods are typically used in combination: optimal baseline subtraction and baseline signal stretch.

3.3.1 Optimal Baseline Subtraction

Optimal Baseline Subtraction (OBS) minimizes baseline subtraction residual by collecting baseline data over a wide range of potential environmental conditions, producing a large database of baseline datasets. Since each dataset is collected under damage-free conditions, this knowledge-based approach is able to accommodate *any* source of benign signal changes, including not only changes in dispersion, but also mode excitability, transducer transfer functions, propagation loss, etc.

It should be pointed out that errors in environmental condition *measurement* (such as temperature, pressure, humidity, etc.) can result in the selection of a sub-optimal dataset. As such, baseline datasets are typically selected based on an adaptive comparison between the test signal and some subset of baseline signals, rather than measurements of the environmental conditions. Depending on the size of the subset, however, this can be a computationally demanding requirement.

Taking the concept of OBS to an extreme, if a baseline dataset is available at *any* arbitrary set of environmental conditions, then perfect baseline subtraction could conceivably be achieved. In reality, however, collecting and storing a set of baseline data for *every possible* combination of environmental conditions is impractical. To minimize computational and storage requirements, it is desirable for the number of baseline datasets to be kept to a minimum. Obviously, if OBS is to be used, some balance must be established between the tolerance for baseline subtraction error and computational and storage demands. Croxford *et al.* [104] addressed this question, and provided some quantitative guidance as to the baseline subtraction residual that can be expected from a given temperature spacing between baseline datasets.

3.3.2 Baseline Signal Stretch

Baseline signal stretch (BSS) is another technique that has been proposed to minimize the baseline subtraction residual that results from *small* environmental changes. Since the algorithm is only realistically capable of addressing relatively small environmental changes, the BSS algorithm has been proposed as a secondary algorithm to augment an OBS implementation [102, 103, 104]. It should be noted that the BSS algorithm does not require any additional measurements or *a priori* information.

The BSS algorithm seeks to compensate for a *slight* change in propagation velocity. Consider a non-dispersive media with the following propagation model, equivalent to (3.4):

$$M(\omega) = X(\omega)\left(\frac{1}{\sqrt{x}}\right)\mathrm{e}^{-j\frac{\omega}{c_g}x}. \tag{3.5}$$

For small environmental changes, the most significant effect is on propagating velocity. Therefore, two signals recorded under different environmental conditions can be represented as follows:

$$M_{\mathrm{a}}(\omega) = X(\omega)\left(\frac{1}{\sqrt{x}}\right)\mathrm{e}^{-j\frac{\omega}{c_{\mathrm{a}}}x}, \tag{3.6}$$

$$M_{\mathrm{b}}(\omega) = X(\omega)\left(\frac{1}{\sqrt{x}}\right)\mathrm{e}^{-j\frac{\omega}{c_{\mathrm{b}}}x}, \tag{3.7}$$

where c_{a} and c_{b} are the group velocity values for each measured signal. Note that thermal expansion and contraction will also change x slightly, however, this effect is negligible for the test cases considered throughout this work and is therefore ignored. To compensate for the difference in group velocity, the BSS algorithm resamples one of the frequency domain signals by a factor of α_{BSS}, where α_{BSS} is chosen to minimize the difference between the two signals:

$$\alpha_{\mathrm{BSS}} = \min_{\alpha} \int |M_{\mathrm{b}}(\omega) - M_{\mathrm{a}}(\alpha\omega)|^2 \, d\omega. \tag{3.8}$$

This approach has been shown to produce significant improvements for α values that are very close to '1', which is the case for very small environmental changes. As α deviates from unity, however, the frequency domain scaling begins to have an effect on the $X(\omega)$ term in addition to the propagation term. This phenomenon effectively limits the amount of compensation that can be achieved, *even in a non-dispersive media*. As such, the combination of OBS and BSS seems a natural combination.

Figure 3.8 shows baseline subtraction results from transducer pair 1-5 at 22.2° C with scattering from the 5 mm through-hole highlighted in gray. Figure 3.8a shows four overlapping signals that are all in very close agreement: (1) baseline data recorded at 22.7° C, (2) the OBS-selected baseline, (3) the test data, and (4) the test data after BSS to match the 22.7° C baseline data. Figure 3.8b highlights the *difference* between these signals by displaying three baseline subtraction results: (1) subtraction of the 22.7° C baseline data from test data, (2) subtraction of the 22.7° C baseline data from the BSS stretched test data, and (3) subtraction of the OBS baseline from the test data. For this particular set of data, the

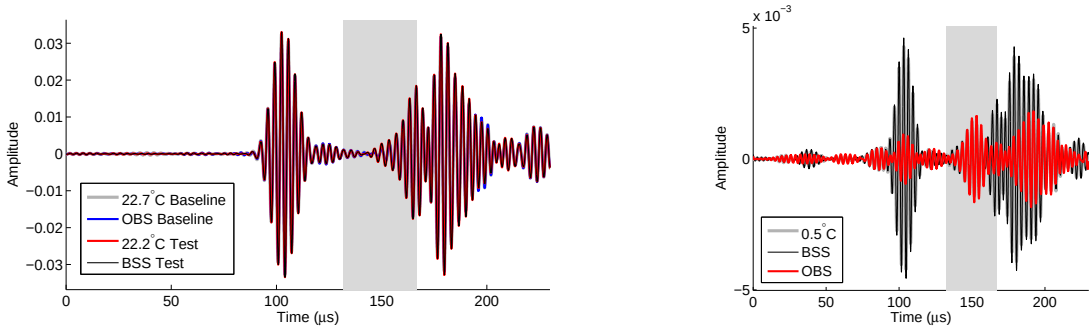

(a) (b)

Figure 3.8: Experimental baseline subtraction data for transducer pair 1-5. Scattering from a 5 mm through-hole is highlighted in the grey region. (a) Baseline data recorded at 22.7° C, baseline data selected through the OBS algorithm, test data recorded at 22.2° C, and test signals after BSS algorithm to match 22.7° C baseline. (b) Baseline subtraction results for test signal and 22.7° C baseline signal, BSS test signal and 22.7° C baseline signal, and test signal and OBS baseline signal.

BSS algorithm does *not* improve upon the OBS performance and is therefore not shown since the results are identical to those of OBS. It is important to point out that the peak amplitude of the scattered energy from the 5 mm through-hole is $\sim 1/30$ the amplitude of the direct arrival, which illustrates the sensitivity of the baseline subtraction operation. From Figure 3.8b, one can see that the scattered energy from damage has the same order of magnitude as the baseline subtraction residual from the direct arrival.

3.4 Conventional Delay-and-Sum Imaging

Conventional delay-and-sum imaging, also referred to as elliptical imaging, is a commonly employed guided wave imaging algorithm [82]. To motivate the need for algorithmic improvements, this section describes the algorithm and provides some representative results. Note that although the work is presented in the context of spatially distributed array elements, it is equally applicable to compact array geometries. For readability, the algorithm described in this section will be referred to as simply “conventional imaging” throughout the remainder of this text.

We first consider the case whereby the envelopes of the scattered signals are used for

imaging. The envelope is obtained by taking the absolute value of the analytic representation of the baseline subtracted, or differenced, signal:

$$s_{ij}^{\mathrm{ENV}}(t) = \left| s_{ij}(t) + j\hat{s}_{ij}(t) \right|, \tag{3.9}$$

where $s_{ij}(t)$ is the differenced signal excited with the ith transducer and received at the jth transducer, $\hat{s}_{ij}(t)$ is the Hilbert transform of the RF scattered field, and $s_{ij}^{\mathrm{ENV}}(t)$ is the envelope signal. For discussion purposes, this section assumes that perfect baseline subtraction is achieved, resulting in differenced signals comprising only the scattered field from the damage. As such, results are shown for simulated data.

Combining the imaging concepts of Wang *et al.* [110] and Michaels and Michaels [111], pixel values for conventional imaging are defined as:

$$P_{x,y} = \int \left| \sum_{i=1}^{n_s-1} \sum_{j=i+1}^{n_s} e_{ijxy} s_{ij}\left(t + \frac{d_{ixy} + d_{jxy}}{c_g} \right) \right|^2 w(t)dt, \tag{3.10}$$

where $w(t)$ is a windowing function, d_{ixy} is the distance from the ith transducer to the pixel location (x, y), c_g is the group velocity, and e_{ijxy} is a weighting coefficient specific to the pixel location and transmitter-receiver pair. The signals $s_{ij}(t)$ are the differenced signals in either RF or envelope format.

At this point, it is desirable to simplify the notation in (3.10). First, it is possible to replace the dual summation with a single summation of n_m terms by re-indexing each term as appropriate:

$$P_{x,y} = \int \left| \sum_{m=1}^{n_m} e_{mxy} s_m\left(t + \frac{d_{mxy}}{c_g} \right) \right|^2 w(t)dt. \tag{3.11}$$

The summation can be described in vector format as a function of the weighting coefficients:

$$P_{x,y} = \int \left| \vec{\mathbf{e}}_{xy}^{\mathrm{H}} \vec{\mathbf{s}}_{xy}(t) \right|^2 w(t)dt, \tag{3.12}$$

where the superscript "H" indicates the Hermetian transpose operation. The first term in the right-hand-side of (3.12), $\vec{\mathbf{e}}_{xy}$, is a column vector containing the weighting coefficients.

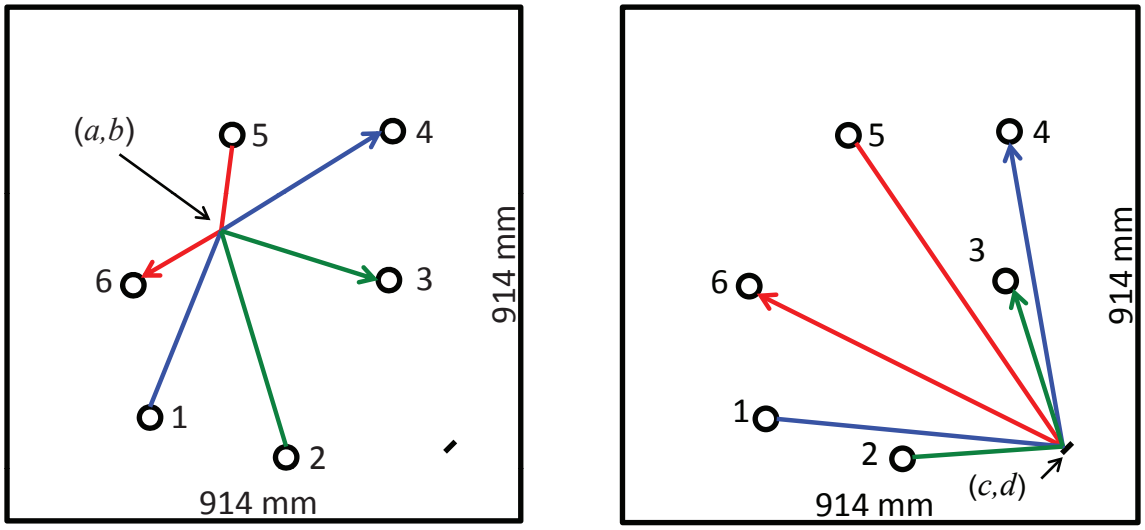

(a) (b)

Figure 3.9: Propagation paths for three selected transducer pairs for (a) pixel location (a,b) and (b) pixel location (c,d).

The second term contains the back-propagated signals, $\vec{\mathbf{s}}_{xy}(t)$, organized as:

$$\vec{\mathbf{s}}_{xy}(t) = \left[\; s_1\left(t + \frac{d_{1xy}}{c_g}\right) \quad \cdots \quad s_{n_m}\left(t + \frac{d_{n_m xy}}{c_g}\right) \; \right]^{\mathrm{T}}. \tag{3.13}$$

To facilitate discussion in the context of MVDR, $\vec{\mathbf{e}}_{xy}$ is referred to as the "look direction." Throughout this text, it is assumed that $\vec{\mathbf{e}}_{xy}$ is normalized to have unit L_2 norm. After expanding the squared term of (3.12) into two complex conjugate terms, (3.12) can be simplified to:

$$P_{xy}^{DS} = \vec{\mathbf{e}}_{xy}^{\mathrm{H}} \mathbf{S}_{xy} \vec{\mathbf{e}}_{xy}. \tag{3.14}$$

In (3.14) the $[n_m \times n_m]$ spatiotemporal correlation matrix, $\mathbf{S}_{xy}$, is calculated over the time-window of interest:

$$\mathbf{S}_{xy} = \int \vec{\mathbf{s}}_{xy}(t)\, \vec{\mathbf{s}}_{xy}^{\mathrm{H}}(t) w(t) dt. \tag{3.15}$$

From (3.14) and (3.15), the pixel value, P_{xy}^{DS}, is maximized when the back-propagated signal vectors, $\vec{\mathbf{s}}_{xy}(t)$, are scalar multiples of the look direction, $\vec{\mathbf{e}}_{xy}$, since their inner product will be maximized.

The two diagrams in Figure 3.9 show the propagation paths for three of the 15 unique transmitter-receiver pairs. Figure 3.9a depicts the paths for location (a, b) and Figure 3.9b

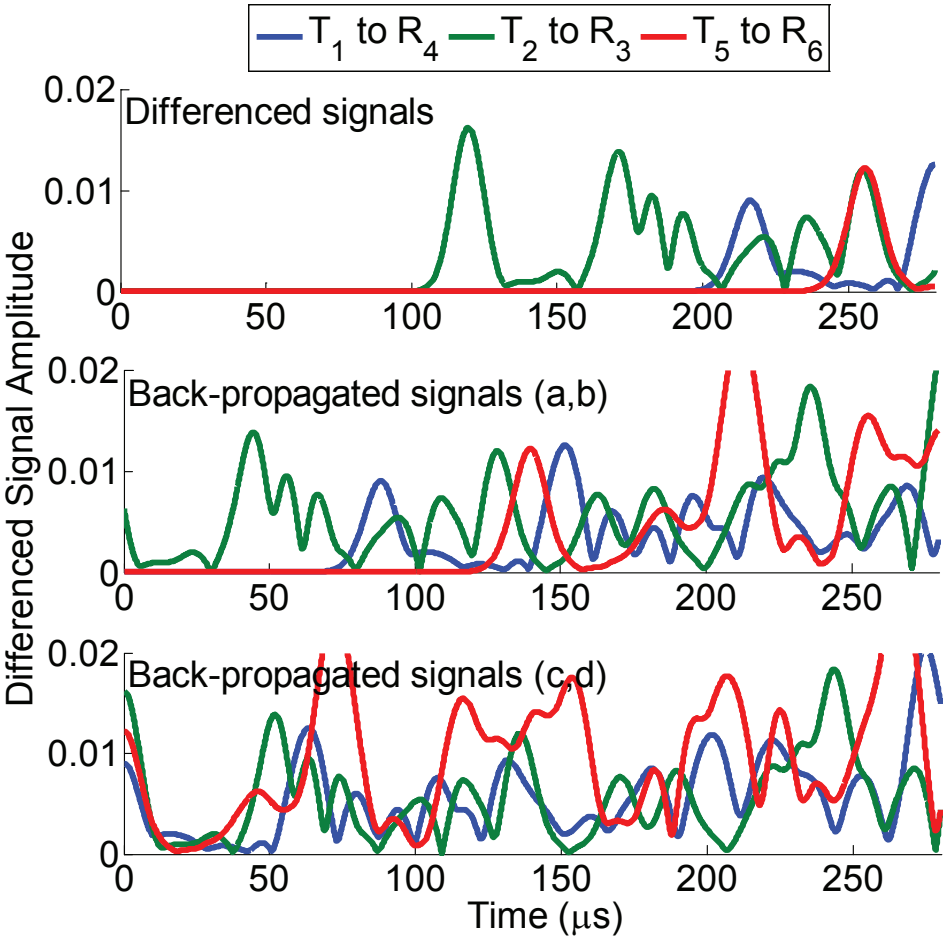

Figure 3.10: Differenced (top) and back-propagated (middle and bottom) signals.

depicts the corresponding paths for location (c, d). The envelopes of the received, differenced simulated signals for the three transmitter-receiver pairs of Figure 3.9 are shown in the top plot of Figure 3.10. Back-propagated signals for pixel locations (a, b) and (c, d), shown in the middle and bottom plots of Figure 3.10, are clearly different. Back-propagated signals at the damage location, (c, d), all have similar appearance and depict scattered energy at time $t = 0$, which is clearly not the case for the back-propagated signals at the non-damage location, (a, b). As a result, the pixel value for (c, d), when calculated as per (3.14), is expected to be higher than that for (a, b) or any other non-damage location.

Figure 3.11 shows the image generated using conventional imaging with a time window of 12 μs, spanning from $t = -6\,\mu$s to $t = +6\,\mu$s, and with the weights inversely proportional

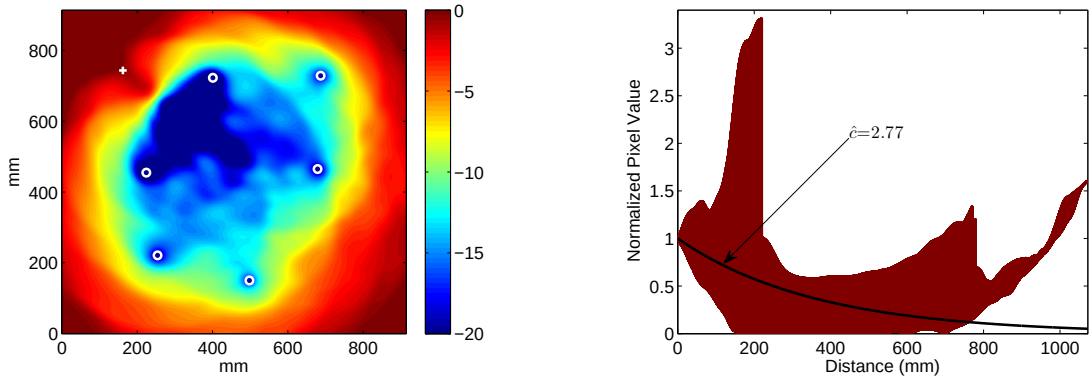

(a) (b)

Figure 3.11: Conventional imaging using simulated envelope signals. (a) Image displayed using a 20 dB scale, and (b) normalized pixel values versus distance for damage location ($\hat{c} = 2.77$).

to the square-root of the product of the propagation distances:

$$\vec{\mathbf{e}}_{xy} \sim \left[\begin{array}{ccc} \frac{1}{\sqrt{d^{\times}_{1xy}}} & \cdots & \frac{1}{\sqrt{d^{\times}_{n_m xy}}} \end{array} \right]^{\mathrm{T}}, \tag{3.16}$$

where $d^{\times}_{mxy}$ is the product of the distances d_{ixy} and d_{jxy} associated with the m^{th} transducer pair. The multiplication of propagation distances is necessary to accurately reflect the geometric spreading from both the source and the scatterer. Note that the weights are selected to maximize the pixel value at the damage location by matching the anticipated amplitude relationship between signals in the back-propagated signal vectors, $\vec{\mathbf{s}}_{xy}(t)$.

In Figure 3.11a, and throughout the entirety of this thesis, images are shown on a 20 dB scale, with the color scale aligned so that the peak value *within a 15 mm radius of the known damage location* corresponds to the top of the color bar. The 15 mm radius was chosen so that *minor* localization errors are ignored. Figure 3.11b is a plot of the pixel values of Figure 3.11a as a function of distance from the simulated damage location. For the case when more than one pixel is located a specific distance from the true damage location, all of the pixel values are plotted, which results in a vertical distribution of points that extends from the smallest pixel value at that distance to the largest. The values are normalized so that the maximum pixel value within a 15 mm radius of the damage site is one. A perfect

image would have a pixel value of one at a distance of zero and all other pixel values would be zero.

Figure 3.11a illustrates the difficulty associated with conventional guided wave imaging. The edge reflections are causing imaging artifacts that are as large as the damage site, and in some cases the artifacts are even three times the magnitude of the damage. As such, damage detection and localization cannot be performed with Figure 3.11a. It should be pointed out that the imaging performance is expected to improve if the plate were larger, reducing the number and amplitude of edge reflection, or if the damage were located further away from the edge, for example, inside the polygon of sensors.

To effectively compare and contrast imaging performance throughout this text, it is useful to establish a single quantitative measure of performance. Previously reported figures of merit, such as described in [113], do provide a means to evaluate images; however, it is desirable to characterize the quality of an image with a single scalar value.

A performance metric is proposed here that takes into account artifact amplitude, distance from damage, and overall noise floor. The proposed metric is the exponential coefficient that results from a least-squares exponential curve fit to the pixel values, arranged as a function of distance from the damage location:

$$\frac{P(x)}{P(0)} \sim e^{-\hat{c}x} \text{ for } x \in X, \tag{3.17}$$

where $P(x)$ is the pixel value as a function of distance from the known damage location, X is the set of all distances. This metric was chosen because it provides a single value that (1) increases (decreases) as the damage location becomes more focused (defocused), (2) increases (decreases) as the overall noise floor is lowered (raised), and (3) increases (decreases) as artifacts are moved towards (away from) the true damage site. In other words, the larger the value of c, the closer the image is to perfect (a single non-zero pixel value at the damage site), and artifacts are penalized more the further they are located from the true damage site. To find $\hat{c}$ and establish the performance metric, a least-squares fit is

performed on the logarithmic values as:

$$\hat{c} = \arg\min_{c} \sum_{x \in X} \left(\ln\left(\frac{P(x)}{P(0)}\right) + cx \right)^2. \tag{3.18}$$

It is also important to note that this metric is only valid if the damage location is precisely known, such as for simulations and controlled experiments. Although this restriction limits widespread applicability, it still provides a mechanism for quantitatively comparing images and algorithms. The exponential curve overlaid on Figure 3.11b represents the curve that minimizes the performance metric of (3.18), which corresponds to $\hat{c} = 2.77$.

3.5 Dispersion compensation

As discussed in Section 3.2, ultrasonic guided waves are typically dispersive, which causes the shape of a wavepacket to spread out as it travels over distance. As such, dispersion compensation improves imaging performance through two effects. First, dispersion compensation compensates for the dispersive spreading effects, increasing the amplitude of and similarity between back-propagated wavepackets and therefore improving imaging performance. Second, since each mode propagates according to a different set of dispersion relations, dispersion compensation for one mode has a tendency to spread out signals that propagate according to other dispersion relations, which improves imaging performance when multiple modes are present in recorded data.

In (3.11) and (3.13), back-propagation of the differenced signals was performed through a simple time-shift. However, this method of back-propagation does not account for the effects of dispersion. Note that any of the back-propagated signals from (3.11) can be expressed in the frequency domain as:

$$\hat{S}(\omega) = S(\omega)\, \mathrm{e}^{+j\frac{\omega}{c_g}d}, \tag{3.19}$$

where $S(\omega)$ is the differenced signal and $\hat{S}(\omega)$ is the frequency domain representation of the back-propagated signal, equivalent to the frequency domain representation of any of the vector elements expressed in (3.13). To perform back-propagation *with dispersion*

compensation, however, the back-propagation operation must account for the frequency-dependence of the wavenumber:

$$\hat{S}(\omega) = S(\omega)\, e^{+jk(\omega)d}, \tag{3.20}$$

which must be performed in the frequency domain and requires explicit knowledge of the dispersion relations, which are expressed as $k(\omega)$ here.

Even if the dispersion relations are known, the frequency domain back-propagation algorithm requires n_w complex multiplications (where n_w is the number of frequency domain values) and an inverse FFT operation for *each measured signal at each pixel*, which is an incredible computational burden. Since the envelope of the time domain signals effectively masks the effects of dispersion, the benefits of performing dispersion compensation do not justify the computational costs. As such, this algorithm is not typically used in guided wave imaging applications.

CHAPTER IV

MINIMUM VARIANCE IMAGING

Traditional guided wave imaging naturally lends itself to the use of modern multi-channel estimation techniques, such as Minimum Variance Distortionless Response (MVDR) [47], also known as Capon's Method [45]. In this chapter the mathematical basis for minimum variance imaging is presented, additional techniques for imaging improvements are proposed, and a brief discussion is provided with experimental results. Large portions of this chapter can be found in Hall and Michaels [125, 126], which is a culmination of the work reported in [127, 128]. The approach has been applied to both isotropic aluminum structures [125] (shown here) as well as quasi-isotropic carbon fiber reinforced polymers [129].

4.1 Mathematical Basis of MVDR

To begin, consider the following eigendecomposition of the correlation matrix in (3.15):

$$\mathbf{S}_{xy} = \sum_{i=1}^{n_m} \lambda_i \vec{\mathbf{v}}_i \vec{\mathbf{v}}_i^{\mathrm{H}}, \tag{4.1}$$

where λ_i are eigenvalues and $\vec{\mathbf{v}}_i$ are unit-norm eigenvectors specific to the correlation matrix $\mathbf{S}_{xy}$. Since the correlation matrix is Hermetian symmetric, each eigenvalue is non-negative and the eigenvectors are orthogonal to one another. Throughout this chapter, the eigenvalues are assumed to be ordered from largest to smallest, so $\vec{\mathbf{v}}_1$ will always be the eigenvector corresponding to λ_1, the largest eigenvalue.

Consider the set of back-propagated signals corresponding to a pixel location that exactly coincides with a scattering location, such as the back-propagated signals for (c, d) in Figure 3.9b. For an ideal scatterer and no additional echoes, each back-propagated signal comprises a common signal, $x(t)$, that is zero outside of the window of interest and scaled

according to some relationship, $\hat{\mathbf{s}}_{cd}$, which is constrained to have unit-norm:

$$\vec{\mathbf{s}}_{cd}(t) = x(t)\hat{\mathbf{s}}_{cd}. \tag{4.2}$$

From the eigendecomposition of the correlation matrix for this simple case, the unit-norm relationship between signals, $\hat{\mathbf{s}}_{cd}$, is equal to $\vec{\mathbf{v}}_1$, the energy of $x(t)$ is equal to λ_1, and all other eigenvalues are zero:

$$\mathbf{S}_{cd} = \int |x(t)|^2 w(t)\hat{\mathbf{s}}_{cd}\,\hat{\mathbf{s}}_{cd}^{\mathrm{H}} dt = \lambda_1 \vec{\mathbf{v}}_1 \vec{\mathbf{v}}_1^{\mathrm{H}}. \tag{4.3}$$

By substituting (4.3) into (3.14), one can see that the pixel value P_{cd}^{DS} is maximized at a value of λ_1 when $\vec{\mathbf{e}}_{cd} = \vec{\mathbf{v}}_1 = \hat{\mathbf{s}}_{cd}$ and minimized at a value of 0 when $\vec{\mathbf{e}}_{cd} \perp \vec{\mathbf{v}}_1$. In other words, if the look direction, $\vec{\mathbf{e}}_{cd}$, accurately reflects the amplitude relationship between signals, the pixel value is maximized.

To reduce image artifacts, it is desirable to minimize the pixel value for any location that does not correspond to damage. By assuming that the look direction, $\vec{\mathbf{e}}_{xy}$, represents the amplitude relationship between signals in the case that damage is present at a pixel location, such as in (3.16), a constrained optimization problem can be constructed:

$$\vec{\mathbf{w}}_{xy} = \min_{\vec{\mathbf{w}}} \vec{\mathbf{w}}^{\mathrm{H}} \mathbf{S}_{xy} \vec{\mathbf{w}} \text{ such that } \vec{\mathbf{w}}^{\mathrm{H}} \vec{\mathbf{e}}_{xy} = 1. \tag{4.4}$$

In words, the constraint of the inner product of $\vec{\mathbf{w}}$ and $\vec{\mathbf{e}}_{xy}$ preserves the pixel value when damage is present at (x,y) and the $\min_{\vec{\mathbf{w}}} \vec{\mathbf{w}}^{\mathrm{H}} \mathbf{S}_{xy} \vec{\mathbf{w}}$ term minimizes the pixel value when damage is absent.

The preservation of pixel values by the constraint can be made clear with a brief example. Recall that the pixel value at (c, d) described in the previous section is maximized at a value of λ_1 when $\vec{\mathbf{e}}_{cd} = \hat{\mathbf{s}}_{cd} = \vec{\mathbf{v}}_1$. Substituting (4.3) into the min term of (4.4) and replacing $\vec{\mathbf{v}}_1$ with $\vec{\mathbf{e}}_{cd}$ yields,

$$\vec{\mathbf{w}}^{\mathrm{H}} \mathbf{S}_{cd} \vec{\mathbf{w}} = \lambda_1 |\vec{\mathbf{w}}^{\mathrm{H}} \vec{\mathbf{e}}_{cd}|^2. \tag{4.5}$$

Therefore, by constraining the inner product of $\vec{\mathbf{w}}$ and $\vec{\mathbf{e}}_{xy}$ to have unit value in (4.4), the pixel value at damage locations is preserved at a value of λ_1.

The optimal solution to this minimization problem can be found through the use of a Lagrange multiplier, α, to satisfy the look direction constraint,

$$L = \vec{\mathbf{w}}^{\mathrm{H}}\mathbf{S}_{xy}\vec{\mathbf{w}} + \alpha\left(\vec{\mathbf{w}}^{\mathrm{H}}\vec{\mathbf{e}}_{xy} - 1\right). \tag{4.6}$$

The Lagrangian L is minimized by taking the derivative of (4.6) with respect to $\vec{\mathbf{w}}$ and setting it equal to zero, which results in:

$$\vec{\mathbf{w}} = -\frac{\alpha}{2}\mathbf{S}_{xy}^{-1}\vec{\mathbf{e}}_{xy}. \tag{4.7}$$

By substituting (4.7) for $\vec{\mathbf{w}}$ into the inner product constraint of (4.4), α can readily be shown to be:

$$\alpha = -\frac{2}{\vec{\mathbf{e}}_{xy}^{\mathrm{H}}\mathbf{S}_{xy}^{-1}\vec{\mathbf{e}}_{xy}}. \tag{4.8}$$

By further substituting (4.8) for α back into (4.7), a closed-form expression for $\vec{\mathbf{w}}_{xy}$ that satisfies (4.4) is obtained as a function of $\vec{\mathbf{e}}_{xy}$:

$$\vec{\mathbf{w}}_{xy} = \frac{\mathbf{S}_{xy}^{-1}\vec{\mathbf{e}}_{xy}}{\vec{\mathbf{e}}_{xy}^{\mathrm{H}}\mathbf{S}_{xy}^{-1}\vec{\mathbf{e}}_{xy}}. \tag{4.9}$$

Using this equation, $\vec{\mathbf{w}}_{xy}$ can be computed at each pixel location.

Minimum variance imaging is performed in a similar fashion to conventional imaging; however, instead of using the look direction directly, the optimal weights, $\vec{\mathbf{w}}_{xy}$, are calculated and used:

$$P_{xy}^{MV} = \vec{\mathbf{w}}_{xy}^{\mathrm{H}}\mathbf{S}_{xy}\vec{\mathbf{w}}_{xy}, \tag{4.10}$$

where $\vec{\mathbf{w}}_{xy}$ is computed as in (4.9), satisfying (4.4).

It is important to point out that a matrix inversion is required to calculate each pixel value. The matrix inversion operation is responsible for the bulk of the computational complexity of minimum variance imaging. Assuming that Gauss-Jordan elimination is used for the matrix inversion, the computational complexity of obtaining each pixel value is $O(n_m^3)$ [130]. Also, for reasons discussed in the following section, the autocorrelation matrix is diagonally loaded by a factor of 0.1 times the largest eigenvalue prior to the inversion operation.

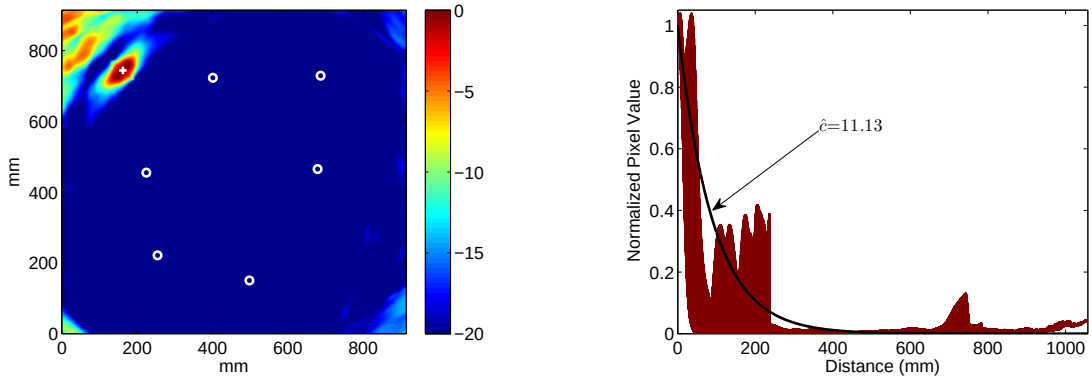

(a) (b)

Figure 4.1: Minimum variance imaging using simulated envelope signals. (a) Image displayed using a 20 dB scale, and (b) normalized pixel values versus distance for damage location ($\hat{c}$ = 11.13).

Figure 3.11 and Figure 4.1 show imaging performance for both conventional imaging and MVDR using the same $\vec{\mathbf{e}}$ as given in (3.16). Visually, Figure 4.1 clearly identifies the damage location with significantly reduced artifacts compared to Figure 3.11.

Note that the MVDR approach to imaging is an optimal solution to (4.4). As such, since (4.4) constrains the weights to reduce any energy that is not in the look direction, a reduction in artifact amplitudes should be expected over conventional imaging using the same look directions.

4.2 Modeling Errors and Regularization

Although MVDR offers substantial improvement over conventional imaging, careful consideration must be given to the operating environment and the implications of inaccurate modeling assumptions. Errors in transducer locations, transducer phase and gain differences, and inaccuracies inherent in the sampled approximation to the covariance matrix all constitute modeling errors that can severely degrade algorithmic performance if they are not accommodated.

As shown in [30], as signal-to-noise ratios increase, adaptive methods such as MVDR

become increasingly sensitive to modeling errors. This sensitivity is in contrast to conventional imaging techniques that become less sensitive to modeling errors as signal-to-noise ratios increase. To address this problem, regularization of the matrix inverse in (4.9) is performed using diagonal loading [131], which is shown to be optimal for a number of constrained optimization problems [132], including (4.9), and also addresses the scenario when an insufficient number of samples are used to generate the covariance matrix. The degree of diagonal loading can be described as some fractional value, α, of the largest eigenvalue, λ_1:

$$\mathbf{S}_{xy}^{-1} = \left(\mathbf{S}_{xy} + \alpha\lambda_1\mathbf{I}_m\right)^{-1}, \tag{4.11}$$

where $\mathbf{I}_m$ is an $[n_m \times n_m]$ identity matrix. Bounds can then be established for α, as described in [30]:

$$\frac{1}{n_m} < \frac{\lambda_1}{\alpha\lambda_1 + \sigma_{n_m}^2} < \frac{1}{\epsilon} \tag{4.12}$$

Here σ_n^2 is the average noise power observed across all differenced signals and ϵ is the degree of modeling error present in the unit look direction, $\vec{\mathbf{e}}_{xy}$. The modeling error is quantified by the norm of the difference between the nominal look direction, $\vec{\mathbf{e}}_{xy}$, and the "true" or "actual" look direction, $\hat{\mathbf{s}}_{xy}$, which accurately reflects the underlying signal relationships within the received signals:

$$\epsilon = \|\vec{\mathbf{e}}_{xy} - \hat{\mathbf{s}}_{xy}\|. \tag{4.13}$$

Since both vectors are constrained to have unit norm, ϵ will be in the range: $0 \leq \epsilon \leq 2$. Rearranging (4.12) to solve for α and assuming a large signal-to-noise ratio ($\lambda_1 \gg \sigma_n^2$) reveals:

$$\epsilon \leq \alpha < n_m. \tag{4.14}$$

The lower bound for α ensures that sufficient regularization is present to accommodate potential error in the look direction, while the upper bound prevents the regularization noise, $\alpha\lambda_1$, from unnecessarily degrading performance.

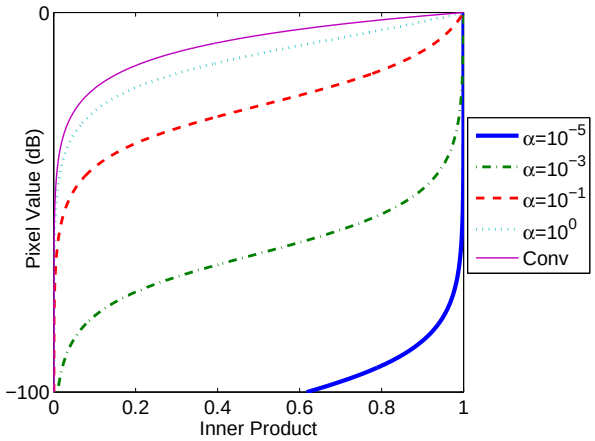

Figure 4.2: Pixel values as a function of inner product between look direction, $\vec{\mathbf{e}}_{xy}$, and largest eigenvector, $\vec{\mathbf{v}}_1$. Four different regularization factors ($\alpha = 10^{-5}, 10^{-3}, 10^{-1}, 10^{0}$) are shown for minimum variance imaging, which can be compared with the conventional case (Conv).

An example is provided here to illustrate the impact of regularization on MVDR performance. Consider a pixel location at which the cross-correlation matrix, $\mathbf{S}_{xy}$, has a single, non-zero eigenvalue, λ_1, that is equal to one and $\vec{\mathbf{v}}_1$ is the ideal steering vector. Recall from (4.5) that the pixel value, P_{xy}^{MV} , is maximized at a value of λ_1 when $\vec{\mathbf{e}}_{xy} = \vec{\mathbf{v}}_1$. Figure 4.2 illustrates the pixel value, P_{xy}^{MV}, as a function of the inner product between the look direction, $\vec{\mathbf{e}}_{xy}$, and $\vec{\mathbf{v}}_1$ for several regularization values. As the regularization is increased, tolerance for inaccuracies in the look direction is also increased. This is apparent in Figure 4.2 by comparing the pixel values that result when the inner product is close to, but not exactly, one. Unfortunately, the tolerance comes at the cost of larger artifacts, which can be seen by comparing the pixel values that result when $\vec{\mathbf{e}}_{xy}$ and $\vec{\mathbf{v}}_1$ are not in agreement and produce an inner product much less than one. Therefore, to maximize the benefit of MVDR, it is desirable to use as little regularization as possible while keeping $\alpha > \epsilon$. To maintain consistency throughout this thesis and allow for inaccuracies in the look direction when working with experimental data, a regularization factor of 10^{-1} is used for all minimum variance imaging.

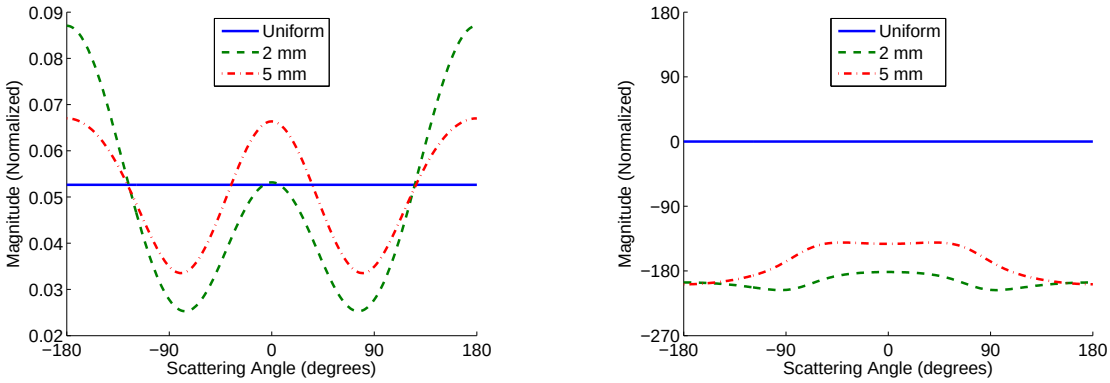

(a) (b)

Figure 4.3: Scattering fields for a uniform scatterer compared with 2 mm and 5 mm through-holes generated as per Grahn [122] for the S_0 mode (incident and scattered). The scattering angle is the angular difference between the incident and scattered waves. (a) Scattering field magnitude (normalized) as a function of angle, and (b) scattering field phase as a function of angle.

4.3 Scattering Characteristics

With minimum variance imaging, the look direction takes on a much more significant role than for conventional imaging. As such, further imaging improvements can be obtained by incorporating additional information into the look direction. Specifically, the look direction can be modified to incorporate information about the scatterer:

$$\vec{\mathbf{e}}_{xy} \sim \left[\begin{array}{ccc} \frac{\psi_{xy}^{1}}{\sqrt{d_{1xy}^{\times}}} & \cdots & \frac{\psi_{xy}^{nm}}{\sqrt{d_{nmxy}^{\times}}} \end{array} \right]^{\mathrm{T}}, \tag{4.15}$$

where ψ_{xy}^{m} corresponds to the scattering coefficient of an incident wave on point (x, y) for the m^{th} transmitter-receiver pair. Note that as before, $\vec{\mathbf{e}}_{xy}$ is scaled to be a unit-norm vector.

Significant effort has been expended by many researchers to accurately describe scattering fields for a number of defects. Surface-breaking defects of various sizes [133], through-thickness holes [134, 135], notches [136], and holes with and without symmetrical notches [137] have been evaluated. As mentioned earlier, all through-hole scattering fields were generated using the low frequency approximation derived by Grahn [122] for the center frequency of the propagating signals (300 kHz for the examples presented here).

In previous images, the scattering field was assumed to be uniformly distributed (refer

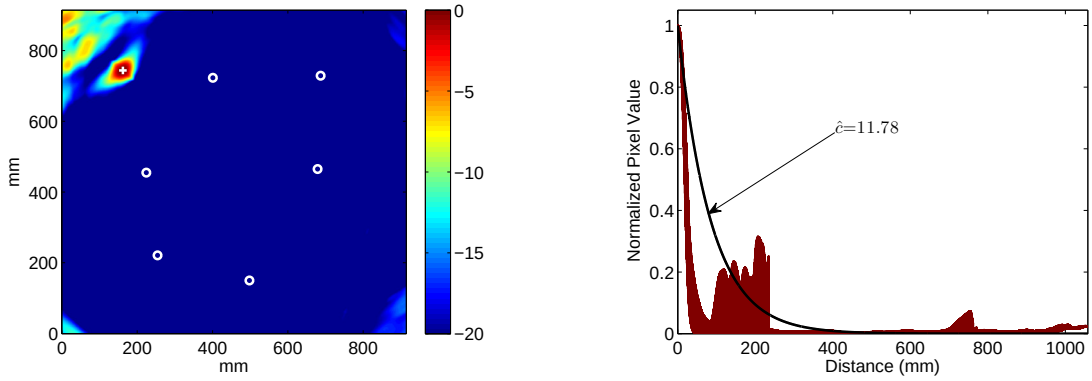

(a) (b)

Figure 4.4: Minimum variance imaging with matched scattering field using simulated envelope signals. (a) Image displayed using a 20 dB scale, and (b) normalized pixel values versus distance from damage location ($\hat{c}$ = 11.78).

to (3.16)); however, the simulation actually used scattering characteristics corresponding to a 6 mm through-hole. Figure 4.3 shows scattered amplitude and phase calculated for a 300 kHz sinusoid incident on a 2 mm through-hole, a 5 mm through-hole, and a uniform scatterer. Note that although the scattering pattern for a through-hole is independent of incident angle, this is not the case for an arbitrary scatterer such as a crack or notch. The concept of a scattering matrix was introduced in [138] to describe far-field scattering from flaws of arbitrary shape.

Figure 4.4 shows the performance improvement obtained by incorporating the appropriate scattering field into the look direction. Note that, unlike the other methods discussed in this section, the use of scattering characteristics improves the peak-to-noise ratio of the image by increasing the peak value with little impact on the noise floor. Figure 4.4 results in a performance metric of $\hat{c}$ = 11.78.

4.4 Phase Information

Another factor that can significantly improve imaging performance is the inclusion of phase information. Imaging with envelope data, as shown in Figures 3.11, 4.1, and 4.4, discards valuable information contained in the received signals. Two signal formats are available to

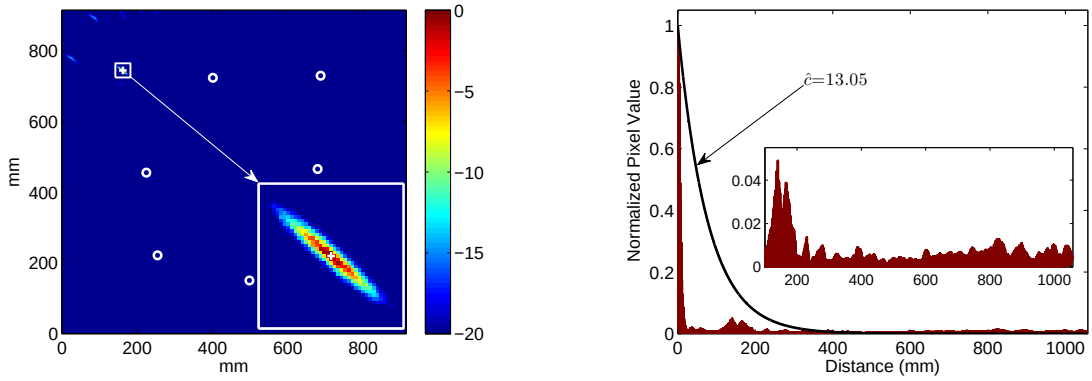

(a) (b)

Figure 4.5: Minimum variance imaging with matched scattering field using simulated analytic signals. (a) Image displayed using a 20 dB scale, and (b) normalized pixel values versus distance from damage location ($\hat{c}$ = 13.05).

convey the phase information of the scattered field for imaging: (1) raw RF and (2) analytic representation. Since both formats contain identical information, imaging performance is expected to be comparable between the two. Since the analytic representation treats the signals as complex values, making phase information about the scattered field easily accessible, the analytic representation is used when phase information is incorporated throughout this text.

Note that the use of phase information in either format may slightly change two aspects of the imaging algorithm as it has been described: (1) dispersion compensation may become necessary, depending on propagation distances and the degree of dispersion present in the frequency range of operation, and (2) scattering fields will need to include complex reflection coefficients, conveying phase information in addition to magnitude, as in Figure 4.3.

Figure 4.5 represents the significant imaging improvements that is obtained from using phase information. A much smaller defect spot size and a significantly lower noise floor are visible. Clearly, the additional phase information provides for significant performance improvement as compared to the use of envelope signals *assuming* that the phase of the signal is accounted for during back-propagation. The performance metric for Figure 4.5 is

$\hat{c} = 13.05$.

There are two fundamental reasons for the significant improvement over Figure 4.4. First, the use of phase information improves the time resolution of the signal. As the time resolution of the signal is increased, the spatial resolution of the image is expected to improve as well. Second, the use of the complex signals for minimum variance imaging reduces the image noise floor by reducing the likelihood that the look direction will accidentally agree with $\vec{\mathbf{v}}_1$.

4.5 Instantaneous Windowing

Imaging performance can be further improved by modifying the window width used for the integration in (3.15). It is assumed that the same time window is used for all pixel locations, and that it is centered at a time that maximizes the signal-to-noise ratio. For example, for the case illustrated in Figure 3.9, the 12 μs integration window is centered at 0 μs.

The length of the time window is determined to balance the need to (1) accurately estimate the correlation matrix and (2) minimize the impact of undesired reflections. For received signals that contain Gaussian white noise, larger time windows provide a mechanism to minimize the effects of noise on the correlation matrix. In contrast, at image locations with artifacts, the pixel value is non-zero because there are non-negligible components of the back-propagated signals that are in agreement with the look direction. Since non-real-time guided wave systems can reduce the level of additive Gaussian white noise to arbitrary levels by averaging a number of waveforms, increasing the window size simply increases the window of opportunity for undesired agreement between the look direction and non-damage related signals. Therefore, improved performance can be achieved by minimizing the window length.

For the case of high-SNR received signals, the correlation matrix may be accurately generated with as little as a single vector that corresponds to a time that maximizes the signal-to-noise ratio. Figure 4.6 depicts imaging performance as a function of window size

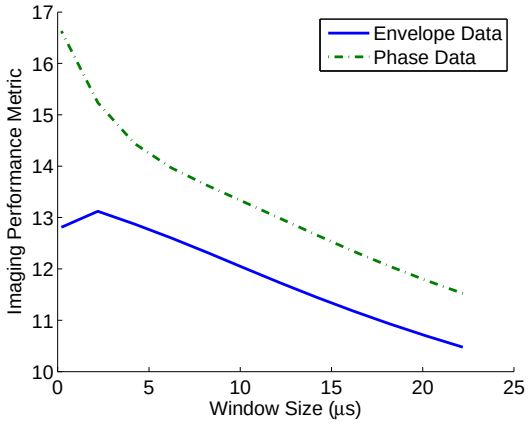

Figure 4.6: Minimum variance imaging performance as a function of window size using simulated data.

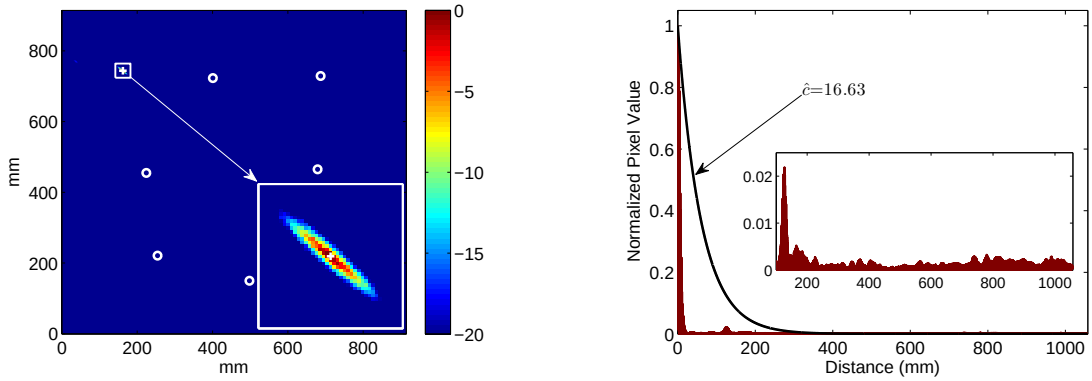

(a) (b)

Figure 4.7: Minimum variance imaging with matched scattering field using simulated analytic signals and an instantaneous window. (a) Image displayed using a 20 dB scale, and (b) normalized pixel values versus distance from damage location ($\hat{c} = 16.63$).

for the simulated case, which uses a Hamming-windowed sinusoid. For more complex excitation signals, it is possible that larger windows may exhibit improved performance.

Note that as the window size is decreased, the correlation matrix used by MVDR becomes underdetermined. As shown previously, however, regularization by diagonal loading is used to mitigate this situation.

Figure 4.7 illustrates imaging performance after reducing the window-size from the 12 μs window used previously to a single digital sample recorded at 5 MHz. The performance metric is increased from 13.05 to 16.63.

When instantaneous windowing is used, the summation interval in (3.15) is reduced to a single point in time, τ. In other words,

$$\mathbf{S}_{xy} = \vec{\mathbf{s}}_{xy}(\tau)\,\vec{\mathbf{s}}_{xy}^{\mathrm{H}}(\tau), \tag{4.16}$$

where τ is a time reference that corresponds to the maximum amplitude of the transmitted signal. For the simulation and experimental examples used throughout this text, $\tau = 0$.

Instantaneous windowing simplifies both conventional and minimum variance imaging. When the correlation matrix is reduced to the form of (4.16), the pixel value calculation for conventional imaging (see (3.14)) becomes:

$$P_{xy}^{DS} = \left|\vec{\mathbf{s}}_{xy}^{\mathrm{H}}(\tau)\,\vec{\mathbf{e}}_{xy}\right|^2. \tag{4.17}$$

From (4.17), the computational complexity for calculating a single pixel value is $O(n_m)$.

The computational benefits of instantaneous windowing are slightly less straightforward for minimum variance imaging. Recall that diagonal loading has already been proposed for inversion of the correlation matrix. The eigendecomposition of a diagonally loaded instantaneous correlation matrix is:

$$\begin{aligned}\hat{\mathbf{S}}_{xy} &= \vec{\mathbf{s}}_{xy}(\tau)\,\vec{\mathbf{s}}_{xy}^{\mathrm{H}}(\tau) + \alpha\lambda_1\mathbf{I}_m \\ &= (1+\alpha)\,\lambda_1\vec{\mathbf{v}}_1\vec{\mathbf{v}}_1^{\mathrm{H}} + \alpha\lambda_1\mathbf{V}_1^{\prime}\mathbf{V}_1^{\prime\mathrm{H}},\end{aligned} \tag{4.18}$$

where $\mathbf{V}_1^{\prime}$ is a set of $n_m - 1$ orthonormal vectors orthogonal to $\vec{\mathbf{v}}_1$. Using the structure of $\hat{\mathbf{S}}_{xy}$ in (4.18), the inverse of $\hat{\mathbf{S}}_{xy}$ is:

$$\hat{\mathbf{S}}_{xy}^{-1} = \frac{1}{(1+\alpha)\,\lambda_1}\vec{\mathbf{v}}_1\vec{\mathbf{v}}_1^{\mathrm{H}} + \frac{1}{\alpha\lambda_1}\mathbf{V}_1^{\prime}\mathbf{V}_1^{\prime\mathrm{H}}. \tag{4.19}$$

Substituting (4.19) into (4.9), the optimal weights that satisfy (4.4) can be expressed as:

$$\vec{\mathbf{w}}_{xy} = \frac{\frac{\vec{\mathbf{v}}_1^{\mathrm{H}}\vec{\mathbf{e}}_{xy}}{(1+\alpha)\lambda_1}\vec{\mathbf{v}}_1 + \frac{1}{\alpha\lambda_1}\mathbf{V}_1^{\prime}\mathbf{V}_1^{\prime\mathrm{H}}\vec{\mathbf{e}}_{xy}}{\frac{\left|\vec{\mathbf{v}}_1^{\mathrm{H}}\vec{\mathbf{e}}_{xy}\right|^2}{(1+\alpha)\lambda_1} + \frac{\phi}{\alpha\lambda_1}}, \tag{4.20}$$

where

$$\phi = \vec{\mathbf{e}}_{xy}^{\mathrm{H}}\mathbf{V}_1^{\prime}\mathbf{V}_1^{\prime\mathrm{H}}\vec{\mathbf{e}}_{xy}. \tag{4.21}$$

From (4.21), ϕ is the squared-norm of the projection of $\vec{\mathbf{e}}_{xy}$ onto the null-space of $\vec{\mathbf{v}}_1$. Therefore, ϕ can be calculated directly from $\vec{\mathbf{e}}_{xy}$ and $\vec{\mathbf{v}}_1$ as:

$$\phi = \left\| \left(\mathbf{I}_m - \vec{\mathbf{v}}_1 \vec{\mathbf{v}}_1^{\mathrm{H}} \right) \vec{\mathbf{e}}_{xy} \right\|^2 = \left\| \vec{\mathbf{e}}_{xy} - \left(\vec{\mathbf{v}}_1^{\mathrm{H}} \vec{\mathbf{e}}_{xy} \right) \vec{\mathbf{v}}_1 \right\|^2 . \tag{4.22}$$

Substituting (4.20) into (4.10) and collecting terms yields

$$P_{xy}^{MV} = \frac{\lambda_1 \left| \vec{\mathbf{v}}_1^{\mathrm{H}} \vec{\mathbf{e}}_{xy} \right|^2}{\left(\left| \vec{\mathbf{v}}_1^{\mathrm{H}} \vec{\mathbf{e}}_{xy} \right|^2 + \phi \frac{1+\alpha}{\alpha} \right)^2}, \tag{4.23}$$

since $\mathbf{V}_1^{\prime\mathrm{H}} \mathbf{S}_{xy} = \mathbf{0}$. The above formulation, along with (4.22), indicates that instantaneous windowing allows each pixel value to be computed without the need to explicitly calculate the correlation matrix, the associated eigenvalues, or a regularized matrix inversion for each pixel. The computational complexity for a single MVDR pixel calculated as in (4.23) is $O(n_m)$, which represents a significant improvement over the more general finite window case of $O(n_m^3)$ and is comparable to the computational requirements of conventional imaging.

4.6 Vectorization

The method employed to implement guided wave imaging in matrix-based software packages such as MATLAB (The Mathworks, Natick, MA) [139, 140], Octave (John W. Eaton) [141], and SciLab (The SciLab Consoritum, Cedex, France) [142], has a significant impact on computation time because of the software package's internal structure. It is well-known that matrix-based software packages perform more efficiently with vectorized data [139, 140]. This section constructs the guided wave imaging algorithms discussed in the previous sections in vectorized format to aid the reader in vectorization of this specific problem.

It is important to note that throughout this section, *all matrix operations are performed element-wise*. The nature of the problem does not lend itself to traditional row-column matrix multiplications, rather the matrix structure is employed here to better adapt the

problem to the software tool. Also, although the convention in this section is to use two-dimensional (2-D) matrices to store pixel-specific data, the dimensionality of the problem can be further reduced to store the 2-D matrices in a 1-D array. The current format was chosen over the alternative for readability purposes and is not expected to have a noticeable impact on computational requirements.

Let $\mathbf{X}$ and $\mathbf{Y}$ be matrices of x- and y-coordinates, respectively, for each pixel location:

$$\mathbf{X} = \begin{bmatrix} x_0 & x_1 & \cdots \\ \vdots & \vdots & \vdots \\ x_0 & x_1 & \cdots \end{bmatrix}, \mathbf{Y} = \begin{bmatrix} y_0 & \cdots & y_0 \\ y_1 & \cdots & y_1 \\ \vdots & \cdots & \vdots \end{bmatrix}. \tag{4.24}$$

Then n_m separate 2-D matrices are generated that correspond to the distance from transmitter to pixel location, $\hat{\mathbf{D}}_m$, and pixel location to receiver, $\check{\mathbf{D}}_m$:

$$\hat{\mathbf{D}}_m = \sqrt{(\mathbf{X} - x_{t(m)})^2 + (\mathbf{Y} - y_{t(m)})^2} \tag{4.25}$$

$$\check{\mathbf{D}}_m = \sqrt{(\mathbf{X} - x_{r(m)})^2 + (\mathbf{Y} - y_{r(m)})^2}, \tag{4.26}$$

where $x_{t(m)}$, $y_{t(m)}$, $x_{r(m)}$, and $y_{r(m)}$ correspond to the x- and y-coordinates of the transmitter and receiver for the m^{th} transmitter-receiver pair.

The instantaneous windowing assumption allows the back-propagated signals to be obtained simply by selecting a single time sample from the differenced signals:

$$\mathbf{S}_m = s_m\left(\tau + \frac{\hat{\mathbf{D}}_m + \check{\mathbf{D}}_m}{c_g}\right). \tag{4.27}$$

Here a 2-D matrix, $\mathbf{S}_m$, is constructed in which each element of $\mathbf{S}_m$ corresponds to a specific time in $s_m(t)$ defined by the argument in (4.27). Note that if a sufficiently high sampling rate is used so that interpolation in the time domain is unnecessary, the argument in (4.27) can be multiplied by the sampling frequency and rounded to the nearest integer to obtain the desired sample index.

From (4.27), if the n_m 2-D matrices are stacked in a third dimension, then $\vec{\mathbf{s}}_{xy}(\tau)$ for each pixel value is stored along the third dimension. An identical structure is used for the $\vec{\mathbf{e}}_{xy}$ and $\vec{\mathbf{v}}_1$ vectors.

The 3-D matrix of $\vec{\mathbf{e}}_{xy}$ vectors is determined as in (3.16). To begin, the unnormalized vectors are calculated:

$$\mathbf{F}_m = \frac{\mathbf{\Psi}_m}{\sqrt{\hat{\mathbf{D}}_m \breve{\mathbf{D}}_m}}, \tag{4.28}$$

where $\mathbf{\Psi}_m$ is a matrix of pixel-specific scattering coefficients for the m^{th} transmitter-receiver pair. The pixel specific norm is then obtained,

$$||\mathbf{F}|| = \sqrt{\sum_{m=1}^{n_m} |\mathbf{F}_m|^2}, \tag{4.29}$$

and finally the pixel-specific vectors are normalized,

$$\mathbf{E}_m = \frac{\mathbf{F}_m}{||\mathbf{F}||}. \tag{4.30}$$

The conventional image is generated as

$$\mathbf{P}^{DS} = \left| \sum_{m=1}^{n_m} \mathbf{S}_m^* \mathbf{E}_m \right|^2, \tag{4.31}$$

where * is the element-wise complex conjugate operation.

To calculate the pixel values for an MVDR image, a 2-D matrix of λ values is calculated:

$$\mathbf{\Lambda}_1 = \sum_{m=1}^{n_m} |\mathbf{S}_m|^2. \tag{4.32}$$

The $\mathbf{\Lambda}_1$ matrix is then used to obtain the eigenvectors:

$$\mathbf{V}_m = \frac{\mathbf{S}_m}{\sqrt{\mathbf{\Lambda_1}}}. \tag{4.33}$$

For convenience, two intermediate matrices are calculated:

$$\mathbf{\Theta} = \sum_{m=1}^{n_m} \mathbf{V}_m^* \mathbf{E}_m \tag{4.34}$$

$$\mathbf{\Phi} = \sum_{m=1}^{n_m} |\mathbf{E}_m - \mathbf{\Theta} \mathbf{V}_m|^2 \tag{4.35}$$

which correspond to the $\vec{\mathbf{v}}_1^{\text{H}} \vec{\mathbf{e}}_{xy}$ and ϕ terms, respectively for the single-pixel case in (4.23). Finally, the MVDR pixel value is calculated using element-wise matrix operations:

$$\mathbf{P}^{MV} = \frac{\mathbf{\Lambda}_1 |\mathbf{\Theta}|^2}{\left| |\mathbf{\Theta}|^2 + \left(\frac{1+\alpha}{\alpha} \right) \mathbf{\Phi} \right|^2}. \tag{4.36}$$

Equation (4.31) and (4.36) reflect the vectorized conventional and minimum variance imaging algorithms, respectively, with instantaneous windowing. Note that complete vectorization of the minimum variance imaging algorithm is not possible without the instantaneous windowing optimization presented in Section 4.5. Vectorization is expected to reduce the computation time required for image generation when using matrix-oriented numerical analysis software.

Simulation data were used to verify the computational complexity of the proposed methods above. Guided wave images were generated using 2 to 24 transducers for five separate cases: (1) minimum variance imaging with traditional matrix inversion computed with for-loops, (2) minimum variance imaging optimized for instantaneous windowing computed with for-loops, (3) minimum variance imaging optimized for instantaneous windowing and computed with vectorized data, (4) conventional imaging computed with for-loops, and (5) conventional imaging computed with vectorized data. For comparison purposes, all images were created using instantaneous windowing, meaning that the correlation matrix (if calculated) is constructed as in (4.16). MATLAB (The Mathworks, Natick, MA) was used to generate the images using a Hewlett-Packard laptop (Hewlett-Packard Co., Palo Alto, CA) with an Intel Core2 Duo CPU (Intel Corp., Santa Clara, CA) operating at 2.26 GHz with 4 GB of RAM and running Windows Vista Home Premium (Microsoft Corp., Redmond, WA). Each image was composed of 7744 pixels, corresponding to a 914 mm $\times$ 914 mm plate imaged with pixels spaced 10.4 mm apart. Images were each generated 20 separate times and the average computation time was recorded.

Figure 4.8 depicts computation time as a function of the number of transducers. Several features of Figure 4.8 are worth noting. First, the optimization for minimum variance imaging presented in Section 4.5 significantly reduces the computational requirements of minimum variance imaging (broken lines) to the point that it can be performed in a comparable amount of time as conventional imaging (solid lines). As mentioned earlier, matrix inversion requires $O\left(n_m^3\right)$ operations, which is compounded by the fact that if n_s transducers

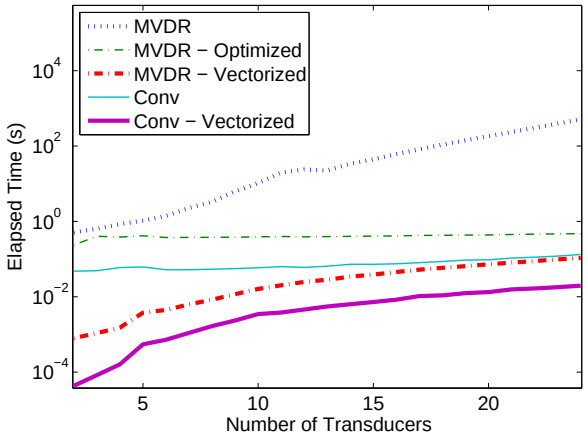

Figure 4.8: Computation time *vs.* number of transducers for five separate cases: (1) minimum variance imaging with traditional matrix inversion computed with for-loops, (2) minimum variance imaging optimized for instantaneous windowing computed with for-loops, (3) minimum variance imaging optimized for instantaneous windowing and computed with vectorized data, (4) conventional imaging computed with for-loops, and (5) conventional imaging computed with vectorized data.

are used for imaging, the number of *pairs* of transducers, $n_m = n_s\left(n_s - 1\right)/2$. As a result, the computation time for minimum variance imaging without optimization grows much faster than any of the other cases as the number of transducers is increased. In contrast, the computation time for minimum variance imaging optimized for instantaneous windowing is a constant multiple of the computation time required for conventional imaging. Another important observation is that, as expected, vectorizing the imaging algorithms further reduces computation time. The initial offset in computation time between images generated with for-loops *vs.* vectorized data is attributed to overhead costs from setup of the for-loop operation. As the number of transducers is increased, the difference in computation time is expected to continue to decrease because the overhead associated with for-loop operation becomes small compared to image computational requirements.

4.7 Discussion

In addition to accurate defect localization, minimized artifacts and improved resolution, there are three factors that are of interest in SHM guided wave images: graceful degradation, sensitivity to the damage location, and the ability to perform defect sizing and characterization.

The improved imaging performance demonstrated in this chapter is largely due to the heightened sensitivity resulting from the use of MVDR and phase information. One concern with increased sensitivity is the risk of algorithmic failure in the presence of noise or modeling errors. Modeling errors can include uncompensated or inaccurate receiver phase, scattering information, and dispersion compensation. Figure 4.2 demonstrates that as $\vec{\mathbf{v}}_1$ and the look direction diverge, the pixel value decays gracefully as a function of the regularization. Therefore, minimum variance imaging with phase information is expected to exhibit graceful degradation in the presence of noise or modeling errors if appropriately regularized.

The pixel value obtained using both minimum variance imaging and conventional imaging was shown in Section 4.1 to be equal to the largest eigenvalue of the correlation matrix when the look direction, $\vec{\mathbf{e}}_{xy}$, is identical to $\vec{\mathbf{v}}_1$. The fact that there is a relationship between the pixel value and largest eigenvalue implies that imaging performance is sensitive to location. When damage is close to the sensors, the propagation distances are short and received signals are strong, resulting in a large λ_1, but when damage is far from the sensors, the received signals are weaker, resulting in a smaller λ_1. Intuitively, normalizing the covariance matrices to have unit norm would correct for this, making the imaging algorithm less sensitive to pixel location. Alternatively, the received signals can be adjusted in amplitude as a function of time or distance to compensate for geometric spreading. In actuality, however, normalization of covariance matrices and time or distance amplitude compensation introduces artifacts because they effectively amplify pixel values that originally had no, or very little, signal present. Without normalization, pixels located further away from the

array (in particular, outside the bounding polygon) do have smaller amplitudes. However, the reduced amplitude has far less of an adverse impact than the artifacts introduced by covariance normalization or signal amplitude compensation.

Finally, defect characterization, including sizing, is a major goal of imaging with SHM and NDE systems. It is desirable for the image to reflect the relative magnitudes of the defects, meaning that a larger damage site should have a larger pixel value. For the simple case of multiple uniform scatterers of varying sizes, minimum variance imaging can produce such relative pixel values if compensation is made for geometric propagation loss. As mentioned in the previous paragraph, however, this comes at the expense of introducing artifacts by amplifying noise in the received signals. In realistic environments, damage sites of different sizes will have different scattering fields. As such, the sensitivity to scattering fields provides an alternative mechanism to characterize both the size and type of damage, which is discussed in Chapter VII.

4.8 Experimental Results

The techniques described throughout this chapter for reducing imaging artifacts have been applied to the experimental data described in Chapter III. The experimental data was obtained at 22.2°C and OBS was used to find the optimal baseline. BSS was then used to match the test data to the baseline signals to minimize the baseline subtraction residual. Expected scattering characteristics for imaging were generated using the technique proposed by Grahn [122] for incident and scattered S_0 waves at 300 kHz, which is the dominant mode here.

Figure 4.9 and Figure 4.10 illustrate imaging performance with experimental data using instantaneous windowing and the envelope of the analytic signal for conventional and minimum variance imaging, respectively. The imaging performance represents a stark improvement over Figure 3.11. The improvement in Figure 4.9 over Figure 3.11 is largely due to the instantaneous windowing, although the use of appropriate scattering behavior

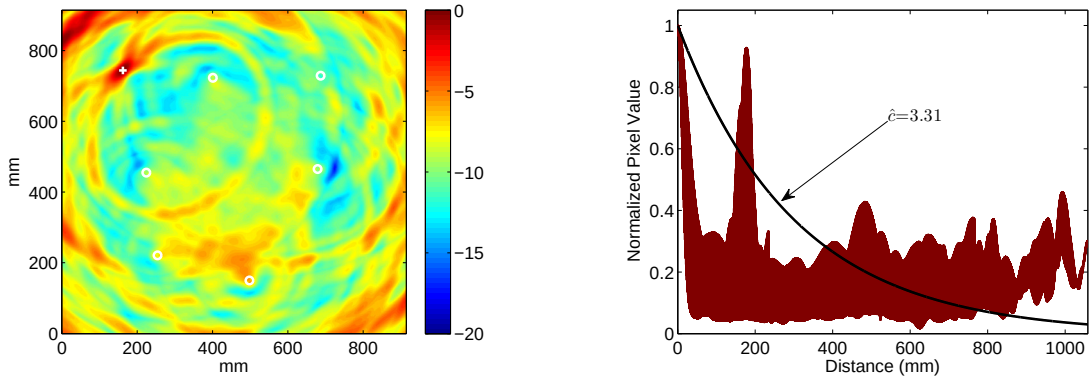

(a) (b)

Figure 4.9: Conventional imaging with experimental data of a 5 mm through-hole. Imaging was performed with the envelope of time domain signals, an instantaneous window, and the 5 mm scattering field generated as per Grahn [122]. (a) Image displayed using a 20 dB scale, and (b) normalized pixel values versus distance from damage location ($\hat{c}$ = 3.31).

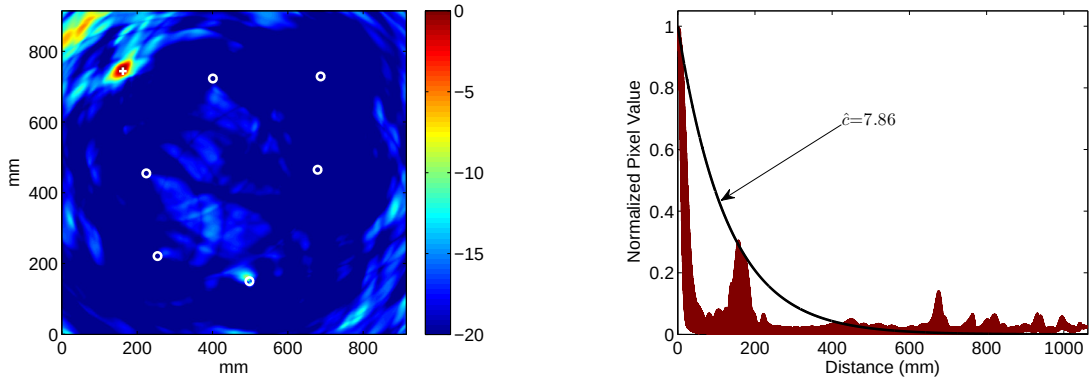

(a) (b)

Figure 4.10: Minimum Variance imaging with experimental data of a 5 mm through-hole. Imaging was performed with the envelope of time domain signals, an instantaneous window, and the 5 mm scattering field generated as per Grahn [122]. (a) Image displayed using a 20 dB scale, and (b) normalized pixel values versus distance from damage location ($\hat{c}$ = 7.86).

also helps. In Figure 4.9 the damage is clearly visible at the damage location, however there are significant imaging artifacts that cannot be distinguished from additional damage. Figure 4.10 demonstrates significant improvement over Figure 4.9 due to the use of MVDR in the imaging algorithm. From Figure 4.10, the damage can be clearly localized with the largest artifact less than half of the amplitude of the pixel value at the damage location.

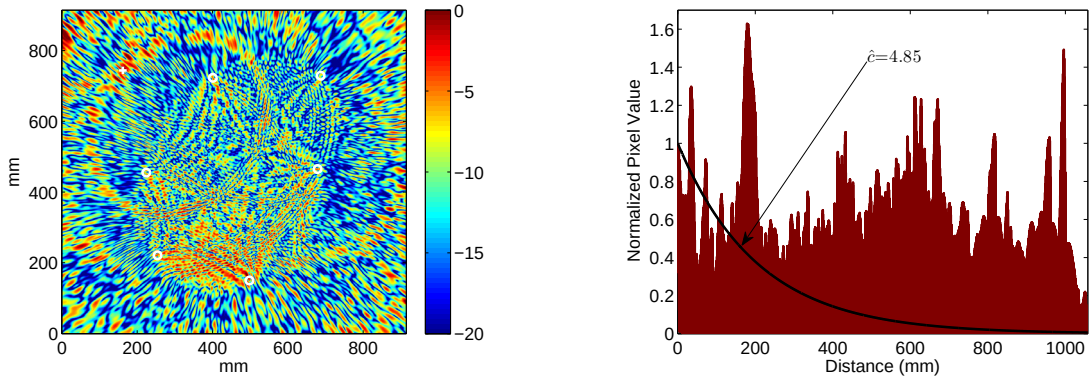

(a) (b)

Figure 4.11: Conventional imaging with experimental data of a 5 mm through-hole. Imaging was performed with the analytic representation of the time domain signals, an instantaneous window, and the 5 mm scattering field generated as per Grahn [122]. (a) Image displayed using a 20 dB scale, and (b) normalized pixel values versus distance from damage location ($\hat{c} = 4.85$).

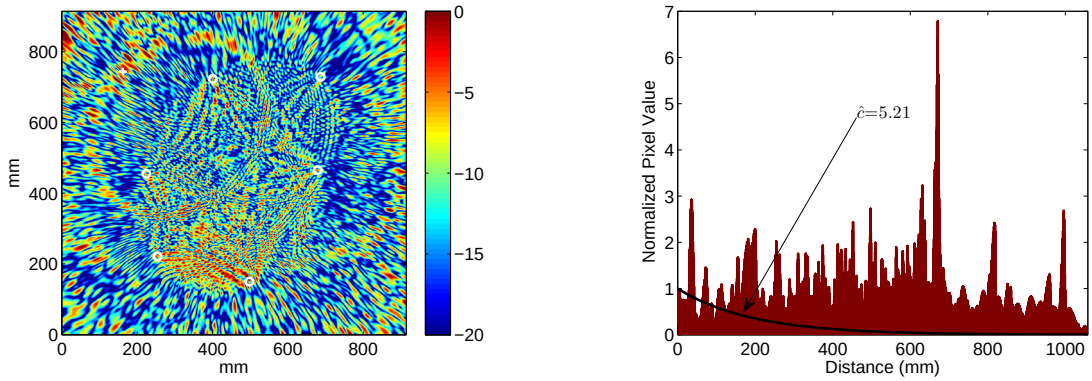

(a) (b)

Figure 4.12: Minimum Variance imaging with experimental data of a 5 mm through-hole. Imaging was performed with the analytic representation of the time domain signals, an instantaneous window, and the 5 mm scattering field generated as per Grahn [122]. (a) Image displayed using a 20 dB scale, and (b) normalized pixel values versus distance from damage location ($\hat{c} = 5.21$).

In contrast to Figure 4.9 and Figure 4.10, which use the *envelope* of the analytic representation of the signals, Figure 4.11 and Figure 4.12 illustrate imaging performance with the analytic signals, themselves for conventional and minimum variance imaging, respectively. These two figures represent very poor imaging performance, with the number and

magnitude of imaging artifacts exceeding that of the actual defect location many times over. This degradation in performance is due to the effects of dispersion, in that the phase of the signal is changing as the wave propagates through the plate. This change in phase causes the back-propagated signals at the damage location to *disagree* with the steering vector, which reduces the amplitude of the pixel at the defect location to the point that it cannot be discerned from noise.

One final point must be made with respect to the performance metric. Contrary to what one would expect based on a visual inspection of Figures 4.9, 4.11 and 4.12, the performance metric values for these three figures is *increasing* ($\hat{c} = 3.31$, $\hat{c} = 4.82$, and $\hat{c} = 5.21$, respectively). The performance metric improvement is associated with the *non-artifact* pixel values, which decrease with the use of the analytic signal (Figures 4.11 and 4.12) over the envelope (Figure 4.9) and again through the use of minimum variance imaging (Figure 4.12) over conventional imaging (Figure 4.11). Notice that the minima in Figure 4.9b are all on the order of 0.05, whereas the minima in Figure 4.11b and Figure 4.12b are much smaller. Since the performance metric is based on a linear fit in the logarithmic domain using *all* of the pixel values, the lower *non-artifact* pixels are producing the overall increase in performance.

4.9 Summary

This chapter has identified four techniques for reducing artifacts typically observed in guided wave imaging. The use of minimum variance imaging was first demonstrated to provide significant improvements over conventional imaging, both using envelope signals. After that, minimum variance images were further improved by incorporating scattering field information into the look direction. The inherent ability of the MVDR algorithm to suppress imaging artifacts was then shown to further enhance images when the analytic representation of the received signals is used, which includes phase information. Finally, for high SNR environments, the use of instantaneous windowing was shown to reduce the

the presence and amplitude of imaging artifacts.

In addition to imaging improvements, the computational demands for minimum variance imaging were shown to be comparable to those of conventional imaging when instantaneous windowing is used. Instantaneous windowing also allows both conventional imaging and minimum variance imaging to be vectorized, resulting in significant improvements in computation time when computed with vector-based software packages, such as MATLAB (The Mathworks, Natick, MA).

The primary contributions of the work presented here includes the application of the MVDR algorithm to *in situ* guided wave imaging applications with spatially distributed arrays, a quantification of the improvements achieved when phase and scattering information are used in conjunction with MVDR, and an identification of the importance of minimizing the window size when operating in a high SNR environment. Additionally, the computational improvements that are obtained by (1) using instantaneous windowing, and (2) tailoring the imaging problem for matrix-based software packages have been identified and quantified. The reduction in computational demands obtained from instantaneous windowing optimization enables the use of minimum variance imaging, with its associated benefits in imaging performance, at computational costs comparable to conventional imaging. For *in situ* guided wave imaging systems with spatially distributed arrays, which must balance system complexity and cost with imaging performance, the improved ability to detect and localize damage has clear significance. The methods illustrated here could also be readily applied to conventional compact bulk and guided wave arrays operating in the near field.

As expected, significant improvement was shown with experimental data when using minimum variance imaging vs conventional imaging with the envelope of the differenced signals. However, when minimum variance imaging was performed with the analytic representation of the differenced signals, both conventional and minimum variance imaging exhibited a visible performance *degradation* (despite an increase in the quantitative performance metric). The marked increase in imaging artifacts was attributed to the effects of

dispersion, which are masked when using the envelope of the signal. In order to address the effects of dispersion, the dispersion relations must first be estimated and then compensated. As such, Chapter V presents the MBPE algorithm for estimating propagation parameters, such as dispersion, with *in situ* sensors and Chapter VI describes two methods for incorporating these estimates into the guided wave imaging algorithm to further improve imaging performance.

CHAPTER V

MODEL-BASED PARAMETER ESTIMATION (MBPE)

The model-based parameter estimation (MBPE) algorithm presented in this chapter provides adaptive estimates of propagation parameters, such as dispersion, transmitter and receiver transfer functions, propagation distances, and propagation loss. These parameters are important to guided wave imaging because they directly affect the amplitude and phase of the propagating waves and if left uncompensated, can result in the degraded imaging performance visible in Figures 4.11 and 4.12. Although these parameters are often assumed *a priori*, errors in these estimates can impose an upper limit on a system's performance, and estimates obtained *in situ* at the time of test are expected to be much more accurate. As discussed in Chapter II, several methods for dispersion estimation are available; however, these methods are not applicable to distributed arrays for a variety of reasons. The MBPE algorithm presented here is not only capable of estimating dispersion relations from a distributed array *in situ* at the time of test, but simultaneously provides estimates of the transmitter and receiver transfer functions, propagation distances, and propagation loss, which are often assumed *a priori*. Large portions of the research discussed in this chapter have been reported in Hall and Michaels [143], which represents a generalization of the work reported in [144, 145, 146].

It should be pointed out that wave propagation is fundamental to a wider range of fields and applications than the specific guided wave imaging problem considered here, and many associated systems employing electromagnetic, acoustic or elastic waves require accurate knowledge of the operating environment to function properly. Like the case considered here, the performance of any of these systems is understandably linked to the accuracy of assumed propagation models and associated parameters. Since the MBPE algorithm

can be tailored to application-specific model assumptions, including cases with multiple transmitter and receiver transfer functions, the approach discussed in this chapter has the potential to be applied to applications outside of the distributed array scenario considered here.

Estimates from the MBPE algorithm are obtained through four basic steps (see Table 5.1). The propagation model assumptions are first defined and a system of linear equations is established using the measured, received signals. The adaptively estimated propagation distances are then obtained using the measured distances, the received signals, and the assumed propagation model. From this point, two solutions are obtained that combine to produce the final set of parameter estimates: (1) the underdetermined linear system of equations is solved through the use of a pseudoinverse operation, and (2) a nonlinear search is performed to obtain the appropriate null-space coefficients to augment the linear solution. The nonlinear search is necessary to enforce some additional constraints that cannot be imposed through the linear system of equations, specifically the integer nature of some of the estimated parameters.

This chapter is organized as follows, first the propagation model and notation are defined in the Problem Setup section. An analysis of the noise is then provided to demonstrate that if the input noise is white Gaussian noise then the log-magnitude and phase noise distributions are *effectively* zero mean; as a result, an estimate of the noise variance is established, which is useful during the nonlinear search portion of the algorithm. Section 5.3 discusses adaptive propagation distance estimation, used to fit the *measured* propagation distances to the propagation model and measured data. The linear solution is obtained in Section 5.4, with a discussion about the significance of the null-space, and Section 5.5 presents the nonlinear search that provides the necessary null-space coefficients. The MBPE algorithm is then summarized, experimental results are presented, and a brief summary concludes the chapter.

5.1 Problem Setup

A propagating wave can be modeled in the frequency domain as:

$$M(\omega) = T(\omega) R(\omega) G(\omega), \tag{5.1}$$

where $M(\omega)$ is the received signal; $T(\omega)$ is the transmitter transfer function, which incorporates all transmitter-specific transfer functions; $R(\omega)$ represents a similar combination of all receiver-specific transfer functions; and finally, $G(\omega)$ represents a distance-dependent transfer function that incorporates both propagation loss and dispersion. $G(\omega)$ can be modeled as

$$G(\omega) = \left(\frac{d}{\alpha}\right)^{-p(\omega)} \mathrm{e}^{-jk(\omega)d}, \tag{5.2}$$

where d is the propagation distance, $p(\omega)$ is referred to as propagation loss, $k(\omega)$ is a frequency-dependent wavenumber, and j is equal to $\sqrt{-1}$. The form of (5.2) is motivated by the well-known far-field behavior for both spherical and cylindrical waves [147], where dispersion is accounted for by the complex exponential term, and the geometric spreading loss, represented as $(d/\alpha)^{-p(\omega)}$, is permitted to vary with frequency to accommodate possible frequency-dependent behavior. The α variable embedded in the geometric spreading loss term accounts for the fact that the inverse distance law only defines proportional relationships (nominally $d^{-1/2}$ or d^{-1}, depending on the application). Note that attenuation from a lossy medium can be handled by incorporating an exponential decay term, such as $\mathrm{e}^{-a(\omega)d}$, into (5.2) either in lieu of or in addition to the geometric spreading loss term. Since experimental validation is performed with guided waves, in which geometric spreading loss dominates attenuation, the algorithm is presented with geometric spreading loss.

The overarching goal of model-based parameter estimation is to obtain data-driven estimates of $T(\omega)$, $R(\omega)$, d, $p(\omega)$, and $k(\omega)$ by leveraging the inherent constraints of the assumed model in (5.1) and (5.2). The general approach to address this nonlinear problem

is to convert it to a linear problem through the logarithm function:

$$\ln\left(M\left(\omega\right)\right) = \ln\left(T\left(\omega\right)\right) + \ln\left(R\left(\omega\right)\right) - p\left(\omega\right)\ln\left(\frac{d}{\alpha}\right) - jk\left(\omega\right)d + j2\pi b. \tag{5.3}$$

When taking the logarithm of a complex number, the imaginary part of the result is constrained to be bounded by $\pm\pi$. Therefore, an integer multiple of 2π must be included in the phase, which necessitates the $j2\pi b$ term in (5.3) where b is an integer. Note that the the real and imaginary parts of (5.3) can be separated into two independent equations:

$$\ln\left(\left|M\left(\omega\right)\right|\right) = \ln\left(\left|T\left(\omega\right)\right|\right) + \ln\left(\left|R\left(\omega\right)\right|\right) - p\left(\omega\right)\ln\left(\frac{d}{\alpha}\right), \tag{5.4a}$$

$$\measuredangle M\left(\omega\right) = \measuredangle T\left(\omega\right) + \measuredangle R\left(\omega\right) - k\left(\omega\right)d + 2\pi b. \tag{5.4b}$$

From a practical standpoint, the received signals are assumed to be digitally sampled in the time domain, and frequency domain measurements are obtained via a fast Fourier transform (FFT). As such, the frequency domain measurements correspond to measurements at discrete frequencies. If these discrete frequencies are spaced sufficiently close to one another, the received signal phase response can be unwrapped by adding or subtracting integer multiples of 2π to eliminate phase discontinuities. To ensure the phase unwrapping operation is performed accurately, the frequency domain measurements must span a continuous spectral band with positive SNR within each frequency bin. By unwrapping the spectrum, the b in (5.4b) becomes consistent across the entire frequency spectrum, which provides an additional model constraint that can be leveraged during parameter estimation. A lower bound can be established for the number of time domain samples, n_n, required to produce sufficiently close sampling in ω. The bound is derived in Appendix A and presented here for succinctness:

$$n_n > \frac{2\pi F_s d_{\max}}{c_{\min}\left[\pi - 2\sin^{-1}\left(\frac{1}{Q_{\min}}\right)\right]}, \tag{5.5}$$

where F_s is the sampling frequency, $d_{\max}$ is the maximum distance propagated for any received signal, $c_{\min}$ is the minimum group velocity at any frequency, and $Q_{\min}$ is the minimum signal-to-noise ratio (SNR) for any frequency. Note that the number of time domain

samples can be increased to satisfy (5.5) by padding received signals with zeros and does not translate to any system operational requirements.

To estimate the large number of unknowns in this problem, multiple $M(\omega)$ measurements are necessary. Therefore, multiple signals are recorded over different propagation distances. The equations described in (5.4a) and (5.4b) can be converted into matrix format to relate information from each of the received signals to each of the parameters of interest:

$$\mathbf{M}_{\Re} = \mathbf{Q}_{\mathrm{T}}\mathbf{T}_{\Re} + \mathbf{Q}_{\mathrm{R}}\mathbf{R}_{\Re} - \vec{\mathbf{d}}^{\curlyvee}\vec{\mathbf{p}}^{\mathrm{T}}, \tag{5.6a}$$

$$\mathbf{M}_{\Im} = \mathbf{Q}_{\mathrm{T}}\mathbf{T}_{\Im} + \mathbf{Q}_{\mathrm{R}}\mathbf{R}_{\Im} - \vec{\mathbf{d}}\,\vec{\mathbf{k}}^{\mathrm{T}} + 2\pi\vec{\mathbf{b}}\,\vec{\mathbf{1}}_{w}^{\mathrm{T}}. \tag{5.6b}$$

Here the "$\Re$" and "$\Im$" matrix subscripts denote the real and imaginary components of the logarithm of the data. The $\mathbf{M}_{\Re}$ and $\mathbf{M}_{\Im}$ matrices are $[n_m \times n_w]$ matrices containing all measured information, where n_m is the number of received signals and n_w is the number of frequencies. The $\mathbf{T}_{\Re}$ and $\mathbf{R}_{\Re}$ matrices correspond to the n_t unknown $\ln(|T(\omega)|)$ and n_r unknown $\ln(|R(\omega)|)$ estimates and the $\mathbf{T}_{\Im}$ and $\mathbf{R}_{\Im}$ matrices similarly correspond to the n_t and n_r unknown $\measuredangle T(\omega)$ and $\measuredangle R(\omega)$ variables, respectively. The $\mathbf{Q}_{\mathrm{T}}$ and $\mathbf{Q}_{\mathrm{R}}$ matrices relate each row of the $\mathbf{M}_{\Re}$ and $\mathbf{M}_{\Im}$ matrices to the appropriate row of $\mathbf{T}_{\Re}$, $\mathbf{T}_{\Im}$, $\mathbf{R}_{\Re}$, and $\mathbf{R}_{\Im}$. The elements of the $\mathbf{Q}_{\mathrm{T}}$ and $\mathbf{Q}_{\mathrm{R}}$ matrices are assumed to be limited to the integers "1" and "0", which is the case for all envisioned scenarios. This construction allows the model to account for either common or multiple transmitter and receiver transfer functions. The $\vec{\mathbf{p}}$ and $\vec{\mathbf{k}}$ vectors are $[n_w \times 1]$ vectors that contain the propagation loss and wavenumber estimates, respectively. The $\vec{\mathbf{b}}$ vector contains each of the n_m integers associated with the unknown multiples of 2π. The $\vec{\mathbf{1}}_w$ vector corresponds to a $[n_w \times 1]$ vector of all-ones. Finally, the "$\curlyvee$" superscript discriminates between the $[n_m \times 1]$ vector, $\vec{\mathbf{d}}$, which contains the propagation distances in vector format, and the $[n_m \times 1]$ vector, $\vec{\mathbf{d}}^{\curlyvee}$, corresponding to the element-wise logarithm of the propagation distances scaled by α:

$$\vec{\mathbf{d}}^{\curlyvee} = \ln\left(\frac{1}{\alpha}\vec{\mathbf{d}}\right). \tag{5.7}$$

It is important to note that α is an integral part of the assumed propagation model and will, therefore, affect the resulting estimates of $\mathbf{T}_{\Re}$, $\mathbf{R}_{\Re}$, and $\vec{\mathbf{p}}$. Throughout this text, the α variable is selected to be the mean measured distance. Although this choice of α is somewhat arbitrary, it has been found to produce reasonable estimates for all three parameters.

Let $\mathbf{P}_{\Delta}$ be a $[n_w \times n_w]$ projection matrix ($\mathbf{P}_{\Delta}\mathbf{P}_{\Delta} = \mathbf{P}_{\Delta}$) corresponding to the null space of the all-ones row-vector, meaning that $\vec{\mathbf{1}}_w^{\mathrm{T}}\mathbf{P}_{\Delta} = \mathbf{0}$. Then the $\mathbf{T}_{\Im}$ and $\mathbf{R}_{\Im}$ matrices of (5.6b) can each be described in further detail as the addition of two separate components, one that is frequency-dependent, $\mathbf{T}_{\Delta}$ and $\mathbf{R}_{\Delta}$, and another that is frequency-independent, $\vec{\boldsymbol{\tau}}$ and $\vec{\boldsymbol{\rho}}$:

$$\mathbf{T}_{\Im} = \mathbf{T}_{\Delta} + \vec{\boldsymbol{\tau}}\,\vec{\mathbf{1}}_w^{\mathrm{T}} \tag{5.8a}$$

$$\mathbf{R}_{\Im} = \mathbf{R}_{\Delta} + \vec{\boldsymbol{\rho}}\,\vec{\mathbf{1}}_w^{\mathrm{T}} \tag{5.8b}$$

where $\mathbf{T}_{\Delta} = \mathbf{T}_{\Im}\mathbf{P}_{\Delta}$ and $\mathbf{R}_{\Delta} = \mathbf{R}_{\Im}\mathbf{P}_{\Delta}$. The wavenumber vector can be similarly decomposed into:

$$\vec{\mathbf{k}} = \vec{\mathbf{k}}_{\Delta} + \kappa\vec{\mathbf{1}}_w \tag{5.9}$$

with $\vec{\mathbf{k}}_{\Delta}^{\mathrm{T}} = \vec{\mathbf{k}}^{\mathrm{T}}\mathbf{P}_{\Delta}$. Note that the decomposition of $\mathbf{T}_{\Im}$, $\mathbf{R}_{\Im}$, and $\vec{\mathbf{k}}$ into frequency-dependent and frequency-independent components is performed here for mathematical convenience and does not necessarily correspond to any physical properties or behavior.

To maximize the flexibility of the proposed model, two additional matrices, $\mathbf{Q}_{\tau}$ and $\mathbf{Q}_{\rho}$, are introduced to relate the frequency-independent values in $\vec{\boldsymbol{\tau}}$ and $\vec{\boldsymbol{\rho}}$ to each measurement in the $\mathbf{M}_{\Re}$ and $\mathbf{M}_{\Im}$ matrices. Under most circumstances, $\mathbf{Q}_{\tau} = \mathbf{Q}_{\mathrm{T}}$ and $\mathbf{Q}_{\rho} = \mathbf{Q}_{\mathrm{R}}$. However, there may be certain scenarios where the transmitter and receiver transfer functions are assumed to be identical, with the exception of some constant phase offset. In those cases, the $\mathbf{Q}_{\tau}$ and $\mathbf{Q}_{\rho}$ matrices may differ from $\mathbf{Q}_{\mathrm{T}}$ and $\mathbf{Q}_{\mathrm{R}}$. Incorporating (5.8) and (5.9) with (5.6b) yields:

$$\mathbf{M}_{\Im} = \mathbf{Q}_{\mathrm{T}}\mathbf{T}_{\Delta} + \mathbf{Q}_{\tau}\vec{\boldsymbol{\tau}}\,\vec{\mathbf{1}}_w^{\mathrm{T}} + \mathbf{Q}_{\mathrm{R}}\mathbf{R}_{\Delta} + \mathbf{Q}_{\rho}\vec{\boldsymbol{\rho}}\,\vec{\mathbf{1}}_w^{\mathrm{T}} - \vec{\mathbf{d}}\,\vec{\mathbf{k}}_{\Delta}^{\mathrm{T}} - \kappa\vec{\mathbf{d}}\,\vec{\mathbf{1}}_w^{\mathrm{T}} + 2\pi\vec{\mathbf{b}}\,\vec{\mathbf{1}}_w^{\mathrm{T}}. \tag{5.10}$$

Since, by definition, $\mathbf{T}_{\Delta}$ and $\mathbf{R}_{\Delta}$ reside in the null space of the all-ones row-vector,

another set of equations can be obtained from (5.10) by right-multiplying $\mathbf{M}_{\Im}$ with $\mathbf{P}_{\Delta}$:

$$\mathbf{M}_{\Im}\mathbf{P}_{\Delta} = \mathbf{Q}_{\mathrm{T}}\mathbf{T}_{\Delta} + \mathbf{Q}_{\mathrm{R}}\mathbf{R}_{\Delta} - \vec{\mathbf{d}}\,\vec{\mathbf{k}}_{\Delta}^{\mathrm{T}}. \tag{5.11}$$

The matrices in (5.6a), (5.10) and (5.11) can be consolidated into a single set of linear equations:

$$\mathbf{AZ} = \mathbf{M}, \tag{5.12}$$

where

$$\mathbf{A} = \begin{array}{c} \begin{matrix} (\underline{1}) & (\underline{2}) & (\underline{3}) & (\underline{4}) & (\underline{5}) & (\underline{6}) & (\underline{7}) & (\underline{8}) & (\underline{9}) & (\underline{10}) \end{matrix} \\ \begin{bmatrix} \mathbf{Q}_{\mathrm{T}} & \mathbf{0} & \mathbf{0} & \mathbf{Q}_{\mathrm{R}} & \mathbf{0} & \mathbf{0} & -\vec{\mathbf{d}}^{\vee} & \vec{\mathbf{0}}_m & \vec{\mathbf{0}}_m & \mathbf{0} \\ \mathbf{0} & \mathbf{Q}_{\mathrm{T}} & \mathbf{Q}_{\tau} & \mathbf{0} & \mathbf{Q}_{\mathrm{R}} & \mathbf{Q}_{\rho} & \vec{\mathbf{0}}_m & -\vec{\mathbf{d}} & -\vec{\mathbf{d}} & 2\pi\mathbf{I}_s \\ \mathbf{0} & \mathbf{Q}_{\mathrm{T}} & \mathbf{0} & \mathbf{0} & \mathbf{Q}_{\mathrm{R}} & \mathbf{0} & \vec{\mathbf{0}}_m & -\vec{\mathbf{d}} & \vec{\mathbf{0}}_m & \mathbf{0} \end{bmatrix} \end{array}, \tag{5.13a}$$

$$\mathbf{Z} = \begin{array}{c} \begin{matrix} (\underline{1}) \\ (\underline{2}) \\ (\underline{3}) \\ (\underline{4}) \\ (\underline{5}) \\ (\underline{6}) \\ (\underline{7}) \\ (\underline{8}) \\ (\underline{9}) \\ (\underline{10}) \end{matrix} \\ \begin{bmatrix} \mathbf{T}_{\Re} \\ \mathbf{T}_{\Delta} \\ \vec{\boldsymbol{\tau}}\,\vec{\mathbf{1}}_w^{\mathrm{T}} \\ \mathbf{R}_{\Re} \\ \mathbf{R}_{\Delta} \\ \vec{\boldsymbol{\rho}}\,\vec{\mathbf{1}}_w^{\mathrm{T}} \\ \vec{\mathbf{p}}^{\,\mathrm{T}} \\ \vec{\mathbf{k}}_{\Delta}^{\mathrm{T}} \\ \kappa\vec{\mathbf{1}}_w^{\mathrm{T}} \\ \vec{\mathbf{b}}\,\vec{\mathbf{1}}_w^{\mathrm{T}} \end{bmatrix} \end{array}, \qquad \text{and} \qquad \mathbf{M} = \begin{bmatrix} \mathbf{M}_{\Re} \\ \mathbf{M}_{\Im} \\ \mathbf{M}_{\Im}\mathbf{P}_{\Delta} \end{bmatrix}. \tag{5.13b}$$

Equation (5.12) represents the generalized propagation model in the format of a nonhomogeneous matrix equation. The matrix **M** contains all frequency domain measurements, **A** represents the assumed propagation model, and **Z** consists of the unknown variables. Note that (5.13a) and (5.13b) represent a general structure for the matrices of (5.12) under

the current model assumptions. Two specific examples for these matrices are provided in Section 5.7.2 and Section 5.7.3. Alternative model assumptions can be accommodated by updating the **Z** and **A** matrices accordingly. Also, it is important to point out that **A** does not contain all model constraints. Specifically, the elements of $\vec{\mathbf{b}}$ are not constrained to be integers.

Throughout this chapter, references are frequently made to the four vector subspaces defined by the fundamental theorem of linear algebra [148]: (1) the column space, range, or image, denoted by a "∥" superscript, (2) the left null space or cokernel, denoted by a "⊀" superscript, (3) the null space or kernel, denoted by a "≠" superscript, and (4) the row space or coimage, denoted by a "=". These four vector subspaces are used in reference to two matrices in particular, which have a profound impact on the algorithm's ability to estimate parameters:

$$\mathbf{Q}_{\text{TR}} = \begin{bmatrix} \mathbf{Q}_{\text{T}} & \mathbf{Q}_{\text{R}} \end{bmatrix}, \tag{5.14a}$$

$$\mathbf{Q}_{\tau\rho} = \begin{bmatrix} \mathbf{Q}_{\tau} & \mathbf{Q}_{\rho} \end{bmatrix}. \tag{5.14b}$$

Here both $\mathbf{Q}_{\text{TR}}$ and $\mathbf{Q}_{\tau\rho}$ are $[n_m \times (n_t + n_r)]$ matrices. Applying this vector space notation, $\mathbf{Q}_{\text{TR}}^{\shortparallel}$ is a matrix of orthonormal column vectors that span the column space of $\mathbf{Q}_{\text{TR}}$. The size of $\mathbf{Q}_{\text{TR}}^{\shortparallel}$ is defined as $[n_m \times n_{\text{TR}}^{\shortparallel}]$. Similar definitions can be made for the other three vector subspaces as well as for the $\mathbf{Q}_{\tau\rho}$ matrix. Building upon the above notation, projection matrices onto these vector subspaces are denoted as **P** matrices with the appropriate superscripts and subscripts. So, $\mathbf{P}_{\text{TR}}^{\nmid}$ is a $[n_m \times n_m]$ projection matrix that projects onto the vector subspace spanned by $\mathbf{Q}_{\text{TR}}^{\nmid}$ (i.e. $\mathbf{P}_{\text{TR}}^{\nmid} = \mathbf{Q}_{\text{TR}}^{\nmid}(\mathbf{Q}_{\text{TR}}^{\nmid})^{\text{T}}$). Note that since $(\mathbf{Q}_{\text{TR}}^{\nmid})^{\text{T}}\mathbf{Q}_{\text{TR}}^{\shortparallel} = \mathbf{0}$, $\mathbf{P}_{\text{TR}}^{\nmid}\mathbf{Q}_{\text{T}} = \mathbf{0}$ and $\mathbf{P}_{\text{TR}}^{\nmid}\mathbf{Q}_{\text{R}} = \mathbf{0}$. Finally, note that the rank-nullity theorem relates the dimensionality of the column space, $n_{\text{TR}}^{\shortparallel}$, and dimensionality of the null space, $n_{\text{TR}}^{\neq}$:

$$n_{\text{TR}}^{\shortparallel} + n_{\text{TR}}^{\neq} = n_t + n_r. \tag{5.15}$$

One last observation about the structure of **A** is in regards to the rank of the matrix. The rank can be determined by examining linearly independent subsets of the columns of

A. Assuming that the number of unknown transmitter and receiver transfer functions is smaller than the number of received signals ($n_t + n_r < n_m$), then $\mathbf{Q}_{\text{TR}}$ and $\mathbf{Q}_{\tau\rho}$ are not full rank. As such, $\vec{\mathbf{d}}$ and $\vec{\mathbf{d}}^{\vee}$ are assumed to be linearly independent of $\mathbf{Q}_{\text{TR}}$ and $\mathbf{Q}_{\tau\rho}$. Therefore, the columns (1), (4), and (7) from (5.13a) span a column space with $n_{\text{TR}}^{\shortparallel} + 1$ dimensions. Similarly, the columns (2), (5), and (8) also span a column space of $n_{\text{TR}}^{\shortparallel} + 1$ dimensions that is orthogonal to the span of columns (1), (4), and (7). Finally, the columns (3), (6), (9), and (10), which are linearly independent of the two previous groups, span an n_m-dimensional column space since column (10) contains an $[n_m \times n_m]$ identity matrix. Therefore, the rank of **A** is:

$$\text{rank}\,(\mathbf{A}) = n_m + 2n_{\text{TR}}^{\shortparallel} + 2. \tag{5.16}$$

5.2 Noise Analysis

One issue when working with any parameter estimation algorithm is the impact of noise. If complex Gaussian white noise is assumed present in the measured frequency spectrum, two separate noise distributions are present in the elements of $\mathbf{M}_{\Im}$ and $\mathbf{M}_{\Re}$, that of phase noise and log-magnitude noise, respectively. This section characterizes the noise distributions by determining their probability distribution functions (PDFs), mean, and variance.

Consider the case of a single noisy measurement, M, that represents a single complex value, $\hat{M}$, that has been corrupted with an additive, circularly symmetric (a.k.a. proper) complex Gaussian random variable, N, with zero mean and variance σ_{N}^2:

$$M = \hat{M} + N. \tag{5.17}$$

The above equation can be described as a single, circularly symmetric complex Gaussian random variable with complex mean, $\mu = \hat{M}$. Recall that the PDF for a complex Gaussian random variable in a Cartesian coordinate system is:

$$p\,(x, y) = \frac{1}{2\pi\sigma_{\text{x}}\sigma_{\text{y}}} \text{e}^{-\frac{1}{2}\left(\frac{(x-\mu_{\text{x}})^2}{\sigma_{\text{x}}^2} + \frac{(y-\mu_{\text{y}})^2}{\sigma_{\text{y}}^2}\right)}. \tag{5.18}$$

Since the noise is circularly symmetric, $\sigma_{\Re}^2 = \sigma_{\Im}^2 = \frac{\sigma_{\mathrm{N}}^2}{2}$. Without any loss of generality, $\hat{M}$ can be taken to be a positive, real values, which means that $(\mu_{\Re}, \mu_{\Im}) = (\left|\hat{M}\right|, 0)$. Substituting these values into (5.18) and converting to polar coordinates, the PDF of M is:

$$\begin{aligned} p_M(r,\theta) &= p(r\cos\theta, r\sin\theta) \\ &= \frac{r}{\pi\sigma_{\mathrm{N}}^2} \mathrm{e}^{\frac{2r|\hat{M}|}{\sigma_{\mathrm{N}}^2}\cos\theta - \frac{r^2+|\hat{M}|^2}{\sigma_{\mathrm{N}}^2}}, \end{aligned} \tag{5.19}$$

where $p_M(r,\theta)$ is the PDF of M in terms of magnitude, r, and phase, θ, assuming that $0 \leq \theta < 2\pi$ and $0 \leq r$. From (5.19), the log-magnitude and phase noise distributions can be characterized.

5.2.1 Log-Magnitude Noise Distribution

Before the log-magnitude distribution can be obtained, the magnitude distribution must be characterized. The PDF of $|M|$ in terms of r, $p_{|M|}(r)$, can be found by integrating (5.19) over all θ:

$$\begin{aligned} p_{|M|}(r) &= \int_0^{2\pi} p_M(r,\theta)\, d\theta \\ &= \frac{2r}{\sigma_N^2} \mathrm{e}^{-\frac{r^2+|\hat{M}|^2}{\sigma_N^2}} I_0\left(\frac{2r\left|\hat{M}\right|}{\sigma_N^2}\right), \end{aligned} \tag{5.20}$$

where $I_0(z)$ is a modified Bessel function of the first kind,

$$I_0(z) = \frac{1}{2\pi}\int_0^{2\pi} \mathrm{e}^{z\cos\theta} d\theta. \tag{5.21}$$

Equation (5.20) is then used to define the *additive* noise associated with $|M|$,

$$|M| = \left|\hat{M}\right| + N_{|\cdot|}, \tag{5.22}$$

where $N_{|\cdot|}$ is a random variable with PDF derived from (5.20):

$$p_{|\cdot|}(\nu) = p_{|M|}\left(\nu + \left|\hat{M}\right|\right). \tag{5.23}$$

To find the PDF of the log-magnitude noise, note that:

$$\begin{aligned}\ln(|M|) &= \ln\left(\left|\hat{M}\right| + N_{|\cdot|}\right) \\ &= \ln\left(\left|\hat{M}\right|\right) + \ln\left(1 + \frac{N_{|\cdot|}}{\left|\hat{M}\right|}\right) \\ &= \ln\left(\left|\hat{M}\right|\right) + N_{\ln|\cdot|}, \end{aligned} \tag{5.24}$$

where

$$N_{\ln|\cdot|} = \ln\left(1 + \frac{N_{|\cdot|}}{\left|\hat{M}\right|}\right). \tag{5.25}$$

The above equation defines the log-magnitude noise, $N_{\ln|\cdot|}$, in terms of the magnitude noise, $N_{|\cdot|}$. Therefore, the PDF of the log-magnitude noise, $p_{\ln|\cdot|}(\nu)$, can be defined in terms of the magnitude PDF, $p_{|\cdot|}(\nu)$:

$$p_{\ln|\cdot|}(\nu) = p_{|\cdot|}(\left|\hat{M}\right|(\mathrm{e}^{\nu} - 1)). \tag{5.26}$$

By combining (5.26), (5.23), and (5.20), the PDF of the log-magnitude noise distribution can be obtained:

$$\begin{aligned} p_{\ln|\cdot|}(\nu) &= p_{|M|}\left(\left|\hat{M}\right|(\mathrm{e}^{\nu} - 1) + \left|\hat{M}\right|\right) \\ &= p_{|M|}\left(\left|\hat{M}\right|\mathrm{e}^{\nu}\right) \\ &= 2Q^2\mathrm{e}^{2\nu - Q^2\left(\mathrm{e}^{2\nu}+1\right)} I_0\left(2Q^2\mathrm{e}^{\nu}\right), \end{aligned} \tag{5.27}$$

where $Q = \left|\hat{M}\right| / \sigma_{\mathrm{N}}$ is referred to as the complex SNR.

Equation (5.27) indicates that the log-magnitude noise distribution, and therefore the resulting mean and variance, is dependent on the complex SNR. Figure 5.1 shows the log-magnitude noise variance *vs*. complex SNR. The same data are presented in Figure 5.2 in the form of the log-magnitude noise standard deviation, which is plotted alongside the log-magnitude mean for direct comparison. Note that although the log-magnitude noise distribution has a *non-zero* mean, the mean is very small relative to the standard deviation. As a result, it is reasonable to treat this distribution as having zero mean and there is little benefit to bias-compensation.

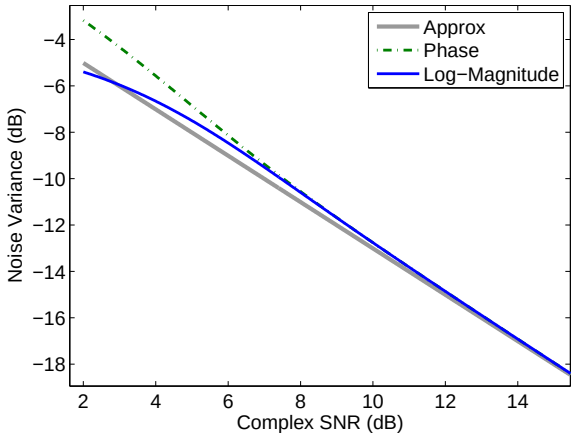

Figure 5.1: Log-magnitude and phase noise variance as a function of complex SNR. Note that the two analytic solutions closely match the approximation for SNR greater than 10 dB.

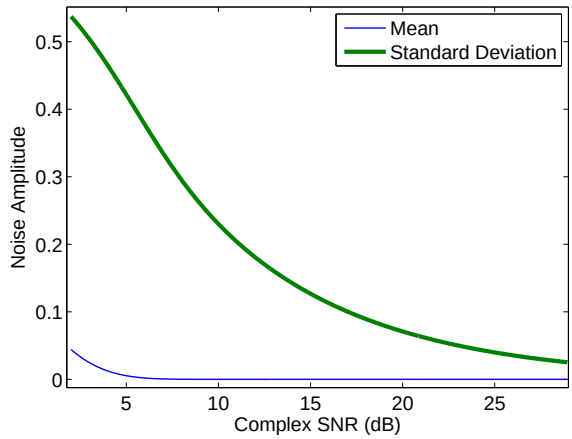

Figure 5.2: Mean and standard deviation of log-magnitude noise *vs.* complex SNR. Although log-magnitude noise has a non-zero mean, the mean is very small compared to the standard deviation.

5.2.2 Phase Noise Distribution

The probability distribution function of the phase noise, $p_{\measuredangle}(\theta)$, can be found by integrating (5.19) over $0 \leq r < \infty$, yielding the following result:

$$\begin{aligned} p_{\measuredangle}(\theta) &= \int_0^{\infty} p_M(r,\theta)\, dr \\ &= \frac{1}{2\pi} e^{-Q^2} \left(1 + Q\cos(\theta)\ \sqrt{\pi} e^{Q^2\cos^2(\theta)} \left(1 + \operatorname{erf}(Q\cos(\theta))\right)\right), \end{aligned} \tag{5.28}$$

where

$$\text{erf}\,(x) = \frac{2}{\sqrt{\pi}} \int_0^x \mathrm{e}^{-t^2} dt. \tag{5.29}$$

Similar to the case for the log-magnitude noise distribution, the phase noise distribution *is* a function of the complex SNR. Unlike the log-magnitude noise distribution, however, the phase noise distribution is zero mean. Figure 5.1 shows the phase-noise variance as a function of complex SNR. Note that as complex SNR increases, the phase and log-magnitude noise variances converge.

5.2.3 Noise Variance Approximation

A linear approximation of the phase and log-magnitude noise variances as a function of complex SNR can be obtained by considering the case of a high SNR signal. Let $N_\Re$ and $N_\Im$ be the orthogonal components of the circularly symmetric complex noise variable, N, in the directions of the real and imaginary axes, respectively. As mentioned earlier, $N_\Re$ and $N_\Im$ each have zero mean and variance $\sigma_\Re^2 = \sigma_\Im^2 = \frac{\sigma_N^2}{2}$. For a high SNR signal, the real and imaginary components of the circularly symmetric noise effectively impact only magnitude and phase, respectively. As such, the phase noise variance is approximately:

$$\sigma_\angle^2 \approx E\left[\arctan^2\left(\frac{N_\Im}{\left|\hat{M}\right|}\right)\right] \approx \frac{1}{2Q^2}, \tag{5.30}$$

since $N_\Im / \left|\hat{M}\right| << 1$ and the small angle approximation allows the arctan function to be approximated by its argument.

To obtain the log-magnitude approximation, note that log-magnitude noise is related to the magnitude noise in (5.25). As a result, the log-magnitude noise variance is effectively:

$$\sigma_{\ln|\cdot|}^2 \approx E\left[\ln^2\left(1 + \frac{N_\Re}{\left|\hat{M}\right|}\right)\right]. \tag{5.31}$$

For this high-SNR case, the logarithmic relationship can be simplified using the Taylor

series expansion of a natural logarithm:

$$\ln\left(1+\frac{N_{\Re}}{\left|\hat{M}\right|}\right) = \frac{N_{\Re}}{\left|\hat{M}\right|} - \frac{1}{2}\left(\frac{N_{\Re}}{\left|\hat{M}\right|}\right)^2 + \frac{1}{3}\left(\frac{N_{\Re}}{\left|\hat{M}\right|}\right)^3 - \cdots$$
$$\approx \frac{N_{\Re}}{\left|\hat{M}\right|}, \tag{5.32}$$

since $N_{\Re} << \left|\hat{M}\right|$. Therefore, the log-magnitude noise variance can be approximated as $\sigma^2_{\ln|\cdot|} \approx \frac{1}{2Q^2}$. This result is identical to the approximation for phase noise.

The phase and log-magnitude noise variance approximation is shown in Figure 5.1 as a thick line for comparison with the analytic solutions. The analytic solutions clearly converge with the simple approximation and thus the approximation derived here can be considered valid for complex SNRs as low as 10 dB.

5.2.4 Noise Model

The above analysis provides a mechanism to model the system noise in the logarithmic domain. Let the measurements contained in the measurement matrix, **M**, be modeled as a matrix of true values, $\hat{\mathbf{M}}$, plus a matrix of additive noise, **N**, similar to (5.17):

$$\mathbf{M} = \hat{\mathbf{M}} + \mathbf{N}. \tag{5.33}$$

The frequency domain noise for each received signal is assumed to be circularly-symmetric i.i.d. Gaussian noise with variance σ^2_{N}. Therefore, each column of **N** is independent of the other columns and has the structure:

$$\vec{\mathbf{N}}_i = \begin{bmatrix} \vec{\mathbf{N}}^{\mathrm{T}}_{\Re i} & \vec{\mathbf{N}}^{\mathrm{T}}_{\Im i} & \vec{\mathbf{N}}^{\mathrm{T}}_{\Im i} \end{bmatrix}^{\mathrm{T}}, \tag{5.34}$$

where $\vec{\mathbf{N}}_i$ is the i^{th} column of **N**, and the $\vec{\mathbf{N}}_{\Re i}$ and $\vec{\mathbf{N}}_{\Im i}$ vectors correspond to the noise present in the i^{th} column of $\mathbf{M}_{\Re}$ and $\mathbf{M}_{\Im}$, respectively. Note that while the $\vec{\mathbf{N}}_{\Re i}$ and $\vec{\mathbf{N}}_{\Im i}$ vectors are independent of one another, the two $\vec{\mathbf{N}}_{\Im i}$ vectors in the above equation, although not exactly the same as written, are *nearly identical* since the third set of linear equations corresponds to $\mathbf{M}_{\Im}\mathbf{P}_{\Delta}$, which effectively subtracts the row mean from each row and has a negligible

impact on the noise. Since the phase noise and log-magnitude noise can be treated as zero mean, the distribution for every element of $\mathbf{N}$ is assumed to have zero mean, $E[\mathbf{N}] = \mathbf{0}$. Further, by using the approximation from the previous section, $\sigma^2_{\ln|\cdot|} \approx \sigma^2_{\angle} \approx \frac{1}{2Q^2}$, the noise variance for each column can be approximated as:

$$\begin{aligned}\sigma_i^2 &= E\left[\vec{\mathbf{N}}_i^{\mathrm{T}}\vec{\mathbf{N}}_i\right] \\ &= E\left[\vec{\mathbf{N}}_{\Re i}^{\mathrm{T}}\vec{\mathbf{N}}_{\Re i}\right] + 2E\left[\vec{\mathbf{N}}_{\Im i}^{\mathrm{T}}\vec{\mathbf{N}}_{\Im i}\right] \\ &= \frac{3}{2}\sum_j \frac{1}{Q_{ij}^2},\end{aligned} \tag{5.35}$$

where Q_{ij} is the complex SNR for the ith column (FFT frequency bin) and jth received signal.

5.3 Distance Vector Estimation

To completely define $\mathbf{A}$ in (5.13a), the distance vector $\vec{\mathbf{d}}$ must be known. Although it is possible to measure the propagation distances, these measurements are subject to measurement errors and may change slightly with variations in the propagation environment (e.g. thermal expansion). As such, the measured distance vector, $\vec{\mathbf{d}}_{\mathrm{m}}$, is constrained to fit the data.

To begin, the n_m-dimensional vector space that $\vec{\mathbf{d}}$ resides in can be divided into two mutually exclusive subspaces based on the $\mathbf{Q}_{\mathrm{TR}}$ matrix, $\mathbf{Q}^{\shortparallel}_{\mathrm{TR}}$ and $\mathbf{Q}^{\perp}_{\mathrm{TR}}$. Note that when the projection matrix, $\mathbf{P}^{\perp}_{\mathrm{TR}}$, is multiplied with the $\mathbf{M}_{\Im}\mathbf{P}_{\Delta}$ product described in (5.11), the distance vector term can be isolated:

$$\mathbf{P}^{\perp}_{\mathrm{TR}}\mathbf{M}_{\Im}\mathbf{P}_{\Delta} = -\mathbf{P}^{\perp}_{\mathrm{TR}}\vec{\mathbf{d}}\,\vec{\mathbf{k}}_{\Delta}^{\mathrm{T}}. \tag{5.36}$$

Inspection of the right-hand-side of (5.36) reveals that every column of $\mathbf{P}^{\perp}_{\mathrm{TR}}\mathbf{M}_{\Im}\mathbf{P}_{\Delta}$ is a scaled version of $\mathbf{P}^{\perp}_{\mathrm{TR}}\vec{\mathbf{d}}$. Since $\vec{\mathbf{k}}_{\Delta}^{\mathrm{T}}$ is unknown, $\vec{\mathbf{d}}$ cannot be obtained directly. It is possible however, to use (5.36) to determine the *direction* of $\mathbf{P}^{\perp}_{\mathrm{TR}}\vec{\mathbf{d}}$. Let $\vec{\mathbf{v}}^{\perp}_{\mathrm{TR}}$ be the unit-norm vector

corresponding to the direction of $\mathbf{P}_{\mathrm{TR}}^{\nu}\vec{\mathbf{d}}$. Then $\vec{\mathbf{v}}_{\mathrm{TR}}^{\nu}$ must satisfy:

$$\vec{\mathbf{v}}_{\mathrm{TR}}^{\nu} = \arg\max_{\vec{\mathbf{v}}} \vec{\mathbf{v}}^{\mathrm{T}} \mathbf{M}_{TR}^{\nu} \left(\mathbf{M}_{TR}^{\nu}\right)^{\mathrm{T}} \vec{\mathbf{v}}, \tag{5.37}$$

where $\mathbf{M}_{TR}^{\nu}$ is defined as

$$\mathbf{M}_{TR}^{\nu} = \mathbf{P}_{\mathrm{TR}}^{\nu} \mathbf{M}_{\Im} \mathbf{P}_{\Delta}. \tag{5.38}$$

Note that $\vec{\mathbf{v}}_{\mathrm{TR}}^{\nu}$ is, by definition, the eigenvector that corresponds to the largest eigenvalue of $\mathbf{M}_{TR}^{\nu} \left(\mathbf{M}_{TR}^{\nu}\right)^{\mathrm{T}}$. Also, although not performed for the examples presented in this text, more accurate estimates of $\vec{\mathbf{v}}_{\mathrm{TR}}^{\nu}$ may be possible by normalizing or weighting the columns of $\mathbf{M}_{TR}^{\nu}$ prior to performing the eigendecomposition.

The distance vector, $\vec{\mathbf{d}}$, can now be defined in terms of $\vec{\mathbf{v}}_{\mathrm{TR}}^{\nu}$, which is the unit-norm projection of $\vec{\mathbf{d}}$ onto $\mathbf{Q}_{\mathrm{TR}}^{\nu}$, and some linear combination of the columns of $\mathbf{Q}_{\mathrm{TR}}^{\shortparallel}$:

$$\vec{\mathbf{d}} = d_{\nu} \vec{\mathbf{v}}_{\mathrm{TR}}^{\nu} + \mathbf{Q}_{\mathrm{TR}}^{\shortparallel} \vec{\mathbf{d}}_{\shortparallel}, \tag{5.39}$$

where the d_{ν} and $\vec{\mathbf{d}}_{\shortparallel}$ variables are scaling coefficients. The scaling coefficients d_{ν} and $\vec{\mathbf{d}}_{\shortparallel}$ are obtained by projecting the *a priori* measured distances, $\vec{\mathbf{d}}_{\mathrm{m}}$, onto $\vec{\mathbf{v}}_{\mathrm{TR}}^{\nu}$ and $\mathbf{Q}_{\mathrm{TR}}^{\shortparallel}$:

$$\begin{bmatrix} d_{\nu} \\ \vec{\mathbf{d}}_{\shortparallel} \end{bmatrix} = \begin{bmatrix} \vec{\mathbf{v}}_{\mathrm{TR}}^{\nu} & \mathbf{Q}_{\mathrm{TR}}^{\shortparallel} \end{bmatrix}^{\mathrm{T}} \vec{\mathbf{d}}_{\mathrm{m}}. \tag{5.40}$$

For completeness, it should be noted that a similar derivation can be performed to find an equivalent $\vec{\mathbf{v}}_{\mathrm{TR}}^{\nu}$ for the logarithm of the scaled distance vector, $\vec{\mathbf{d}}^{\curlyvee}$. The exclusive use of phase-response data over log-magnitude data was chosen for convenience. Alternatively, both the magnitude and phase information could be used to make a combined estimate. However, since the $\vec{\mathbf{d}}$ and $\vec{\mathbf{d}}^{\curlyvee}$ vectors are related by an exponential function, combining $\vec{\mathbf{v}}_{\mathrm{TR}}^{\nu}$ estimates requires a nonlinear search. Since satisfactory results are obtained with only phase information, the additional complexity associated with combining distance vector estimates from both magnitude and phase information is omitted in the interest of simplicity.

5.4 Linear Solution and Model Null-Space

The general solution to (5.12) can be obtained by applying the Moore-Penrose pseudoinverse [149], denoted by "†", and accounting for the null-space of the **A** matrix:

$$\mathbf{Z} = \mathbf{A}^{\dagger}\mathbf{M} + \mathbf{A}^{\neq}\mathbf{C}_{\mathrm{A}}^{\neq}, \tag{5.41}$$

where $\mathbf{A}^{\dagger} = \left(\mathbf{A}^{\mathrm{T}}\mathbf{A}\right)^{-1}\mathbf{A}^{\mathrm{T}}$, the columns of $\mathbf{A}^{\neq}$ form a basis for the null space of **A**, and $\mathbf{C}_{\mathrm{A}}^{\neq}$ is a matrix of unknown coefficients. In Section 5.2 it was shown that the phase noise has zero mean and the log-magnitude noise can be safely approximated as zero mean. As such, the pseudoinverse operation used in (5.41) provides the least-squares approximation to the values in **Z**. Note that obtaining the first term of (5.41) is not computationally demanding since the $\mathbf{A}^{\dagger}$ matrix is not frequency-dependent and need only be calculated once.

For the problem formulation considered here, the null space of **A** can be characterized by inspection of (5.13a). To begin, decompose the $\mathbf{Q}_{\mathrm{TR}}^{\neq}$ matrix into two sub-matrices:

$$\mathbf{Q}_{\mathrm{TR}}^{\neq} = \begin{bmatrix} \mathbf{Q}_{\mathrm{(T)R}}^{\neq} \\ \mathbf{Q}_{\mathrm{T(R)}}^{\neq} \end{bmatrix}, \tag{5.42}$$

where $\mathbf{Q}_{\mathrm{(T)R}}^{\neq}$ is a $[n_t \times n_{\mathrm{TR}}^{\neq}]$ sub-matrix and $\mathbf{Q}_{\mathrm{T(R)}}^{\neq}$ is a $[n_r \times n_{\mathrm{TR}}^{\neq}]$ sub-matrix. Assuming that $\vec{\mathbf{d}}$ and $\vec{\mathbf{d}}^{\vee}$ are linearly independent of $\mathbf{Q}_{\mathrm{T}}$ and $\mathbf{Q}_{\mathrm{R}}$, then the null space of **A** is spanned by five

sets of vectors, namely:

$$\mathbf{A}^{\neq} = \begin{array}{c} \\ (\underline{1}) \\ (\underline{2}) \\ (\underline{3}) \\ (\underline{4}) \\ (\underline{5}) \\ (\underline{6}) \\ (\underline{7}) \\ (\underline{8}) \\ (\underline{9}) \\ (\underline{10}) \end{array} \begin{array}{c} \begin{array}{ccccc} \mathbf{A}_{\Re}^{\neq} & \mathbf{A}_{\Im}^{\neq} & \mathbf{A}_{\tau}^{\neq} & \mathbf{A}_{\rho}^{\neq} & \vec{\mathbf{a}}_{\kappa}^{\neq} \end{array} \\ \begin{bmatrix} \mathbf{Q}_{(\mathrm{T})\mathrm{R}}^{\neq} & \mathbf{0} & \mathbf{0} & \mathbf{0} & \vec{0}_t \\ \mathbf{0} & \mathbf{Q}_{(\mathrm{T})\mathrm{R}}^{\neq} & \mathbf{0} & \mathbf{0} & \vec{0}_t \\ \mathbf{0} & \mathbf{0} & \mathbf{I}_t & \mathbf{0} & \vec{0}_t \\ \mathbf{Q}_{\mathrm{T}(\mathrm{R})}^{\neq} & \mathbf{0} & \mathbf{0} & \mathbf{0} & \vec{0}_r \\ \mathbf{0} & \mathbf{Q}_{\mathrm{T}(\mathrm{R})}^{\neq} & \mathbf{0} & \mathbf{0} & \vec{0}_r \\ \mathbf{0} & \mathbf{0} & \mathbf{0} & \mathbf{I}_r & \vec{0}_r \\ 0 & 0 & 0 & 0 & 0 \\ 0 & 0 & 0 & 0 & 0 \\ 0 & 0 & 0 & 0 & 1 \\ \mathbf{0} & \mathbf{0} & -\frac{1}{2\pi}\mathbf{Q}_{\tau} & -\frac{1}{2\pi}\mathbf{Q}_{\rho} & \frac{1}{2\pi}\vec{\mathbf{d}} \end{bmatrix} \end{array}. \tag{5.43}$$

The fact that the columns of $\mathbf{A}^{\neq}$ reside in the null space of $\mathbf{A}$ can be verified by inspection of (5.13a) and (5.43). To verify that the entire null space of $\mathbf{A}$ is spanned by the columns of $\mathbf{A}^{\neq}$, first note that each column of $\mathbf{A}^{\neq}$ is independent of all other columns, and then consider that there are $2n_{\mathrm{TR}}^{\neq} + n_t + n_r + 1$ columns. Since the dimensions of $\mathbf{A}$ are $[3n_m \times (3(n_t + n_r + 1) + n_m)]$, the rank-nullity theorem states that:

$$\mathrm{rank}\,(\mathbf{A}) + \mathrm{nullity}\,(\mathbf{A}) = 3(n_t + n_r + 1) + n_m, \tag{5.44}$$

Substituting (5.15) and (5.16) into the above equation and solving for nullity ($\mathbf{A}$) yields:

$$\mathrm{nullity}\,(\mathbf{A}) = 2n_{\mathrm{TR}}^{\neq} + n_t + n_r + 1. \tag{5.45}$$

Since there are $2n_{\mathrm{TR}}^{\neq} + n_t + n_r + 1$ columns in $\mathbf{A}^{\neq}$ that are linearly independent and reside in the null space of $\mathbf{A}$, these columns span the null space of $\mathbf{A}$.

The first two sets of vectors, $\mathbf{A}_{\Re}^{\neq}$ and $\mathbf{A}_{\Im}^{\neq}$, account for potential ambiguities in the magnitude and phase relationship between the transmitter and receiver transfer functions. Consider a simple example: regardless of the actual phase estimates of the transmitter and

receiver transfer functions, no net change would result in the phase estimate of model-generated signals if *all* of the transmitter phase estimates are shifted by some angular offset, θ, and *all* of the receiver phase estimates are shifted by a corresponding negative phase offset, $-\theta$. This type of ambiguity, and the analogous scenario with log-magnitude scaling, is captured by the $\mathbf{A}_{\Re}^{\neq}$ and $\mathbf{A}_{\Im}^{\neq}$ null-spaces. Unless additional constraints are available for $\mathbf{T}_{\Im}$ or $\mathbf{R}_{\Im}$, the sub-space defined by $\mathbf{A}_{\Re}^{\neq}$ and $\mathbf{A}_{\Im}^{\neq}$ can be ignored from an estimation standpoint since the ambiguity cannot be resolved.

The third and fourth sets of vectors, $\mathbf{A}_{\tau}^{\neq}$ and $\mathbf{A}_{\rho}^{\neq}$, relate additional phase offsets in the transmitter and receiver phase estimates with corresponding shifts in the $\vec{\mathbf{b}}$ vector estimate. Notice that as the $\mathbf{A}_{\tau}^{\neq}$ and $\mathbf{A}_{\rho}^{\neq}$ columns are scaled by integer multiples of 2π, the resulting phase offsets for the transmitter and receiver transfer functions are changed by integer multiples of 2π, which results in effectively unchanged transmitter and receiver phase responses. Additionally, since the elements of $\mathbf{Q}_{\tau}$ and $\mathbf{Q}_{\rho}$ are *integer* values, then 2π integer multiples of $\mathbf{A}_{\tau}^{\neq}$ and $\mathbf{A}_{\rho}^{\neq}$ result in integer shifts in the $\vec{\mathbf{b}}$ vector estimate. This repetitive behavior indicates that the $\measuredangle T(\omega)$, $\measuredangle R(\omega)$, and $\vec{\mathbf{b}}$ estimates are not unique. This conclusion is somewhat intuitive since any 2π offset in $\measuredangle T(\omega)$ or $\measuredangle R(\omega)$ results in an identical set of signals. Unlike the first two sets of vectors, $\mathbf{A}_{\tau}^{\neq}$ and $\mathbf{A}_{\rho}^{\neq}$ cannot be ignored, since they influence the $\vec{\mathbf{b}}$ vector estimate.

Finally, the fifth null-space vector set, $\vec{\mathbf{a}}_{\kappa}^{\neq}$, is a single vector. If, like the $\mathbf{Q}_{\tau}$ and $\mathbf{Q}_{\rho}$ matrices that are assumed to have only "1" and "0" elements, the $\vec{\mathbf{d}}$ vector can be multiplied by some value to produce an all-integer vector, then the κ estimate is not unique. As a result, a unique κ solution is only mathematically possible if the $\vec{\mathbf{d}}$ vector contains at least one irrational element. Although a requirement for an irrational distance is impractical, it is relatively easy to select a set of distances such that only one solution can be accepted as a realistic parameter value. A lower bound for the proximity of potential solutions is derived in Appendix B. Like the $\mathbf{A}_{\tau}^{\neq}$ and $\mathbf{A}_{\rho}^{\neq}$ vector sets, the $\vec{\mathbf{a}}_{\kappa}^{\neq}$ vector also affects the $\vec{\mathbf{b}}$ vector estimate and cannot be ignored.

The $\mathbf{A}_{\tau}^{\neq}$, $\mathbf{A}_{\rho}^{\neq}$, and $\vec{\mathbf{a}}_{\kappa}^{\neq}$ vector sets all have an impact on the $\vec{\mathbf{b}}$ vector estimate. Two additional model constraints can be applied to assist in the $\vec{\mathbf{b}}$ vector estimate. First, the assumed model dictates that κ, $\vec{\tau}$, $\vec{\rho}$, and $\vec{\mathbf{b}}$ are all frequency-independent. Therefore, the coefficients in $\mathbf{C}_{\mathrm{A}}^{\neq}$ of (5.41) that impact the κ, $\vec{\tau}$, $\vec{\rho}$, and $\vec{\mathbf{b}}$ estimates must also be frequency-independent. Additionally, the $\vec{\mathbf{b}}$ vector is constrained to be an all-integer vector. To enforce this final constraint in the model parameter estimates, a nonlinear search is required.

5.5 Nonlinear Search

In Section 5.4, the linear least-squares estimate of $\mathbf{Z}$ in (5.41) was shown to include some linear combination of the column vectors described in (5.43). Of these five sets of vectors, three sets of vectors ($\mathbf{A}_{\tau}^{\neq}$, $\mathbf{A}_{\rho}^{\neq}$, and $\vec{\mathbf{a}}_{\kappa}^{\neq}$) are associated with the $\vec{\mathbf{b}}$ estimate, which must be an all-integer vector for the estimated model parameters to agree with the data. A nonlinear search is described here to identify a solution that satisfies the all-integer constraint. The general approach taken is to first obtain a frequency-independent estimate of $\vec{\mathbf{b}}$ using the linear solution presented in the previous section, then search for null-space coefficients that force the $\vec{\mathbf{b}}$ estimate to be an all integer vector.

The use of an unwrapped phase response ensures that the all-integer $\vec{\mathbf{b}}$ vector is constant across all measured frequencies. Therefore, a $\vec{\mathbf{b}}$ estimate can be described as a function of frequency-independent null-space coefficients, $\vec{\mathbf{c}}$:

$$\begin{aligned}\vec{\mathbf{b}}(\vec{\mathbf{c}}) &= \mathbf{B}\mathbf{Z}(\vec{\mathbf{c}})\,\vec{\mathbf{\Sigma}} \\ &= \mathbf{B}\left(\mathbf{A}^{\dagger}\mathbf{M} + \begin{bmatrix} \mathbf{A}_{\tau}^{\neq} & \mathbf{A}_{\rho}^{\neq} & \vec{\mathbf{a}}_{\kappa}^{\neq} \end{bmatrix} \vec{\mathbf{c}}\;\vec{\mathbf{1}}_{w}^{\mathrm{T}}\right)\vec{\mathbf{\Sigma}}, \end{aligned} \tag{5.46}$$

where $\mathbf{B} = \begin{bmatrix} \mathbf{0} & \mathbf{I}_{s} \end{bmatrix}$ is a $[n_m \times 3(n_t + n_r + 1) + n_m]$ matrix that isolates the elements of $\mathbf{Z}$ corresponding to the $\vec{\mathbf{b}}$ values, $\vec{\mathbf{c}}\;\vec{\mathbf{1}}_{w}^{\mathrm{T}}$ corresponds to the frequency-independent portion of the coefficients in $\mathbf{C}_{\mathrm{A}}^{\neq}$, and $\vec{\mathbf{\Sigma}}$ is a $[n_w \times 1]$ vector that performs a weighted average over frequency.

5.5.1 Optimal Weights

In this section, the optimal weights, $\vec{\mathbf{\Sigma}}^{\bullet}$, for combining the frequency-dependent estimates of $\vec{\mathbf{b}}$ are derived. Let $\mathbf{B}_{\mathrm{A}}^{=}$ be the collection of n_w separate estimates of $\vec{\mathbf{b}}$ obtained by applying the pseudo-inverse of $\mathbf{A}$ to the measurement matrix $\mathbf{M}$. Since $\vec{\mathbf{b}}$ is independent of frequency, each of these estimates corresponds to a single, true, underlying vector, $\hat{\mathbf{b}}_{\mathrm{A}}^{=}$, plus additive noise:

$$\begin{aligned}\mathbf{B}_{\mathrm{A}}^{=} &= \mathbf{B}\mathbf{A}^{\dagger}\mathbf{M} \\ &= \mathbf{B}\mathbf{A}^{\dagger}\hat{\mathbf{M}} + \mathbf{B}\mathbf{A}^{\dagger}\mathbf{N} \\ &= \hat{\mathbf{b}}_{\mathrm{A}}^{=}\vec{\mathbf{1}}_w^{\mathrm{T}} + \mathbf{N}_{\mathrm{b}}. \end{aligned} \tag{5.47}$$

where $\mathbf{M}$ is defined in (5.33) and $\mathbf{N}_{\mathrm{b}}$ is another $[n_m \times n_w]$ matrix of additive noise constructed as $\mathbf{B}\mathbf{A}^{\dagger}\mathbf{N}$. Since each element of $\mathbf{N}_{\mathrm{b}}$ is constructed from a linear combination of the elements of $\mathbf{N}$, the noise present in each element of $\mathbf{N}_{\mathrm{b}}$ has effectively zero mean. In addition, since each column of $\mathbf{N}$ is independent of the others, each column of $\mathbf{N}_{\mathrm{b}}$ is also independent of the other columns in $\mathbf{N}_{\mathrm{b}}$.

The optimal weights, $\vec{\mathbf{\Sigma}}^{\bullet}$, are selected to satisfy:

$$\vec{\mathbf{\Sigma}}^{\bullet} = \arg\min_{\vec{\mathbf{\Sigma}}} E\left[\|\mathbf{B}_{\mathrm{A}}^{=}\vec{\mathbf{\Sigma}} - \hat{\mathbf{b}}_{\mathrm{A}}^{=}\|^2\right], \qquad \text{such that} \qquad \vec{\mathbf{1}}_w^{\mathrm{T}}\vec{\mathbf{\Sigma}} = 1, \tag{5.48}$$

where $E[\cdot]$ is the expected value operator and the $\vec{\mathbf{1}}_w^{\mathrm{T}}\vec{\mathbf{\Sigma}} = 1$ constraint ensures that the weights sum to 1. The solution to (5.48) can be found using a Lagrange multiplier, α, to satisfy the summation constraint,

$$L = E\left[\left(\mathbf{B}_{\mathrm{A}}^{=}\vec{\mathbf{\Sigma}} - \hat{\mathbf{b}}_{\mathrm{A}}^{=}\right)^{\mathrm{T}}\left(\mathbf{B}_{\mathrm{A}}^{=}\vec{\mathbf{\Sigma}} - \hat{\mathbf{b}}_{\mathrm{A}}^{=}\right)\right] + \alpha\left(\vec{\mathbf{\Sigma}}^{\mathrm{T}}\vec{\mathbf{1}}_w - 1\right). \tag{5.49}$$

The Lagrangian, L, is minimized by taking the derivative of (5.49) with respect to $\vec{\mathbf{\Sigma}}$, setting it equal to zero, and solving for $\vec{\mathbf{\Sigma}}$:

$$\vec{\mathbf{\Sigma}}^{\bullet} = \mathbf{U}^{-1}\vec{\mathbf{1}}_w\left(\|\hat{\mathbf{b}}_{\mathrm{A}}^{=}\|^2 - \frac{\alpha}{2}\right), \tag{5.50}$$

where

$$\mathbf{U}^{-1} = \left(\|\hat{\mathbf{b}}_{\mathrm{A}}^{=}\|^2 \vec{\mathbf{1}}_w \vec{\mathbf{1}}_w^{\mathrm{T}} + \mathbf{\Omega}_{\mathrm{N}} \right)^{-1} \tag{5.51}$$

and

$$\begin{aligned} \mathbf{\Omega}_{\mathrm{N}} &= E\left[\mathbf{N}_{\mathrm{b}}^{\mathrm{T}} \mathbf{N}_{\mathrm{b}} \right] \\ &= \begin{bmatrix} \sigma_{\mathrm{b}1}^2 & 0 & \cdots \\ 0 & \sigma_{\mathrm{b}2}^2 & \\ \vdots & & \ddots \end{bmatrix}. \end{aligned} \tag{5.52}$$

Note that a large reduction in terms during the Lagrangian minimization is possible because $E\left[\mathbf{N}_{\mathrm{b}}\right] = \mathbf{0}$. Each $\sigma_{\mathrm{b}i}^2$ element corresponds to $E\left[\begin{array}{cc} \vec{\mathbf{N}}_{\mathrm{b}i}^{\mathrm{T}} & \vec{\mathbf{N}}_{\mathrm{b}i} \end{array} \right]$, where $\vec{\mathbf{N}}_{\mathrm{b}i}$ is the ith column vector of $\mathbf{N}_{\mathrm{b}}$. Substituting (5.50) into the $\vec{\mathbf{1}}_w^{\mathrm{T}} \vec{\mathbf{\Sigma}} = 1$ constraint of (5.48), $\|\hat{\mathbf{b}}_{\mathrm{A}}^{=}\|^2 - \frac{\alpha}{2}$ can be found:

$$\left(\|\hat{\mathbf{b}}_{\mathrm{A}}^{=}\|^2 - \frac{\alpha}{2} \right) = \frac{1}{\vec{\mathbf{1}}_w^{\mathrm{T}} \mathbf{U}^{-1} \vec{\mathbf{1}}_w}. \tag{5.53}$$

Finally, a closed-form solution to (5.48) is obtained by substituting (5.53) into (5.50):

$$\vec{\mathbf{\Sigma}}^{\bullet} = \frac{\mathbf{U}^{-1} \vec{\mathbf{1}}_w}{\vec{\mathbf{1}}_w^{\mathrm{T}} \mathbf{U}^{-1} \vec{\mathbf{1}}_w} \propto \begin{bmatrix} \frac{1}{\sigma_{\mathrm{b}1}^2} & \frac{1}{\sigma_{\mathrm{b}2}^2} & \cdots \end{bmatrix}^{\mathrm{T}}. \tag{5.54}$$

The proportionality with the inverse noise variance can be seen by noting that the structure of $\mathbf{U}^{-1}$ naturally lends itself to the Woodbury Matrix Identity [150], also known as the matrix inversion lemma. According to this identity formula, $\mathbf{U}^{-1}$ can be calculated as:

$$\mathbf{U}^{-1} = \mathbf{\Omega}_{\mathrm{N}}^{-1} - \frac{\mathbf{\Omega}_{\mathrm{N}}^{-1} \vec{\mathbf{1}}_w \vec{\mathbf{1}}_w^{\mathrm{T}} \mathbf{\Omega}_{\mathrm{N}}^{-1}}{\frac{1}{\|\hat{\mathbf{b}}_{\mathrm{A}}^{=}\|^2} + \vec{\mathbf{1}}_w^{\mathrm{T}} \mathbf{\Omega}_{\mathrm{N}}^{-1} \vec{\mathbf{1}}_w} \tag{5.55}$$

where

$$\mathbf{\Omega}_{\mathrm{N}}^{-1} = \begin{bmatrix} \frac{1}{\sigma_{\mathrm{b}1}^2} & 0 & \cdots \\ 0 & \frac{1}{\sigma_{\mathrm{b}2}^2} & \\ \vdots & & \ddots \end{bmatrix}. \tag{5.56}$$

The relationship expressed in (5.54) indicates that the optimal weights are proportional

to the inverse of the frequency-dependent noise variance. Since $\mathbf{N}_\mathrm{b} = \mathbf{B}\mathbf{A}^\dagger\mathbf{N}$, the frequency-dependent noise variance can be derived, similar to (5.35):

$$\begin{aligned}\sigma^2_{\mathrm{b}i} &= E\left[\vec{\mathbf{N}}^\mathrm{T}_{\mathrm{b}i}\vec{\mathbf{N}}_{\mathrm{b}i}\right] \\ &= E\left[\vec{\mathbf{N}}^\mathrm{T}_{i}\boldsymbol{\Gamma}\vec{\mathbf{N}}_{i}\right] \\ &= \frac{1}{2}\vec{\boldsymbol{\gamma}}^\mathrm{T}\left(\frac{1}{\vec{\mathbf{Q}}_i}\right),\end{aligned} \tag{5.57}$$

where $\boldsymbol{\Gamma} = (\mathbf{A}^\dagger)^\mathrm{T}\mathbf{B}^\mathrm{T}\mathbf{B}\mathbf{A}^\dagger$, $\vec{\boldsymbol{\gamma}}$ is a $[3n_m \times 1]$ vector containing the diagonal elements of $\boldsymbol{\Gamma}$, $\vec{\mathbf{Q}}_i$ is a $[3n_m \times 1]$ vector of squared complex SNR values for the ith column of $\mathbf{M}$, and the rightmost division operation is an element-wise inversion. The column-specific, squared complex SNR values, $\vec{\mathbf{Q}}_i$, can be approximated in a single matrix, $\mathbf{Q}$:

$$\mathbf{Q} \approx \begin{bmatrix}\mathbf{I}_s \\ \mathbf{I}_s \\ \mathbf{I}_s\end{bmatrix}\frac{\mathrm{e}^{2\mathbf{M}_\Re} - \vec{\boldsymbol{\sigma}}^2_\mathrm{m}\vec{\mathbf{1}}^\mathrm{T}_w}{\vec{\boldsymbol{\sigma}}^2_\mathrm{m}\vec{\mathbf{1}}^\mathrm{T}_w}, \tag{5.58}$$

where $\mathrm{e}^{2\mathbf{M}_\Re}$ is an element-wise exponential operation that produces a $[n_m \times n_w]$ matrix of squared magnitude values, $\vec{\boldsymbol{\sigma}}^2_\mathrm{m}$ is a $[n_m \times 1]$ vector of complex noise variance measurements corresponding to each received signal, and the division operation is again performed element-wise. The set of three identity matrices accounts for the structure of $\vec{\mathbf{N}}_i$ discussed in (5.34). With $\mathbf{Q}$ obtained as in (5.58), the optimal weights can be approximated as:

$$\vec{\boldsymbol{\Sigma}}^\bullet \propto \begin{bmatrix}\frac{1}{\sigma^2_{\mathrm{b}1}} & \frac{1}{\sigma^2_{\mathrm{b}2}} & \cdots\end{bmatrix}^\mathrm{T} \propto \frac{1}{\vec{\boldsymbol{\gamma}}^\mathrm{T}(1/\mathbf{Q})}, \tag{5.59}$$

with the division operations again performed element-wise. Note that even though each $\vec{\mathbf{b}}$ element is specific to one of the received signals, a single, composite $\vec{\boldsymbol{\Sigma}}^\bullet$ is used here since data from multiple signals contribute to the n_w estimates of $\vec{\mathbf{b}}$ contained in $\mathbf{B}^=_\mathrm{A}$.

5.5.2 Multidimensional Search

The definition of $\vec{\mathbf{b}}$ as a function of $\vec{\mathbf{c}}$ in (5.46) can be used to search for a value of $\vec{\mathbf{c}}$ that produces an all-integer estimate. The search is performed by finding $\hat{\mathbf{c}}_b$ such that:

$$\hat{\mathbf{c}}_b = \arg\min_{\vec{\mathbf{c}}} \|\vec{\mathbf{b}}(\vec{\mathbf{c}}) - [\![\vec{\mathbf{b}}(\vec{\mathbf{c}})]\!]\|^2. \tag{5.60}$$

Here $\vec{\mathbf{b}}(\vec{\mathbf{c}})$ is defined as in (5.46) and $[\![\cdot]\!]$ is the round function, which rounds each element towards the nearest integer.

Although the nonlinear search can be performed as written, the error surface associated with (5.60) is multi-dimensional and has an infinite number of local minima. As such, the *entire* search space of possible $\vec{\mathbf{c}}$ values must be evaluated. Such an exhaustive search is computationally demanding and time intensive.

5.5.3 Modified Search

A modification to the approach described in (5.60) was developed to avoid an exhaustive multidimensional search by taking advantage of the null-space structure. Let $\hat{\mathbf{c}}_b$ be defined as a set of null-space coefficients that result in an all-integer $\vec{\mathbf{b}}$ vector estimate, $\vec{\mathbf{b}}(\hat{\mathbf{c}}_b)$. The $\hat{\mathbf{c}}_b$ vector has the following sub-components corresponding to the $\mathbf{A}_\tau^{\neq}$, $\mathbf{A}_\rho^{\neq}$, and $\vec{\mathbf{a}}_\kappa^{\neq}$ matrices from (5.43):

$$\hat{\mathbf{c}}_b = \begin{bmatrix} \vec{\mathbf{c}}_\tau^{\,\mathrm{T}} & \vec{\mathbf{c}}_\rho^{\,\mathrm{T}} & \hat{c}_\kappa \end{bmatrix}^{\mathrm{T}} = \begin{bmatrix} \vec{\mathbf{c}}_{\tau\rho}^{\,\mathrm{T}} & \hat{c}_\kappa \end{bmatrix}^{\mathrm{T}}, \tag{5.61}$$

where $\vec{\mathbf{c}}_{\tau\rho}^{\,\mathrm{T}} = \begin{bmatrix} \vec{\mathbf{c}}_\tau^{\,\mathrm{T}} & \vec{\mathbf{c}}_\rho^{\,\mathrm{T}} \end{bmatrix}^{\mathrm{T}}$ and $\hat{c}_\kappa$ results in the true estimate of κ when all other parameters are correctly estimated. Then $\vec{\mathbf{b}}(\hat{\mathbf{c}}_b)$ from (5.46) can be decomposed as:

$$\begin{aligned} \vec{\mathbf{b}}(\hat{\mathbf{c}}_b) &= \mathbf{B}\mathbf{A}^{\dagger}\mathbf{M}\vec{\mathbf{\Sigma}} + \mathbf{B}\begin{bmatrix} \mathbf{A}_\tau^{\neq} & \mathbf{A}_\rho^{\neq} & \vec{\mathbf{a}}_\kappa^{\neq} \end{bmatrix}\hat{\mathbf{c}}_b \\ &= \vec{\mathbf{b}}_\kappa(\hat{c}_\kappa) + \vec{\mathbf{b}}_{\tau\rho}\left(\vec{\mathbf{c}}_{\tau\rho}\right), \end{aligned} \tag{5.62}$$

with the $\vec{\mathbf{b}}_\kappa(\hat{c}_\kappa)$ and $\vec{\mathbf{b}}_{\tau\rho}\left(\vec{\mathbf{c}}_{\tau\rho}\right)$ vectors defined as

$$\vec{\mathbf{b}}_\kappa(\hat{c}_\kappa) = \mathbf{B}\mathbf{A}^{\dagger}\mathbf{M}\vec{\mathbf{\Sigma}} + \frac{\hat{c}_\kappa}{2\pi}\vec{\mathbf{d}}, \tag{5.63a}$$

$$\vec{\mathbf{b}}_{\tau\rho}\left(\vec{\mathbf{c}}_{\tau\rho}\right) = -\frac{1}{2\pi}\mathbf{Q}_{\tau\rho}\vec{\mathbf{c}}_{\tau\rho}. \tag{5.63b}$$

The above equations can be obtained from (5.62) through the definitions of $\mathbf{A}_{\tau}^{\neq}$, $\mathbf{A}_{\rho}^{\neq}$, and $\vec{\mathbf{a}}_{\kappa}^{\neq}$ in (5.43) and $\mathbf{Q}_{\tau\rho}$ from (5.14b).

The $\vec{\mathbf{c}}_{\tau}$ and $\vec{\mathbf{c}}_{\rho}$ vectors that make up $\vec{\mathbf{c}}_{\tau\rho}$ are associated with the $\mathbf{A}_{\tau}^{\neq}$ and $\mathbf{A}_{\rho}^{\neq}$ vector sets, which were shown in Section 5.4 to relate additional phase offsets of the transmitter and receiver transfer functions to corresponding changes in the $\vec{\mathbf{b}}$ estimate. Since these phase offsets result in identical solutions as each $\vec{\mathbf{c}}_{\tau}$ and $\vec{\mathbf{c}}_{\rho}$ coefficient is increased by an integer multiple of 2π, the "true" vectors, $\hat{\mathbf{c}}_{\tau}$ and $\hat{\mathbf{c}}_{\rho}$, are largely irrelevant. In other words, *any* $\vec{\mathbf{c}}_{\tau\rho}$ vector that results in an all-integer estimate of $\vec{\mathbf{b}}$ is equally valid.

With this in mind, note that for certain structures of $\mathbf{Q}_{\tau\rho}$, bounds can be placed on the $\vec{\mathbf{c}}_{\tau}$ and $\vec{\mathbf{c}}_{\rho}$ element values and still allow for all possible $\vec{\mathbf{b}}_{\tau\rho}\left(\vec{\mathbf{c}}_{\tau\rho}\right)$ values (within a modulo 2π range). For example, if the $\mathbf{Q}_{\mathrm{TR}}$ and $\mathbf{Q}_{\tau\rho}$ matrices have no more than two "1" values per row (which is envisioned for all applications), then each element of the $\vec{\mathbf{b}}_{\tau\rho}\left(\vec{\mathbf{c}}_{\tau\rho}\right)$ vector can be constrained to lie between ±1. These boundaries for $\vec{\mathbf{b}}_{\tau\rho}\left(\vec{\mathbf{c}}_{\tau\rho}\right)$, combined with (5.62), provide a bound for each individual element of $\vec{\mathbf{b}}(\hat{\mathbf{c}}_b)$:

$$\lfloor \vec{\mathbf{b}}_{\kappa}(\hat{c}_{\kappa}) \rfloor \le \vec{\mathbf{b}}(\hat{\mathbf{c}}_b) \le \lceil \vec{\mathbf{b}}_{\kappa}(\hat{c}_{\kappa}) \rceil, \tag{5.64}$$

where $\hat{\mathbf{c}}_b$ and $\hat{c}_{\kappa}$ are defined as in (5.61) and the $\lceil\cdot\rceil$ and $\lfloor\cdot\rfloor$ operations denote element-wise ceiling and floor operations, respectively. Equation (5.64) implies that given the true scalar value $\hat{c}_{\kappa}$, each integer element of $\vec{\mathbf{b}}(\hat{\mathbf{c}}_b)$ must be one of two integer values, either $\lfloor \vec{\mathbf{b}}_{\kappa}(\hat{c}_{\kappa}) \rfloor$ or $\lceil \vec{\mathbf{b}}_{\kappa}(\hat{c}_{\kappa}) \rceil$, resulting in 2^M possible vectors. To determine the appropriate combination of M integer operations, note that (5.63b) requires $\vec{\mathbf{b}}_{\tau\rho}\left(\vec{\mathbf{c}}_{\tau\rho}\right)$ to lie in the column space of $\mathbf{Q}_{\tau\rho}$.

Let c represent a potential value of $\hat{c}_{\kappa}$. The best combination of integer operations, $\hat{\mathbf{h}}$, for a given c is chosen to satisfy:

$$\hat{\mathbf{h}}(c) = \underset{\vec{\mathbf{h}} \in \mathfrak{H}}{\arg\min} \| \mathbf{P}_{\tau\rho}^{\neq} \left(f\left(\vec{\mathbf{b}}_{\kappa}(c), \vec{\mathbf{h}} \right) - \vec{\mathbf{b}}_{\kappa}(c) \right) \|, \tag{5.65}$$

where $\vec{\mathbf{h}}$ is a binary vector contained in $\mathfrak{H}$, the set of all vectors containing only "1" and "0"

elements, and the function $f\left(\vec{\mathbf{b}}, \vec{\mathbf{h}}\right)$ is performed element-wise:

$$f\left(b_i, h_i\right) = \begin{cases} \lfloor b_i \rfloor & \text{if } h_i = 0, \\ \lceil b_i \rceil & \text{if } h_i = 1. \end{cases} \tag{5.66}$$

In (5.65), the $f\left(\vec{\mathbf{b}}_\kappa(c), \vec{\mathbf{h}}\right)$ term is an estimate of the all-integer $\vec{\mathbf{b}}(\hat{\mathbf{c}}_b)$ vector, given a $\hat{c}_\kappa$ estimate, c, and an $\vec{\mathbf{h}}$ vector defining the combination of integer operations. The difference operation, $f\left(\vec{\mathbf{b}}_\kappa(c), \vec{\mathbf{h}}\right) - \vec{\mathbf{b}}_\kappa(c)$, corresponds to the resulting $\vec{\mathbf{b}}_{\tau\rho}\left(\vec{\mathbf{c}}_{\tau\rho}\right)$ estimate from this combination of c and $\vec{\mathbf{h}}$. Finally, the projection operation and norm provide a measure of the portion of the $\vec{\mathbf{b}}_{\tau\rho}\left(\vec{\mathbf{c}}_{\tau\rho}\right)$ estimate that cannot be accommodated by the model since $\vec{\mathbf{b}}_{\tau\rho}\left(\vec{\mathbf{c}}_{\tau\rho}\right)$ must reside in the column space of $\mathbf{Q}_{\tau\rho}$.

The structure of (5.65) can be adapted to find the most appropriate $\hat{c}_\kappa$value:

$$\hat{c}_\kappa = \arg\min_c \|\mathbf{P}^{\mu}_{\tau\rho}\left(f\left(\vec{\mathbf{b}}_\kappa(c), \hat{\mathbf{h}}(c)\right) - \vec{\mathbf{b}}_\kappa(c)\right)\|, \tag{5.67}$$

where $\hat{\mathbf{h}}(c)$ and $f\left(\vec{\mathbf{b}}, \vec{\mathbf{h}}\right)$ are defined as in (5.65) and (5.66), respectively.

Substituting $\vec{\mathbf{b}}_{\tau\rho}\left(\vec{\mathbf{c}}_{\tau\rho}\right) = f\left(\vec{\mathbf{b}}_\kappa(\hat{c}_\kappa), \hat{\mathbf{h}}(\hat{c}_\kappa)\right) - \vec{\mathbf{b}}_\kappa(\hat{c}_\kappa)$ into (5.63b), $\vec{\mathbf{c}}_{\tau\rho}$ is obtained from an estimate of $\hat{c}_\kappa$:

$$\vec{\mathbf{c}}_{\tau\rho} = -2\pi\mathbf{Q}^{\dagger}_{\tau\rho}\left(f\left(\vec{\mathbf{b}}_\kappa(\hat{c}_\kappa), \hat{\mathbf{h}}(\hat{c}_\kappa)\right) - \vec{\mathbf{b}}_\kappa(\hat{c}_\kappa)\right) + \mathbf{Q}^{\neq}_{\tau\rho}\vec{\mathbf{c}}_{\tau\rho}. \tag{5.68}$$

Similar to the case for $\mathbf{A}^{\neq}_{\Re}$ and $\mathbf{A}^{\neq}_{\Im}$ discussed in Section 5.4, the $\mathbf{Q}^{\neq}_{\tau\rho}$ in the above equation represents a null space that describes the phase offset ambiguity between the transmitter and receiver transfer functions. Without any further model constraints, this null space, like the $\mathbf{A}^{\neq}_{\Re}$ and $\mathbf{A}^{\neq}_{\Im}$ subspaces, can be ignored.

Equation (5.67) indicates that for every c value considered in the search for $\hat{c}_\kappa$, an independent $\hat{\mathbf{h}}(\vec{\mathbf{c}})$ must first be found, which requires the comparison of 2^{n_m} potential $\vec{\mathbf{h}}$ vectors. While this one-dimensional search is an improvement over the multidimensional search described in Section 5.5.2, it *is* computationally intensive, particularly since n_m grows exponentially with the number of transducers.

One method to further streamline the nonlinear search is to introduce additional *a priori* information about the *anticipated* values of κ. For example, nominal values for κ can be calculated based on the propagating environment (material, thickness, propagation mode). Based on these nominal values, the search space for (5.67) can be limited to values that result in dispersion estimates that are in the vicinity of the nominal values. Note that although *a priori* information is used at this point, it is not being used to estimate parameters, rather the nominal information selects between parameters that satisfy both the measured data and model constraints.

5.6 Model-Based Parameter Estimation Summary and Discussion

The model-based parameter estimation algorithm is summarized in Table 5.1. This table illustrates that even though the derivation is somewhat complicated, the implementation is straightforward and tractable. The algorithm is built upon the assumption that the system of linear equations in (5.12) accurately reflects the behavior of the recorded signals in $\mathbf{M}$. The algorithm also assumes that sufficient samples are used to ensure that the phase response can be accurately unwrapped. Note that for the phase response to be accurately unwrapped, the frequencies of interest must span a continuous band of spectral content with positive SNR at each discrete frequency.

In addition to the above assumptions, it may be possible to incorporate additional constraints into the model to further constrain the resulting estimates. For example, realistic dispersion relations for the frequencies of interest may be monotonic and bounds may be available for the first or second derivatives of the transmitter and receiver transfer functions. For the purposes considered here, however, all parameters are able to be approximated to a satisfactory degree with the imposed constraints and additional constraints are unnecessary complications.

Table 5.1: Summary of model-based parameter estimation algorithm for characterizing wave propagation in a homogeneous medium.

Problem Setup: The application-specific propagation model is determined and all measurements are described in terms of the model parameters.

- Define $\mathbf{Q}_{\mathrm{T}}$, $\mathbf{Q}_{\mathrm{R}}$, $\mathbf{Q}_{\tau}$, and $\mathbf{Q}_{\rho}$ based on model assumptions.
- Define $\mathbf{M}$, $\vec{\boldsymbol{\sigma}}^2_{\mathrm{m}}$ and $\vec{\mathbf{d}}_{\mathrm{m}}$ with measured data.
  - Limit frequencies of interest to a continuous spectrum.
  - Positive SNR in each FFT bin.
  - Unwrap phase responses in $\mathbf{M}_{\Im}$.

Distance Vector Estimation: *A priori* distance measurements are projected onto data- and model-driven unit-vectors to obtain an estimate of the actual distance vector.

- Compute $\vec{\mathbf{v}}^{\measuredangle}_{\mathrm{TR}}$ as the eigenvector corresponding to the largest eigenvalue of $\mathbf{P}^{\measuredangle}_{\mathrm{TR}}\mathbf{M}_{\Im}\mathbf{P}_{\Delta}\mathbf{M}^{\mathrm{T}}_{\Im}\mathbf{P}^{\measuredangle}_{\mathrm{TR}}$ as per (5.37).
- Use (5.40) to compute coefficients: $\begin{bmatrix} d_{\measuredangle} \\ \vec{\mathbf{d}}_{\shortparallel} \end{bmatrix} = \begin{bmatrix} \vec{\mathbf{v}}^{\measuredangle}_{\mathrm{TR}} & \mathbf{Q}^{\shortparallel}_{\mathrm{TR}} \end{bmatrix}^{\mathrm{T}} \vec{\mathbf{d}}_{\mathrm{m}}$.
- Estimate distance vector $\vec{\mathbf{d}} = d_{\measuredangle}\vec{\mathbf{v}}^{\measuredangle}_{\mathrm{TR}} + \mathbf{Q}^{\shortparallel}_{\mathrm{TR}}\vec{\mathbf{d}}_{\shortparallel}$ as per (5.39).
- Define $\mathbf{A}$ with $\vec{\mathbf{d}}$ estimate as shown in (5.13a).

Nonlinear Search: The null-space coefficients $\vec{\mathbf{c}}_{\tau}$, $\vec{\mathbf{c}}_{\rho}$, and $\hat{c}_{\kappa}$ are found to augment the linear solution.

- Estimate optimal weighting coefficients, $\vec{\boldsymbol{\Sigma}}^{\bullet}$, as in (5.59).
- Search for $\hat{c}_{\kappa} = \arg\min_{c} \| \mathbf{P}^{\measuredangle}_{\tau\rho} \left(f\left(\vec{\mathbf{b}}_{\kappa}(c), \hat{\mathbf{h}}(c)\right) - \vec{\mathbf{b}}_{\kappa}(c) \right) \|$ as in (5.67), where $\hat{\mathbf{h}}(c)$ and $f(\cdot)$ are defined in (5.65) and (5.66).
- Compute $\vec{\mathbf{c}}_{\tau\rho} = -2\pi\mathbf{Q}^{\dagger}_{\tau\rho}\left(f\left(\vec{\mathbf{b}}_{\kappa}(\hat{c}_{\kappa}), \hat{\mathbf{h}}(\hat{c}_{\kappa})\right) - \vec{\mathbf{b}}_{\kappa}(\hat{c}_{\kappa})\right)$ from (5.68).

Final Solution: Combine nonlinear search results with least-squares solution to obtain final estimate of $\mathbf{Z}$.

- Calculate $\mathbf{Z} = \mathbf{A}^{\dagger}\mathbf{M} + \begin{bmatrix} \mathbf{A}^{\neq}_{\tau} & \mathbf{A}^{\neq}_{\rho} & \vec{\mathbf{a}}^{\neq}_{\kappa} \end{bmatrix} \begin{bmatrix} \vec{\mathbf{c}}_{\tau} \\ \vec{\mathbf{c}}_{\rho} \\ \hat{c}_{\kappa} \end{bmatrix} \vec{\mathbf{1}}^{\mathrm{T}}_{w}$ as in (5.41).

5.7 Experimental Validation

The model-based parameter estimation technique for wave propagation in a homogeneous medium has been applied to two separate experimental datasets: (1) guided waves excited by a single transmitter and recorded by multiple identical receivers at various distances from the transmitter, and (2) guided waves propagating between sensor pairs of a distributed array composed of six PZT transducers, each with independent transmit and receive transfer functions. Although the two examples presented here are based on the S_0 and A_0 guided wave modes, it is important to note that the algorithm is applicable to any wave-based application for which the analyzed signals behave according to the assumed propagation model. This section describes the experimental setup, model assumptions, and assumption-specific algorithmic details, and then presents parameter estimation results.

Algorithmic performance is a challenging concept when working with experimental data since the estimated parameters cannot be compared to "true" parameter values. The concept of "model fit" will be used here, which entails substituting the estimated parameters into the assumed model and comparing the resulting signals with measured data. This technique provides a mechanism to gauge how well the assumed model and estimated parameters are able to describe the measured data. Presumably, if the algorithm is able to accurately describe the measured signals, then the parameters are likely to be accurately estimated. This assumption has been found to be true to a large degree with one exception – in many cases multiple dispersion curve offsets, κ, can be used to describe the data equally well.

5.7.1 Experimental Setup

Figure 5.3 illustrates the experimental setup for the first multi-signal scenario considered here. A single PZT transducer excites the fundamental symmetric, S_0, and anti-symmetric, A_0, modes of a $1524 \times 2438 \times 3.18$ mm plate of 6061 aluminum, which is

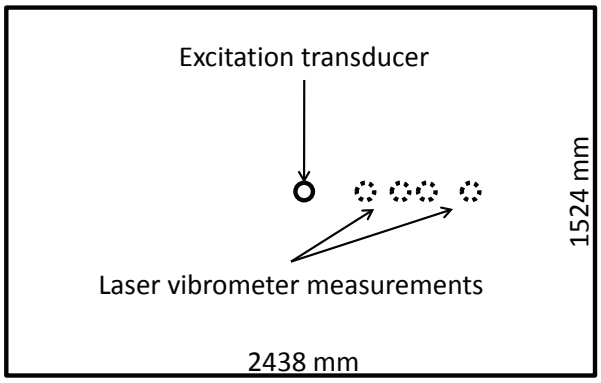

Figure 5.3: Experimental setup for laser-vibrometer data. Guided waves are excited by a single transmitter and recorded at multiple distances with a scanning laser vibrometer.

assumed to be isotropic and homogeneous. Only two modes are excited because the frequency range of the excitation signal is below the cutoff frequency of higher-order modes [124]. The signals are recorded by a scanning laser vibrometer at distances of 545 mm, 606 mm, 626 mm, and 687 mm from the transmitter along a single radial line; therefore $\vec{\mathbf{d}}_m = [\ 545 \quad 606 \quad 626 \quad 687\ ]^T$. The measurement distances and plate size were specifically chosen to allow the direct arrival of each mode to be isolated in the time domain without overlap with the other mode or reflections from either mode, which allows each mode to be handled independently by the approach proposed here. Since 200 waveforms were averaged to produce each measurement, the noise-floor for each laser vibrometer recording was more than 60 dB below the power of the largest frequency component. As such, the $\vec{\sigma}_m^2$ vector elements, for both modes, were set to 0.001 times the power of the largest frequency component in each respective signal.

The second set of experimental data corresponds to the experimental setup described in Chapter III. The measured distance vector for the second experimental dataset, sorted for readability and expressed in mm, was obtained by measuring the physical distance from transducer to transducer for each transmitter-receiver pair:

$$\begin{aligned}\vec{\mathbf{d}}_m = [&236 \quad 254 \quad 264 \quad 286 \quad 321 \quad 363 \quad 379 \quad \ldots \\ &410 \quad 455 \quad 490 \quad 523 \quad 538 \quad 581 \quad 609 \quad 667]^T.\end{aligned} \tag{5.69}$$

For this second dataset, the signals were oversampled and thus occupy a very narrow range in the frequency domain. Therefore, the electronic noise levels, $\vec{\sigma}_{\mathrm{m}}^2$, were estimated by computing the power spectrum of each signal and then selecting the median value. The resulting $\vec{\sigma}_{\mathrm{m}}^2$ vector is:

$$\begin{aligned}\vec{\sigma}_{\mathrm{m}}^2 = \; & [0.017 \quad 0.018 \quad 0.013 \quad 0.005 \quad 0.003 \quad 0.005 \quad 0.001 \quad \ldots \\ & 0.004 \quad 0.004 \quad 0.005 \quad 0.003 \quad 0.003 \quad 0.002 \quad 0.003 \quad 0.001]^{\mathrm{T}},\end{aligned} \tag{5.70}$$

where each element of $\vec{\sigma}_{\mathrm{m}}^2$ above corresponds to the propagation distance in (5.69). Note that the noise floor varies slightly between transducer pairs and is not dependent on propagation distance. Although the transducers do excite both S_0 and A_0 modes, the S_0 mode is sufficiently dominant to treat the recorded signals as single-mode. All boundary reflections were removed from the recorded waveforms by windowing the direct arrivals.

Signal processing was performed with MATLAB (The Mathworks, Natick, MA) running on a Hewlett-Packard laptop (Hewlett-Packard Co., Palo Alto, CA) with an Intel Core2 Duo CPU (Intel Corp., Santa Clara, CA) operating at 2.26 GHz with 4 GB of RAM and running Windows Vista Home Premium (Microsoft Corp., Redmond, WA). The model-based parameter estimation algorithm was configured to evaluate 1000 potential $\hat{c}_\kappa$ values for each algorithm execution, which required less than 1 second to complete for the first dataset (four received signals). In contrast, the second dataset (15 received signals) required approximately 80 seconds to complete. For both cases, the modified non-linear search described in Section 5.5.3 consumed over 90% of the computation time.

5.7.2 Common Transfer Functions

The first set of model assumptions to be discussed corresponds to the case where the transmit and receive transfer functions are assumed to be identical for all recorded signals, i.e., all signals share a common transmitter and receiver transfer function. Note that because all transmitter and receiver transfer functions are identical, the transmitter and receiver transfer functions cannot be distinguished from one another. As such, the $\mathbf{Q}_{\mathrm{R}}$ and $\mathbf{Q}_\rho$ matrices

are null and $\mathbf{Q}_{\mathrm{T}} = \mathbf{Q}_{\tau} = \mathbf{Q}_{\mathrm{TR}} = \mathbf{Q}_{\tau\rho} = \vec{\mathbf{1}}_m$. Under these assumptions, the structures for $\mathbf{A}$ and $\mathbf{Z}$ are:

$$\mathbf{A} = \begin{bmatrix} \vec{\mathbf{1}}_m & \vec{\mathbf{0}}_m & \vec{\mathbf{0}}_m & -\vec{\mathbf{d}}^{\vee} & \vec{\mathbf{0}}_m & \vec{\mathbf{0}}_m & \mathbf{0} \\ \vec{\mathbf{0}}_m & \vec{\mathbf{1}}_m & \vec{\mathbf{1}}_m & \vec{\mathbf{0}}_m & -\vec{\mathbf{d}} & -\vec{\mathbf{d}} & 2\pi\mathbf{I}_s \\ \vec{\mathbf{0}}_m & \vec{\mathbf{1}}_m & \vec{\mathbf{0}}_m & \vec{\mathbf{0}}_m & -\vec{\mathbf{d}} & \vec{\mathbf{0}}_m & \mathbf{0} \end{bmatrix}, \mathbf{Z} = \begin{bmatrix} \mathbf{T}_{\Re} + \mathbf{R}_{\Re} \\ \mathbf{T}_{\Delta} + \mathbf{R}_{\Delta} \\ (\vec{\tau} + \vec{\rho})\,\vec{\mathbf{1}}_w^{\mathrm{T}} \\ \vec{\mathbf{p}}^{\,\mathrm{T}} \\ \vec{\mathbf{k}}^{\mathrm{T}} \\ \kappa\vec{\mathbf{1}}_w^{\mathrm{T}} \\ \vec{\mathbf{b}}\vec{\mathbf{1}}_w^{\mathrm{T}} \end{bmatrix}. \tag{5.71}$$

Since the $\mathbf{Q}_{\mathrm{TR}}^{\shortparallel}$ matrix is a single vector with identical-valued elements, the final estimate of $\vec{\mathbf{d}}$ is obtained by projecting $\vec{\mathbf{d}}_{\mathrm{m}}$ onto two unit vectors, $\vec{\mathbf{v}}_{\mathrm{TR}}^{\nu}$ and $\mathbf{Q}_{\mathrm{TR}}^{\shortparallel}$. Note that for the first set of experimental data, two modes are present. Since the propagation distances are identical for both modes, the $\mathbf{M}_{\Im}$ matrix used in (5.38) is composed of an SNR-weighted sum of the $\mathbf{M}_{\Im}$ for each mode, which ensures that all available data are used to estimate $\vec{\mathbf{d}}$.

Analysis of $\mathbf{A}^{\neq}$ reveals that the entire null space of $\mathbf{A}$ is spanned by two vectors, $\mathbf{A}_{\tau}^{\neq}$ and $\vec{\mathbf{a}}_{\kappa}^{\neq}$. Since $\mathbf{Q}_{\mathrm{TR}} = \vec{\mathbf{1}}_m$, the $\mathbf{Q}_{\mathrm{TR}}^{\neq}$, $\mathbf{A}_{\Re}^{\neq}$ and $\mathbf{A}_{\Im}^{\neq}$ matrices are null. Similarly, since $\mathbf{Q}_{\tau} = \vec{\mathbf{1}}_m$ and $\mathbf{Q}_{\rho}$ is null, $\mathbf{A}_{\tau}^{\neq}$ is a single vector and $\mathbf{A}_{\rho}^{\neq}$ is null.

Figure 5.4 shows model fit results that reflect the ability of this model to fit the first set of experimental data. The *x*-axis of the waterfall plot corresponds to time, while the *y*-axis reflects propagation distance. Each of the four measured time domain signals is independently scaled for presentation purposes and displayed in Figure 5.4 with a vertical offset equal to the measured propagation distance. The estimated signals are generated by substituting the estimated parameters into the propagation model and are presented in a similar fashion, with signal scaling identical to the scaling used for the corresponding measured signals and vertical offset equal to the estimated distances. Errors in distance estimates are manifested as vertical separations between the measured and estimated signals, errors in propagation loss estimates result in amplitude discrepancies, and errors in dispersion or

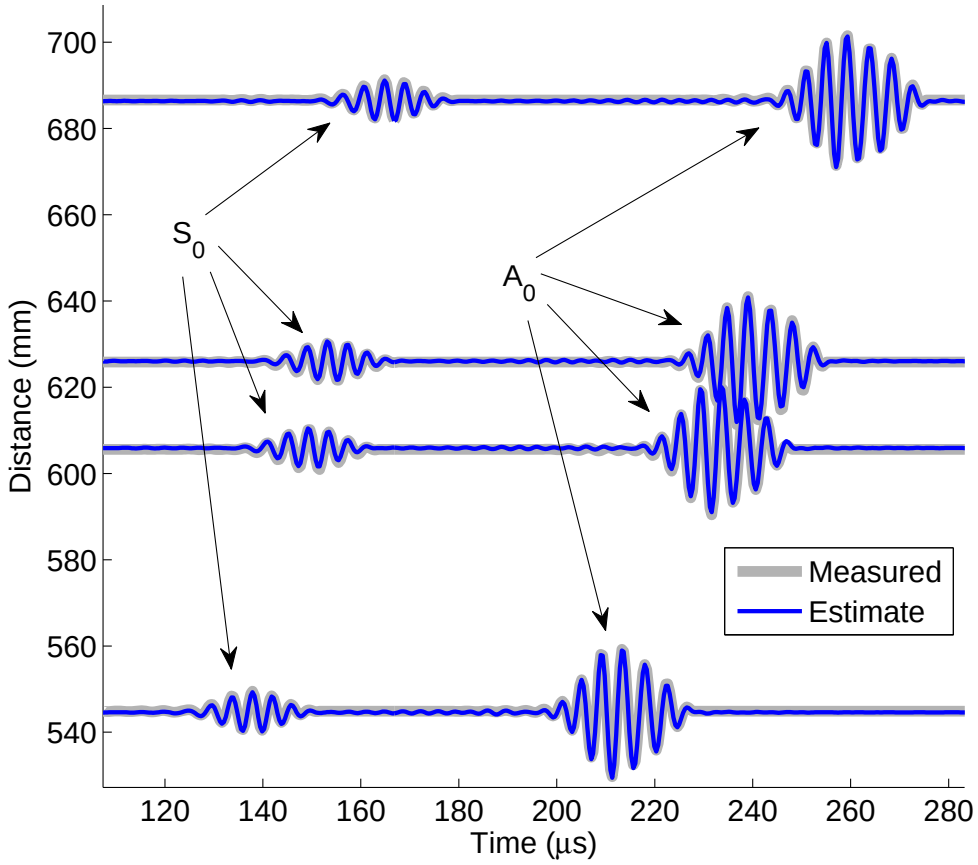

Figure 5.4: Model fit results for experimental data under assumptions that all transmitter and receiver transfer functions are identical. Guided waves are excited by a single transmitter and recorded at multiple distances with a scanning laser vibrometer.

transfer function estimates impact the signal shapes and amplitudes. Figure 5.4 indicates excellent model fit between the estimated model parameters and measured data. Since the same PZT transducer and laser vibrometer were used for all recorded signals, the assumption about identical transmitter and receiver transfer functions is valid. Even if the PZT transducer is not isotropic, the fact that the signals were recorded along a single radial line from the transmitter ensures that the transmitter transfer function is identical for all of the signals.

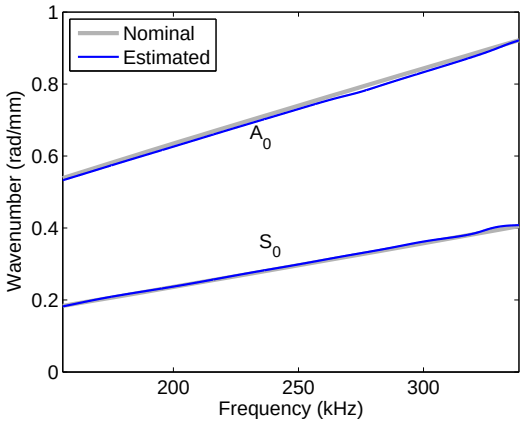

Figure 5.5: Comparison of wavenumber *vs.* frequency dispersion estimates for experimental data under assumptions that all transmitter and receiver transfer functions are identical. Guided waves are excited by a single transmitter and recorded at multiple distances with a scanning laser vibrometer.

Figure 5.5 compares the estimated dispersion curves for each mode to nominal dispersion curves for a 3.18 mm thick aluminum plate. Although a perfect match is not expected because of temperature, pressure, and thickness discrepancies, the estimates closely match the nominal values. Note that with only four received signals, the error surface associated with (5.67) has an infinite number of periodic local minima. The appropriate $\hat{c}_\kappa$ was selected by bounding the nonlinear searches to produce a S_0 wavenumber between 0 and 0.402 rad/mm and an A_0 wavenumber between 0.402 and 0.817 rad/mm for the lowest frequency considered (156 kHz).

In contrast, Figure 5.6 represents the model fit for the same common transfer function assumptions but when applied to the second set of experimental data, which uses 15 different pairs of six separate transducers. Note that since the number of recorded signals is different for the two datasets, (5.71) was updated accordingly, which is the only change between the handling of the two datasets. Although all of the transducers are of the same size and shape and similarly bonded to the plate, algorithmic performance is somewhat degraded in comparison to Figure 5.4. In Figure 5.6, almost all signal estimates exhibit visible phase offsets from the measured signals.

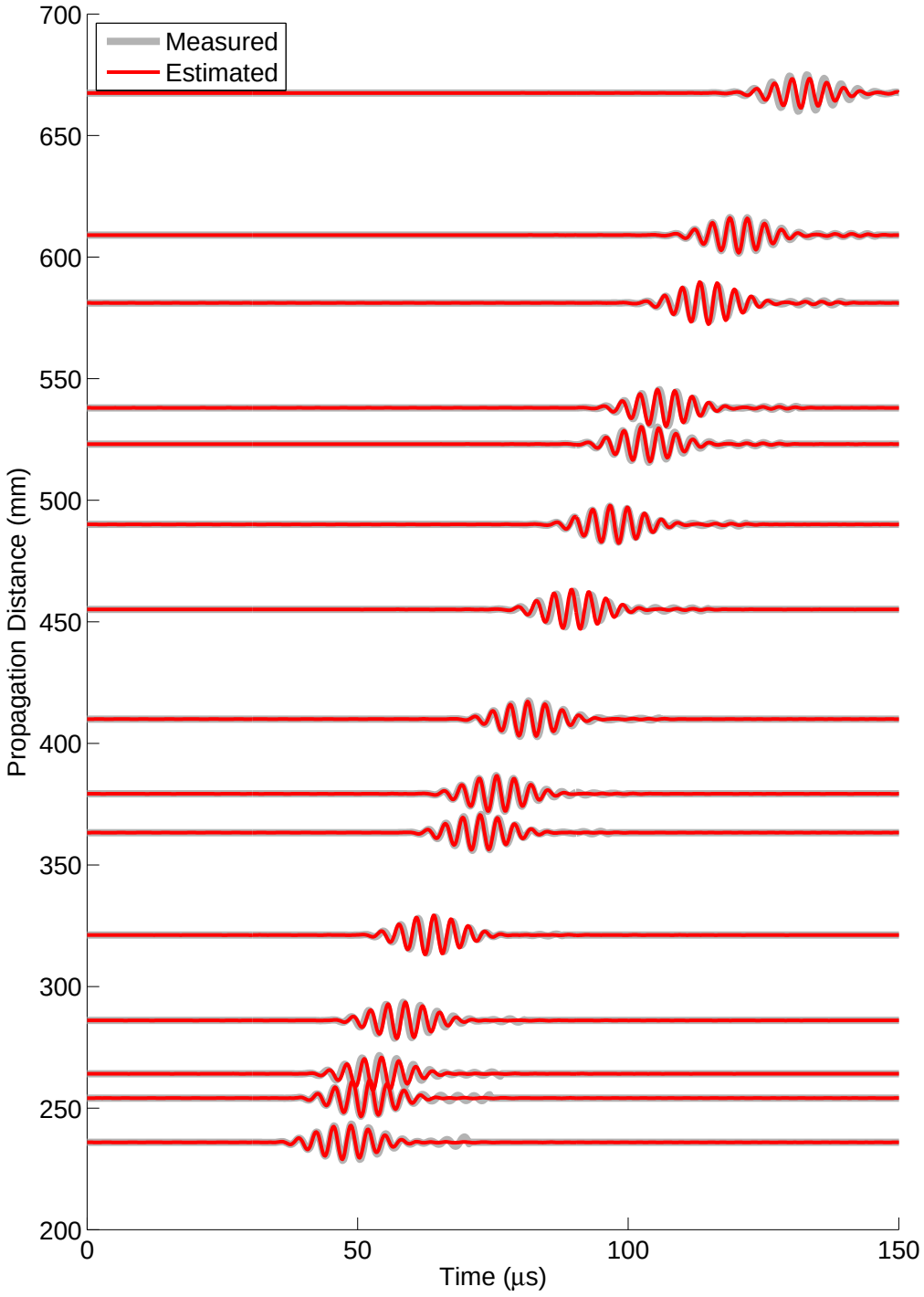

Figure 5.6: Model fit results for experimental data under assumptions that all transmitter and receiver transfer functions are identical. Guided waves were generated with 15 unique transmitter-receiver pairs from a sparse, distributed array of six permanently attached transducers.

5.7.3 Independent Transfer Functions

In contrast to Section 5.7.2, the assumed propagation model is expanded to accommodate transducer-specific transmit and receive transfer functions. Recall from Chapter III that a round-robin data acquisition scheme was used to collect data. Therefore, for the second dataset, Transducer 1 is never used to record and Transducer 6 is never used to transmit. As such, matrices are defined so that the algorithm estimates five transmitter transfer functions (1-5) and five receiver transfer functions, (2-6), and their respective phase offsets. The $\mathbf{Q}_{\mathrm{T}}$, $\mathbf{Q}_{\mathrm{R}}$, $\mathbf{Q}_{\tau}$, and $\mathbf{Q}_{\rho}$ matrices are thus defined as follows:

$$\mathbf{Q}_{\mathrm{T}} = \mathbf{Q}_{\tau} = \begin{bmatrix} 1 & 1 & 1 & 1 & 1 & 0 & 0 & 0 & 0 & 0 & 0 & 0 & 0 & 0 & 0 \\ 0 & 0 & 0 & 0 & 0 & 1 & 1 & 1 & 1 & 0 & 0 & 0 & 0 & 0 & 0 \\ 0 & 0 & 0 & 0 & 0 & 0 & 0 & 0 & 0 & 1 & 1 & 1 & 0 & 0 & 0 \\ 0 & 0 & 0 & 0 & 0 & 0 & 0 & 0 & 0 & 0 & 0 & 0 & 1 & 1 & 0 \\ 0 & 0 & 0 & 0 & 0 & 0 & 0 & 0 & 0 & 0 & 0 & 0 & 0 & 0 & 1 \end{bmatrix}^{\mathrm{T}} \tag{5.72a}$$

$$\mathbf{Q}_{\mathrm{R}} = \mathbf{Q}_{\rho} = \begin{bmatrix} 1 & 0 & 0 & 0 & 0 & 0 & 0 & 0 & 0 & 0 & 0 & 0 & 0 & 0 & 0 \\ 0 & 1 & 0 & 0 & 0 & 1 & 0 & 0 & 0 & 0 & 0 & 0 & 0 & 0 & 0 \\ 0 & 0 & 1 & 0 & 0 & 0 & 1 & 0 & 0 & 1 & 0 & 0 & 0 & 0 & 0 \\ 0 & 0 & 0 & 1 & 0 & 0 & 0 & 1 & 0 & 0 & 1 & 0 & 1 & 0 & 0 \\ 0 & 0 & 0 & 0 & 1 & 0 & 0 & 0 & 1 & 0 & 0 & 1 & 0 & 1 & 1 \end{bmatrix}^{\mathrm{T}}. \tag{5.72b}$$

Unlike the prior case, the $\mathbf{Q}_{\mathrm{T}}$ and $\mathbf{Q}_{\mathrm{R}}$ matrices defined above have a column-space spanning nine dimensions ($n_{\mathrm{TR}}^{\shortparallel} = 9$), which means that the projection matrix $\mathbf{P}_{\mathrm{TR}}^{\nprec}$ projects onto a six-dimensional space ($n_{\mathrm{TR}}^{\nprec} = 15 - n_{\mathrm{TR}}^{\shortparallel} = 6$) and the $\mathbf{Q}_{\mathrm{TR}}^{\shortparallel}$ matrix is composed of nine orthonormal vectors. Therefore, the final estimate of $\vec{\mathbf{d}}$ is obtained by projecting $\vec{\mathbf{d}}_{\mathrm{m}}$ onto a ten-dimensional space (one dimension for $\vec{\mathbf{v}}_{\mathrm{TR}}^{\nprec}$ and nine dimensions for $\mathbf{Q}_{\mathrm{TR}}^{\shortparallel}$).

Figure 5.7 depicts the $\|\mathbf{P}_{\tau\rho}^{\nprec}\left(f\left(\vec{\mathbf{b}}_{\kappa}(c), \hat{\mathbf{h}}(c)\right) - \vec{\mathbf{b}}_{\kappa}(c)\right)\|$ values from (5.67) for both sets of model assumptions. Notice that the more accurate model results in lower error values in general, which is due primarily to the dimensionality of $\mathbf{Q}_{\tau\rho}^{\nprec}$.

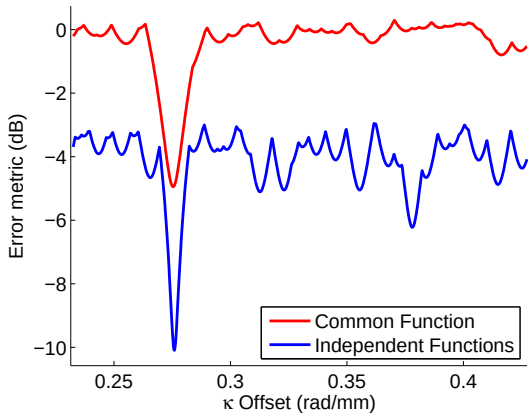

Figure 5.7: Comparison of error metric values for the nonlinear search using experimental data from a sparse, distributed array of six transducers. Note that the error is plotted as a function of the $k(\omega)$ estimate for the lowest frequency at which $k(\omega)$ estimation is performed (105 kHz). The overall error is lower and minima more pronounced for the case of transducer-specific transfer functions.

Figure 5.8 is analogous to Figure 5.6 for the previous set of model assumptions. However, Figure 5.8 reflects a significantly improved model fit. The additional degrees of freedom in the $\vec{\mathbf{d}}$ estimate (ten degrees of freedom *vs.* two for the common transducer model) allow a much better estimate of the propagation distances. All measured signals appear to be well-approximated, both in shape and amplitude, which indicates accurate estimates of both the independent transfer functions as well as the dispersion curve. The small vertical offsets are attributed to inaccuracies in the distance measurements.

The composite transmitter-receiver transfer functions for each recorded waveform are shown in Figure 5.9. The thick line in the foreground corresponds to the single estimate of the common transmitter-receiver transfer function from the previous section. The 15 thin lines in the background correspond to the 15 independent transmitter-receiver transfer function estimates (i.e. the inverse Fourier transforms of $T_1(\omega)R_2(\omega)$, $T_1(\omega)R_3(\omega)$, $\cdots$, $T_5(\omega)R_6(\omega)$). This figure illustrates that the 15 transducer pairs are best modeled by slightly different transfer functions, which is the cause of the minor phase error visible in Figure 5.6.

Finally, Figure 5.10 depicts the estimated dispersion curves for the two sets of assumptions. Note that for this particular case, the dispersion estimates are in very close agreement. This is not surprising, particularly since the independent transfer function estimates are so similar to one another. Had the transducer functions exhibited larger discrepancies, the model mismatch would likely manifest itself as error in the wavenumber estimate. The difference between the estimated and nominal dispersion relations is likely due to the realities of the experimental setup (plate thickness, temperature, humidity, pressure, etc.).

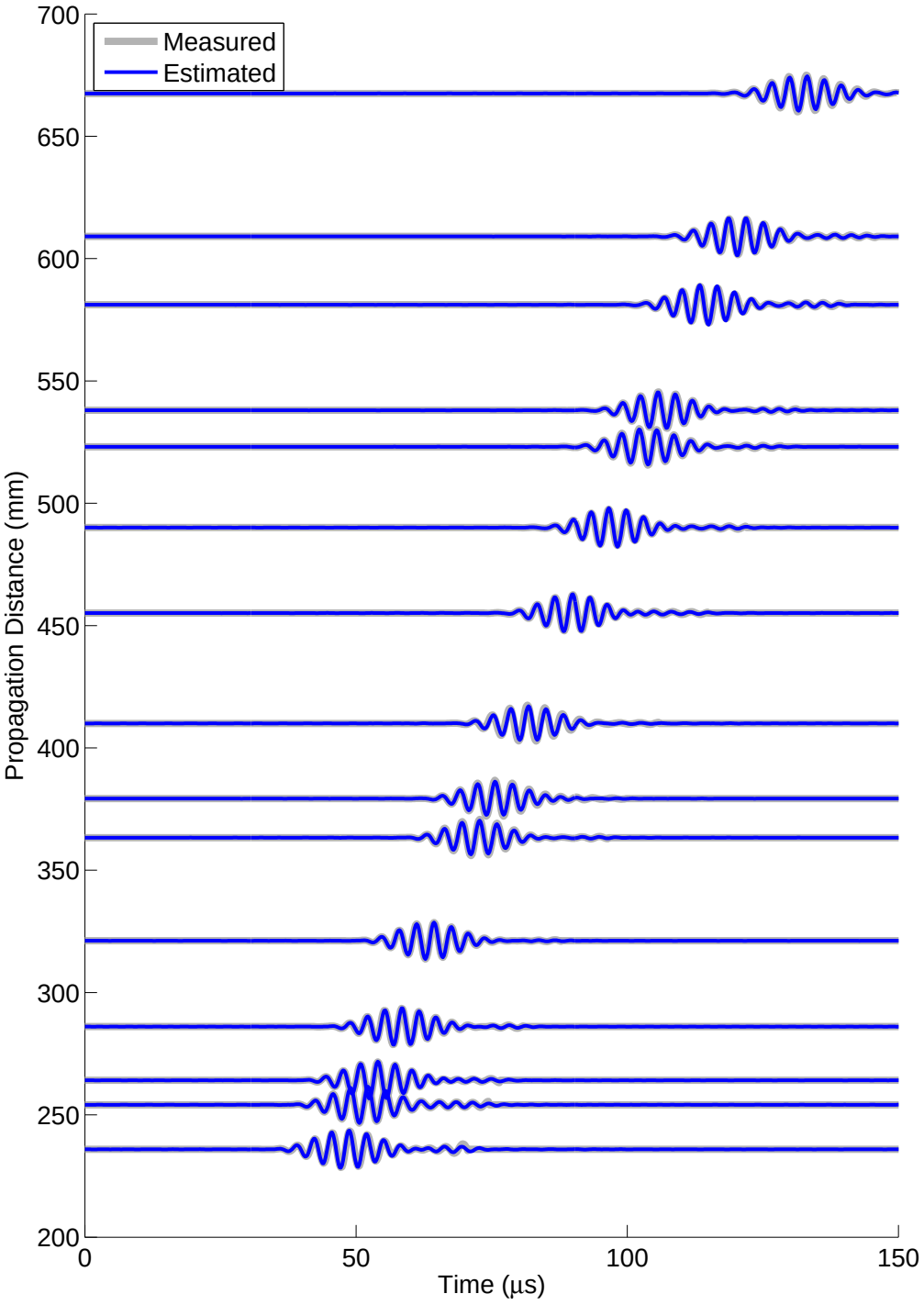

Figure 5.8: Model fit results for experimental data under assumptions that transmitter and receiver transfer functions are transducer-specific. Guided waves were generated with 15 unique transmitter-receiver pairs from a sparse, distributed array of six permanently attached transducers.

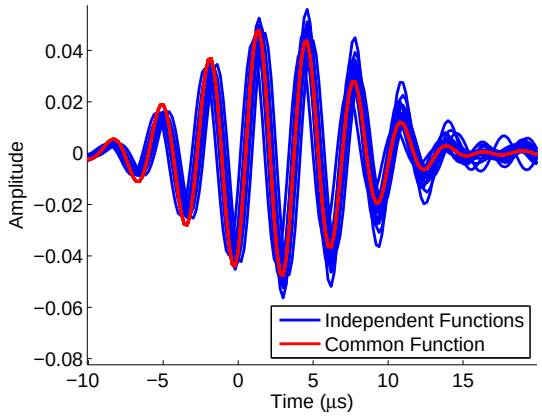

Figure 5.9: Comparison of composite transmitter-receiver transfer functions estimated using experimental data from a sparse, distributed array of six transducers. For the common transfer function case, a single transmitted signal is assumed (thick line). When independent transfer functions are modeled, each composite signal is associated with a unique transmitter-receiver combination (thin lines).

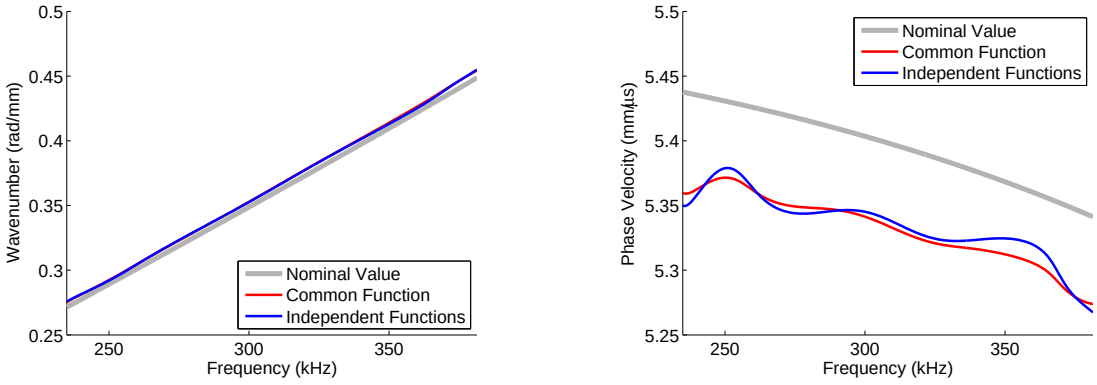

Figure 5.10: Comparison of (a) wavenumber *vs.* frequency and (b) phase velocity estimates for experimental data from a sparse, distributed array of six transducers.

5.8 Summary

This chapter has presented a model-based approach that estimates wave propagation parameters from a set of recorded signals. A general wave propagation model is presented and a linear system of equations is constructed. Circularly-symmetric complex noise is analyzed in the context of the associated phase and log-magnitude noise distributions, which are both shown to have effectively zero mean and variances proportional to the square of the complex SNR for SNR values greater than 10 dB. The algorithm obtains a closed-form estimate of the propagation distances by projecting *a priori* measured distances onto two or more orthonormal vectors based on the propagation model and measured data. The remaining model parameters are obtained by first solving a linear system of equations and then augmenting the linear solution with a nonlinear search to incorporate integer-based model constraints. The nonlinear search is performed with a streamlined single-dimensional search. Algorithmic performance is demonstrated with two sets of experimental data using guided waves that correspond to two different sets of model assumptions, demonstrating that the proposed generalized framework can be readily adapted to meet individual application needs.

The primary contribution of this chapter is a model-based algorithm for characterizing wave propagation in a homogeneous medium with minimal *a priori* information. This approach allows systems incorporating acoustic, electromagnetic, or elastic waves to characterize dispersion curves, propagation loss, propagation distances, as well as transmitter and receiver transfer functions *in situ* at the time of test, thereby avoiding potentially erroneous *a priori* assumptions.

From the perspective of guided wave imaging, the MBPE algorithm presents a method to adaptively estimate the transducer transfer functions, dispersion relations, propagation loss, and transducer spacings of a distributed array, *in situ*, without the need for any additional measurements or equipment. This information can then be used to further improve guided wave imaging performance through parameter compensation techniques discussed

in Chapter VI.

CHAPTER VI

PARAMETER COMPENSATION

Chapter IV introduced minimum variance imaging, which exhibits significant improvements in imaging performance when phase information is used in the imaging algorithm. The trade-off, however, is that the use of phase information makes the algorithm more sensitive to errors in *a priori* assumptions about the phase of the back-propagated signals. These errors come from several sources, including differences in transducer transfer functions, scattering fields, and dispersion. The poor imaging performance demonstrated in Figure 4.9 and Figure 4.10 highlights the need to compensate for these sources of error.

Chapter V presented the model-based parameter estimation (MBPE) method to characterize the propagation environment *in situ* at the time of test. The algorithm is capable of simultaneously estimating propagation parameters from a sparse, distributed array of ultrasonic transducers, such as the dispersion relations, transducer transfer functions, propagation distances, and propagation loss.

This chapter investigates methods for integrating the adaptive parameter estimates from MBPE into the guided wave imaging process. Section 6.1 introduces the concept of the ω–k mapping algorithm, which can be used to perform dispersion compensation *efficiently*, in contrast to the frequency domain back-propagation algorithm discussed in Chapter III. Section 6.2 then uses the ω–k mapping algorithm to improve imaging performance by compensating the *differenced* signals for the transducer transfer functions and dispersion. Both nominal and MBPE parameter estimates are used to experimentally demonstrate the benefits of *in situ* parameter estimation. Finally, Section 6.3 discusses the benefits and challenges of compensating for parameters *prior to* baseline subtraction.

6.1 Frequency-wavenumber (ω–k) mapping

The ω–k mapping algorithm can be described as a conversion from the time/frequency domains to the distance/wavenumber domains. The algorithm was originally proposed by Wilcox [85]. To begin, recall from (3.3) the LTI system model for a guided wave after propagating a distance d in a *lossless* media can be represented in the time domain as:

$$\begin{aligned} m(t) &= \int_{-\infty}^{+\infty} M(\omega)\, \mathrm{e}^{j\omega t} d\omega \\ &= \int_{-\infty}^{+\infty} X(\omega)\, \mathrm{e}^{-j(k(\omega)d-\omega t)} d\omega. \end{aligned} \tag{6.1}$$

The above equation can be considered as a spatio-temporal solution to the 1-D wave equation, evaluated at $x = 0$. The more general solution, for any propagation distance, x, is

$$m(x,t) = \int_{-\infty}^{+\infty} X(\omega)\, \mathrm{e}^{-jk(\omega)d} \mathrm{e}^{j(k(\omega)x+\omega t)} d\omega, \tag{6.2}$$

where the positive x-direction has been chosen to be *opposite* the direction of propagation. Note that for time $t = 0$, the above equation becomes:

$$m(x) = \int_{-\infty}^{+\infty} X(\omega)\, \mathrm{e}^{jk(\omega)(x-d)} d\omega. \tag{6.3}$$

Recall the following well known relationships for dispersive materials from (3.1) and (3.2):

$$\omega = c_p(\omega)\, k(\omega), \tag{6.4a}$$

$$d\omega = c_g(\omega)\, dk, \tag{6.4b}$$

where $c_p(\omega)$ and $c_g(\omega)$ are the phase and group velocity, respectively, expressed as functions of radian frequency. Also note that if the wavenumber-frequency relationship, $k(\omega)$, is monotonically increasing, it can be expressed alternatively as $\omega(k)$, since there is a unique one-to-one relationship. Equation (6.2) can be rewritten by first substituting $c_g(\omega)\, dk$ for $d\omega$,

$$m(x) = \int_{-\infty}^{+\infty} X(\omega)\, c_g(\omega)\, \mathrm{e}^{jk(\omega)(x-d)} dk, \tag{6.5}$$

and then expressing ω as a function of k,

$$m(x) = \int_{-\infty}^{+\infty} X(k)\, e^{jk(x-d)} dk, \tag{6.6}$$

where $k(\omega(k)) = k$ and $X(k) = X(\omega(k))\, c_g(\omega(k))$. The above equation indicates that the inverse Fourier transform of $X(k)$, which is a signal in the *distance domain*, will contain a *dispersion-free* wavepacket at d. Note that the dispersion-free wavepacket is *not* identical to the original wavepacket, $x(t)$, since the frequency domain signal was mapped into the wavenumber domain with $\omega(k)$ and multiplied by $c_g(\omega(k))$. In practice, the dispersion-free wavepacket appears very similar to the dispersion-free time domain wavepacket since the ω–k mapping is *nearly* linear (see Figure 3.4).

Another important point is that the ω–k mapping shown here can be applied to the entire $M(\omega)$ signal without any *a priori* knowledge of the d values associated with each wavepacket. Summarizing (6.1)-(6.6), the ω–k mapping algorithm can be performed as:

$$m(x) = \int_{-\infty}^{+\infty} M(\omega(k))\, c_g(\omega(k))\, e^{jkx} dk, \tag{6.7}$$

which only requires a Fourier transform of the measured signals, knowledge of the dispersion relations, $k(\omega)$ and $c_g(\omega)$, resampling of $M(\omega)$ and $c_g(\omega)$ at regularly spaced k, and an inverse Fourier transform operation.

Figure 6.1 demonstrates the dramatic impact that dispersion compensation can have on dispersive signals. For demonstration purposes, the excitation signal was chosen to be a single-cycle, Hamming-windowed, 300 kHz oscillation, which significantly increases the bandwidth of the signal. The increased bandwidth translates to a larger range of propagation velocities, and therefore the effects of dispersion are similarly increased. The simulated signal contains four echoes, corresponding to propagation distances of 100, 200, 550, 575, and 600 mm. Note that in Figure 6.1a the individual arrival times have been obscured by signal spreading and interference between signals. After compensating for dispersion, however, the distance domain signals clearly depict each of the five arrivals at the corresponding distance.

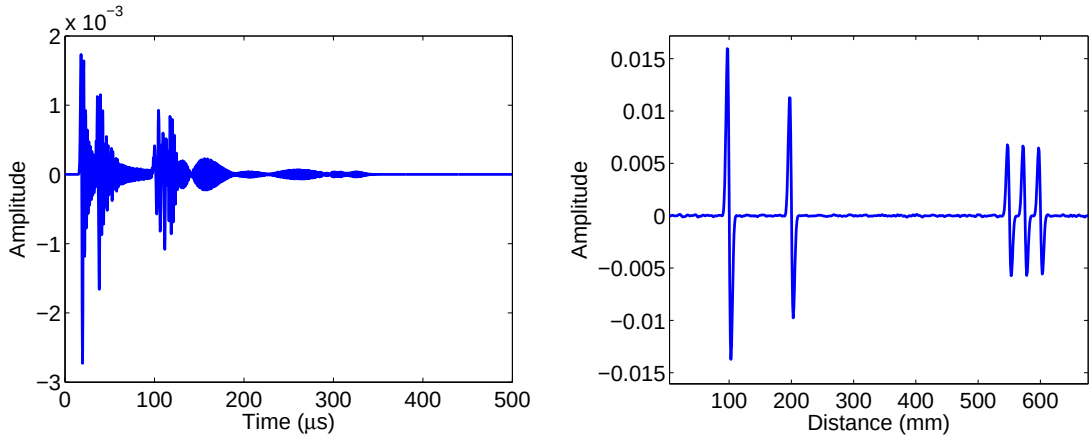

Figure 6.1: Demonstration of ω–k mapping algorithm with simulated data for a single-cycle Hamming-windowed sinusoid with center frequency of 300 kHz. (a) Time domain signals after propagating 100, 200, 550, 575, and 600 mm. (b) Corresponding dispersion compensated distance domain signals.

This approach to dispersion compensation has a distinct advantage over the frequency domain back-propagation algorithm introduced in Chapter II in that an entire guided wave image can be generated by performing the ω–k algorithm *once* per measured signal (as opposed to once per measured signal *per pixel*). This represents a *dramatic* reduction in computational complexity, and is therefore adopted for all dispersion compensated guided wave images throughout this chapter.

6.2 Parameter Compensation after Baseline Subtraction

Recall from Chapter IV, that when analytic signals (with phase information) were used within the guided wave imaging algorithms, imaging performance was severely degraded. This section demonstrates the progression of performance improvements obtained by (1) compensating for dispersion through the ω–k mapping algorithm with nominal wavenumbers, (2) performing the mapping algorithm with MBPE estimates of the wavenumbers, and (3) further compensating for variations in transducer transfer functions as measured by the MBPE algorithm.

To facilitate comparison, some minor signal conditioning is performed in addition to

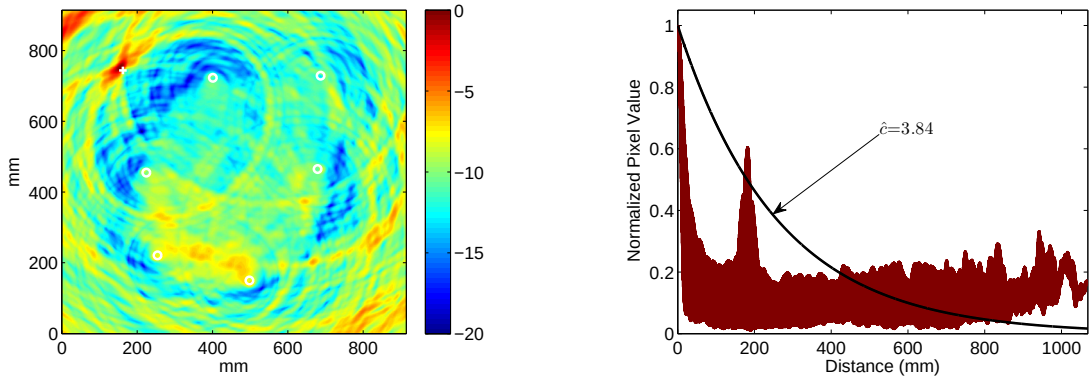

(a) (b)

Figure 6.2: Conventional imaging with experimental data of a 5 mm through-hole. Imaging was performed with the envelope of distance domain signals mapped with nominal parameter values, an instantaneous window, and the 5 mm scattering field generated as per Grahn [122]. (a) Image displayed using a 20 dB scale, and (b) normalized pixel values versus distance from damage location ($\hat{c}$ = 3.84).

the ω–k mapping algorithm for all dispersion-compensated images. The transfer function for the propagating wave is first deconvolved from the received signal *prior to* performing the mapping algorithm. The propagating wave is assumed to be the excitation function, unless MBPE estimates are available, in which case the combined $T(\omega)R(\omega)$ product is used. This operation must be performed before the mapping algorithm because the ω–k mapping algorithm changes the propagating wavepacket. Although a number of methods are available to perform the deconvolution, frequency domain division will be used throughout this text. It is well understood that deconvolution in the frequency domain creates some numerical instability issues due to division by small numbers. For that reason it is implied that any frequency domain division operation is accompanied with additional filtering to address these issues. The deconvolution operation avoids any artifacts or issues that may arise from the spectral changes associated with the ω–k mapping, e.g. a remapped spectrum may not produce a wavepacket with maximum amplitude at the center.

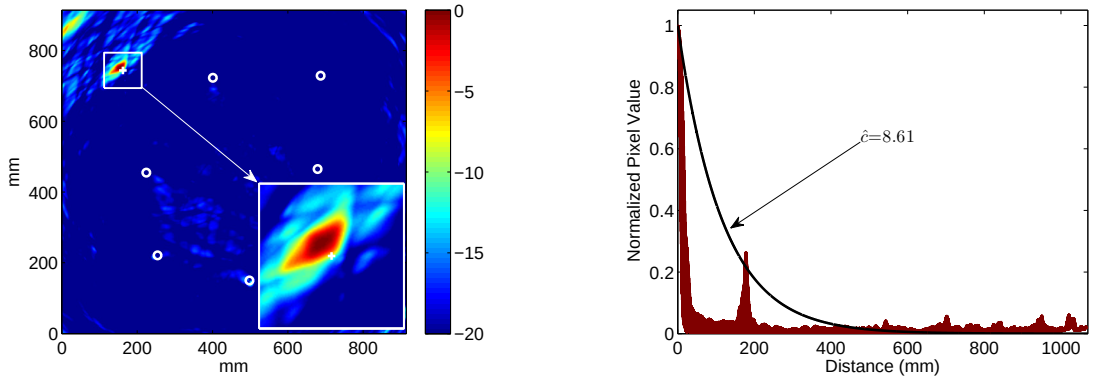

(a) (b)

Figure 6.3: Minimum variance imaging with experimental data of a 5 mm through-hole. Imaging was performed with the envelope of distance domain signals mapped with nominal parameter values, an instantaneous window, and the 5 mm scattering field generated as per Grahn [122]. (a) Image displayed using a 20 dB scale, and (b) normalized pixel values versus distance from damage location ($\hat{c}$ = 8.61).

6.2.1 Dispersion Compensation with Nominal Dispersion Relations

The experimental time domain signals described in Chapter III and used for imaging in Chapters III and IV were converted to the distance domain using the ω–k mapping algorithm described in the previous section using *nominal* dispersion curves computed using the Vallen Dispersion software (Vallen Systeme GmbH, Munich, Germany). Unlike the time domain signals that exhibit dispersive effects, such as wavepacket spreading and the associated amplitude loss, the dispersion-compensated signals are expected to maintain the wavepacket shape and decay according to a $1/\sqrt{d}$ geometric spreading loss. Figure 6.2 and Figure 6.3 depict conventional and minimum variance imaging performance, respectively, with the envelope of the analytic representation of the distance domain signals. These figures represent a relatively minor improvement over the time domain images generated in Chapter IV, indicating that the envelope of the time domain signal is not changing significantly as the wavepacket propagates over distance.

In contrast, the *phase* of the wavepacket does change significantly as the wavepacket

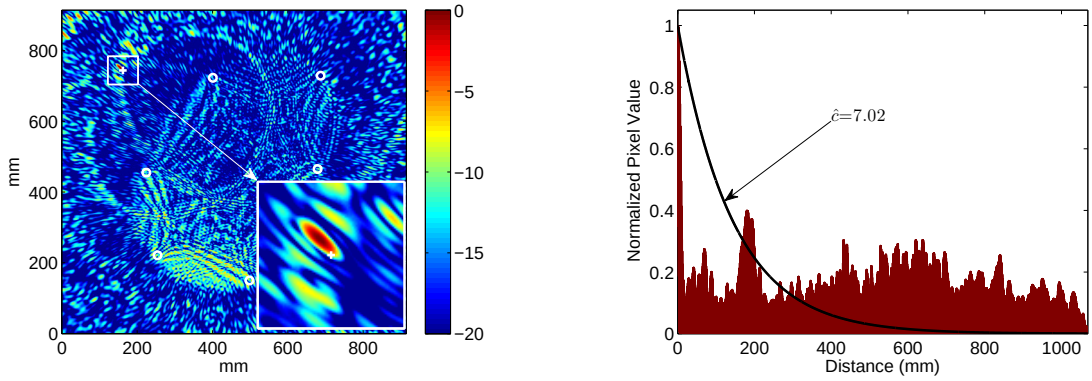

(a) (b)

Figure 6.4: Conventional imaging with experimental data of a 5 mm through-hole. Imaging was performed with complex (analytic) distance domain signals mapped with nominal parameter values, an instantaneous window, and the 5 mm scattering field generated as per Grahn [122]. (a) Image displayed using a 20 dB scale, and (b) normalized pixel values versus distance from damage location ($\hat{c}$ = 7.02).

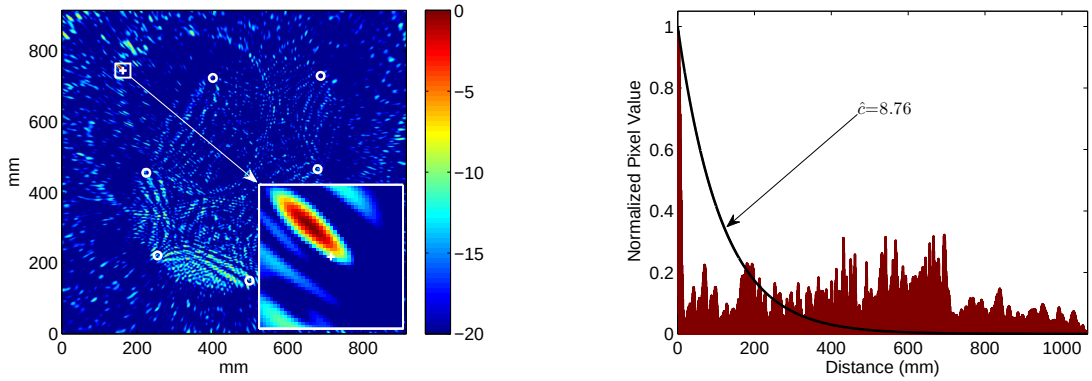

(a) (b)

Figure 6.5: Minimum variance imaging with experimental data of a 5 mm through-hole. Imaging was performed with complex (analytic) distance domain signals mapped with nominal parameter values, an instantaneous window, and the 5 mm scattering field generated as per Grahn [122]. (a) Image displayed using a 20 dB scale, and (b) normalized pixel values versus distance from damage location ($\hat{c}$ = 8.76).

propagates over distance. The phase changes caused significant image degradation in Figure 4.11 and Figure 4.12. Figure 6.4 and Figure 6.5 illustrate conventional and minimum variance imaging performance, respectively, with the analytic representation of the distance

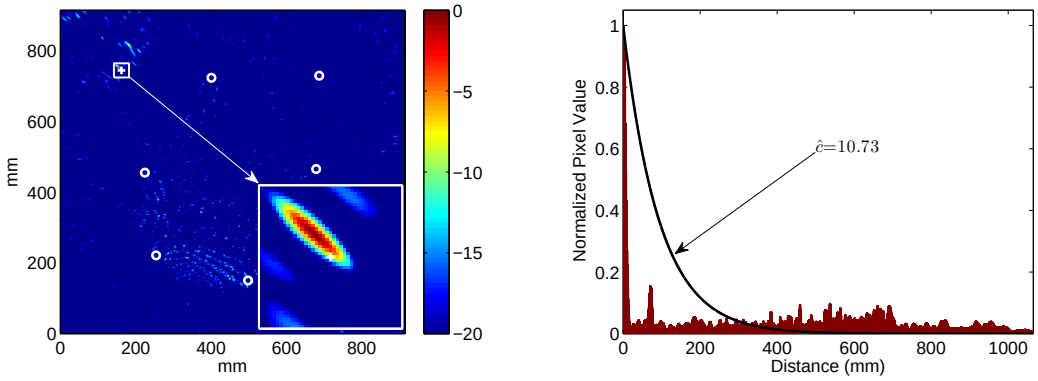

(a) (b)

Figure 6.6: Minimum variance imaging with experimental data of a 5 mm through-hole. Imaging was performed with complex (analytic) distance domain signals mapped with MBPE dispersion estimate and nominal transducer transfer functions, an instantaneous window, and the 5 mm scattering field generated as per Grahn [122]. (a) Image displayed using a 20 dB scale, and (b) normalized pixel values versus distance from damage location ($\hat{c}$ = 10.73)

domain signals. These figures represent a notable improvement over the time domain images presented in Chapter 4. Note that the increased noise floor observed in Figure 6.5, as compared to the simulated equivalent of Figure 4.7, is most likely due to the combination of imperfect baseline subtraction, imperfect dispersion compensation, and errors in the approximated scattering characteristics. These inaccuracies affect imaging performance twofold: not only are imaging artifacts created by poor baseline subtraction performance, but inaccurate model assumptions result in the peak not reaching the maximum possible value, which is manifested as an increased noise floor.

6.2.2 Dispersion Compensation with MBPE Estimates

Figure 6.6 illustrates minimum variance imaging performed with signals converted to the distance domain using $k(\omega)$ estimates obtained with the MBPE algorithm presented in Chapter V. The image represents an improvement over Figure 6.5 both through improved damage localization as well as fewer imaging artifacts.

From Figure 5.10, the $c_p(\omega)$ estimates differ from the nominal values by approximately

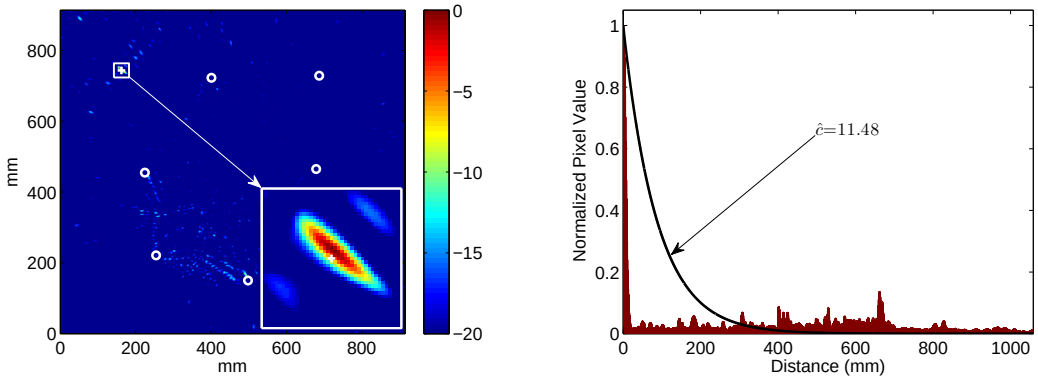

(a) (b)

Figure 6.7: Minimum variance imaging with experimental data of a 5 mm through-hole. Imaging was performed with complex (analytic) distance domain signals mapped with adaptive MBPE parameter estimates, an instantaneous window, and the 5 mm scattering field generated as per Grahn [122]. (a) Image displayed using a 20 dB scale, and (b) normalized pixel values versus distance from damage location ($\hat{c}$ = 11.48)

0.05 mm/μs at 300 kHz, or about 1%. As the propagation distance increases, this relatively small difference produces significant changes in the phase of back-propagated signals. For example, consider a 300 kHz sinusoid propagating in a non-dispersive media with a propagation velocity of 5.35 mm/μs. The distance domain signal is generated by simply re-assigning the sampling times to propagation distances. In this case, a 1% difference in propagation velocity represents a 90° phase discrepancy after just 450 mm of propagation. As such, the imaging performance improvement observed in Figure 6.6 is expected since the $k(\omega)$ estimate obtained from MBPE is expected to be more accurate than than the nominal curve. It should be pointed out that the reduction in artifacts in Figure 6.6 over Figure 6.5 is due to an increase in the pixel value of the damage location rather than any significant change in the noise floor.

In addition to the effects of dispersion, variations in transducer transfer functions can also degrade imaging performance. Figure 6.7 displays the imaging performance that is achieved by deconvolving the transducer transfer functions obtained from the MBPE algorithm prior to performing the ω–k mapping algorithm with MBPE $k(\omega)$ estimates. This

operation removes the *minor* phase variations between transducer transfer functions visible in Figure 5.9. Since the estimated parameters are very similar to the 7-cycle Hamming-windowed toneburst excitation, only minor improvement can reasonably be expected. For more dramatic variations in transducer transfer functions, for example if the phase for one or more transducers is inverted or if the transducers exhibit sensitivity (i.e. magnitude) variations, compensating for the adaptively estimated transducer transfer functions is expected to have a more pronounced impact.

Figure 6.7 demonstrates that adaptive parameter estimates obtained *in situ* at the time of test can be successfully incorporated into the MVDR algorithm to achieve superior imaging performance. Although only adaptive estimates of dispersion and transducer transfer functions have been demonstrated here, additional improvement can reasonably be expected through the compensation of both adaptively estimated propagation distances and propagation loss.

6.3 Parameter Compensation Before Baseline Subtraction

In addition to improving guided wave imaging performance, adaptive parameter estimates also offer the potential to perform environmentally robust baseline subtraction *without* the database of baseline signals required by OBS. By compensating for the environmentally dependent propagation parameters, $T(\omega)$, $R(\omega)$, and $k(\omega)$, *before* baseline subtraction, the differencing operation can isolate changes due to defects or damage *and avoid artifacts due to environmental changes*.

Consider a deployed SHM system in which the environmental conditions are allowed to change. As a result, the transmitter transfer function, $T(\omega)$, receiver transfer function,

$R(\omega)$, and frequency-dependent wavenumber, $k(\omega)$, may not be consistent between measurements. Two measurements are obtained from the system under two different environmental conditions:

$$M_{\mathrm{b}}(\omega) = T_{\mathrm{b}}(\omega) R_{\mathrm{b}}(\omega) \sum_{i=0}^{\infty} \Psi_{\mathrm{b}i}(\omega) \mathrm{e}^{-jk_{\mathrm{b}}(\omega)d_i}, \tag{6.8a}$$

$$M_{\mathrm{c}}(\omega) = T_{\mathrm{c}}(\omega) R_{\mathrm{c}}(\omega) \sum_{i=0}^{\infty} \Psi_{ci}(\omega) \mathrm{e}^{-jk_{\mathrm{c}}(\omega)d_i} + T_{\mathrm{c}}(\omega) R_{\mathrm{c}}(\omega) \Psi_{\times}(\omega) \mathrm{e}^{-jk_{\mathrm{c}}(\omega)d_{\times}}, \tag{6.8b}$$

where $\Psi(\omega)$ is a transfer function representing both scattering and propagation loss for the i^{th} scatterer. The subscript "b" indicates that the transfer function or wavenumber is associated with the damage-free baseline signal, a "c" subscript indicates a parameter associated with the current, or test signal, and a "$\times$" subscript corresponds to a damage site in the structure. Note that in a realistic system with boundaries, multiple wave packets would likely be observed from a single damage site. However, a single wavepacket is considered here for simplicity without any loss of generality.

In order to compensate for the *difference* in environmentally dependent parameters, accurate estimates of the dispersion relations, $k(\omega)$, and transmitter and receiver transfer functions, $T(\omega)$ and $R(\omega)$, for *both* the baseline and test signals are required. With this information, the signals can be deconvolved with their respective transmitter and receiver transfer functions,

$$\bar{M}_{\mathrm{b}}(\omega) = \frac{M_{\mathrm{b}}(\omega)}{T_{\mathrm{b}}(\omega) R_{\mathrm{b}}(\omega)} = \Gamma_{\mathrm{b}}(\omega) \sum_{i=0}^{\infty} \Psi_{\mathrm{b}i}(\omega) \mathrm{e}^{-jk_{\mathrm{b}}(\omega)d_i}, \tag{6.9a}$$

$$\bar{M}_{\mathrm{c}}(\omega) = \frac{M_{\mathrm{c}}(\omega)}{T_{\mathrm{c}}(\omega) R_{\mathrm{c}}(\omega)} = \Gamma_{\mathrm{c}}(\omega) \sum_{i=0}^{\infty} \Psi_{ci}(\omega) \mathrm{e}^{-jk_{\mathrm{c}}(\omega)d_i} + \Gamma_{\mathrm{c}}(\omega) \Psi_{\times}(\omega) \mathrm{e}^{-jk_{\mathrm{c}}(\omega)d_{\times}}, \tag{6.9b}$$

where $\Gamma(\omega)$ represents the deconvolved and filtered transducer transfer function. With ideal deconvolution and filtering, $\Gamma(\omega)$ will be a "1" over a fixed spectral range.

The environmental and frequency dependent wavenumber values, $k_c(\omega)$ and $k_b(\omega)$, can then be compensated using the ω–k mapping described earlier in this chapter:

$$\begin{aligned}\bar{M}_b(k) =& \bar{M}_b(\omega_b(k))\, c_g(\omega_b(k)) \\ =& \Gamma_b(k) \sum_{i=0}^{\infty} \Psi_{bi}(k)\, e^{-jkd_i}, \end{aligned} \tag{6.10a}$$

$$\begin{aligned}\bar{M}_c(k) =& \bar{M}_c(\omega_c(k))\, c_g(\omega_c(k)) \\ =& \Gamma_c(k)\, \Psi_\times(k)\, e^{-jkd_\times} + \\ & \Gamma_c(k) \sum_{i=0}^{\infty} \Psi_{ci}(k)\, e^{-jkd_i}. \end{aligned} \tag{6.10b}$$

In the above equations $\Gamma(k) = \Gamma(\omega(k))\, c_g(\omega(k))$ and $\Psi(k) = \Psi(\omega(k))$.

Finally, if $\Gamma_c(k) \approx \Gamma_b(k)$ and $\Psi_{ci}(k) \approx \Psi_{bi}(k)$, then baseline subtraction can be performed effectively with the distance domain signals:

$$\bar{m}_c(x) - \bar{m}_b(x) \approx \gamma_c(x - d_\times) * \psi_\times(x - d_\times), \tag{6.11}$$

where $\bar{m}_b(x)$, $\bar{m}_c(x)$, $\gamma_b(x)$, and $\psi_\times(x)$ are the inverse Fourier transforms of $\bar{M}_b(k)$, $\bar{M}_c(k)$, $\Gamma_b(k)$, and $\Psi_\times(k)$, respectively. Equation (6.11) indicates that the results of baseline subtraction will contain a scattered wavepacket located at $d_\times$.

Two important points should be raised here with respect to the $\bar{M}(k)$ functions. First, even if the $\Psi_{ci}(\omega)$ and $\Psi_{bi}(\omega)$ signals are *identical* in the frequency domain, each of these transfer functions will be mapped to the wavenumber domain *differently*. Therefore, in order for the wavenumber domain versions to be identical, or nearly identical, the $\Psi_{ci}(\omega)$ and $\Psi_{bi}(\omega)$ signals must be approximately uniform over frequency and not change significantly due to environmental effects. Similarly, the mapping from frequency domain to wavenumber domain does not ensure that the mapped wavenumber domains are *overlapping*. As such, some filtering of the $\bar{M}(k)$ waveforms is necessary to isolate the overlapping spectra.

6.3.1 Simulated Example

A simulated example is provided here to help demonstrate parameter compensation before baseline subtraction. Simulations were performed for the 914 mm $\times$ 914 mm $\times$ 3.18 mm aluminum plate depicted in Figure 3.1b over a range of temperatures from 22-39° C. Temperature-dependent dispersion relations were computed using the Vallen Dispersion software program (Vallen Systeme GmbH, Munich, Germany) with both the longitudinal and shear velocities changing by 0.001 mm/(μs°C). The excitation signals were also simulated with slight amplitude (0.05%/°C) and phase (0.03 rad/°C) changes in the excitation signals. No damage was simulated; therefore, baseline subtraction results are expected to be zero.

Figure 6.8 illustrates the model-fit performance of the baseline signals in both the time- and frequency domains for the simulated array at 22° C. Both plots depict the direct arrival signals with a thick gray line. The thin, colored lines are generated using parameter estimates from the MBPE algorithm and are colored according to the propagation distance. Algorithmic performance can be gaged by observing the model fit performance, which is a measure of how well the estimated direct arrivals, generated with parameter estimation results, agree with the measured, direct arrivals. Figure 6.8 represents excellent model fit, indicating that the MBPE algorithm is able to correctly identify the underlying parameters.

The estimated dispersion relations over the range of temperatures are shown in Figure 6.9 as wavenumber *vs*. frequency. As with Figure 6.8, the true values are shown with thick gray lines and the estimated values are overlaid in color (color coded according to the simulated temperature). Figure 6.9 indicates how little the dispersion relations change with temperature. For the 2 kHz frequency range shown, the rate of change is approximately 1.5×10^{-5}mm/(μs°C).

Figure 6.10 illustrates the simulated signals associated with transducers three and six of Figure 3.1b. Each signal is color-coded according to the temperature at which it was recorded. The inset of Figure 6.10a highlights how much the direct arrivals are changing

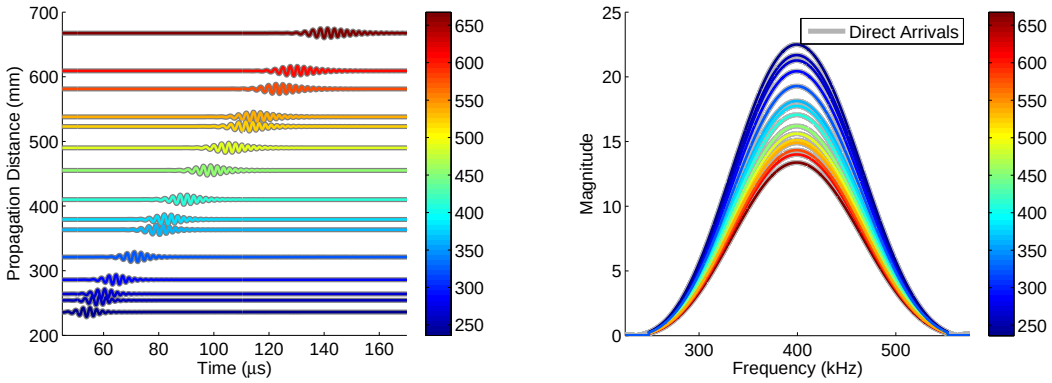

Figure 6.8: Comparison of all simulated signals associated with the spatially distributed array at 22° C and those generated with estimated parameters. Signals are color-coded according to transducer spacing. (a) Time domain waterfall plot. Signals are scaled for presentation purposes. (b) Frequency domain.

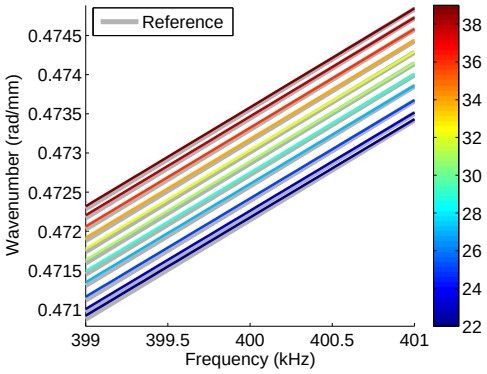

Figure 6.9: Comparison of wavenumber estimates over temperature. The narrow frequency range of 2 kHz is used to highlight how little the frequency-wavenumber relationship changes with frequency.

with temperature. Subsequent echoes can be expected to exhibit even greater change with temperature due to the increased propagation distance. As a result, significant residual energy will remain after baseline subtraction in the time domain, even though there is no damage present.

Figure 6.10b shows the frequency domain signals after deconvolution with the $T(\omega)$ and $R(\omega)$ transfer function estimates obtained from the MBPE algorithm. From the inset, the relationship between signals becomes clear: the deconvolved signals appear slightly

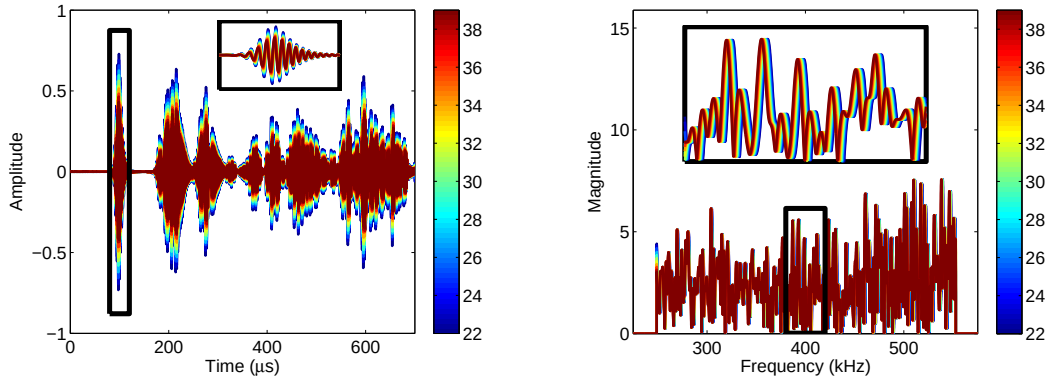

(a) (b)

Figure 6.10: Comparison of one simulated signal from the spatial array color-coded according to temperature displayed in (a) time domain signals and (b) deconvolved frequency domain signals.

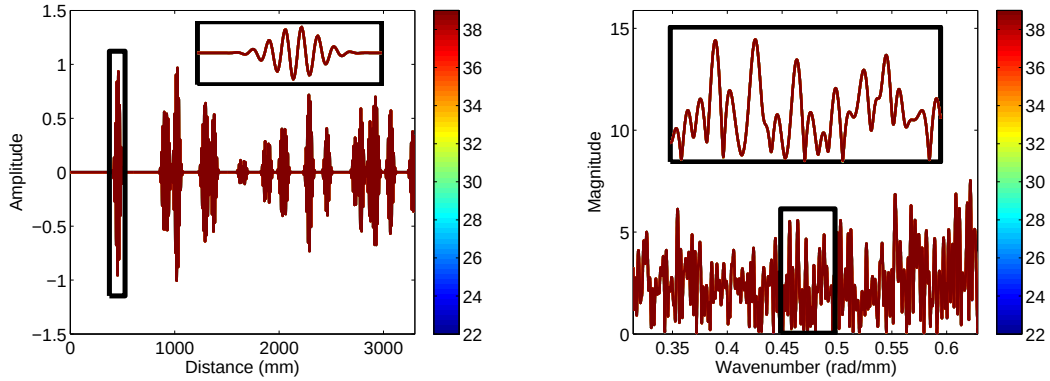

(a) (b)

Figure 6.11: Comparison of one simulated signal from the spatial array color-coded according to temperature displayed in (a) distance domain and (b) wavenumber domain.

shifted in the frequency domain. This behavior is a result of slight changes in $k(\omega)$ between measurements and is not necessarily uniform across the entire spectrum.

Figure 6.11 contains the signals from Figure 6.10 mapped from the frequency domain to the wavenumber domain using the temperature-dependent $k(\omega)$ estimates. Both the distance domain signals and wavenumber domain signals are in excellent agreement over the entire range of simulated temperatures. The degree of agreement can be seen in Figure 6.12, which shows the difference between distance domain estimates. From Figure 6.12, the

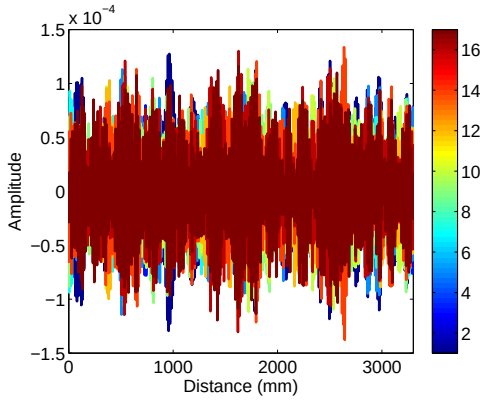

Figure 6.12: Differences between distance domain estimates generated using ideal direct arrivals, color-coded according to temperature difference.

distance domain signals are in agreement to four significant digits. The distance domain signals provide a clear improvement over the dispersive time domain signals in that the temperature and propagation dependence have both been removed. In addition to compensating for the temperature dependence, the signals in the distance domain are much easier to interpret since they are dispersion free.

6.3.2 Implementation Challenges

Performing parameter compensation *before* baseline subtraction is attractive because it provides robustness to homogeneous environmental changes without the need for OBS. However, although simple in concept, baseline subtraction with compensated signals presents some significant challenges for practical implementations. Small errors in parameter estimation, deconvolution, ω–k mapping, or overall propagating assumptions can result in significant baseline subtraction residuals. This section briefly describes these sources of error and their anticipated impact on baseline subtraction.

6.3.2.1 Direct Arrivals

The first implementation challenge is associated with the MBPE algorithm. Parameter estimation error with the MBPE algorithm is directly related to model-mismatch between the direct arrivals and the assumed propagation model. This model-mismatch is usually the

result of the presence of an additional propagating mode, an undesired reflection, or even direct arrival truncation in the time domain.

Figure 6.13 shows the magnitude response of a set of simulated direct arrivals in which several of the signals are slightly truncated in the time domain, shown with thick, gray lines. Truncation of a signal may be necessary in some scenarios when an undesired reflection or second mode has temporal overlap with a direct arrival. The corresponding parameter estimation results are overlaid. Recall that the parameter estimation algorithm must be performed over a continuous spectrum and requires positive SNR at each frequency. The spectral truncation visible in Figure 6.13 is a result of this requirement and is completely unrelated to the time domain truncation that is causing the ripples in the magnitude responses. As a whole, there is a stark contrast between Figure 6.13 and Figure 6.8. Since the direct arrivals do not behave according to the assumed propagation model of the MBPE algorithm, the algorithm is unable to accurately identify the underlying parameters. As such, the model fit results are visibly degraded.

For the case of direct arrival truncation considered here, the average standard deviation of the difference between the estimated and true frequency response values is 0.38 (approximately 4% of the average magnitude response). These small parameter errors, however, can be problematic for baseline subtraction. The impact of the erroneous estimates in Figure 6.13 on deconvolution and frequency-wavenumber mapping are discussed in the following two sections.

6.3.2.2 Deconvolution Error

This section considers the baseline subtraction residuals that result from deconvolution error. For this discussion, let the two recorded signals from the previous section be identical, $M_{\mathrm{c}}(\omega) = M_{\mathrm{b}}(\omega)$, and let the baseline signal, $M_{\mathrm{b}}(\omega)$, be deconvolved and converted to the

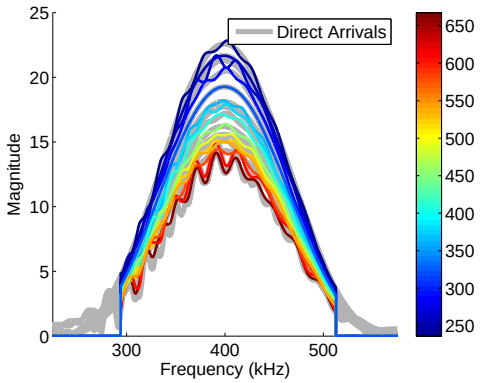

Figure 6.13: Comparison of all simulated signals associated with a spatially distributed array at 22° C and those generated with estimated parameters when time domain truncation is present in the direct arrivals. Signals are color-coded according to transducer spacing.

wavenumber domain perfectly. In mathematical terms, the following case is considered:

$$\bar{M}_{\mathrm{b}}(k) = \hat{\Gamma}(k) \sum_{i=0}^{\infty} \Psi_i(k)\, \mathrm{e}^{-jkd_i}, \tag{6.12a}$$

$$\bar{M}_{\mathrm{c}}(k) = \Gamma_{\mathrm{c}}(k) \sum_{i=0}^{\infty} \Psi_i(k)\, \mathrm{e}^{-jkd_i}, \tag{6.12b}$$

where $\hat{\Gamma}(k)$ is the "true" transfer functions that is common to both signals. If $\Gamma_{\mathrm{c}}(k)$ is described as a sum of $\hat{\Gamma}(k)$ and the deconvolution error, $\Gamma_{\delta}(k)$:

$$\Gamma_{\mathrm{c}}(k) = \hat{\Gamma}(k) + \Gamma_{\delta}(k), \tag{6.13}$$

then the baseline subtraction residual can be expressed as:

$$\bar{M}_{\mathrm{c}}(k) - \bar{M}_{\mathrm{b}}(k) = \Gamma_{\delta}(k) \sum_{i=0}^{\infty} \Psi_i(k)\, \mathrm{e}^{-jkd_i}. \tag{6.14}$$

From (6.14), a deconvolution error produces a baseline residual signal that mimics the propagation distance, scattering characteristics, and propagation loss of the original signal. Therefore a baseline subtraction residual resulting from imperfect deconvolution will mimic the distance-dependent decay of the baseline signal. Figure 6.14a shows the baseline subtraction residual that results when deconvolution is performed with $T(\omega)$ and $R(\omega)$ estimates from the truncated direct arrivals of the previous section. The residual is much larger than the original simulation without deconvolution error. The apparent shift between

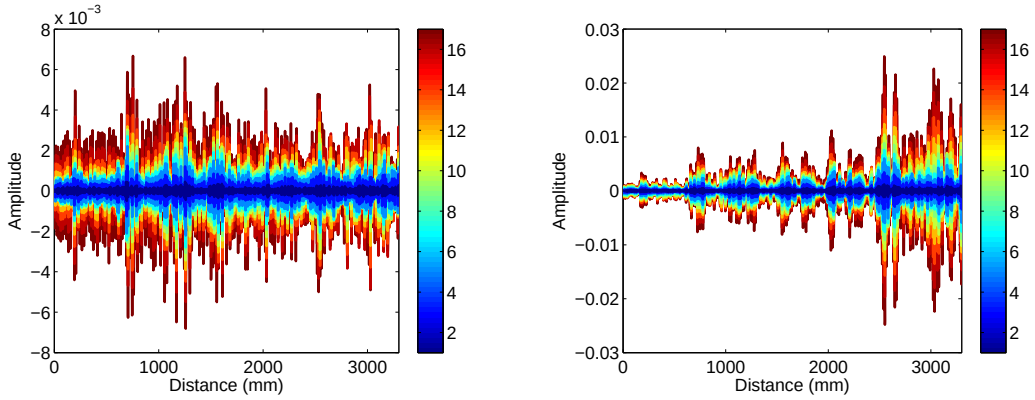

Figure 6.14: Differences between distance domain estimates generated using imperfect parameter estimates due to truncation, color-coded according to temperature difference. (a) Deconvolution error. (b) Mapping error.

wavepackets between Figure 6.11a and Figure 6.14a is a result of the leading edge of the direct arrival being truncated in the time domain, which results in the largest baseline subtraction residual at the leading edge of the wavepacket.

It should be noted here that the deconvolution error described in this section can also result from two additional phenomena. First, the *lack* of deconvolution can cause a similar effect as that shown in Figure 6.14a. Consider the case when the transmitter and receiver transfer functions are identical but deconvolution is not performed, $\Gamma(\omega) = T(\omega) R(\omega)$. During the ω–k mapping operation, each transfer function will be mapped differently since $\omega_c(k) \neq \omega_b(k)$. As a result, differencing the mapped signals will result in some baseline subtraction residual. The severity of the residual will be dependent on both the spectral shape of $\Gamma(\omega)$ as well as the difference between $\omega_c(k)$ and $\omega_b(k)$.

6.3.2.3 Dispersion Error

If the dispersion relations used for conversion from the frequency domain to the wavenumber domain are inaccurate, then the signals in the wavenumber domain will contain some inherent inaccuracies as well. This section investigates the implications of an imperfect ω–k mapping operation. To isolate the effects of an imperfect mapping, begin with two

identical functions from (6.9), in which both $\Gamma(\omega)$ and $\Psi_i(\omega)$ are uniform over frequency, representing a best-case scenario. The ω–k mapping results in the following wavenumber domain signals:

$$\bar{M}_{\mathrm{b}}(k) = \Gamma(k) \sum_{i=0}^{\infty} \Psi_i(k)\, \mathrm{e}^{-j\hat{k}d_i}, \tag{6.15a}$$

$$\bar{M}_{\mathrm{c}}(k) = \Gamma(k) \sum_{i=0}^{\infty} \Psi_i(k)\, \mathrm{e}^{-jk_{\mathrm{c}}d_i}, \tag{6.15b}$$

where the $\Gamma(k)$ and $\Psi_i(k)$ subscripts have been simplified for this example to underscore that they are identical between signals. The k_{c} term in (6.15a) can be described as the true wavenumber, $\hat{k}$, plus some offset, $k_\delta(k)$:

$$k_{\mathrm{c}} = \hat{k} + k_\delta(k). \tag{6.16}$$

Substituting the above equation into (6.15):

$$\bar{M}_{\mathrm{b}}(k) = \Gamma(k) \sum_{i=0}^{\infty} \Psi_i(k)\, \mathrm{e}^{-j\hat{k}d_i}. \tag{6.17a}$$

$$\bar{M}_{\mathrm{c}}(k) = \Gamma(k) \sum_{i=0}^{\infty} \Psi_i(k)\, \mathrm{e}^{-jk_\delta(k)d_i} \mathrm{e}^{-j\hat{k}d_i}, \tag{6.17b}$$

From (6.17), the effects of an imperfect mapping become clear: the i^{th} wavepacket of the test signal will exhibit a phase error of $k_\delta(k)\, d_i$. In other words, ω–k mapping errors will result in a baseline subtraction error that increases over distance.

If the dispersion error, $k_\delta(k)$, is expressed as a polynomial,

$$k_\delta(k) = \sum_{i=0}^{\infty} \kappa_i k^i, \tag{6.18}$$

then the effects of low-order dispersion errors can be conceptualized relatively easily. For example, if the dispersion error is a constant offset, then the resulting error is a phase offset that increases linearly with distance, $\kappa_0 d_i$. Further, if the wavenumber error is linear with a zero intercept, $k_\delta(k) = \kappa_1 k$, then the resulting error is a *distance* offset that increases by a factor of κ_1 with distance. Analysis of higher order modes becomes slightly less intuitive, but can be envisioned as minor changes in location, phase, and shape with distance.

Figure 6.14b depicts the baseline subtraction residual associated with the erroneous $k(\omega)$ estimates from Section 6.3.2.1. It should be noted that the ratio between $k_\delta(k)$ and k is approximately 10^{-3}. However, even with such a small error, the impact on baseline subtraction is significant, particularly for long distances. This highlights the sensitivity of the baseline subtraction algorithm to minor errors in $k(\omega)$.

6.3.2.4 Additional Environmental Effects

In addition to the sources of error already considered, there are several potential sources of error that are indirectly related to the MBPE algorithm and parameter compensation *prior to* baseline subtraction. Specifically, these are associated with inaccurate assumptions about the propagation environment.

For example, the presence of an additional propagating mode effectively introduces *both* a deconvolution and dispersion error, simultaneously. This is because $T(\omega)$ and $R(\omega)$ are mode-specific and the dispersion relations of each mode, $k(\omega)$, will change independently of the other.

Wilcox showed that while energy associated with the primary guided wave mode is largely compressed in the distance domain during the ω–k mapping algorithm, the energy associated with any secondary guided wave mode is spread out over distance [85]. Although this behavior is beneficial for signal analysis, it is the *change* between two distance domain signals that is of significance for baseline subtraction, and a secondary propagating mode will not change in the same manner as the primary mode. As such, significant baseline subtraction residual can be expected from additional propagating modes.

Figure 6.15 shows typical distance domain error that occurs when an undesired mode is present. Array simulations described in the previous section were repeated with the addition of the A_0 mode, where the amplitude ratio of S_0 to A_0 was 10:1. Parameter estimates from the mode-pure simulations were used for deconvolution and spectral mapping to isolate the model mismatch behavior. Figure 6.15a shows the presence of several additional

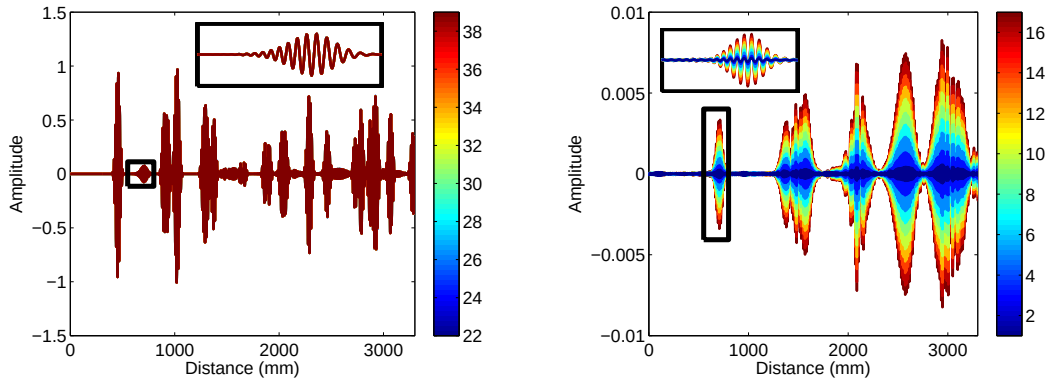

Figure 6.15: Effects of a second mode. The ratio of S_0 to A_0 is 10:1.. (a) Distance domain estimates, color-coded according to temperature, and (b) Difference between distance domain estimates, color-coded according to temperature difference.

"echoes" compared to Figure 6.11a, such as the one shown in the inset. These additional "echoes" are due to the mismatch between the $k(\omega)$ of each mode. Figure 6.15b shows that the residual differences between the distance domain estimates increase over temperature at the location of these "echoes" from the second mode. It should be pointed out that the system response to an additional mode is dependent on both the magnitude ratio and the relationship between the $k(\omega)$ for each mode. Therefore, while the case presented here is a representative example, mode impurity may have more or less severe impacts in other frequency ranges, for other modes, or with other materials.

Another challenge is that environmental factors affecting the dispersion relations and transmitter and receiver transfer functions, such as temperature, pressure, and humidity, may also influence the propagation loss and scattering characteristics of structural reflectors. Like dispersion error discussed in the previous section, uncompensated changes in propagation loss will result in baseline subtraction residuals that increase with distance. On the other hand, changes in scattering characteristics will only affect those wavepackets associated with the changing scatterer. In addition to affecting the magnitude and phase

of scattered energy, environmental changes can also be expected to influence both the excitability of each mode and degree of mode conversion that occurs at each structural reflector, which can cause additional problems due to the presence of varying degrees of secondary propagating modes. As a result, algorithmic performance cannot be expected to be completely independent of the environment for complex structures.

Finally, signals that propagate over long distances and are exposed to broad temperature ranges will be negatively affected by thermal expansion. The coefficient of thermal expansion in metals is typically on the order of 10^{-5} °C^{-1}. For SHM applications that operate over a 10° C range, this translates to a 0.1 mm shift for each meter of propagation. If the operating frequency is 400 kHz, the wavelength is only 13 mm, which means that thermal expansion can result in a non-trivial phase error of $3°/\text{m}$. Therefore, although thermal expansion is not a significant issue for laboratory experiments, it is an issue that will need to be addressed in practical implementations. One interesting aspect of the thermal expansion problem in distance domain signals, is that it is equivalent to a change in propagation velocity in a non-dispersive time domain signal and can be addressed by performing BSS in the distance domain.

6.4 Discussion

The baseline subtraction problem is an inherently ill-conditioned problem, meaning that small changes or errors in the baseline or test signals can result in relatively large changes or errors in the differenced signals. Considering that scattered energy from a defect or damage will result in a signal 1-2 orders of magnitude smaller than a signal propagating the same distance with non-absorbing geometric reflections, there is very little tolerance for parameter estimation error. For example, to ensure baseline subtraction residual is 20 dB lower than (0.01 times) the amplitude of the original signal, the phase of the environmentally compensated baseline and test signals must be within 0.6° ($0.01(180/\pi)$). Taking this one step further, if the direct arrival propagates 500 mm and $k_\delta(k)$ from (6.18) is assumed

to be a constant offset (which may be unfairly pessimistic), this phase requirement translates to κ_0 less than 2×10^{-5} rad/mm (0.01/500), requiring 5 significant digits in the MBPE wavenumber estimates.

Guided wave imaging, on the other hand, is somewhat better conditioned than the baseline subtraction problem. Small errors in parameter estimates result in small errors in the pixel value computation. In fact, the sensitivity of minimum variance imaging to transducer transfer function and wavenumber estimation errors can be controlled somewhat through the regularization factor, α. Even with a relatively small α, indicating a heightened sensitivity, a small phase error in the back-propagated, differenced signal will result in a comparable change in pixel value.

In addition to the heightened sensitivity to parameter estimation error, baseline subtraction with environmentally compensated signals also requires some additional assumptions about the propagating environment that are inherently accommodated through the knowledge-based OBS method. First, $\Psi_{ci}(\omega)$ and $\Psi_{bi}(\omega)$ are assumed to (1) have a uniform power spectrum over the frequency-range of interest and (2) not change with the environment. Neither of these assumptions have been experimentally validated, and may have a significant impact on the baseline subtraction residual if they do not hold. Additionally, the parameter compensation methods discussed in this chapter are only applicable to propagation environments with a single propagating mode. The previous section illustrates the negative effects of an additional propagating mode on baseline subtraction with environmentally compensated signals. In contrast, OBS accommodates both of these issues by recording the exact system response for any potential environmental condition.

6.5 Summary

This chapter has presented two methods for incorporating adaptive model-based parameter estimates into guided wave imaging algorithms. The chapter first introduced the ω–k mapping algorithm, which provides a computationally efficient means to compensate for dispersion. Parameter compensation *after* baseline subtraction was then demonstrated with both nominal and adaptively estimated parameters. A significant improvement was shown with adaptive parameter estimates obtained through the MBPE algorithm presented in Chapter V, which is attributed to the fact that the adaptive estimates of the dispersion relations and transducer transfer functions were obtained from measured data obtained at the time of test. Finally, the concept of parameter compensation *before* baseline subtraction was introduced, which provides a potential mechanism to compensate for homogeneous environmental changes without the need for a database of baseline signals. Although parameter compensation *prior to* baseline subtraction was validated via simulation, this approach was shown to be extremely sensitive to parameter estimation errors, which may preclude its use in practical applications.

The primary contribution of this chapter is the incorporation of adaptive parameter estimates from the MBPE algorithm into ultrasonic guided wave imaging. The example provided with experimental data illustrates the significant improvement in imaging that can be achieved through the combination of parameter compensation with adaptive parameter estimates and minimum variance imaging. Another contribution is the concept of parameter compensation *prior to* baseline subtraction. The ability to perform accurate baseline subtraction over a range of environmental conditions is necessary for the use of SHM in large structures that cannot easily be taken out of service, such as ship hulls, bridge gusset plates, storage tanks, etc. Although several issues were raised that prevent the practicality of the approach at this time, the method presents a viable tool to perform environmentally robust baseline subtraction without OBS and may become practical as SHM technology matures. The chapter also places the problem of baseline subtraction and prior work in the

context of a commonly accepted propagation model, which yields a deeper understanding of potential sources of error and their effects on baseline subtraction residual. Finally, this chapter represents the first known application of the ω–k mapping algorithm to sparse, distributed array imaging.

CHAPTER VII

ADDITIONAL GUIDED WAVE IMAGING CONCEPTS

This chapter introduces two additional concepts associated with guided wave imaging that were originally reported in [151, 152]. First, the issue of sparse, distributed array configurations is addressed. A performance ratio is proposed that quantifies the ability of an array to perform simultaneous defect detection and localization. Physical characteristics of the array, including the number of sensors, their placement relative to one another, and the sensor array's relationship to the interrogation structure are all evaluated using this performance ratio with minimum variance imaging. The performance ratio is then used to evaluate some of the signal processing techniques discussed in Chapters III and IV: the choice of excitation function, imaging algorithm, and data type (envelope data *vs*. analytic signals). The second concept is related to *characterizing* damage (in addition to detecting and locating it). Damage characterization is shown to be possible with experimental data using minimum variance imaging and scattering behavior obtained from FEM simulations.

7.1 Array Configurations

Chapters III, IV, and VI have demonstrated that *all* images generated from guided wave imaging algorithms include some degree of artifacts that result from waves that have reflected from both structural boundaries and internal scatterers. These imaging artifacts can degrade imaging performance and therefore the ability of an array to detect and localize damage. Several factors impact the sensitivity of a guided wave system to scattered and reflected energy: (1) the imaging algorithm, (2) the physical array configuration, such as aperture size, number of sensors, and sensor pattern, and (3) structural characteristics, such as structure geometry and damage scattering behavior.

After generating an image with a guided wave imaging technique, damage detection

and localization can then be performed. Damage detection and localization present two distinctly different challenges that share substantial overlap. On one hand, damage localization identifies the most likely location of damage, typically by identifying the maximum pixel value in an image. The location of the maximum pixel value in an image, however, does not necessarily indicate that damage is present in the structure; even a damage-free image will have a maximum pixel value. Damage detection, on the other hand, identifies whether or not damage is present in a structure and is typically accomplished by establishing a threshold that, if exceeded, indicates the presence of damage. These two challenges are interrelated for guided wave images since each pixel is calculated independently. If a threshold for damage detection can be established on a pixel-specific basis, the threshold is by definition location dependent, and damage localization is thus achieved automatically.

The concept of establishing pixel-specific thresholds for damage detection, which was recently proposed by Flynn and Todd [153, 154], represents a departure from previous guided wave imaging performance metrics that are focused on image quality. These image quality metrics typically characterize the performance of an array by comparing the pixel value at one or more potential damage locations to the pixel values at all non-damage locations for a single image. The use of pixel-specific thresholds, however, foregoes this requirement and provides a more complete picture of an array's ability to perform simultaneous damage detection and localization *throughout the structure*.

Since so many variables are associated with characterizing array performance, the scope of this section is restricted to a single defect in a specific structure. A performance ratio is first proposed to quantify array performance. The remaining sections then use this performance ratio to evaluate the impact of imaging algorithm selection; physical characteristics of the array, such as aperture size, number of transducers, and sensor pattern; scattering characteristics of the defect; and excitation function.

7.1.1 Pixel-Specific Performance Ratio

As mentioned above, damage detection is focused on determining whether or not damage is present in a structure. By performing damage detection on a pixel-specific basis, damage localization is automatically achieved. To perform damage detection, a pixel-specific threshold, T_{xy}, must be established that satisfies:

$$\max_{ij \neq xy} P_{xy}\left(D_{ij}\right) < T_{xy} < P_{xy}\left(D_{xy}\right), \tag{7.1}$$

where $P_{ab}\left(D_{gh}\right)$ is the pixel value at location (a, b) when damage is present at (g, h). The above equation states that the threshold, T_{xy}, must be set so that it is *smaller* than the pixel value when damage is present at (x, y) and *larger* than the maximum pixel value at (x, y) when damage is present elsewhere in the structure. To maximize robustness to system noise, model errors, etc., the following performance ratio should be as large as possible for all pixel locations, (x, y):

$$\hat{P}_{xy} = \frac{P_{xy}\left(D_{xy}\right)}{\max_{ij \neq xy} P_{xy}\left(D_{ij}\right)}. \tag{7.2}$$

In words, $\hat{P}_{xy}$ is the ratio of the pixel value at (x, y) when damage is present at (x, y) to the maximum pixel value at (x, y) when damage is present somewhere else in the structure, referred to as the maximum artifact value at (x, y). If $\hat{P}_{xy} > 1$ for all pixel locations, then pixel-specific thresholds can be established throughout the structure and any pixel value that exceeds the pixel-specific threshold must also correspond to the most-likely damage location. Therefore, damage detection and localization can be automated with a single comparison between an image and set of pixel-specific thresholds.

From a statistical perspective, it should be noted that $\hat{P}_{xy}$ has a direct impact on the probability of damage detection, false-detect, and miss for location (x, y). Rather than using the ratio from (7.2), an alternative, more comprehensive statistical model could be employed that incorporates the probability of damage occurring at any given pixel location, as well as the associated costs of false-detects and misses. This is the general approach

taken by Flynn and Todd [153, 154]; however, their work effectively focuses on the pixel value when damage is present and does not consider imaging artifacts.

Direct calculation of $\hat{P}_{xy}$ requires simulation of the structure and array configuration for every possible damage location. This can be extremely computationally demanding when attempting to identify an array configuration that optimizes the pixel-specific performance ratio. As such, only the most demanding of applications (such as high-performance aerospace or space-borne) are likely to merit an extensive search for optimal array geometries. The cases presented here, however, are intended to demonstrate to the reader those factors that most strongly influence array performance.

7.1.2 Finite Element Modeling

As discussed in Chapter IV, the performance of minimum variance imaging is dependent on the agreement of the steering vector used to calculate the pixel value, $\vec{\mathbf{e}}_{xy}$, and the relationship between back-propagated signals, $\hat{\mathbf{s}}_{xy}$. Since the steering vectors are largely defined by the scattering coefficients, ψ_{mxy}, accurate knowledge of scattering coefficients is necessary to maximize imaging performance.

As part of a collaborative effort with the University College London, Dr. Paul Fromme used three-dimensional finite element modeling (FEM) with the ABAQUS® software suite to generate anticipated scattering fields for a notch using nominal 6061 aluminum material properties [152]. The FEM simulation used explicit time integration, with linear brick elements of 1.25 mm in the direction along the notch, 1 mm in the direction of the notch thickness, and 0.795 mm through the plate thickness. Excitation of the S_0 mode was performed using opposing out-of-plane point-sources located at the top and bottom edges of the plate with a 5-cycle Hamming-windowed toneburst at 400 kHz. Out-of-plane measurements were obtained from one surface of the plate on a 49 mm $\times$ 61.25 mm grid centered at the notch. Since both the excitation and the notch are symmetric about the center of the plate and out-of-plane measurements are used, recorded data were assumed to contain pure

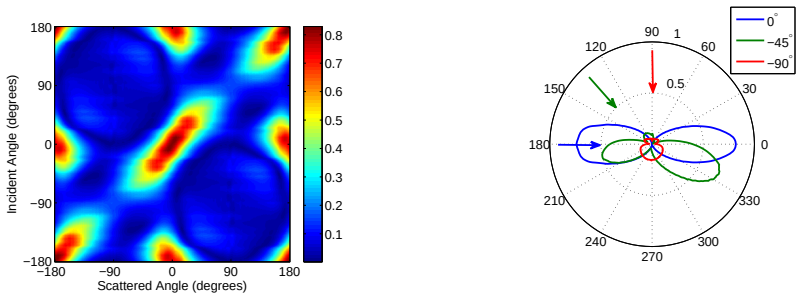

(a) (b)

Figure 7.1: S_0 scattering behavior of a 15 mm long notch perpendicular to an incident S_0 wave at 0° shown for (a) all incident and scattered angles and (b) for incident angles of 0°, -45°, and -90°. Arrows indicate the direction of the incident wave relative to the center of the polar plot.

S_0. Because notches scatter energy differently depending on incident angle, the FEM simulations were repeated for incident waves over a 90° range at 5° increments. The symmetries of a through-thickness notch allow the scattering behavior for the remaining incident angles to be inferred from these simulations.

The FEM simulation data generated by Dr. Fromme were used to obtain scattering behavior through the same baseline subtraction technique described for guided wave imaging. FEM simulation data obtained without the notch present were subtracted from FEM data obtained with a notch. Differenced information from the rectangular grid was spatially interpolated to obtain measurements located at 1° increments along a circle of radius 24 mm centered at the notch location. To better match the frequency content of the experimental data, the interpolated signals were deconvolved with the excitation function (5-cycle Hamming-windowed toneburst at 400 kHz) and filtered with a 12-cycle Hamming-windowed toneburst at 300 kHz. Each of these 360 signals was then converted to the frequency domain and the magnitude and phase of the signal at 300 kHz was used to determine anticipated scattering behavior. All scattering behavior estimates were normalized to have a magnitude of 1 if the differenced signal is the same amplitude and phase as a direct arrival that has propagated the same distance.

Figure 7.1 shows the S_0 scattering behavior observed from FEM simulations for a

15 mm × 2 mm × 3.18 mm notch oriented along the *y*-axis (±90° notch orientation). Figure 7.1a depicts the magnitude of the *differenced* signal as a function of both incident and scattered angle for *all* angles. Here both the incident and scattered angles refer to the wave propagation direction, and are independent from one another. This means that for a scatterer located at the origin, the incident angle for a wave propagating from left to right, along the *x*-axis, is 0° and from bottom to top, along the *y*-axis, is 90°. Similarly, scattered energy propagating from the origin to the right has a scattered angle of 0° and from the origin downward is a scattered angle of -90°, regardless of the incident angle. Figure 7.1b represents the same information as Figure 7.1, displayed as a polar plot for incident angles of 0°, -45°, and -90°. The color-coded arrows depict the incident wave propagation direction. These figures show that for the 0° incident wave, the signal is largely reflected back towards the source, producing two large lobes. The lobe in the forward (0°) direction corresponds to the *lack* of signal that will be evident in the differenced signal due to the "shadowing" effect of the notch, while the lobe in the backward (180°) direction corresponds to the reflected wave. Figure 7.1 highlights the directionally dependent nature of the scatterer, with dependencies both on the incident and scattered angle.

7.1.3 Simulation Details

Performance ratios were obtained by simulating the plate and calculating images for a single defect located at 20 mm increments in each direction of the plate (2025 total defect locations). Note that although $P_{xy}\left(D_{xy}\right)$ is accurate for each location considered, the $\max_{ij\neq xy} P_{xy}\left(D_{ij}\right)$ term in (7.2) is not necessarily maximized for the simulations considered here since defect locations are restricted to discrete locations. Thus, as defect spacing is reduced, performance ratios will either remain at the same levels or decrease. Therefore defect increments must be sufficiently small to ensure that the resulting performance ratios are not overly optimistic.

The simulation setup is similar to the simulations described in Chapter III. In almost

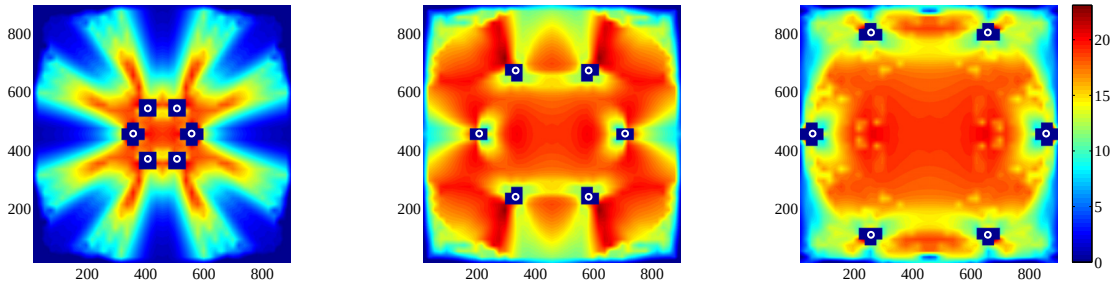

(a) (b) (c)

Figure 7.2: Performance ratio maps on a dB scale with minimum variance imaging using a 6-sensor circular array with 100 mm, 250 mm, and 400 mm radius aperture size.

all simulations, the excitation function is a *three*-cycle Hamming windowed sinusoid at 300 kHz. The exception is when generating Figure 7.7, where the excitation signal is either a three-, five-, or seven-cycle Hamming windowed sinusoid at 300 kHz. Unless otherwise indicated, scattering behavior corresponds to a point-like, uniform scatterer, and all imaging is performed in the time domain with the envelope of of the signals.

To aid in analysis, pixel values adjacent to transducers or defect locations were ignored when computing the denominator of (7.2). The large pixel values associated with these locations prevent useful data from being extracted from the performance ratio maps. All pixel-specific performance ratios are shown on a dB scale.

7.1.4 Physical Array Configuration

The physical array configuration has a significant impact on performance. The array configuration is characterized by the aperture size, number of sensors, sensor pattern, and orientation of the array relative to the structure. In effect, the array configuration determines the spatial information that is obtained from the structure. An exhaustive study of all possible configurations is clearly impossible, so a small subset of examples has been chosen to demonstrate typical performance impacts from each of these factors.

First and foremost, the array aperture size appears to have the most significant impact.

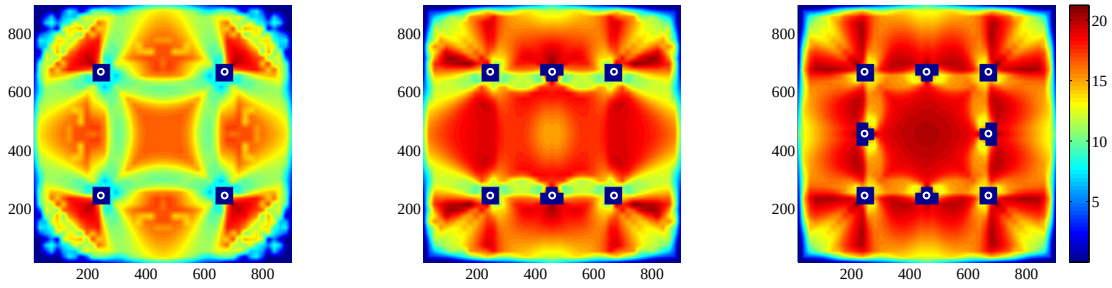

Figure 7.3: Performance ratio maps generated with minimum variance imaging and a four, six, and eight-sensor rectangular pattern.

Figure 7.2 demonstrates pixel-specific performance ratios using minimum variance imaging for six-sensor circular arrays with radii of (a) 100 mm, (b) 250 mm, and (c) 400 mm (in addition, a six-sensor circular array with a radius of 17 mm is shown in Figure 7.5c). The performance ratio maps are clearly affected by aperture size. Although the effects of edge reflections are present in all simulations, the effects appear to be more pronounced for the 100 mm and 250 mm radii arrays. Since the overall performance ratio value decreases as the aperture is increased from 250 mm to 400 mm, Figure 7.2 also suggests that for a given application, sensor pattern, and interrogation structure, some optimal aperture size exists.

The number of sensors also plays a significant role in array performance. Performance ratio maps for four, six, and eight-sensor rectangular patterns are shown for minimum variance imaging in Figure 7.3. Figure 7.3 indicates that, in general, the addition of sensors provides an *overall* increase in the performance ratio throughout the structure but does not appear to increase the *maximum* performance ratio. One can also infer from Figure 7.3 that since the performance ratio values in the immediate vicinity of the transducers are *lower* than those further from the transducers (particularly the center of the structure in Figure 7.3c), the addition of transducers will *not necessarily* increase the overall performance of the array.

Figures 7.2b and Figure 7.4 demonstrate four different sensor patterns for a six sensor array with approximately the same aperture sizes (a fifth can be found in Figure 7.3b).

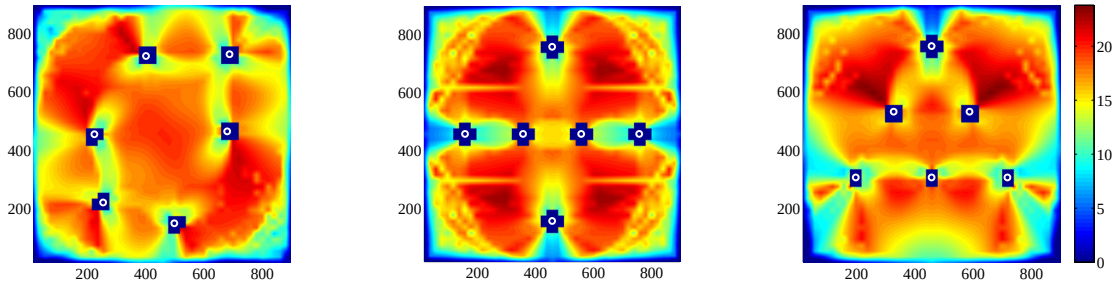

(a) (b) (c)

Figure 7.4: Performance ratio maps with minimum variance imaging using a 6-sensor array arranged in (a) the experimental sensor arrangement, (b) a cross pattern, and (c) a triangular pattern.

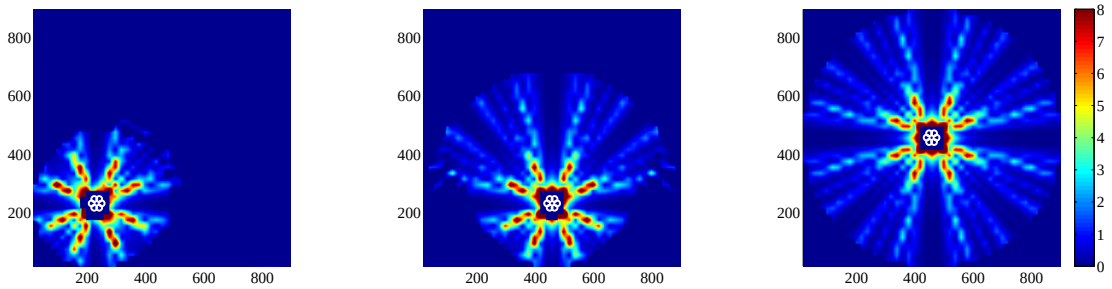

(a) (b) (c)

Figure 7.5: Performance ratio maps with minimum variance imaging using a compact 6-sensor array at three different locations on the interrogation structure.

Sensor patterns that exhibit spatial periodicity that resembles that of the interrogation structure can be expected to exhibit spatially periodic performance ratios. This can be observed throughout Figure 7.3, where the spatial periodicity of the performance ratio is strongest. Similar to the number of sensors, the sensor pattern appears to affect the spatial distribution of performance rather than the peak performance.

The location and orientation of an array with respect to the interrogation structure must also be considered. Figure 7.5 shows the performance ratio for a compact, six-sensor circular array with a 17 mm radius at three different locations on the structure. For this particular structure, the imaging performance is clearly improved by centering the array in the structure; however, this observation may not hold for all structures. Figure 7.5 indicates that optimal placement of a small array does little to improve array performance compared to

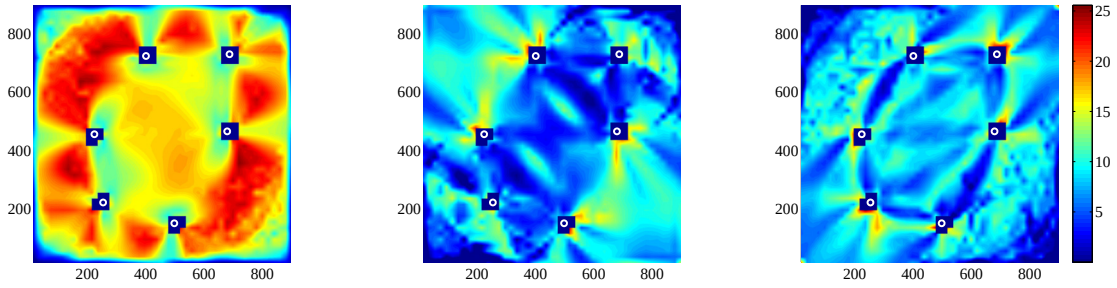

(a) (b) (c)

Figure 7.6: Performance ratio maps generated with minimum variance imaging and various scattering types: (a) 5 mm through-hole, (b) +45° notch and (c) -45° notch.

the benefits of increasing the array aperture.

Finally, the scattering behavior of anticipated defects also plays a noticeable role in array performance and should be considered when selecting an array configuration. Defects that exhibit highly directional scattering patterns will not distribute energy in the same manner as point-like scatterers and, as such, the pixel values and performance ratios will vary with scattering characteristics. Figure 7.6 shows performance ratio maps for a 5 mm through-hole, and two 15 mm notches oriented at ±45°. These three scattering types are of interest because while the point-like scattering used up to this point redirects energy isotropically, providing a *general* indication of imaging performance, the through-hole and notch are directional. The through-hole and notch differ in that the scattering behavior for a through-hole is independent of the incident angle, while the scattering behavior of a notch is highly dependent of angle. This concept is explored in more detail by Fromme [155]. Figure 7.6 indicates that the ability of an array to detect and locate a defect is dependent on the scattering behavior of a defect, and therefore anticipated defect types must be considered in choosing an array configuration.

7.1.5 Signal Processing

The choice of excitation function, imaging algorithm, and data format also play a critical role in imaging performance. Similar to the last section, this section uses performance ratio

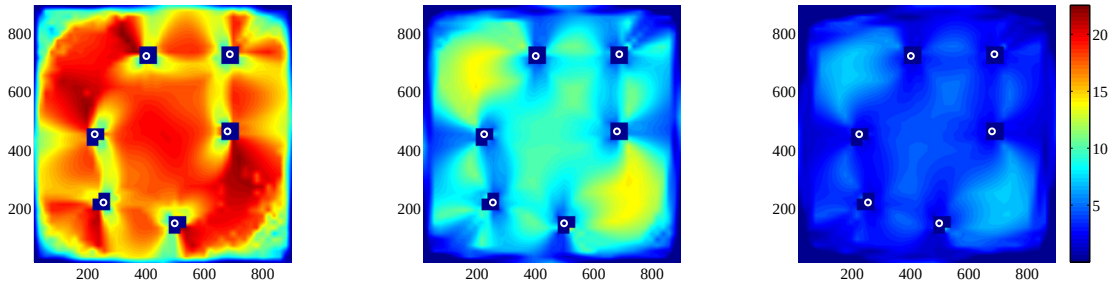

(a) (b) (c)

Figure 7.7: Performance ratio maps generated with minimum variance imaging and a (a) three-, (b) five-, or (c) seven-cycle Hamming-windowed, 300 kHz toneburst.

maps to illustrate the impact that each of these factors has on the ability to simultaneously detect and locate damage.

7.1.5.1 Excitation Function

The excitation function plays a tremendous role in the ability to detect and locate damage. Although the range of possible excitation functions is far too extensive to evaluate in their entirety, Figure 7.7 demonstrates the performance ratio maps for three-, five-, and seven-cycle Hamming-windowed tonebursts centered at 300 kHz. There is a marked performance improvement as the time-support, and therefore spatial-support, of the excitation function is reduced. This is to be expected, since the longer duration excitation signals will have additional overlap with echoes. The trade-off for compact time-support is, however, a broader bandwidth and the associated increase in dispersive effects. Chapters III, IV, and VI, dealt with the effects of dispersion and associated methods to adaptively estimate and compensate for them. Therefore, Figure 7.7 serves to underscore the *combined* benefits that come from dispersion compensation: not just improved imaging performance, but an ability to use wider-bandwidth excitation signals.

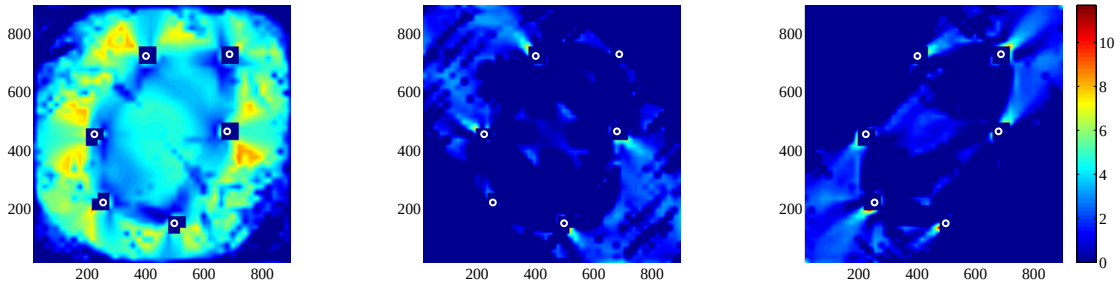

(a) (b) (c)

Figure 7.8: Performance ratio maps generated with conventional imaging and various scattering types: (a) 5 mm through-hole, (b) +45° notch and (c) -45° notch.

7.1.5.2 Imaging Algorithm

An imaging algorithm inherently strikes a balance between sensitivity to the direct arrival of scattered energy and robustness to reflections of scattered energy (and errors in *a priori* information, which is beyond the scope of this section). In contrast to Figure 7.6, Figure 7.8 depicts performance ratio maps for *conventional* imaging in the presence of a 5 mm through-hole, and two 15 mm notches oriented at ±45°. Comparing Figure 7.6 to Figure 7.8, minimum variance imaging clearly offers significant improvements over conventional imaging. This improvement is expected, since the MVDR weight vectors are selected specifically to reduce the pixel value when the back-propagated signals do not agree with the steering vector, $\vec{\mathbf{e}}_{xy}$. What may not be expected is the degree of improvement. The maximum performance ratio is approximately 11 dB in Figure 7.8a, while Figure 7.6a exhibits performance ratios in excess of 25 dB. In fact, approximately 60% of Figure 7.8b and Figure 7.8c have performance ratios less than 1 (< 0 dB), which means that these pixel locations will have a higher amplitude when damage is located elsewhere in the structure than when damage is actually at that location. Alternatively, the minimum variance imaging algorithm provides pixel-specific performance ratios much greater than 1 for over 98% of the structure.

One concern that has been raised with respect to minimum variance imaging is associated with the inherent sensitivity of the algorithm to potentially inaccurate scattering

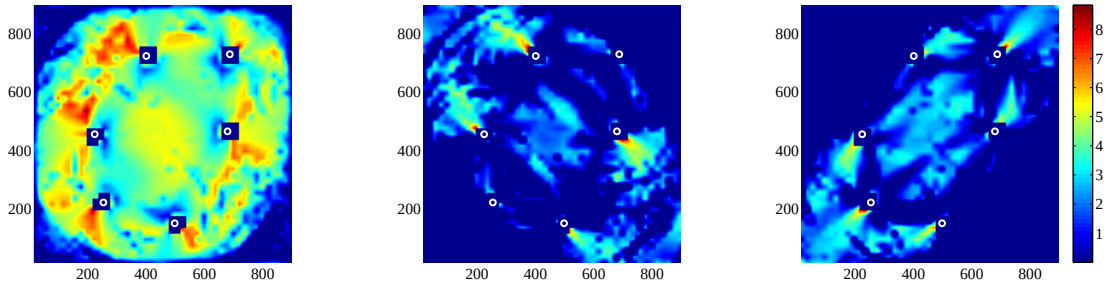

(a) (b) (c)

Figure 7.9: Performance ratio maps generated with conventional imaging when no scattering information is available under the following conditions: (a) 5 mm through-hole, (b) +45° notch and (c) -45° notch.

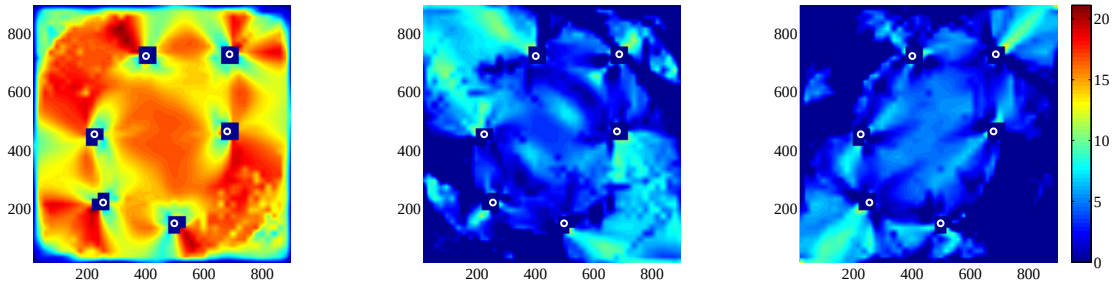

(a) (b) (c)

Figure 7.10: Performance ratio maps generated with minimum variance imaging when no scattering information is available under the following conditions: (a) 5 mm through-hole, (b) +45° notch and (c) -45° notch.

assumptions. For example, consider the case when no scattering assumptions can be made about the defect. How severe will the degradation in minimum variance imaging performance be? Should conventional imaging be used when scattering information is not available?

Figure 7.9 and Figure 7.10 contain performance ratio maps for a 5 mm through-hole, +45° 15 mm notch, and -45° 15 mm notch, for conventional and minimum variance imaging, *when no scattering assumptions are made*. These can be compared directly to Figure 7.8 and Figure 7.6 to see the performance degradation that can be expected when scattering information is unavailable, or cannot be assumed. It should be pointed out that the "brightening" of many of the pixels in Figure 7.9b and Figure 7.9c is simply due to the

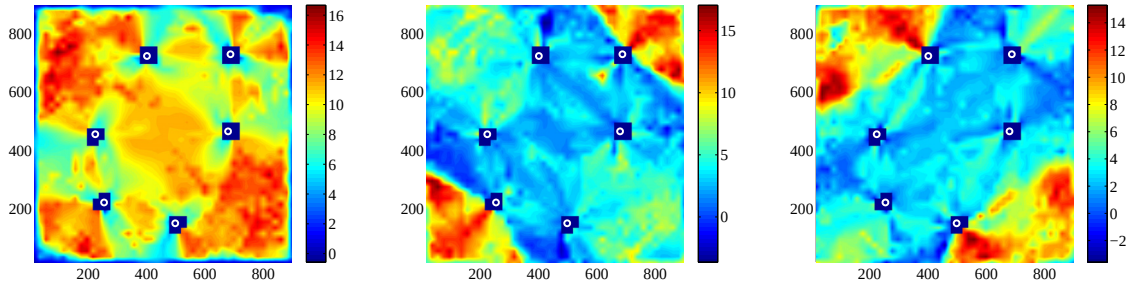

(a) (b) (c)

Figure 7.11: Comparison of performance ratio maps when minimum variance imaging is used *vs*. conventional imaging for: (a) 5 mm through-hole, (b) +45° notch and (c) -45° notch.

shift in color-scale; the performance ratio is largely unchanged. Although both algorithms exhibit some minor degradation in performance (perhaps even less than one might expect), minimum variance imaging provides superior performance ratios values over conventional imaging, *even when no scattering assumptions are made*.

To underscore the advantages of minimum variance imaging over conventional imaging under erroneous scattering assumptions, Figure 7.11 graphically illustrates the *improvement* observed between Figure 7.9 and Figure 7.10. Each pixel value in Figure 7.11 was obtained by subtracting the pixel values of Figure 7.9 (in dB) from those of Figure 7.10 (in dB). Figure 7.11 indicates that although 1-2% of the structure suffer a degradation in performance ratio of up to -4 dB, minimum variance imaging offers an improvement of up to 14 dB for the vast majority of the structure, compared to conventional imaging.

7.1.5.3 Phase Information

Chapter IV and VI demonstrated with simulated and experimental data, respectively, the significant improvement that can be achieved when phase information is used in the imaging algorithm. Figure 7.12 demonstrates the performance ratio maps when the analytic signals are used for imaging the same types of scatterers as in Figure 7.6 (which used the *envelope* of the analytic signals). As expected, the performance ratio maps all exhibit

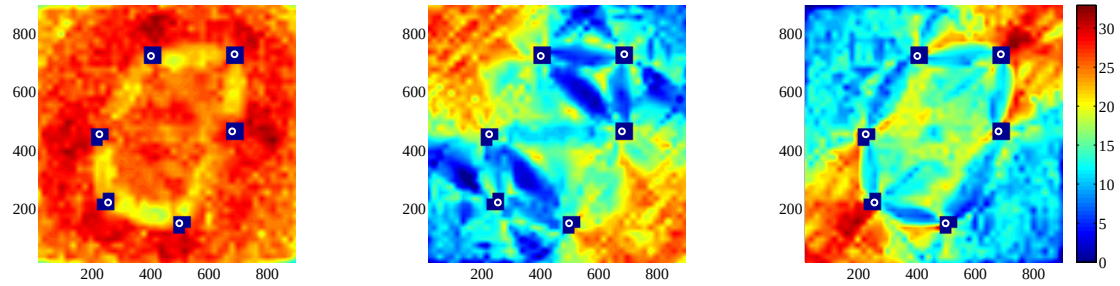

(a) (b) (c)

Figure 7.12: Performance ratio maps generated with minimum variance imaging and various scattering assumptions when phase information is used: (a) 5 mm through-hole, (b) +45° notch and (c) -45° notch.

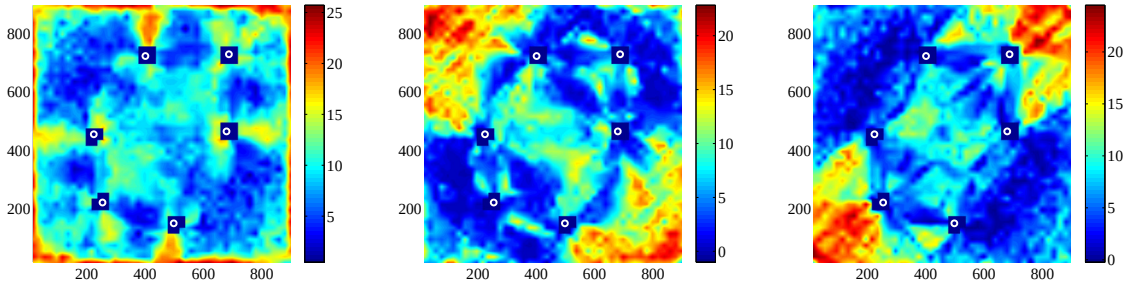

(a) (b) (c)

Figure 7.13: Comparison of performance ratio maps when phase information is used *vs.* envelope data for: (a) 5 mm through-hole, (b) +45° notch and (c) -45° notch.

improved ratios. To highlight the degree of improvement, Figure 7.13 depicts the *improvement* observed when using phase information over envelope data, similar to Figure 7.11. Figure 7.13 indicates that although there are a few areas of the structure (52 mm^2 in Figure 7.13b and 16 mm^2 in Figure 7.13c) that experience a degradation in performance ratio of up to -1 dB, most of the structure experiences a performance ratio improvement of 10-25 dB when phase information is used.

7.2 Damage Characterization

In addition to damage detection and localization, elliptical guided wave imaging algorithms also offer the potential to perform damage characterization. The geometric structure of a

damage site or defect, such as size, orientation, etc., has a profound impact on the scattering behavior. Significant efforts have been conducted to characterize and experimentally validate the scattering behavior of guided waves for through and partial through-thickness holes [134, 156, 135, 157, 122], notches [136, 158], and cracks [137, 159]. Since guided wave imaging algorithms have the ability to incorporate the anticipated scattering behavior of potential defects, these imaging algorithms can be used to distinguish between defect types. More specifically, the sensitivity of minimum variance imaging to anticipated scattering behavior allows the algorithm to clearly distinguish between damage types. This approach is similar to that used by Zhang *et al.* [138], which characterizes the scattering field of potential defects using bulk waves.

Damage characterization is performed by generating minimum variance images for various scattering assumptions and determining which image contains the strongest response at the potential damage location. The damage characteristics corresponding to scattering assumptions that cause the strongest response are taken to be the characteristics of the defect or damage.

7.2.1 Experimental Results

Experimental data was collected as described in Chapter III. Rather than use damage-free baseline data for baseline subtraction, however, baseline signals are chosen to be the data collected just prior to the introduction of each notch. This isolates the scattered energy from each notch without the complications of scattering from multiple defects. In the interest of simplicity, the envelope of the time domain signals is used for all imaging and parameter compensation is *not* performed.

Figure 7.14 illustrates damage characterization results when *conventional* imaging is used to characterize damage. Each subfigure of Figure 7.14 was generated with scattering assumptions corresponding to a 15 mm notch with orientations ranging from -75° to +90° in 15° increments. All scattering assumptions were based on FEM simulations described

in Section 7.1.2. The use of conventional imaging for damage characterization leaves some ambiguity as to the notch orientation, as significant peaks can be observed in the lower right corner for many of the images. One can identify consistent imaging artifacts visible between transducer pairs 1-2, 2-3, and 5-6 throughout Figure 7.14. These artifacts are characteristic of poor baseline subtraction and are likely due to small temperature variations that occurred during data acquisition.

Figure 7.15 illustrates damage characterization results using minimum variance imaging and *the same data* as used for Figure 7.14. Since Figure 7.15i clearly has the strongest response in the area of interest, the notch can be correctly discerned to be oriented at +45°. Figure 7.14 and Figure 7.15 demonstrate that while conventional imaging is unable to identify the damage type, minimum variance imaging is able to provide a clear indication of the notch orientation, and is therefore capable of performing damage characterization.

Figure 7.16 depicts minimum variance imaging results for scattering assumptions corresponding to a 15 mm notch oriented from -75° to 90° in 15° increments, similar to Figure 7.15, when a -45° notch is located in the center of the plate. The notch location in the center of the array is particularly challenging since it is a relatively large defect and strongly affects the direct arrivals of several transducer-receiver pairs. Although some of the imaging artifacts visible between transducers is likely due to some degree of baseline subtraction error, the fact that the notch is located in the direct path between transducers certainly contributes to these artifacts as well. Similarly, since the notch is located relatively close to *all* transducers (as compared to the previous case), geometric reflections of the scattered signals are expected to be much stronger. As such, the location of the notch may be contributing to the artifacts located outside of the array polygon. Even in the presence of these imaging artifacts, however, the minimum variance images in Figure 7.16 accurately indicate a notch orientation of -45° based on the observed scattering behavior from just six transducers.

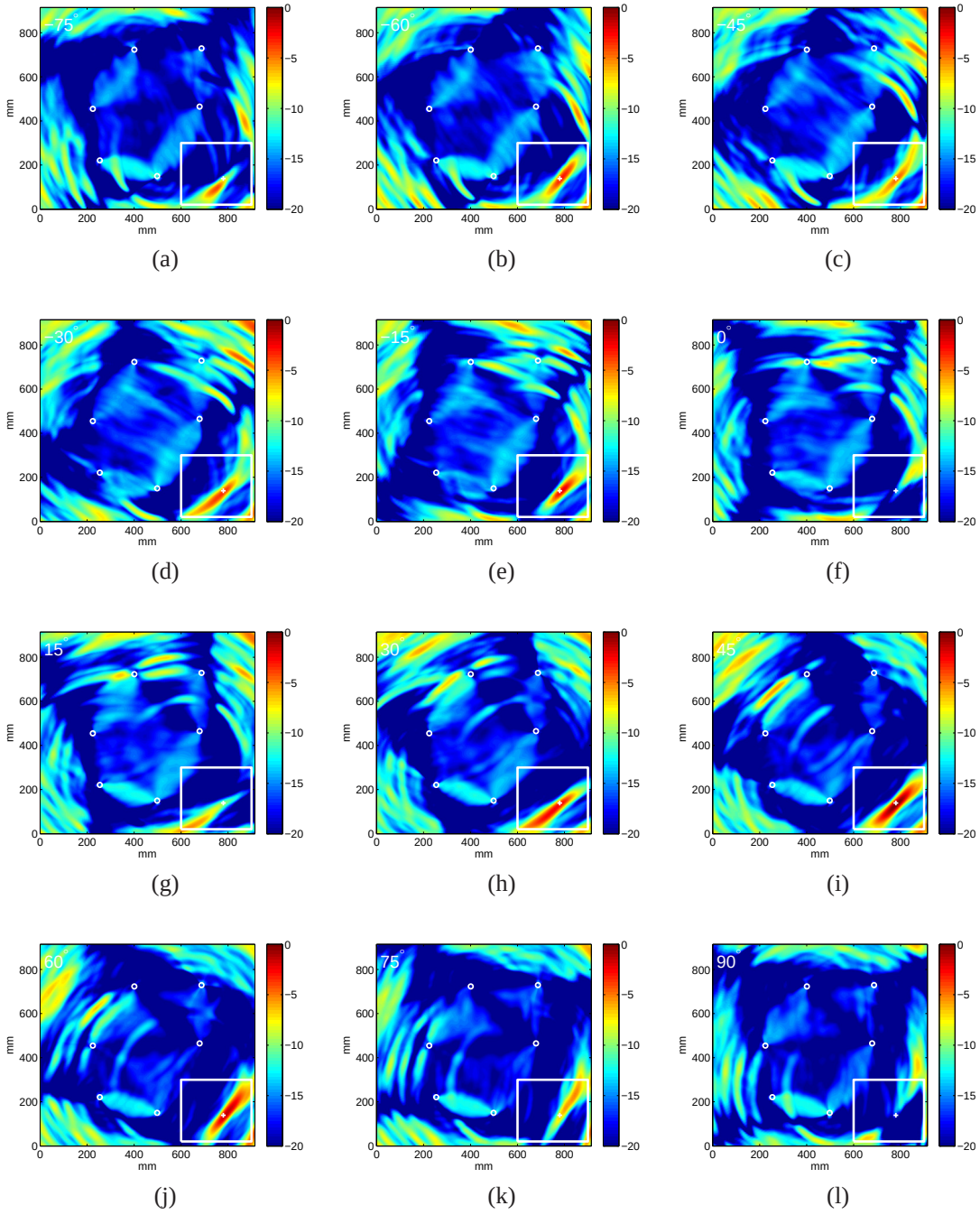

(a) (b) (c)

(d) (e) (f)

(g) (h) (i)

(j) (k) (l)

Figure 7.14: Comparison of conventional imaging results generated with +45° notch data and anticipated scattering behavior based on FEM simulations of a 15 mm through-thickness notch. (a)-(l) correspond to notch angles -75° to +90° in 15° increments. The white square indicates the area of interest based on conventional imaging.

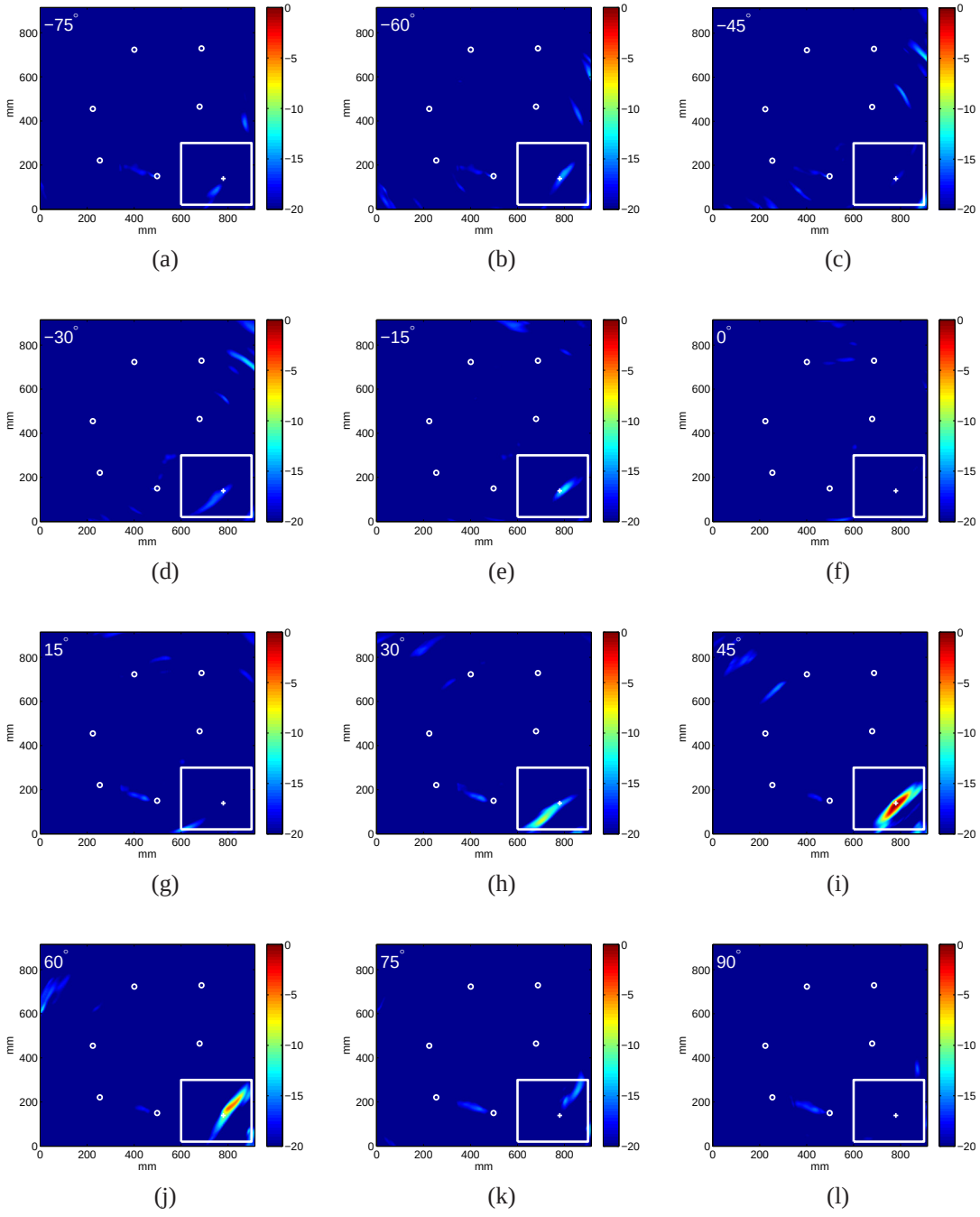

Figure 7.15: Comparison of minimum variance imaging results generated with +45° notch data and anticipated scattering behavior based on FEM simulations of a 15 mm through-thickness notch. (a)-(l) correspond to notch angles -75° to +90° in 15° increments. The white square indicates the area of interest based on conventional imaging.

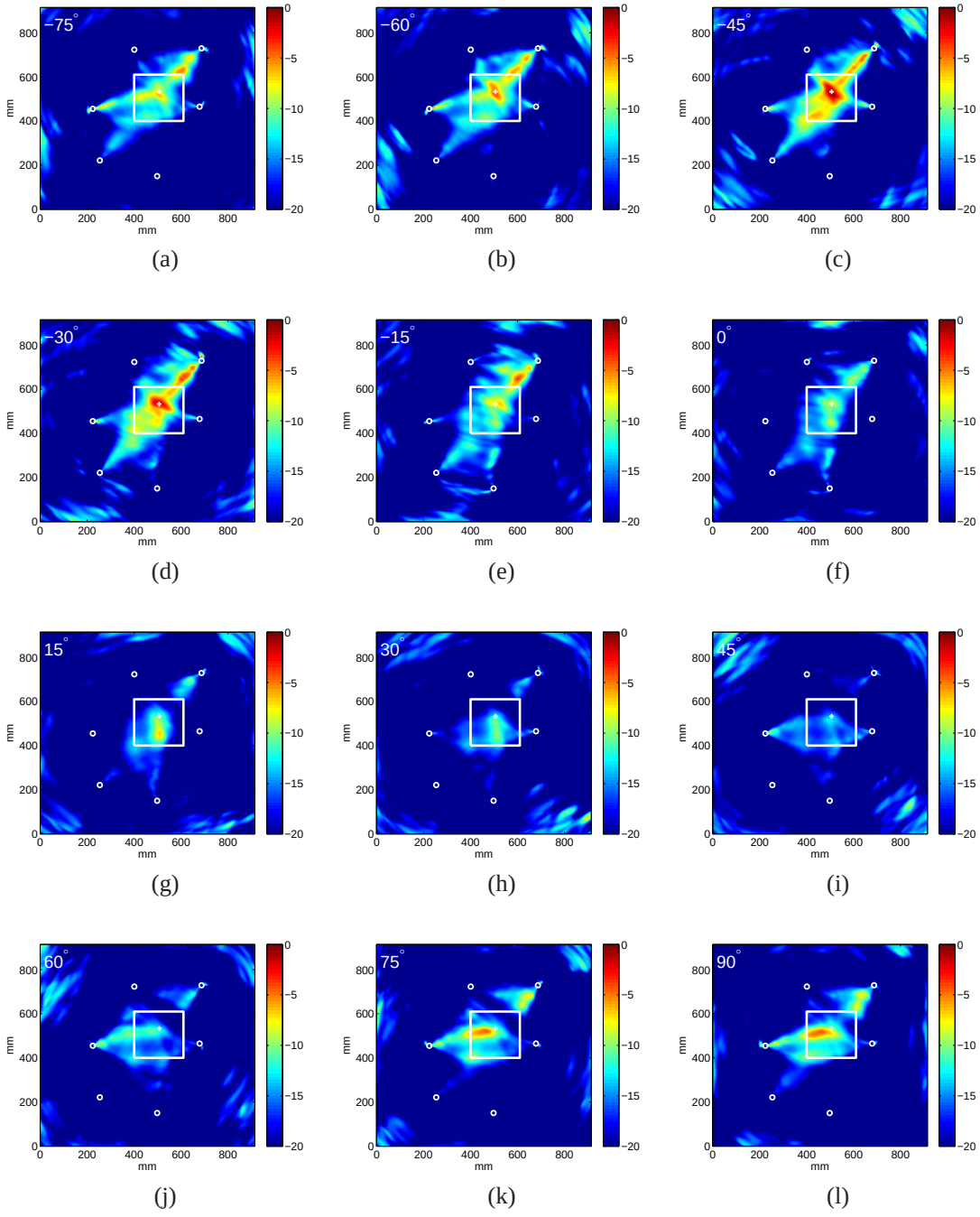

Figure 7.16: Comparison of minimum variance imaging results generated with -45° notch data and anticipated scattering behavior based on FEM simulations of a 15 mm through-thickness notch. (a)-(l) correspond to notch angles -75° to +90° in 15° increments. The white square indicates the area of interest based on conventional imaging.

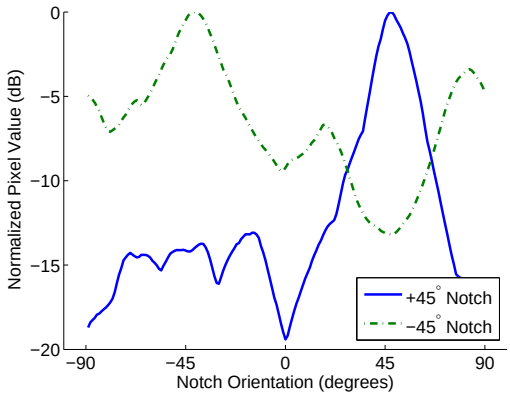

Figure 7.17: Maximum pixel value of minimum variance images shown as a function of assumed notch orientation for actual notches oriented ±45°.

The images presented in Figure 7.15 and Figure 7.16 correspond to large, 15° increments, that allow the reader to visualize the process. However, this becomes impractical as the orientation intervals are reduced. Figure 7.17 depicts the maximum pixel value for minimum variance images generated with scattering assumptions corresponding to notch orientations with 1° intervals. From Figure 7.17, the maximum pixel value is obtained when a notch of +47° is assumed for the +45° notch and when a notch of -38° is assumed for the -45° notch. The 2°-7° discrepancy in notch orientation may be due to any number of issues that have been raised throughout this text, including imperfect baseline subtraction, dispersive effects, errors in scattering assumptions, etc..

The experimental results shown in Figures 7.15, 7.16, and 7.17 demonstrate that minimum variance imaging with a sparse, distributed array of transducers *is* capable of characterizing the orientation of simulated damage. The approach demonstrated here for discerning notch orientation can be reasonably expected to successfully characterize other damage features as well, including type, size, depth, and shape, and also points to the need for more extensive FEM work.

7.3 Summary

This chapter has introduced a performance metric and method to analyze the ability of a distributed array to *simultaneously* detect and localize defects, demonstrated the effects

of array geometry and signal processing on that performance metric, and shown that in addition to detection and localization, damage *characterization* is also possible through the use of minimum variance imaging.

To address the fact that imaging artifacts are an inherent part of guided wave imaging, a pixel-specific performance ratio was defined that is the ratio of the pixel value when damage is present at that location to the maximum artifact value at that pixel location when damage is present elsewhere in the structure. Although the use of a pixel-specific ratio for array performance characterization can be computationally demanding, requiring the simulation of all possible damage types and locations, it provides a clear indication of how robust the array configuration is to system noise and modeling errors and whether or not simultaneous damage detection and localization can be performed.

Array aperture size, excitation function, phase information, and the choice of guided wave imaging algorithm were all shown to have a significant impact on array performance for the cases considered. Minimum variance imaging provided performance ratios that were an order of magnitude better than conventional imaging. The number of sensors, sensor pattern, and defect characteristics were also shown to impact performance ratios, although not to the same degree as imaging algorithm, excitation function, and aperture size. Finally, it is important to point out that *all* of the characteristics evaluated here are dependent on the specific interrogation structure. A structurally centered circular array of a specific radius may be optimal for one structure, yet perform miserably for another. This is because the performance ratio, $\hat{P}_{xy}$, is largely driven by the imaging artifacts, which are produced by scattered energy reflected from geometric features.

The ability to extract information about potential defects, such as size, depth, and orientation, can be used to discriminate between actual damage and benign changes or artifacts and provide supporting information for decisions regarding stress state, remaining life, and/or the need for additional inspection, repair, or replacement. Such decisions lie at the core of condition-based maintenance schedules, which are critical to aircraft airworthiness

and sustainment. Minimum variance imaging has been shown to be capable of performing damage characterization by using various scattering assumptions, which are obtained with FEM simulation, to generate multiple images of the structure. The damage characteristics that create the strongest pixel value at the defect location are taken to be those of the damage site or defect. The approach was shown to be effective with experimental data for 15 mm notches located both inside and outside the array polygon, in two different orientations.

CHAPTER VIII

CONCLUSIONS

The research presented here has investigated the benefits and challenges of adaptive dispersion compensation and ultrasonic guided wave imaging for SHM. Guided wave imaging techniques offer a promising tool for performing SHM in large plate-like structures, such as commercial aircraft skins, ship hulls, and storage tanks. The incorporation of MVDR into guided wave imaging algorithms, combined with the ability to adaptively estimate and compensate for guided wave propagation parameters, such as dispersion and composite transducer transfer functions, represents a significant contribution to the establishment of guided wave imaging as an economical method for long term monitoring of plate-like structures.

The incorporation of MVDR into conventional delay-and-sum imaging was introduced in Chapter IV along with three additional methods to improve imaging performance: use of expected scattering behavior, phase information, and instantaneous windowing. Instantaneous windowing was also shown to allow a re-formulation of the imaging algorithm that does not require a matrix inversion operation, significantly reducing computational requirements to the same order of magnitude as conventional imaging and allowing for vectorization of the problem, further improving computational efficiency. The proposed imaging algorithm and performance enhancement techniques were shown to significantly improve imaging performance with both simulated and experimental data, as indicated by a quantitative error metric.

A model-based parameter estimation (MBPE) algorithm was also developed and presented in Chapter V to adaptively estimate dispersion, transducer-specific transfer functions, transducer spacings, and propagation loss. Parameter estimation results from an *in*

situ sensor array were obtained from experimental data and compared to nominal values. In addition, measured signals were approximated with the parameter estimates, demonstrating that the assumed propagation model is capable of accurately describing the experimental data.

The adaptively estimated propagation parameters were incorporated into the ω–k mapping algorithm to perform adaptive dispersion compensation. Chapter VI investigated the benefits and challenges of performing dispersion compensation either before or after baseline subtraction, and quantified the impact that adaptive dispersion compensation has on guided wave imaging results.

Chapter VII presented a method to characterize the performance of a sparse, distributed array. A performance metric was established to quantify the ability of an array to identify damage throughout the entire interrogation structure. The imaging algorithm employed, excitation function, number of sensors, sensor arrangement, array aperture, and array location were all evaluated. For the aluminum plate used throughout this work and a point-like defect, the imaging algorithm, excitation function, and array aperture size were demonstrated to have the three largest impacts on overall performance.

Finally, a method to perform damage characterization was proposed in Chapter VII. The algorithm takes advantage of the sensitivity of minimum variance imaging to characterize defects or damage. Damage characterization, in the form of determining the orientation of a notch, was performed with experimental data for two different notch locations and orientations.

8.1 Conclusions

Several conclusions can be made from this work. First, the benefits of minimum variance imaging far exceed the minor additional computational demands. As such, there is little reason not to use minimum variance imaging in place of conventional delay-and-sum imaging.

Second, progressive improvements in guided wave imaging performance were demonstrated by incorporating scattering information, deconvolving the transducer transfer functions, and compensating for dispersion. Therefore, further guided wave imaging improvements can be reasonably be expected by the continued incorporation of *accurate* additional information.

Although parameter compensation can be performed *prior to* baseline subtraction, the baseline subtraction problem is ill-conditioned and *extremely* sensitive to errors in the parameter estimates. It was shown to work with simulation data, but due to the number of additional assumptions required, is not likely to be practical. In contrast, parameter compensation *after* baseline subtraction has been shown to be capable of producing noticeable imaging improvements without hypersensitivity to errors. Therefore, parameter compensation should be performed *after* baseline subtraction and the use of baseline subtraction algorithms like OBS and BSS.

Finally, identification of an optimal array configuration is a non-trivial task. The performance of an array is dependent on a large number of variables, including the interrogation structure, excitation function, and imaging algorithm. From the initial investigation presented in Chapter VII, it is highly unlikely that *any* arrangement of sensors will allow conventional imaging to out-perform minimum variance imaging. Similarly, the time- and/or spatial-support of the excitation function plays an equally strong role in performance. As the excitation function becomes more compact in time, however, the bandwidth of the signal increases, which in turn increases the effects of dispersion. These competing effects underscore the need for adaptive parameter estimation and dispersion compensation.

8.2 Contributions

The primary contributions of this work are (1) the adaptation of the MVDR algorithm to *in situ* guided wave imaging algorithms, (2) the development of a model-based algorithm for adaptively estimating wave propagation parameters with minimal *a priori* information,

(3) the incorporation of these adaptively estimated parameters into guided wave imaging algorithms through the ω–k mapping algorithm, (4) a methodology for quantitatively characterizing the ability of an array to detect and locate damage throughout a structure, and (5) a methodology for characterizing defects or damage using guided waves generated from a spatially distributed array.

Incorporation of MVDR into the conventional imaging algorithm was quantitatively shown to provide significant imaging improvement with minimal additional computational complexity. In addition, by reformulating the elliptical guided wave imaging algorithm into a multi-channel estimation problem, a wide range of covariance techniques can now be applied.

Although used exclusively to characterize ultrasonic guided waves in this text, the MBPE algorithm allows *any* system incorporating acoustic, electromagnetic, or elastic waves to characterize dispersion curves, propagation loss, propagation distances, as well as transmitter and receiver transfer functions *in situ* at the time of test, thereby avoiding potentially erroneous *a priori* assumptions. At this time, the MBPE algorithm is the *only* method available to simultaneously obtain all of these parameters with *in situ* measurements and minimal *a priori* assumptions.

The incorporation of MBPE parameter estimates into the ω–k mapping algorithm provides a powerful tool to leverage the adaptive parameter estimates for the benefit of guided wave imaging applications. The use of distance domain signals for sparse, distributed array imaging has been shown to be a computationally efficient method to perform dispersion compensation with adaptively estimated parameters.

Since imaging artifacts are an inherent part of guided wave imaging algorithms, the geometry of the structure under consideration is a key factor in array performance. The imaging performance of a specific sparse, distributed array configuration can now be quantitatively characterized for a specific structure using the methodology presented in Chapter VII. This initial investigation into array configurations identified the significance of the

imaging algorithm, excitation function, and array aperture size.

The ability to *characterize* defects or damage with a sparse, distributed array represents a new capability for SHM systems and is made possible through the use of minimum variance imaging. Since remaining useful life and stress state are directly related to fatigue crack size, damage characterization is an important step towards the use of ultrasonic guided waves for condition-based maintenance.

8.3 Future Work

The work performed to date has created a solid theoretical basis for adaptive parameter estimation and minimum variance imaging. However, a considerable amount of work remains if ultrasonic guided wave imaging is ever to become a feasible alternative to current in-service NDE inspections.

First, now that both MPBE and minimum variance imaging have been successfully demonstrated experimentally in the laboratory, it is crucial to apply both algorithms to more realistic, and therefore both larger and more complex, structures. Regardless of how realistic the interrogation structure is, it is important that the size and complexity be increased simultaneously. Small laboratory experiments of *complex* structures present an unrealistically challenging environment because of the excessive amplitude and quantity of echoes from boundary reflections. As such, future experiments should be careful to increase both the *size* of the interrogation structure in addition to increasing complexity.

The work presented here has demonstrated a significantly improved ability to detect, locate, and characterize defects such as through-holes and/or notches. It is important, however, for a similar ability to be demonstrated with more practical defect and damage types, such as fatigue cracks, missing fasteners, corrosion, etc.

Finally, it appears that one of the major remaining hurdles for the widespread adoption of ultrasonic guided wave imaging is the establishment of quantitative probability of detection (POD) and probability of false alarm (PFA) metrics. Although the method

demonstrated in Chapter VII represents a first step in this direction, such an analysis is very difficult and appears to only be possible with a simulation of the structure for every possible damage type and location. Until POD and PFA can be quantified, however, SHM is unlikely to be adopted for long-term monitoring of structures that affect the health and safety of human life.

APPENDIX A

REQUIRED SAMPLES FOR MBPE

This appendix derives (5.5), which presents a lower bound for the number of samples required to perform MBPE. Group velocity and receiver distance estimation is based on measured differences in the phase-response of each received signal. The phase-response of a single-mode direct arrival is described as in (5.4b):

$$\angle M(\omega) = \angle T(\omega) + \angle R(\omega) - k(\omega)\, d + 2\pi b. \tag{A.1}$$

The challenges associated with the modulo nature of the phase information can be addressed through the use of an unwrapped phase-response. As discussed in Section 5.1, an assumption must be made that the maximum angular change between two adjacent frequencies of each received signal is less than π. Ignoring the impact of noise, the angular change between two adjacent frequencies of a Fast Fourier Transform (FFT) is obtained from (A.1) as:

$$\begin{aligned}\left(\frac{\partial}{\partial\omega}\angle M(\omega)\right)\Delta\omega &= \left(\frac{\partial}{\partial\omega}\angle T(\omega) + \frac{\partial}{\partial\omega}\angle R(\omega) - d\frac{\partial}{\partial\omega}k(\omega)\right)\Delta\omega, \\ &= \left(\frac{\partial}{\partial\omega}\angle T(\omega) + \frac{\partial}{\partial\omega}\angle R(\omega) - \frac{d}{c_g(\omega)}\right)\Delta\omega,\end{aligned} \tag{A.2}$$

where $\Delta\omega$ is the spacing between FFT frequency bins and $c_g(\omega)$ is the group velocity, defined as $\partial\omega/\partial k(\omega)$ in (3.2). The impact of noise on the phase-response is related to the SNR for that specific frequency, $Q(\omega)$. The maximum angular deviation in phase for a specific frequency due to noise with magnitude $|N|$ is

$$\Delta\theta(\omega) = \sin^{-1}\left(\frac{|N|}{|M(\omega)|}\right) = \sin^{-1}\left(\frac{1}{Q(\omega)}\right) \tag{A.3}$$

For the angular change between frequencies to be less than π for any ω, the angular change between two adjacent frequencies due to the signal, (A.2), and twice the maximum angular

deviation that is possible from either bin due to noise, (A.3) must sum to less than π:

$$2\sin^{-1}\left(\frac{1}{Q_{\min}}\right)+\left|\frac{\partial}{\partial\omega}\angle T(\omega)+\frac{\partial}{\partial\omega}\angle R(\omega)-\frac{d_{\max}}{c_{\min}}\right|\Delta\omega<\pi \tag{A.4}$$

Here, the minimum SNR of any frequency, $Q_{\min}$, the maximum distance between transmitter and any receiver, $d_{\max}$, and the minimum group velocity for any propagating mode at any excited frequency, $c_{\min}$, are used to preserve the inequality and extend the bound to any receiver, propagating mode, and excited frequency. Note that for many cases, including the case described here, the derivative of the transmitter and receiver phase-responses in (A.4) can be safely ignored because they will be much smaller than the $d_{\max}/c_{\min}$ term. Substituting $\Delta\omega = 2\pi F_s/n_n$ where F_s is the sampling frequency and n_n is the number of samples, (A.4) can be rearranged as:

$$n_n > \frac{2\pi F_s d_{\max}}{c_{\min}\left[\pi - 2\sin^{-1}\left(\frac{1}{Q_{\min}}\right)\right]}, \tag{A.5}$$

which is presented in (5.5). Note that the number of samples can be increased to n_n or greater by padding the direct arrival signals with zeros and, thus, does not translate to any operational system requirements.

APPENDIX B

PROXIMITY OF κ OFFSET VALUES FOR MBPE

It is possible to establish a lower-bound on the ambiguity of κ. To begin, let κ be re-defined as a summation of the actual or true value, $\hat{\kappa}$, and some error, κ_δ:

$$\kappa = \hat{\kappa} + \kappa_\delta. \tag{B.1}$$

Also, redefine the all-integer vector, $\vec{\mathbf{b}}$, similarly:

$$\vec{\mathbf{b}} = \hat{\mathbf{b}}_{\mathrm{A}}^{=} + \vec{\mathbf{b}}_\delta, \tag{B.2}$$

where $\hat{\mathbf{b}}_{\mathrm{A}}^{=}$ corresponds to the true all-integer vector and $\vec{\mathbf{b}}_\delta$ is an *all-integer error term*. Finally, recall the system of linear equations used to model the phase response of the measured direct arrivals from (5.10):

$$\mathbf{M}_\Im = \mathbf{Q}_{\mathrm{T}}\mathbf{T}_\Delta + \mathbf{Q}_\tau \vec{\boldsymbol{\tau}}\, \vec{\mathbf{1}}_w^{\mathrm{T}} + \mathbf{Q}_{\mathrm{R}}\mathbf{R}_\Delta + \mathbf{Q}_\rho \vec{\boldsymbol{\rho}}\, \vec{\mathbf{1}}_w^{\mathrm{T}} - \vec{\mathbf{d}}\, \vec{\mathbf{k}}_\Delta^{\mathrm{T}} - \kappa \vec{\mathbf{d}}\, \vec{\mathbf{1}}_w^{\mathrm{T}} + 2\pi \vec{\mathbf{b}}\, \vec{\mathbf{1}}_w^{\mathrm{T}}. \tag{B.3}$$

The ambiguity of κ arises from the fact that the system of linear equations in (B.3) describe the received signals, $\mathbf{M}_\Im$, equally well when $\vec{\mathbf{d}}\,\kappa_\delta$ is an *all integer vector*. Mathematically, this is equivalent to:

$$\vec{\mathbf{d}}\,\kappa_\delta = 2\pi \vec{\mathbf{b}}_\delta. \tag{B.4}$$

Let α be scalar value such that $\alpha\vec{\mathbf{d}}$ is an all-integer vector. Then the smallest value of κ_δ that satisfies (B.4), $\kappa_{\min}$, must satisfy:

$$\kappa_{\min} = \frac{2\pi\alpha}{\gcd\left(\alpha\vec{\mathbf{d}}\right)}. \tag{B.5}$$

Here $\gcd(\cdot)$ represents the greatest common denominator for all vector elements within the parentheses.

Since there are some uncertainties in receiver distances, both due to measurement uncertainty and the finite size of the transducers, a path accuracy is defined as

$$d_\delta = 10^{\lceil \log_{10}(2d_t) \rceil}, \tag{B.6}$$

where d_t is the uncertainty of the effective transducer location and $\lceil \cdot \rceil$ represents the ceiling function. Let $\vec{\mathbf{d}}_\mathrm{m}$ be the measured (nominal) distance vector. Given the uncertainty in distance measurement indicated by d_δ, it is possible that $\vec{\mathbf{d}}_m / d_\delta$ is very close to an all-integer vector. Therefore, (B.5) can be modified to bound κ_min:

$$\kappa_\mathrm{min} \geq \frac{2\pi}{d_\delta \gcd\left(\left[\!\left[\frac{1}{d_\delta}\vec{\mathbf{d}}_\mathrm{m}\right]\!\right]\right)}. \tag{B.7}$$

As $d_\delta \to 0$, κ_min approaches a stable value.

REFERENCES

[1] FAA, *Federal Aviation Regulations*. Title 14: Part 43, 2009.

[2] FAA, *Federal Aviation Regulations*. Title 14: Part 91, 2009.

[3] of Naval Operations, C., *The Naval Aviation Maintenance Program (NAMP)*. OPNAVINST 4790.2J, 2005.

[4] Michaels, J. E. and Michaels, T. E., "Detection of structural damage from the local temporal coherence of diffuse ultrasonic signals," *IEEE Trans. Ultrason., Ferroelectr., Freq. Control*, vol. 52, no. 10, pp. 1769–1782, 2005.

[5] Zhao, X., Gao, H., Zhang, G., Ayhan, B., Yan, F., Kwan, C., and Rose, J. L., "Active health monitoring of an aircraft wing with embedded piezoelectric sensor/actuator netork: I. Defect detection, localization, and growth monitoring," *Smart Mater. Struct.*, vol. 16, pp. 1208–1217, 2007.

[6] Michaels, T. E., Michaels, J. E., Mi, B., and Ruzzene, M., "Damage detection in plate structures using sparse ultrasonic transducer arrays and acoustic wavefield imaging," in *Review of Progress in QNDE*, vol. 24, pp. 938–945, 2005.

[7] Rose, J. L., "A baseline and vision of ultrasonic guided wave inspection potential," *J. Pressure Vessel Technol.*, vol. 124, pp. 273–282, 2002.

[8] Giurgiutiu, V., *Structural Health Monitoring with Piezoelectric Wafer Active Sensors*. San Diego: Academic Press, 2008.

[9] Ackerman, A. J., "America's abundant electricity and the ASME boiler code," *IEEE Trans. Aerosp. Electron. Sys.*, vol. AES-15, no. 6, pp. 787–793, 1979.

[10] Hellier, C. J., *Handbook of Nondestructive Evaluation*. McGraw-Hill Professional, 2001.

[11] Pierce, A. D., *Acoustics: An Introduction to Its Physical Principles and Applications*. Acoustical Society of America, 1989.

[12] Newton, I., *Philosophiae Naturalis Principia Mathematica*. Royal Society London, 1687.

[13] Rayleigh, J. W. S., *The Theory of Sound*. Dover, 1945.

[14] Rayleigh, L., "On waves propagated along the plane surface of an elastic solid," *Proc. Lond. Math. Soc.*, vol. 17, pp. 4–11, 1885.

[15] Rayleigh, L., "On the free vibrations of an infinite plate of homogeneous isotropic elastic matter," *Proc. Lond. Math. Soc.*, vol. 20, pp. 225–234, 1889.

[16] Lamb, H., "On waves in an elastic plate," *Proc. Royal Soc. Lond.*, vol. 93, no. 648, pp. 114–128, 1917.

[17] Viktorov, I. A., ed., *Rayleigh and Lamb Waves: Physical Theory and Applications*. Plenum Press, 1967.

[18] Sokolov, S. Y., "On the problem of the propagation of ultrasonic oscillations in various bodies," *Elec. Nachr. Tech.*, vol. 6, pp. 454–460, 1929.

[19] Sokolov, S. Y., "Ultrasonic methods of detecting internal flaws in metal articles," *Zavodskaya Laoratoriya*, vol. 4, pp. 1468–1473, 1935.

[20] Mulhauser, O., *Verfahren zur Zustandsbestimmung von Werkstoffen, Besonders zur Ermittlung von Fehlern Darin*. German patent: 569,598, 1933.

[21] Firestone, F. A., *Flaw Detecting Device and Measuring Instrument*. United States Patent: 2,280,226, 1940.

[22] Sproule, D. O., *Echo Sounding Installation*. United States Patent: 2,252,275, 1939.

[23] Kino, G. S., "Acoustic imaging for nondestructive evaluation," *Proc. IEEE*, vol. 67, no. 4, pp. 510–525, 1979.

[24] Braun, F., "On directed wireless telegraphy," *Electrician*, vol. 57, pp. 222–224, 244–248, 1906.

[25] Somer, J. C., "Electronic sector scanning for ultrasonic diagnosis," *Ultrasonics*, vol. 6, no. 3, pp. 153–159, 1968.

[26] Whittington, K. R. C., B. D., "Electronic steering and focussing of ultrasonic beams in tube inspection," *Ultrasonics*, vol. 7, no. 1, pp. 20–25, 1969.

[27] Thomenius, K. E., "Evolution of ultrasound beamformers," in *IEEE Ultrason. Symp.*, pp. 1615–1622, 1996.

[28] Olympus NDT Inc., www.olympus-ims.com/en/ultrasonics/intro-to-pa.

[29] Drinkwater, B. W. and Wilcox, P. D., "Ultrasonic arrays for non-destructive evaluation: A review," *NDT & E Int.*, vol. 39, no. 7, pp. 525–541, 2006.

[30] Johnson, D. and Dudgeon, D., *Array Signal Processing Concepts and Techniques*. Prentice Hall Professional, 1993.

[31] Mailloux, R. J., "Phased array theory and technology," *Proc. IEEE*, vol. 70, no. 3, pp. 246–291, 1982.

[32] Mailloux, R. J., *Phased Array Antenna Handbook*. Norwood: Artech House, Inc, 2005.

[33] Krim, H. and Viberg, M., "Two decades of array signal processing research," *IEEE Signal Process. Mag.*, vol. 13, no. 4, pp. 67–94, 1996.

[34] Claerbout, J. F., "Detection of *P*-waves from weak sources at great distances," *Geophysics*, vol. 29, no. 2, pp. 197–211, 1964.

[35] Burg, J. P., "Three-dimensional filtering with an array of seismometers," *Geophysics*, vol. 29, no. 5, pp. 693–713, 1964.

[36] Wiener, N., *Extrapolation, Interpolation and Smoothing of Stationary Time Series*. John Wiley and Sons, 1949.

[37] Backus, M., Burg, J., Baldwin, D., and Bryan, E., "Wide-band extraction of mantle *P* waves from ambient noise," *Geophysics*, vol. 29, no. 5, pp. 672–692, 1964.

[38] Wiggins, R. A. and Robinson, E. A., "Recursive solution to the multichannel filtering problem," *J. Geophys. Res.*, vol. 70, no. 8, pp. 1885–1891, 1965.

[39] Robinson, E. A., "Mathematical development of discrete filters for detection of nuclear explosions," *J. Geophys. Res.*, vol. 68, no. 19, pp. 5559–5567, 1963.

[40] Widrow, B., Mantey, P. E., Griffiths, L. J., and Goode, B. B., "Adaptive antenna systems," *Proc. IEEE*, vol. 55, no. 12, pp. 2143–2159, 1967.

[41] Widrow, B. and Hoff, M. E., J., "Adaptive switching circuits," *IRE WESCON Conv. Rec.*, vol. 4, pp. 96–104, 1960.

[42] Griffiths, L. J., "A simple adaptive algorithm for real-time processing in antenna arrays," *Proc. IEEE*, vol. 57, no. 10, pp. 1696–1704, 1969.

[43] Capon, J., Greenfield, R. J., and Kolker, R. J., "Multidimensional maximum-likelihood processing of a large aperture seismic array," *Proc. IEEE*, vol. 55, no. 2, pp. 192–211, 1967.

[44] Griffiths, L. J., "A comparison of multidimensional Wiener and maximum-likelihood filters for antenna arrays," *Proc. IEEE*, vol. 55, no. 11, pp. 2045–2047, 1967.

[45] Capon, J., "High-resolution frequency-wavenumber spectrum analysis," *Proc. IEEE*, vol. 57, no. 8, pp. 1408–1418, 1969.

[46] Claerbout, J. F., "A summary, by illustrations, of least-squares filters with constraints," *IEEE Trans. Inf. Theory*, vol. IT-14, no. 2, pp. 269–272, 1968.

[47] Frost, O. L., "An algorithm for linearly constrained adaptive array processing," *Proc. IEEE*, vol. 60, no. 8, pp. 926–935, 1972.

[48] Owsley, N. L., "Enhanced minimum variance beamforming," *Underwater Acoustic Data Processing*, 1989.

[49] Abraham, D. A. and Owsley, N. L., "Beamforming with dominant mode rejection," in *OCEANS '90*, pp. 470–475, 1990.

[50] Lorenz, R. G. and Boyd, S. P., "Robust minimum variance beamforming," *IEEE Trans. Signal Process.*, vol. 53, no. 5, pp. 1684–1696, 2005.

[51] He, J., Liu, Z., and Wong, K. T., "Linearly constrained minimum-geometric power adaptive beamforming using logarithmic moments of data containing heavy-tailed noise of unknown statistics," *IEEE Antennas Wireless Propag. Lett.*, vol. 6, pp. 600–603, 2007.

[52] Mann, J. A. and Walker, W. F., "A constrained adaptive beamformer for medical ultrasound: Initial results," in *IEEE Ultrason. Symp.*, pp. 1807–1810, 2002.

[53] Wang, Z., Li, J., and Wu, R., "Time-delay- and time-reversal-based robust Capon beamformers for ultrasound imaging," *IEEE Trans. Med. Imag.*, vol. 24, no. 10, pp. 1308–1322, 2005.

[54] Synnevag, J.-F., Austeng, A., and Holm, S., "Adaptive beamforming applied to medical ultrasound imaging," *IEEE Trans. Ultrason., Ferroelectr., Freq. Control*, vol. 54, no. 8, pp. 1606–1613, 2007.

[55] Holfort, I. K., Gran, F., and Jensen, J. A., "Broadband minimum variance beamforming for ultrasound imaging," *IEEE Trans. Ultrason., Ferroelectr., Freq. Control*, vol. 56, no. 2, pp. 314–325, 2009.

[56] Firestone, F. A. and Ling, D. S., J., *Method and means for generating and utilizing vibrational waves in plates*. United States Patent: 2,536,128, 1951.

[57] Worlton, D. C., "Ultrasonic testing with Lamb waves," *Nondestructive Testing*, vol. 15, pp. 218–222, 1957.

[58] Grigsby, T. N. and Tajchman, E. J., "Properties of Lamb waves relevant to the ultrasonic inspection of thin plates," *IRE Trans. Ultrason. Eng.*, vol. 8, no. 1, pp. 26–33, 1961.

[59] Jansen, D. P. and Hutchins, D. A., "Lamb wave tomography," in *IEEE Ultrason. Symp.*, pp. 1017–1020, 1990.

[60] McKeon, J. C. P. and Hinders, M. K., "Parallel projection and crosshole Lamb wave contact scanning tomography," *J. Acoust. Soc. Am.*, vol. 106, no. 5, pp. 2568–2577, 1999.

[61] Malyarenko, E. V. and Hinders, M. K., "Fan beam and double crosshole Lamb wave tomography for mapping flaws in aging aircraft structures," *J. Acoust. Soc. Am.*, vol. 108, no. 4, pp. 1631–1639, 2000.

[62] Prasad, S. M., Balasubramaniam, K., and Krishnamurthy, C. V., "Structural health monitoring of composite structures using Lamb wave tomography," *Smart Mater. Struct.*, vol. 13, no. 5, pp. N77–N79, 2004.

[63] Hou, J., Leonard, K. R., and Hinders, M. K., "Automatic multi-mode Lamb wave arrival time extraction for improved tomographic reconstruction," *Inverse Prob.*, vol. 20, pp. 1873–1888, 2004.

[64] Malyarenko, E. V. and Hinders, M. K., "Ultrasonic Lamb wave diffraction tomography," *Ultrasonics*, vol. 39, pp. 269–281, 2001.

[65] Subbarao, P. M. V., Munshi, P., and Muralidhar, K., "Performance of iterative tomographic algorithms applied to non-destructive evaluation with limited data," *NDT & E Int.*, vol. 30, no. 6, pp. 359–370, 1997.

[66] Kak, A. C. and Slaney, M., *Principles of Computerized Tomographic Imaging*. New York: IEEE, 1988.

[67] Deutsch, W. A. K., Cheng, A., and Achenbach, J. D., "Self-focusing of Rayleigh waves and Lamb waves with a linear phased array," *Res. Nondestruct. Eval.*, vol. 9, no. 2, pp. 81–95, 1997.

[68] Fink, M., "Time reversal of ultrasonic fields - Part I: Basic principles," *IEEE Trans. Ultrason., Ferroelectr., Freq. Control*, vol. 39, no. 5, pp. 555–566, 1992.

[69] Beardsley, B., Peterson, M., and Achenbach, J. D., "A simple scheme for self-focusing of an array," *J. Nondestruct. Eval.*, vol. 14, no. 4, pp. 169–179, 1995.

[70] Monkhouse, R. S. C., Wilcox, P. D., and Cawley, P., "Flexible interdigital PVDF transducers for the generation of Lamb waves in structures," *Ultrasonics*, vol. 35, no. 7, pp. 489–498, 1997.

[71] Rose, J. L., Pelts, S. P., and Quarry, M. J., "A comb transducer model for guided wave NDE," *Ultrasonics*, vol. 36, no. 1-5, pp. 163–169, 1998.

[72] Zhu, W. and Rose, J. L., "Lamb wave generation and reception with time-delay periodic linear arrays: A BEM simulation and experimental study," *IEEE Trans. Ultrason., Ferroelectr., Freq. Control*, vol. 46, no. 3, pp. 654–664, 1999.

[73] Monkhouse, R. S. C., Wilcox, P. D., Lowe, M. J. S., Dalton, R. P., and Cawley, P., "The rapid monitoring of structures using interdigital Lamb wave transducers," *Smart Mater. Struct.*, vol. 9, no. 3, pp. 304–309, 2000.

[74] Wilcox, P. D., Lowe, M. J. S., and Cawley, P., "Lamb and SH wave transducer arrays for the inspection of large areas of thick plates," in *Review of Progress in QNDE*, pp. 1049–1056, 2000.

[75] Holmes, C., Drinkwater, B. W., and Wilcox, P. D., "Post-processing of the full matrix of ultrasonic transmit-receive array data for non-destructive evaluation," *NDT & E Int.*, vol. 38, no. 8, pp. 701–711, 2005.

[76] Giurgiutiu, V. and Bao, J., "Embedded-ultrasonics structural radar for in situ structural health monitoring of thin-wall structures," *Struct. Health Monit.*, vol. 3, no. 2, pp. 121–140, 2004.

[77] Wilcox, P. D., "Omni-directional guided wave transducer arrays for the rapid inspection of large areas of plate structures," *IEEE Trans. Ultrason., Ferroelectr., Freq. Control*, vol. 50, no. 6, pp. 699–709, 2003.

[78] Wilcox, P. D., Lowe, M. J. S., and Cawley, P., "Omnidirectional guided wave inspection of large metallic plate structures using an EMAT array," *IEEE Trans. Ultrason., Ferroelectr., Freq. Control*, vol. 52, no. 4, pp. 653–665, 2005.

[79] Fromme, P., Wilcox, P. D., Lowe, M. J. S., and Cawley, P., "On the development and testing of a guided ultrasonic wave array for structural integrity monitoring," *IEEE Trans. Ultrason. Ferroelectr. Freq. Control*, vol. 53, no. 4, pp. 777–785, 2006.

[80] Velichko, A. and Wilcox, P. D., "Guided wave arrays for high resolution inspection," *J. Acoust. Soc. Am.*, vol. 123, no. 1, pp. 186–196, 2008.

[81] Wilcox, P., Lowe, M., and Cawley, P., "The effect of dispersion on long-range inspection using ultrasonic guided waves," *NDT & E Int.*, vol. 34, no. 1, pp. 1–9, 2001.

[82] Michaels, J. E., "Detection, localization and characterization of damage in plates with an *in situ* array of spatially distributed sensors," *Smart Mater. Struct.*, vol. 17, no. 035035, 2008.

[83] Croxford, A. J., Wilcox, P. D., Drinkwater, B. W., and Konstantinidis, G., "Strategies for guided-wave structural health monitoring," *Proc. Royal Soc. A*, vol. 463, pp. 2961–2981, 2007.

[84] Sicard, R., Goyette, J., and Zellouf, D., "A numerical dispersion compensation technique for time recompression of Lamb wave signals," *Ultrasonics*, vol. 40, pp. 727–732, 2002.

[85] Wilcox, P. D., "A rapid signal processing technique to remove the effect of dispersion from guided wave signals," *IEEE Trans. Ultrason., Ferroelectr., Freq. Control*, vol. 50, no. 4, pp. 419–427, 2003.

[86] Sicard, R., Goyette, J., and Zellouf, D., "A SAFT algorithm for Lamb wave imaging of isotropic plate-like structures," *Ultrasonics*, vol. 39, pp. 487–494, 2002.

[87] Sachse, W. and Pao, Y.-H., "On the determination of phase and group velocities of dispersive waves in solids," *J. Appl. Phys.*, vol. 49, no. 8, pp. 4320–4327, 1978.

[88] Peters, F. and Petit, L., "A broad band spectroscopy method for ultrasound wave velocity and attenuation measurement in dispersive media," *Ultrasonics*, vol. 41, no. 357-363, 2003.

[89] Hutchins, D. A., Lundgren, K., and Palmer, S. B., "A laser study of transient Lamb waves in thin materials," *J. Acoust. Soc. Am.*, vol. 85, no. 4, pp. 1441–1448, 1989.

[90] Kwun, H. and Bartels, K. A., "Experimental observation of elastic-wave dispersion in bounded solids of various configurations," *J. Acoust. Soc. Am.*, vol. 99, no. 2, pp. 962–968, 1996.

[91] Prosser, W. H., Seale, M. D., and Smith, B. T., "Time-frequency analysis of Lamb modes," *J. Acoust. Soc. Am.*, vol. 105, no. 5, pp. 2669–2676, 1999.

[92] Neithammer, M., Jacobs, L. J., Qu, J., and Jarzynski, J., "Time-frequency representation of Lamb waves," *J. Acoust. Soc. Am.*, vol. 109, no. 5, pp. 97–102, 2001.

[93] Alleyne, D. and Cawley, P., "A two-dimensional Fourier transform method for the measurement of propagating multimode signals," *J. Acoust. Soc. Am.*, vol. 89, no. 3, pp. 1159–1168, 1991.

[94] Holland, S., Kosel, T., Weaver, R., and Sachse, W., "Determination of plate source, detector separation from one signal," *Ultrasonics*, vol. 38, no. 1-8, pp. 620–623, 2000.

[95] Konstantinidis, G., Wilcox, P. D., and Drinkwater, B. W., "An investigation into the temperature stability of a guided wave structural health monitoring system using permanently attached sensors," *IEEE Sensors J.*, vol. 7, no. 5, pp. 905–912, 2007.

[96] Scalea, F. L. d. and Salamone, S., "Temperature effects in ultrasonic Lamb wave structural health monitoring systems," *J. Acoust. Soc. Am.*, vol. 124, no. 1, pp. 161–173, 2008.

[97] Weaver, R. L. and Lobkis, O. I., "Temperature dependence of diffuse field phase," *Ultrasonics*, vol. 38, no. 1-8, pp. 491–494, 2000.

[98] Lu, Y. and Michaels, J. E., "A methodology for structural health monitoring with diffuse ultrasonic waves in the presence of temperature variations," *Ultrasonics*, vol. 43, pp. 717–731, 2005.

[99] Croxford, A. J., Wilcox, P. D., Konstantinidis, G., and Drinkwater, B. W., "Strategies for overcoming the effect of temperature on guided wave structural health monitoring," *Proc. SPIE*, vol. 6532, no. 65321T, pp. 1–10, 2007.

[100] Konstantinidis, G., Drinkwater, B. W., and Wilcox, P. D., "The temperature stability of guided wave structural health monitoring systems," *Smart Mater. Struct.*, vol. 15, pp. 967–976, 2006.

[101] Raghavan, A. and Cesnik, E. S., "Effects of elevated temperature on guided-wave structural health monitoring," *J. Intel. Mat. Syst. Str.*, vol. 19, no. 12, pp. 1383–1398, 2008.

[102] Wilcox, P. D., Croxford, A. J., Michaels, J. E., Lu, Y., and Drinkwater, B. W., "A comparison of temperature compensation methods for guided wave structural health monitoring," in *Review of Progress in QNDE*, vol. 27, pp. 1453–1460, 2008.

[103] Croxford, A. J., Wilcox, P. D., and Drinkwater, B. W., "Quantification of sensor geometry performance for guided wave SHM," *Proc. SPIE*, vol. 7295, no. 72951H, pp. 1–10, 2009.

[104] Croxford, A. J., Moll, J., Wilcox, P. D., and Michaels, J. E., "Efficient temperature compensation strategies for guided wave structural health monitoring," *Ultrasonics*, vol. 50, no. 4-5, pp. 517–528, 2010.

[105] Gao, H., Shi, Y., and Rose, J. L., "Guided wave tomography on an aircraft wing with leave in place sensors," in *Review of Progress in QNDE*, vol. 24, pp. 1788–1794, 2005.

[106] Hay, T. R., Royer, R. L., Gao, H., Zhao, X., and Rose, J. L., "A comparison of embedded sensor Lamb wave ultrasonic tomography approaches for material loss detection," *Smart Mater. Struct.*, vol. 15, pp. 946–951, 2006.

[107] Malinowski, P., Wandowski, T., Trendafilova, I., and Ostachowicz, W., "A phased array-based method for damage detection and localization in thin plates," *Struct. Health Monit.*, vol. 8, no. 1, pp. 5–15, 2009.

[108] Heimiller, R. C., Belyea, J. E., and Tomlinson, P. G., "Distributed array radar," *IEEE Trans. Aerosp. Electron. Sys.*, vol. 19, no. 6, pp. 831–839, 1983.

[109] Flaig, A. and Arce, G. R., "Nearfield spot-beamforming with distributed arrays," in *IEEE Sensor Array and Multichannel Signal Processing Workshop*, pp. 390–394, 2000.

[110] Wang, C. H., Rose, J. T., and Chang, F.-K., "A synthetic time-reversal imaging method for structural health monitoring," *Smart Mater. Struct.*, vol. 13, pp. 415–423, 2004.

[111] Michaels, J. E. and Michaels, T. E., "Enhanced differential methods for guided wave phased array imaging using spatially distributed piezoelectric transducers," in *Review of Progress in QNDE*, vol. 25, pp. 837–844, 2006.

[112] Michaels, J. E., Croxford, A. J., and Wilcox, P. D., "Imaging algorithms for locating damage via *in situ* ultrasonic sensors," in *IEEE Sens. Appl. Symp.*, pp. 63–67, 2008.

[113] Michaels, J. E. and Michaels, T. E., "Guided wave signal processing and image fusion for in situ damage localization in plates," *Wave Motion*, vol. 44, no. 482-492, 2007.

[114] Croxford, A. J., Wilcox, P. D., and Drinkwater, B. W., "Guided wave SHM with a distributed sensor network," *Proc. SPIE*, vol. 6935, no. 69350E, pp. 1–9, 2008.

[115] Su, Z., Wang, X., Chen, Z., Ye, L., and Wang, D., "A built-in active sensor network for health monitoring of composite structures," *Smart Mater. Struct.*, vol. 15, pp. 1939–1949, 2006.

[116] Li, F., Su, Z., Ye, L., and Meng, G., "A correlation filtering-based matching pursuit (CF-MP) for damage identification using Lamb waves," *Smart Mater. Struct.*, vol. 15, pp. 1585–1594, 2006.

[117] Lemistre, M. and Balageas, D., "Structural health monitoring system based on diffracted Lamb wave analysis by multiresolution processing," *Smart Mater. Struct.*, vol. 10, pp. 504–511, 2001.

[118] Su, Z., Wang, X., Chen, Z., and Ye, L., "A hierarchical data fusion scheme for identifying multi-damage in composite structures with a built-in sensor network," *Smart Mater. Struct.*, vol. 16, pp. 2067–2079, 2007.

[119] Su, Z., Cheng, L., Wang, X., Yu, L., and Zhou, C., "Predicting delamination of composite laminates using an imaging approach," *Smart Mater. Struct.*, vol. 18, pp. 1–8, 2009.

[120] Moll, J., Schulte, R. T., Hartmann, B., Fritzen, C.-P., and Nelles, O., "Multi-site damage localization in anisotropic plate-like structures using an active guided wave structural health monitoring system," *Smart Mater. Struct.*, vol. 19, pp. 1–16, 2010.

[121] Kundu, T., Das, S., Martin, S. A., and Jata, K. V., "Locating point of impact in anisotropic fiber reinforced composite plates," *Ultrasonics*, vol. 48, pp. 193–201, 2008.

[122] Grahn, T., "Lamb wave scattering from a circular partly through-thickness hole in a plate," *Wave Motion*, vol. 37, pp. 63–80, 2003.

[123] Michaels, J. E., Lee, S. J., Hall, J. S., and Michaels, T. E., "Multi-mode and multi-frequency guided wave imaging via chirp excitation," *Proc. SPIE*, vol. 7984, no. 79840I, pp. 1–11, 2011.

[124] Rose, J. L., *Waves in Solid Media*. Cambridge University Press, 1999.

[125] Hall, J. S. and Michaels, J. E., "Minimum variance ultrasonic imaging applied to an *in situ* sparse guided wave array," *IEEE Trans. Ultrason., Ferroelectr., Freq. Control*, vol. 57, no. 10, pp. 2311–2323, 2010.

[126] Hall, J. S. and Michaels, J. E., "Computational efficiency of ultrasonic guided wave imaging algorithms," *IEEE Trans. Ultrason., Ferroelectr., Freq. Control*, vol. 58, no. 1, pp. 244–248, 2011.

[127] Michaels, J. E., Hall, J. S., Hickman, G., and Krolik, J., "Sparse array imaging of change-detected signals by minimum variance processing," in *Review of Progress in QNDE*, vol. 28, pp. 642–649, 2009.

[128] Michaels, J. E., Hall, J. S., and Michaels, T. E., "Adaptive imaging of damage from changes in guided wave signals recorded from spatially distributed arrays," *Proc. SPIE*, vol. 7295, no. 729515, pp. 1–11, 2009.

[129] Hall, J. S., McKeon, P., Satyanarayan, L., Michaels, J. E., Declercq, N. F., and Berthelot, Y. H., "Minimum variance guided wave imaging in a quasi-isotropic composite plate," *Smart Mater. Struct.*, vol. 20, no. 2, p. 025013, 2011.

[130] Hammerlin, G. and Hoffmann, K.-H., *Numerical Mathematics*. Undergraduate Texts in Mathematics: Readings in Mathematics, New York: Springer, 1991.

[131] Carlson, B. D., "Covariance matrix estimation errors and diagonal loading in adaptive arrays," *IEEE Trans. Aerosp. Electron. Sys.*, vol. 24, no. 4, pp. 397–401, 1988.

[132] Cox, H., Zeskind, R. M., and Owen, M. M., "Robust adaptive beamforming," *IEEE Trans. Acoust. Speech Signal Process.*, vol. ASSP-35, no. 10, pp. 1365–1376, 1987.

[133] Cho, Y., Hongerholt, D. D., and Rose, J. L., "Lamb wave scattering analysis for reflector characterization," *IEEE Trans. Ultrason., Ferroelectr., Freq. Control*, vol. 44, no. 1, pp. 44–52, 1997.

[134] McKeon, J. C. P. and Hinders, M. K., "Lamb wave scattering from a through hole," *J. Sound and Vib.*, vol. 224, no. 5, pp. 843–862, 1999.

[135] Diligent, O., Grahn, T., BostrÃűm, A., Cawley, P., and Lowe, M. J. S., "The low-frequency reflection and scattering of the S0 Lamb mode from a circular through-thickness hole in a plate: finite element, analytical and experimental studies," *J. Acoust. Soc. Am.*, vol. 111, no. 1, pp. 64–74, 2002.

[136] Lowe, M. J. S. and Diligent, O., "Low-frequency reflection characteristics of the S0 Lamb wave from a rectangular notch in a plate," *J. Acoust. Soc. Am.*, vol. 111, no. 1, pp. 64–74, 2002.

[137] Chang, Z. and Mal, A., "Scattering of Lamb waves from a rivet hole with edge cracks," *Mech. Mater.*, vol. 31, pp. 197–204, 1999.

[138] Zhang, J., Drinkwater, B. W., and Wilcox, P. D., "Defect characterization using an ultrasonic array to measure the scattering coefficient matrix," *IEEE Trans. Ultrason., Ferroelectr., Freq. Control*, vol. 55, no. 10, pp. 2254–2265, 2008.

[139] Mathworks, "Techniques for improving performance: vectorizing loops," *MATLAB User Guide*, 2010.

[140] Mathworks, "Code vectorization guide," *MATLAB Product Support*, 2010.

[141] Eaton, J. W. *GNU Octave Manual*, 2002.

[142] van Dijk, L. E. and Spiel, C. L. *SciLab Bag of Tricks: The SciLab-2.5 Infrequently Asked Questions*, 2000.

[143] Hall, J. S. and Michaels, J. E., "Model-based parameter estimation for characterizing wave propagation in a homogeneous medium," *Inverse Prob.*, vol. 27, no. 3, p. 035002, 2011.

[144] Hall, J. S. and Michaels, J. E., "On a model-based calibration approach to dynamic baseline estimation for structural health monitoring," in *Review of Progress in QNDE*, vol. 28, pp. 896–903, 2009.

[145] Hall, J. S. and Michaels, J. E., "Model-based *in situ* parameter estimation of ultrasonic guided waves in an isotropic plate," in *Review of Progress in QNDE*, vol. 29, pp. 137–144, 2010.

[146] Hall, J. S. and Michaels, J. E., "A model-based approach to dispersion and parameter estimation for ultrasonic guided waves," *J. Acoust. Soc. Am.*, vol. 127, no. 2, pp. 920–930, 2010.

[147] Achenbach, J. D., *Wave Propagation in Elastic Solids*. New York: American Elsevier, 1973.

[148] Strang, G., "The fundamental theorem of linear algebra," *Am. Math. Mon.*, vol. 100, no. 9, pp. 848–855, 1993.

[149] Penrose, R., "A generalized inverse for matrices," *P. Camb. Philol. S.*, vol. 51, pp. 406–413, 1955.

[150] Woodbury, M. A., "Inverting Modified Matrices," *Memorandum Rept. 42, Statistical Research Group, Princeton University*, 1950.

[151] Hall, J. S. and Michaels, J. E., "Analysis of distributed sparse array configurations for guided wave imaging applications," in *Review of Progress in QNDE*, vol. 30, pp. 859–866, 2011.

[152] Hall, J. S., Fromme, P., and Michaels, J. E., "Ultrasonic guided wave imaging for damage characterization," in *Aircraft Airworthiness and Sustainment Conference*, 2011.

[153] Flynn, E. B. and Todd, M. D., "A Bayesian approach to optimal sensor placement for structural health monitoring with application to active sensing," *Mech. Syst. Signal Pr.*, vol. 24, pp. 891–903, 2010.

[154] Flynn, E. B. and Todd, M. D., "Optimal placement of piezoelectric actuators and sensors for detecting damage in plate structures," *J. Intel. Mat. Syst. Str.*, vol. 21, pp. 265–174, 2010.

[155] Fromme, P., "SHM of large structures using guided waves for crack detection," in *Review of Progress in QNDE*, vol. 30, 2011.

[156] Fromme, P. and Sayir, M. B., "Measurement of the scattering of a Lamb wave at a through hole in a plate," *J. Acoust. Soc. Am.*, vol. 111, no. 3, 2002.

[157] Wang, C. H. and Chang, F.-K., "Scattering of plate waves by a cylindrical inhomogeneity," *J. Sound and Vib.*, vol. 282, pp. 429–451, 2005.

[158] Fromme, P., "Influence of guided ultrasonic wave scattering directionality on the detection sensitivity for SHM of fatigue cracks," *Proc. SPIE*, vol. 7650, no. 76501M, pp. 1–10, 2010.

[159] Fromme, P. and Sayir, M. B., "Detection of cracks at rivet holes using guided waves," *Ultrasonics*, vol. 40, no. 1-8, pp. 199–203, 2002.